Jets from Spinning Black Holes in Active Galactic Nuclei

Dissertation

zur

Erlangung des Doktorgrades (Dr. rer. nat.)

der

Mathematisch-Naturwissenschaftlichen Fakultät

der

Rheinischen Friedrich-Wilhelms-Universität Bonn

vorgelegt von

Ioana Duţan

aus

Bukarest, Rumänien

Bonn, im Oktober 2010

Angefertigt mit Genehmigung der Mathematisch-Naturwissenschaftlichen Fakultät
der Rheinischen Friedrich-Wilhelms-Universität Bonn

Promotionskommission:

1. Erstgutachter und Betreuer:	Prof. Dr. Peter L. Biermann, Max Planck Institute for Radio Astronomy, Bonn
2. Zweitgutachter:	Prof. Dr. Uli Klein, Argelander Institute for Astronomy, Bonn
3. Fachnahes Mitglied:	PD Dr. Jörg Pretz, Institute of Physics, Bonn
4. Fachangrenzendes Mitglied:	Prof. Dr. Jens Franke, Mathematical Institute of the University of Bonn

Tag der Promotion: 31 Januar 2011

Diese Dissertation ist auf dem Hochschulschriftenserver der ULB Bonn
http : //hss.ulb.uni − bonn.de/diss_online
elektronisch publiziert. Das Erscheinungsjahr ist 2011.

To my parents.

Acknowledgments

This thesis could not have been completed without the generosity and assistance of a large number of people to whom I would like to express my gratitude.

I am grateful to Peter L. Biermann, my thesis adviser, for the possibility he gave me to work on a subject I like and for his support that he made available in a number of ways. In particular, I would like to thank him for comprehensive and stimulating discussions, valuable suggestions and comments on this thesis and on my other manuscripts.

I am also grateful to the second referee, Uli Klein, for reviewing this thesis. I also thank Jörg Pretz and Jens Franke, who kindly agreed to join the examination committee.

I would like to thank my thesis committee (Peter L. Biermann, Uli Klein, Anton J. Zensus, and Frank Bertoldi) for offering suggestions to solve several problems encountered in my research.

This work was supported by the International Max Planck Research School (IMPRS) for Astronomy and Astrophysics at the Universities of Bonn and Cologne, being performed at the Max Planck Institute for Radio Astronomy, Bonn, in the Theory group. I am also grateful to Gerd Weigelt, the director of the Infrared Astronomy Department, for providing me with financial support during the final stage of this work.

Furthermore, I would like to thank Ken-Ichi Nishikawa, Yosuke Mizuno, and Shinji Koide, my collaborators on General Relativistic Magnetohydrodynamic Simulations of Jet Formation, for providing me with their simulation code and for their scientific support and encouragement. The simulations were performed on a machine at the National Center for Supercomputing Applications at the University of Illinois at Urbana-Champaign, USA, through a research project whose principal investigator is Ken-Ichi Nishikawa. The results of this collaboration are presented in Chapter 4.

I would like to thank Laurenţiu Caramete, my office mate, for providing me with a complete sample of active galactic nuclei, which is a part of the work for his PhD thesis. This has made it possible for me to extend the application of the model for Ultra-high-energy Cosmic Rays developed in Chapter 3 to observational data. I also thank him for his friendship, patience, and help in ways too numerous to mention.

I thank Alex Curuţiu for his expertise whenever I was stuck with a problem in my programs, as well as for his friendship.

I also thank Alan Roy, Iván Aguido, and Manuel Peruchio (from the VLBI group) for insights into observational research of active galactic nuclei.

I am grateful to Michelle Fekety for proofreading this thesis and my other manuscripts, as well as for her friendship and kind assistance in dealing with bureaucratic procedures and many hassles.

It is a pleasure to thank my colleagues and friends for a lot of help, for numerous discussions either related to science or just about life itself, and for creating a friendly atmosphere in which I could enjoy the work at this thesis. Beside those already mentioned, I thank Hyunjoo Kim, Laura Gómez, Sînziana Păduroiu, Leonardo Castañeda, and Traian Popescu, with whom I spent a longer time in Bonn. There are Petru Ghenuche and Valeriu Tudose, abroad, who were there when I needed most. I would also like to thank my best friend back in Romania, Melania Chiciuc, for her never-ending support.

I also acknowledge my Master's thesis co-adviser at the University of Bucharest, Mircea Rusu, for his influence on my studies and more. It is quite difficult to catch in a few

words his qualities as a professor, and as a person in general. It was a real privilege for me to have him as a mentor.

At the end, I would like to thank my father especially for encouraging me in keeping my way and trying harder. I also thank my mother, in memoriam. Many of her words have been guiding me through life.

Contents

Abstract

Relativistic jets are highly collimated plasma outflows that can be present in extragalactic radio sources, which are associated with active galactic nuclei (AGN). Observations give strong support for the idea that a supermassive black hole (BH), surrounded by an accretion disk, is harbored in the center of an AGN. The jet power can be generally provided by the accretion disk, by the BH rotation, or both. Such powerful jets can also be sites of the origin of ultra-high-energy cosmic rays (UHECRs). In this work, we study the jet formation from rapidly-spinning BHs in the framework of General Relativity and General Relativistic Magnetohydrodynamics, as well as the acceleration of UHECRs in AGN jets.

Magnetic connection model for launching relativistic jets from a Kerr black hole: Despite intense efforts to understand the processes responsible for formation of the AGN jets, we still face the problem of exactly how to explain them. Here, we present a model for launching relativistic jets in active galactic nuclei (AGN) from an accreting Kerr black hole (BH) through the rotation of the space-time in the BH ergosphere, where the gravitational energy of the accretion disk, which can be increased by the BH rotational energy transferred to the ergospheric disk via closed magnetic field lines that connect the BH to the disk (BH-disk magnetic connection), is converted into jet energy. The main role of the BH-disk magnetic connection is to provide the source of energy for the jets when the mass accretion rate is very low. We assume that the jets are launched from the ergospheric disk, where the rotational effects of the space-time become much stronger. The rotation of the space-time channels a fraction of the disk energy (i.e., the accreting rest mass-energy plus the BH rotational energy deposited into the disk by magnetic connection) via a magnetic flow into a population of particles that escape from the disk surfaces, carrying away mass, energy, and angular momentum in the form of jets and allowing the remaining disk gas to accrete. We use general-relativistic conservation laws for the structure of the ergospheric disk to calculate the mass flow rate into the jets, the launching power of the jets, and the angular momentum transported by the jets. As far as the BH is concerned, it can (i) spin up by accreting matter and (ii) spin down due to the magnetic counter-acting torque on the BH. We found that a stationary state of the BH ($a_* = \text{const}$) can be reached if the mass accretion rate is larger than $\dot{m} \sim 0.001$. For $\dot{m} < 0.001$, the BH spins down continuously, unless a large amount of matter is provided. In this picture, the maximum AGN lifetime can be much longer than $\sim 10^7$ yr when using the BH spin-down power. Next, we derive (i) the relation between the BH spin-down power and the particle maximum energy in the jets and (ii) the relation between the BH spin-down power and the observed radio flux-density from flat-spectrum core sources. In the limit of the spin-down power regime, the model proposed here can be regarded as a variant of the Blandford-Znajek mechanism, where the BH rotational energy is transferred to the ergospheric disk and then used to drive the jets rather than transported, via Poynting flux, to remote astrophysical loads from where matter-dominated jets can form. As a result, the jets driven from an ergospheric disk can have a relatively strong power for low mass accretion rates.

Ultra-high-energy Cosmic Ray contribution from the spin-down power of black holes: The possibility to trace sources of UHECRs is of crucial importance to particle astronomy, as it can improve constraints on Galactic and extragalactic magnetic fields, set upper limits on Lorentz invariance, and probe the AGN engine as an acceleration mechanism. A considerable improvement was achieved by trying to identify the nature of

UHECRs using ground detector arrays' data as, for instance, Auger data. We propose a model for the UHECR contribution from the spin-down power of BHs in low-luminosity active galactic nuclei (LLAGN) with energy flow along the jet $L_{\rm jet} \leqslant 10^{46}$ erg s^{-1}. This is in contrast to the opinion that only powerful AGN can accelerate particles of energy $\geqslant 100$ EeV. Assuming that the UHECRs (protons) are accelerated (with a power-law energy distribution) by shocks in the AGN jets, one can evaluate the maximum energy of the particles under both the spatial limit and synchroton emission losses. Under the conditions of the proposed model, we rewrite the equations which describe the synchrotron self-absorbed emission of a non-thermal particle distribution to obtain the observed radio flux-density from flat-spectrum core sources. In general, the jet power provides the UHECR luminosity and so, its relation to the observed radio flux-density. As a result, we obtain the expressions for the minimum luminosity and flux of the UHECR as a function of the observed radio flux-density and jet parameters. First, we apply the model to Cen A and M87, two possible sources of UHECRs, and then use a complete sample of 29 steep-spectrum radio sources (Caramete 2010), with a total flux density greater than 0.5 Jy at 5 GHz, to make predictions for the maximum particle energy, luminosity, and flux of the UHECRs. We found that the particles can be accelerated to energies higher than 100 EeV, despite the fact that the jet power is $\leqslant 10^{46}$ erg s^{-1}. The present Auger data indicate that Cen A is a noteworthy source of UHECRs, and our model calculations suggest that Cen A is indeed a very strong candidate. However, the UHECR-AGN correlation should be substantiated with further statistics, from Auger and other observatories.

General relativistic magnetohydrodynamics simulation of jet formation from Kerr black holes: The first general relativistic magnetohydrodynamics (GRMHD) code for numerically simulating jet formation from accreting BHs was developed by Koide et al. (1999) using the conservation form of the ideal GRMHD equations on fixed geometry (either Schwarzschild or Kerr). Using the GRMHD code of Koide et al., we present numerical results of jet formation from a thin accretion disk co-rotating with a rapidly-spinning BH ($a_* = 0.95$). We found that the jet consists of (i) a gas pressure-driven component and (ii) an electromagnetically-driven component which is developed inside the former. This is different from the previous results obtained by Koide et al., where the jet has two separately components (the pressure-driven and electromagnetically-driven components). As the time evolves, the disk plasma loses angular momentum by the magnetic field torque and falls towards the BH. When the rapid infall of plasma encounters the disk plasma that is decelerated by centrifugal forces near the BH, a shock is produced inside the disk at $\sim 3\,r_{\rm S}$ ($r_{\rm S}$ denotes the Schwarzschild radius). The high pressure behind the shock pushes the plasma outward by gas-pressure forces and pinches it into a collimated jet. As a result, a gas pressure-driven component of the jet is produced. On the other hand, the electromagnetically-driven component of the jet has two origins: one associated with the extraction of the BH rotational energy in the BH ergosphere and the other one with the twisting of the magnetic field far from the BH. The maximum velocity of the plasma in the jet is $\sim 0.4\,c$, which is considerable lower than the velocity of the inner parts of some AGN jets for which the observations indicate relativistic speeds. However, the outer parts of the jet can have mildly- and sub-relativistic speeds. Despite this low velocity in the inner part of the jet, the electromagnetically-driven component of the jet is important by itself as it shows that the extraction of the rotational energy from the BH via a Penrose-like process in the BH ergosphere is possible, though for transient jets. Further development of the code may accomplish the attempt to fully match the AGN observational data.

Acronyms

ADM:	Arnowitt-Deser-Misner (formalism)
AGN:	Active Galactic Nuclei
BLRG:	Broad-Line Radio Galaxy
BH:	Black Hole
CFL:	Courant-Friedrichs-Lewy (stability condition)
CR:	Cosmic Ray
FIDO:	FIDucial Observer
GR:	General Relativity
GRB:	Gamma-Ray Bursts
GRMHD:	General Relativistic MagnetoHydroDynamics
GZK:	Greisen-Zatsepin-Kuzmin (cutoff)
HiRes:	High Resolution (Fly's Eye experiment)
LLAGN:	Low Luminosity Active Galactic Nuclei
MHD:	MagnetoHydroDynamics
MRI:	MagnetoRotational Instability
LINER:	Low-Ionization Nuclear Emission-line Region (galaxy)
NLRG:	Narrow-Line Radio Galaxy
OVV:	Optically Violent Variable (quasars)
PDE:	Partial Differential Equation
QUASARS:	QUAuasiStellar Radio Source
SED:	Spectral Energy Distribution
STVD:	Simplified Total Variation Diminishing (method)
TVD:	Total Variation Diminishing (method)
UHE:	Ultra High Energy
UHECR:	Ultra-High-Energy Cosmic Ray
VCV:	Véron-Cetty & Véron Catalog
VLBI:	Very Long Baseline Interferometry
ZAMO:	Zero Angular Momentum Observer

Most Used Mathematical Symbols

a:	BH spin (angular momentum)
$a_* = a/r_\mathrm{g}$:	BH spin parameter
α:	lapse function in 3+1 split
B:	strength of magnetic field
$\beta = v/c$:	velocity in units of speed of light
$\beta = p_\mathrm{gas}/p_\mathrm{mag}$:	plasma beta
β^i:	shift vector in 3+1 split
c:	speed of light
$\mathcal{D}$:	general-relativistic correction function
$\mathcal{D}_\mathrm{j}$:	Doppler factor of the jet
E:	particle's energy
$E^\dagger$:	particle's specific energy
η:	efficiency of jet launching
F_CR:	CR flux
$g_{\mu\nu}$:	metric tensor
G:	Newtonian gravitational constant
γ:	Lorentz factor of the jet
γ_{ij}:	spatial 3-metric
Γ:	specific heat ratio
h:	specific enthalpy
L:	energy flow along the jet
L_CR:	CR luminosity
$L^\dagger$:	particle's specific angular momentum
M:	BH mass
$\dot{M}$:	mass accretion rate
$\dot{M}_\mathrm{Edd}$:	Eddington mass accretion rate
$\dot{M}_\mathrm{jets}$:	mass outflow rate (in the jets)
$\dot{m} = \dot{M}/\dot{M}_\mathrm{Edd}$:	mass accretion rate in units of $\dot{M}_\mathrm{Edd}$
Ω_D:	angular velocity of the accretion disk
Ω_H:	angular velocity of the BH
p:	spectral index
p:	gas pressure
P_jets:	power of the jets
q_jets:	mass outflow parameter
r:	radial coordinate
$r_\mathrm{g} = GM/c^2$:	gravitational radius
r_H:	radius of the BH horizon
r_ms:	radius of the innermost stable (circular) orbit
r_sl:	radius of the stationary limit surface
$r_\mathrm{S} = 2GM/c^2$:	Schwarzschild radius
ρ:	gas density
$T^{\mu\nu}$:	energy-momentum tensor
τ_ν:	optical depth

Preface

Active galactic nuclei are galaxies whose nucleus (or central core) spectrum cannot be explained by standard stellar physics, e.g., a dense stellar cluster of massive stars or a stellar mass BH. The most successful general interpretation is now a spinning supermassive BH ($M \sim 10^7 - 10^9\,M_\odot$), as a result of the discovery of compact X-ray sources (in the late sixties and early seventies), which was followed by a large amount of work on BHs and accretion onto BHs from both theoretical and observational point of views. The BH is supposed to be surrounded by a rotating accretion disk, which supplies the BH with gas and magnetic fields. A distinctive feature of an AGN is the jet, which can extend far beyond the host galaxy, in some cases as much as a few Mpc (e.g., ~ 4.38 Mpc for 3C 236 and ~ 4.69 Mpc for J1420 – 0545). Curtis (1918) was the first to observe a jet in the M87 galaxy, which he described as a "curious straight ray" being "apparently connected with the nucleus by a thin line of matter. The ray is brightest at its inner edge, [...]."

One of the major processes at the center of an AGN is the accretion of disk matter onto the BH. The disk matter is heated and the excessive radiation energy is emitted, due to the viscosity of the accretion disk. Close to the BH, the accretion disk can convert the rest mass-energy of the infalling matter onto the BH into output energy of either radiation or jets. Theoretically, up to 42 percent of the rest mass-energy of the accreting matter can be converted into radiation if the BH rotates at its maximum spin (Bardeen 1970). The fact that quasars[1] are more abundant in the early universe suggests that, when the BH has had little matter available in the host galaxy to consume, they stop shining (i.e., the ratio between their nucleus luminosity and the Eddington luminosity[2] becomes less than about 0.01). The jet formation is usually associated with a mass accretion rate onto the BH ($\dot{M}$) that is less than the Eddington accretion rate [$\dot{M}_{\rm Edd} = L_{\rm Edd}/(\varepsilon c^2)$, where ε is the efficiency of converting the accretion disk energy into radiation, usually being taken as 0.1]. When the mass accretion rate is $10^{-2}\dot{M}_{\rm Edd} \lesssim \dot{M} \lesssim \dot{M}_{\rm Edd}$, the jet production in AGN might be intermittent [i.e., it might be in a flaring mode (e.g., Ulvestad & Ho 2001)], as it has been observed in microquasars for more than one decade (Pooley & Fender 1997; Rodríguez &

[1]Quasars point to an early epoch in the history of the universe when the universe was less than a billion years old and a sixth of its current size. At the beginning of the sixties, observations of certain radio-emitting objects, thought to be stars, resulted in spectra which showed unusual properties for a star. In 1963, these spectra were explained by very large Doppler-shifted emission lines. This amount corresponds to a receding velocity which is a large fraction of the speed of light, therefore these objects must have emitted the now-a-days observed radiation a very long time ago. Since in a short exposure optical image one saw only the compact nucleus, these objects were indistinguishable from a star, and they were, therefore, termed quasistellar radio sources (quasars). Later on, it became clear that only a small fraction of quasars, about 10 percent, have hundreds to thousands of times stronger radio emission than optical emission. Historically, the first identification of an object (3C 295) with a member of a galaxy cluster at an unusual redshift was obtained by Minkowski (1960). In 1962-1963, independent studies of the objects 3C 273 and 3C 48 by Hazard et al. (1963), Oke (1963), Schmidt (1963), and Greenstein & Matthews (1963) suggested that these objects can be of extragalactic origin, with redshifts reflecting the Hubble expansion. It turns out that these objects were the first quasars ever discovered.

[2]For a system with a spherical accretion, the Eddington luminosity represents a theoretical upper limit to its luminosity, and it is obtained by equating the outward nuclear continuum radiation pressure with the inward gravitational force. This procedure yields: $L_{\rm Edd} = 1.3 \times 10^{47}(M/10^9 M_\odot)$ erg s^{-1}. Though, super-Eddington luminosities were observed in some accreting binary systems [e.g., King (2010) and references therein].

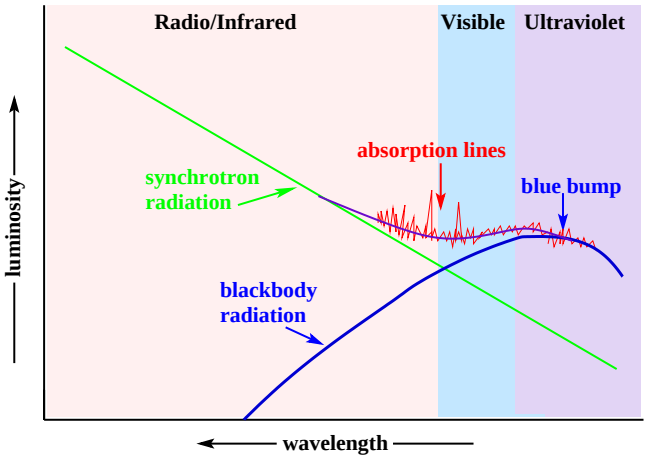

Figure 0.1: Schematic representation of the typical spectrum of a quasar.

Mirabel 1997). The jets have the most obvious observational effects in the radio band, where radio interferometry arrays can be used to study the synchrotron radiation emitted by the jets down to sub-parsec scales. However, they radiate in all wavelengths from radio to γ-ray via the synchrotron and inverse-Compton processes. The synchrotron emission observed from the AGN jets implies that magnetic fields must be present in the jets as well. From radio polarization observations, the magnetic field in the jets looks relatively ordered.

Over the last four decades or so, a considerable amount of theoretical work has been aimed at explaining the role of the BH and its accretion disk in the mechanism of jet formation in AGN, with particular emphasis on the power source of such a jet. The AGN jets are believed to be powered by (i) the accretion disk, (ii) the BH rotation, or (iii) both. In the first case, the jets may either be launched only electromagnetically (e.g., Blandford 1976; Lovelace 1976) or by (General Relativistic) Magnetohydrodynamics processes at the inner region of the accretion disk (e.g., Blandford & Payne 1982; Koide et al. 1999; McKinney & Gammie 2004). In the second case, the jets may be powered by the Blandford-Znajek mechanism (Blandford & Znajek 1977); that is, the energy flux of the jets is provided by conversion of the BH rotational energy into Poynting flux, which is then dissipated at large distances from the BH by current instabilities, as these instabilities become important when the jet slows down (Lyutikov & Blandford 2002). For the third case, we developed a model that is presented in Chapter 2. [But also see Wang et al. (2008).] Despite intense efforts to understand the AGN jets by either theoretical modeling and numerical simulation or by observation, clear answers to numerous questions have not been found yet, such as those related to the processes responsible for their formation, acceleration, and collimation, as well as their composition of normal or pair plasma and magnetic fields.

The majority of AGN shows broad emission over the entire electromagnetic spectrum. Their broad-band spectrum [or spectral energy distribution (SED)] is a combination of thermal and non-thermal synchrotron emission and is by far wider than that of a normal galaxy. The spectra can provide clues about the physical processes taking place in the AGN and help distinguish different types among the AGN. Furthermore, many AGN show strong emission lines and variability of their radiation flux. AGN spectra can show (i) strong optical emission lines (in many cases with abnormal line-intensity ratios); (ii) patterns of high or low-ionization, (iii) a power-law (of different slopes) in the radio/infrared band due to the synchrotron emission of the jets (which can extend to optical and X-ray bands for very powerful jets), (iv) an infrared excess from the thermal radiation, which is re-emitted by

dust grains in the torus (see below), (v) an unusual ultraviolet excess (called the "big blue bump") that ranges from the visual to ultraviolet band and peaks at about 3000 Å , which is produced by thermal radiation from the accretion disk, (vi) a soft X-ray excess, whose origin is under debate (e.g., Miniutti et al. 2008), or (vii) very densely distributed narrow absorption lines in the quasar spectra which are thought to be produced by intervening, tenuous intergalactic clouds at various redshifts (see Fig. 0.1 for the typical spectrum of a quasar). Furthermore, a good indicator of an AGN is the presence of a compact radio core, when available.

Observations give strong support for a unification scheme of the AGN. This unification is based (i) on the bolometric luminosity of the source ($L_{\rm bol}$), (ii) on the Eddington ratio ($L_{\rm bol}/L_{\rm Edd}$), (iii) on the radio properties of the source, and (iv) on the orientation of the source with respect to the line of sight, provided that the symmetry axis of the AGN is identified with the symmetry axis of the jet[3] (Antonucci 1993; Urry & Padovani 1995). Since all these objects present quite heterogenous properties, it is difficult to construct a single scheme to unify them. However, they still can be separated into classes, and some of these classes might share the same underlying physics, looking different just because they are seen from other angles of view. In a simple manner, the AGN can be (i) of high-luminosity or low-luminosity,[4] (ii) of Type 1 (unobscured) or Type 2 (obscured), or (iii) radio-loud or radio-quiet. These classes will be discussed further in this section. One should keep in mind that we do not know with certainly whether the low-luminosity AGN are or not scaled-down versions of the high-luminosity ones. They might be separated by different physical and spectroscopical properties. Figure 0.2 shows a schematic representation of the AGN from the unification point of view.

The bolometric luminosity of a source is derived directly from its SED, when the measurements are available. Otherwise, $L_{\rm bol}$ is estimated by applying some bolometric corrections derived from a set of well-observed calibrator sources (Ho 2008). This is usually obtained by taking the optical B-band (which is centered at the wavelength $\lambda = 4400$ Å) as a reference point, which, in the case of low-luminosity AGN, is not a suitable technique. This is in part because their optical continuum measurements are scarce and the optical/UV region of the SED depends on the source extinction; in this case an extrapolation from the bolometric luminosity in the X-band is typically used. Based on the bolometric luminosity, AGN are classified as (i) **high-luminosity AGN** (e.g., quasars) with $L_{\rm bol} \sim 10^{46} - 10^{48}$ erg s^{-1} or (ii) **low-luminosity AGN** (LLAGN) with $L_{\rm bol} < 10^{45}$ erg s^{-1}, going as far down as $\sim 10^{37}$ erg s^{-1} (Ho 2009). From lower to higher luminosity, the LLAGN are, for instance, absorption-line nuclei, transition objects, low-ionization nuclear emission-line region galaxies (LINERs),[5] and Seyfert galaxies (see below). Radio galaxies are also found among the LLAGN (e.g., M87 and Centaurus A). In the spectra of LLAGN, the big blue bump is very weak or absent, which is in contrast to the high-luminosity AGN. LLAGN are much more common as they are associated with nearby AGN, and therefore easier to

[3]If every AGN episode involves a spin-flip of the central BH, then there is a third axis.

[4]Sometimes the highest luminosity is in a waveband which we do not know. Until rather recently we did not know that there were AGN which emit most in gamma rays. It can be possible that there are AGN that emit most in neutrinos.

[5]Here, we include the LINERs in discussion, although newer interpretations of the LINER ionization mechanism indicate that galaxies with LINER spectra might not be AGN at all [e.g., Schawinski et al. (2010) and references therein].

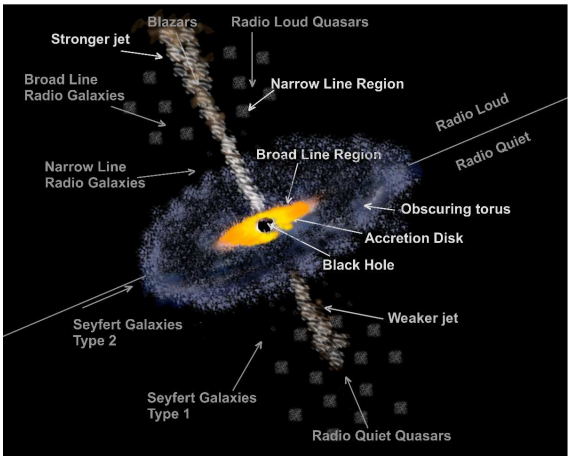

Figure 0.2: AGN unification scheme. Many of the differences among the AGN may be only due to a different orientation of the source with respect to the observer. Grey arrow indicates the viewing angle.

sample. By comparison, a normal galaxy has a bolometric luminosity $\lesssim 10^{42}$ erg s^{-1}, where the bulk of its luminosity is emitted in the optical band and is mainly produced by stars. Therefore, for very low-luminosity AGN, good techniques must be employed in order to separate the optical emission of the nucleus from that of its host galaxy.

The distinctive features of AGN are the broad-line regions (BLRs), as well as the narrow-line regions (NLRs), whose major ionization mechanism is the photoionization by the continuum radiation produced by the accretion disk. Consequently, these regions produce broad lines (with widths up to 10^4 km s^{-1}) and narrow lines (with a width ~ 100 km s^{-1}), respectively, in the AGN spectra. A key element in the unification scheme is the obscuring dusty torus, or other geometrical form. A direct view to the central BH and to the BLRs results in **type 1 AGN**, whereas a blocked view of the BLRs yields **type 2 AGN**. In the latter case, the existence of hidden BLRs can be revealed in polarized light (Antonucci 1993), as well as through X-ray spectroscopy Mushotzky (1982); Lawrence & Elvis (1982). Therefore, the two types of AGN might be the same phenomenon, but they look different only because the observer orientation with respect to the dusty torus is not the same. The size of the obscuring torus was originally predicted by theoretical calculations to be hundreds of parsecs, where the (compact) torus was associated with a dusty, optically thick region of a hydromagnetic wind flowing outward from the middle part of the accretion disk. However, high-resolution infrared observations indicate that the torus size is just about a few parsecs (Elitzur 2006). Elitzur explained that this difference occurs as a result of the clumpy nature of the torus.

Very low-luminosity AGN lack BLRs (Laor 2003). This might occur as a result of the underlying physics, which may impose an upper limit to the line width. A possible explanation might be provided through the model developed by Elitzur & Shlosman (2006). Their model predicts that for a bolometric luminosity below $\sim 10^{42}$ erg s^{-1}, the dusty torus disappears and the release of the accreting rest mass-energy switches from hydromagnetic disk winds to radio jets.

AGN can also be classified as **radio quiet** or **radio loud** based on their radio properties, which are, in fact, due to the synchrotron emission of the jets. This classification is usually made based on the value of the radio loudness parameter (R), which is defined as the ratio of observed radio-to-optical flux density.[6] In many studies of the radio loudness

[6]The observed flux density (F_ν) is defined as the observed flux (F) per observing frequency interval ($\Delta\nu$).

of AGN, the radio flux was measured at 5 GHz and the optical flux in the B-band. The radio-quiet AGN ($R \sim 0.1 - 1$) are much more numerous than the radio-loud AGN ($R \sim 100 - 1000$), where a deficit of sources is shown in between of them (e.g., Kellermann et al. 1989; Barvainis et al. 2005). Another criterion for the radio loudness of AGN was proposed by Miller et al. (1990), which is based only on the radio luminosity of the source; i.e., the delimitation between radio-quiet and radio-loud AGN is set to the radio luminosity at 5 GHz of $P_{5\mathrm{GHz}} \sim 10^{25}$ W Hz^{-1} sr^{-1} (10^{32} erg s^{-1} Hz^{-1} sr^{-1}).

Powerful jets usually end in a strong shock against the intergalatic medium at the so-called hotspot, and then the outflow plasma inflates the lobes of the source. For radio-loud AGN, the contribution from the jets and lobes dominates the luminosity of the AGN, at least in the radio band. In the case of radio-quiet AGN, the radio emission is rather weak and the morphology of the jet is different from that of the radio-loud sources, in the sense that the jet usually does not end in a strong shock at the hotspot but it is rather disrupted relatively close to the host galaxy. The reason for observing these two types of AGN may not necessarily imply just a weak jet; in principle, it could also be due to a unusual cosmic-ray electron spectrum. Under the assumption that the jets are powered by the Blandford-Znajek mechanism, Blandford (1990) suggested that the observed radio loud/quiet dichotomy might be explained based on the hypothesis that the jets in radio-loud AGN could be driven by rapidly-spinning BHs, whereas the jets in radio-quiet AGN are driven by slowly-rotating BHs. This is also known as the "spin paradigm." It is known that the radio galaxies (which are radio-loud AGN) reside in giant ellipticals and Seyfert galaxies (which are radio-quiet) in disk (spiral and lenticular) galaxies [e.g., Ho & Peng (2001) and references therein]. Sikora et al. (2007) studied the population of radio loud/quiet AGN and showed that, when the total radio emission of the AGN is considered, the AGN split into two different populations. Specifically, the AGN hosted by giant elliptical galaxies can be about 1000 times louder than the AGN hosted by disk galaxies. This "spin paradigm" can also be related to the cosmological evolution of BHs (i.e., merging and accretion histories) in their host galaxies (Volonteri et al. 2007), since the galaxies themselves (ellipticals or disks) evolved in a different manner.

Radio-quiet AGN have (i) high bolometric luminosity like radio-quiet quasars, which usually reside in giant elliptical galaxies, and (ii) low bolometric luminosity like Seyfert galaxies (Seyfert 1943), which are mainly found in spirals, as well as LINERs. There are two types of Seyfert galaxies: Type 1 Seyfert galaxies, which have two sets of emission lines in their optical spectra, narrow and broad lines, and Type 2 Seyfert galaxies, which show only the narrow line component. Seyfert 1s are predominantly more luminous radio sources than Seyfert 2s (Ulvestad & Ho 2001), and their upper bolometric luminosity is $\sim 10^{45}$ erg s^{-1}. By analogy with Seyfert galaxies, radio-quiet quasars are of (i) type 1, which are optically-unobscured and their spectra show the blue bump, as well as the broad emission lines, and (ii) type 2, which are obscured having quasar-like luminosities

The observed radio flux represents the rate of flow of radio waves, being equal to $F = L/4\pi d^2$, where L is the source luminosity and d is the distance to the source. If L refers to the observed monochromatic luminosity at one specific frequency, it has the units erg s^{-1} Hz^{-1}. Instead, if L refers to the integrated luminosity over a corresponding frequency band, it has the units erg s^{-1}. Observationally, the AGN radio emission can be either extended or core-dominated, the latter being specified by the radio flux at an intermediate frequency (~ 1 GHz) which is dominated by that of a single radio emission component whose size is ~ 1 kpc (Blandford & Königl 1979). For beamed emission, the observed flux is enhanced by the Doppler factor to a power which depends on the structure of the jet (see Chapter 3). If the source is extended, the observed flux is also taken per steradian.

but not strong optical nuclear continuum or broad line emission. Type 2 quasars might be the evolutionary precursors of type 1 quasars; however, they are intrinsically different [e.g., Vir Lal & Ho (2010) and references therein]. An intriguing question is whether there are type 2 quasars at high luminosity as well.

Radio-loud AGN have (i) high bolometric luminosity like radio-loud quasars, optically violent variable (OVV) quasars, and broad-line radio galaxies[7] (BLRGs), and (ii) low-luminosity like the narrow-line radio galaxies (NLRGs), which have emission-line spectra similar to those of Seyfert 2s (e.g., M87 and Centaurus A) and the BL Lac objects. BL Lac objects show a lack of strong optical emission or absorption lines in their spectra. On the other hand, the OVVs show large variations ($> 0.1\,\mathrm{mag}$) in their optical flux on short timescales (e.g., a day). Collectively, BL Lac objects, OVVs, and highly polarized quasars are called blazars. They are mainly described as rapidly variable, having polarized optical, radio, and X-ray emission. All known blazars are radio sources which have a high radio luminosity combined with a flatness of their radio spectrum and show apparent superluminal motions. Eddington ratios of the BL Lac objects are generally lower than those of the radio-loud quasars, with a rough separation at $L_{\mathrm{bol}}/L_{\mathrm{Edd}} \sim 0.01$.

In the view of the standard unification scheme of AGN, Seyfert 1s and BLRGs may differ from Seyfert 2s and NLRGs, respectively, only by the orientation of the obscuring torus. BL Lac objects and OVVs are both face-on versions of radio sources. In other words, the compact radio sources are extended radio sources viewed along their relativistic jets, where the relativistically Doppler-boosted emission from the innermost parts of the jet exceeds the unboosted emission from the surrounding extended radio source. Furthermore, LLAGN do not seem to follow the unification scheme since the BLR, as well as the obscuring torus, is actually missing and not just hidden (Elitzur & Ho 2009). However, further characteristics of AGN will continue to be revealed as theoretical models and observational techniques improve. Nevertheless, whatever difficulties are posed when constructing a unification scheme of AGN, the presence of BHs in the heart of AGN and their spectacular jets which mark the dynamics of AGN is well established.

In this work, we try to provide new insights into the physics of jet formation from spinning BHs at the center of an AGN, as well as into the UHECR acceleration process by such a jet. In the beginning, we give a short introduction to rotating (Kerr) BHs. In Chapter 2, we present a model for launching relativistic jets in AGN from the ergospheric region of an accretion disk surrounded a Kerr BH, as a fraction of the disk energy (i.e., the accreting rest mass-energy plus the BH rotational energy transferred to the ergospheric disk via BH-disk magnetic connection) is converted into jet energy. In Chapter 3, we propose a model for ultra-high-energy cosmic ray contribution from the spin-down power of BHs in LLAGN. In Chapter 2, we present General Relativistic Magnetohydrodynamics numerical results of jet formation from a rapidly-spinning BH. In the end, we present an outlook and describe future plans.

[7]The radio galaxies were first observed in the forties and have become well known since the mid-fifties, by which time the Third Cambridge Catalog (3C) had been released. Radio galaxies can be extended (e.g., Cygnus A) or core-dominated (e.g., blazars). Fanaroff & Riley (1974) classified extended radio galaxies according to their radio morphology. They determined the ratio between the two brightest peaks and the total extent of the source, and then classified the sources having a ratio lower than 0.5 as class I and the sources with a ratio greater than 0.5 as class II. These classes have been called FR-I and FR-II ever since. More specifically, the brightest radio-emitting region is located near the center of the source in FR-Is (e.g., Centaurus A), but at the extremities of the sources in FR-IIs (e.g., Cygnus A). Furthermore, in FR-I the extended emission is usually not easily detected, since its surface brightness is so weak.

Chapter 1

Introduction to Kerr Black Holes

1.1 Introduction

Albert Einstein's theory of general relativity is the extension of the special relativity to non-inertial frames. Its formulation has its root in the so-called weak principle of equivalence (Galileo principle of equivalence); that is, in a gravitational field, all bodies fall with the same acceleration. In general relativity, the Minkowski space-time (of special relativity) is replaced with a curved (pseudo-)Riemannian space-time, in which there are generally no preferred coordinate systems. There are two results of special relativity important for general relativity: (i) the intrinsic properties of space-time are described by the metric and (ii) the trajectories of the free-falling test particles[1] are time-like geodesics of that metric. But in a curved space-time, initially parallel geodesics do not remain parallel. The same thing happens to two free-falling observers who are initially at rest in a non-uniform gravitational field. They will not remain at rest with respect to each other; therefore, their geodesics will not remain parallel. This observation is the key idea in general relativity, which is to identify the free-falling test particles in a gravitational field with the inertial observers of special relativity. Consequently, in general relativity the metric describes the gravitational field by specifying (through its time-like geodesics) the motion of the free-falling observers.

The space-time of general relativity is a four-dimensional differentiable manifold endowed with a metric. Generally, manifolds are mathematical tools for analyzing a surface by describing it as a collection of overlapping, simple surfaces smoothly related to each other. The overlapping of simple surfaces makes it easier to move from one surface to another. Therefore, in curved space-time, one needs to consider coordinate patches (sub-regions of space-time which can be covered by one coordinate system) with overlap transition functions that cover the entire space. Let us consider two events, say A and B, very close to each other, where the difference in each of their four generalized coordinates $(x^\mu, \mu = 0, 1, 2, 3)$ is an infinitesimal quantity. The "distance" between these events is given by

$$ds^2 = g_{\mu\nu} dx^\mu dx^\nu, \tag{1.1}$$

where the quantities $g_{\mu\nu}$ are the components of the metric tensor. The metric tensor

[1] A test particle is defined as having no charge, negligible gravitational binding energy compared to its rest mass, and negligible angular momentum, being small enough that inhomogeneities of the gravitational field within its volume have a negligible effect on its motion.

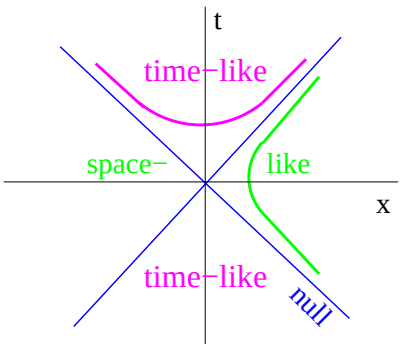

Figure 1.1: The space-time diagram for generalized coordinates.

at each point of the space-time is covariant, symmetric ($g_{\mu\nu} = g_{\nu\mu}$), and nondegenerate ($\det g_{\mu\nu} \neq 0$), with a signature of either -2 or +2, depending on convention.

For any vector v^μ, the metric assigns the real number $||v||^2 = g_{\mu\nu}v^\mu v^\nu$, where $||v||$ is the norm of the vector. Since the space-time in general relativity is a pseudo-Riemannian manifold, the vector squared norm can be positive, negative, or null, and consequently, the vector is called time-like, space-like, or null.[2] The space-time diagram for generalized coordinates is shown in Fig. 1.1.

In Riemannian geometry, a key notion is the connection (or parallel transport), which allows one to compare what happens at two distant points of a curved space. The connection coefficients (or Christoffel symbols) can be calculated directly from the metric and its first derivatives, though they are not the components of a tensor themselves. The derivative of a tensor on a differentiable manifold is called the covariant derivative and represents the generalization of the ordinary partial derivative in the Euclidean space to an arbitrary manifold.

The theory of general relativity is a result of Einstein's attempt to find the relativistic equivalent of Poisson's equation $\nabla^2\varphi = -4\pi G\rho$, where φ is the gravitational potential of a distribution of matter with the density ρ and G is the constant of gravitation. Heuristically, the first step is to replace the mass density with the time-time component of the tensor describing a physical system, in the limit of a weak field. The tensor in question is the stress energy-momentum tensor of the matter, $T^{\mu\nu}$. The second step is to look for a tensor whose components involve the metric tensor and its first and second derivative, assuring a second-order partial differential equation generalizing the Poisson equation, whose divergence vanishes. The quantity which distinguishes between a flat and curved space-time is the Riemann tensor, whose trace is the Ricci tensor $R_{\mu\nu}$. In covariant form, Einstein's equations read

$$\boxed{R_{\mu\nu} - \frac{1}{2}g_{\mu\nu}R = \frac{8\pi G}{c^2}T_{\mu\nu}}, \tag{1.2}$$

where c is the speed of light. The left hand side of the Eq. 1.2 represents the so-called Einstein tensor $G_{\mu\nu}$, and $R = R^\mu_\mu = g^{\mu\nu}R_{\mu\nu}$ is the curvature scalar. The covariant derivative of both tensors $G_{\mu\nu}$ and $T_{\mu\nu}$ vanishes. Equation 1.2 shows that the gravitational field can be described by a purely geometric quantity, its source being the matter tensor.

[2]The metric can have the signature -2, i.e., the signs of the diagonal components are, in order, (+ - - -), thus, the squared norm is positive for time-like vectors and negative for space-like vectors. When the metric has the signature +2 (- + + +), the squared norm is negative for time-like vectors and positive for space-like vectors.

In general relativity, there is complete freedom in choosing the coordinate system; i.e., a given space-time can be represented by different coordinates. Even though the metric tensor components depend on the coordinate system, the space-time itself does not. The physical events happen independently of our observations, as Einstein stated; therefore, it must be possible to express physical laws that take the same form whatever coordinate system one chooses. The laws are called covariant, and Einstein's principle is the principle of general covariance. Furthermore, all physical laws that hold in flat space-time can be expressed in terms of vectors and tensors, provided that the derivatives are replaced with the covariant derivatives.

Schwarzschild solution

The first solution of the Einstein's vacuum field equations was found by Schwarzschild (1916). It is assumed that the field outside of a distribution of mass M does not change with time and has a spherical symmetry. Schwarzschild started from a general line element for the assumed symmetry and, then, determined the metric coefficients by integrating the field equations. He then found the line element that forms the exact solution of Einstein's equation with a suitable transformation of the rectangular-like coordinates to the spherical-like coordinates (r, θ, ϕ, and t). The latter coordinates are called the Schwarzschild coordinates, and the frame of reference that they form is called the Schwarzschild reference frame. The frame is static and non-deformable, and it can be thought as a coordinate lattice formed by weightless rigid robes which fill the whole space-time. The robes intersections give spatial positions, and at each intersection there is a clock which can be synchronized with all the others by sending and receiving light signals. The radial coordinate r is defined through the surface area $4\pi r^2$ of the sphere of constant r. The point given by $r = 0$ represents the center of the symmetry. The metric can be rewritten as

$$\boxed{ds^2 = -\left(1 - \frac{r_\mathrm{s}}{r}\right) dt^2 + \left(1 - \frac{r_\mathrm{s}}{r}\right)^{-1} dr^2 + r^2 \left(d\theta^2 + \sin^2\theta \, d\phi\right)}, \tag{1.3}$$

where $r_\mathrm{s} = 2MG/c^2$ is the Schwarzschild radius. The factor $(1 - r_\mathrm{s}/r)$ in the second term reflects the curvature of the three-dimensional space-time. The rate of the flow of the physical (proper) time, τ, at a given point does not coincide with the t-coordinate. It is specified by $d\tau = \sqrt{-g_{tt}}\, dt$. Far from the gravitational source ($r \to \infty$), $g_{tt} \to 1$ and, therefore, $d\tau = dt$; that is, t is the physical time measured by an observer removed to infinity. The parameterization $t = \text{const}$ for the events means simultaneity in the entire reference frame for the observers being at rest in this frame.

Schwarzschild's solution becomes singular at $r = r_\mathrm{s}$ or $r = 0$. On the surface $r = r_\mathrm{s}$, the norm of the time-like Killing vector is $g_{tt} = 0$, so that the world lines of the particles becomes null (or light-like). These world lines coincide with the photon world line, thus the light cones of all events on the surface $r = r_\mathrm{s}$ are tangent to the surface. Therefore, this surface can be crossed only in one direction, and it is called the event horizon. The world lines are time-like for $r > r_\mathrm{s}$ and space-like for $r < r_\mathrm{s}$. The acceleration of free-falling particles goes to infinity as they approach the event horizon. All particles passing through the horizon will be falling in towards $r = 0$, but to an observer outside the horizon, it appears to take an infinite amount of time. The singularity at $r = r_\mathrm{s}$ is a physical singularity only in the Schwarzschild reference frame; that is, it is just not possible to extend the Schwarzschild reference frame as a rigid and non-deformable reference frame

beyond $r = r_s$. The singularity at $r = 0$ is, however, a true singularity of the space-time for which the curvature tensor diverges itself. The singularities of coordinate systems are typical in general relativity. In general, they can be removed by suitable transformations to another set of coordinates. Therefore, to solve the Einstein's field equations, special coordinate systems must be chosen, though the chosen coordinates may not cover the entire space-time.

1.2 Kerr solution

Kerr solution (Kerr 1963, 2007) of Einstein's vacuum field equations describes the external field of an isolated source at rest having non-zero angular momentum.[3] The solution discovered by Kerr is not a result of an attempt to directly solve the general equations for a stationary axisymmetric space-time. The solution is a consequence of studying the vacuum space-times that have algebraically special curvature tensors. An example of an algebraically special metric is the Kerr-Schild metric (Kerr & Schild 1965a,b; Kerr 2007). Kerr metric itself belongs to the Kerr-Schild algebraical class and, consequently, it can be written in a Kerr-Schild form. This form was used by Kerr to show that the Kerr space-time is asymptotically flat and rotates. By applying the Kerr-Schild formalism, one can construct new solutions of the Einstein field equations from the Minkowski space-time and its null geodesic vector fields, which can then be applied to some energy momentum content, like the vacuum or the electromagnetic field. Schwarzschild solution can be also written in a Kerr-Schild form.

To find the solution, Kerr looked for the symmetries of the space-time. The metric admits two Killing vectors, which are associated with the time translations and rotations about the axis of the symmetry. The space-time is stationary and one can choose a time-independent reference frame, which can be transformed in the Lorentz frame at infinity. Kerr found such a reference frame and expressed the Kerr-Schild form of the metric in this coordinates as

$$\boxed{\begin{aligned} ds^2 = &\left(1 - \frac{2Mr}{\Sigma}\right) dt^2 + \left(1 + \frac{2Mr}{\Sigma}\right) dr^2 + \Sigma d\theta^2 + \left[\left(r^2 + a^2\right) + \frac{2Mr}{\Sigma} a^2 \sin^2\theta\right] \sin^2\theta \, d\phi^2 \\ &+ \frac{4Mr}{\Sigma} dt \, dr - \frac{4Mra\sin^2\theta}{\Sigma} dt \, d\phi - 2a\sin^2\theta \left(1 + \frac{2Mr}{\Sigma}\right) dr \, d\phi \end{aligned}}, \tag{1.4}$$

where $\Sigma = r^2 + a^2 \cos^2\theta$. Since the metric is asymptotically flat, the parameter M can be identified with the mass of the field source and the parameter a with its angular momentum. The metric of Eq. 1.4 resembles the Boyer-Lindquist form of the Kerr metric, the latter metric being simpler, though. For $a = 0$, the Kerr metric is reduced to the Schwarzschild metric.

The Kerr geometry is believed to be the late-time limit reached by gravitational collapse of any rotating body (Novikov & Thorne 1973a; Hawking & Ellis 1973; Frolov & Novikov 1998). If the body contracts to a size less than its gravitational radius, a **black hole**[4] is formed. The velocity required to leave the boundary of the BH (or the

[3] Throughout the rest of the chapter, we use geometrical units: $c = G = 1$.

[4] The term "black hole" was popularized by Wheeler (1968). It is not clear who actually invented this

event horizon) equals the speed of light. Since the speed of light is an absolute limit on the propagation speed for any physical signal, nothing can escape from the region inside the BH. All the properties of the matter that formed the BH are gone except for the mass, angular momentum, and electric charge (which is known as the "no hair" theorem). They are just slightly smaller than those the body had before the collapse, because the gravitational waves carry off a part of the total energy and angular momentum of the body during the collapse.

1.3 Kerr black holes in Boyer-Lindquist coordinates

In this section, we describe the Kerr space-time outside of a rotating and uncharged BH in the most commonly used coordinates of Boyer & Lindquist (1967). Even though the metric in these coordinates has a pathological behavior at the event horizon, its structure is simpler and describes the space-time exterior to the event horizon very well. As we shall see in Chapter 4, in the case of the General Relativistic Magnetohydrodynamics simulations of jets formation from Kerr BHs, using the Kerr-Schild coordinates may be a better choice to overcome the numerical problems that occur when approaching the BH event horizon.

In the Boyer-Lindquist coordinates (t, r, θ, ϕ), the Kerr metric reads

$$\boxed{\begin{aligned} ds^2 = &-\left(1-\frac{2Mr}{\Sigma}\right)dt^2 - \frac{4Mar\sin^2\theta}{\Sigma}dtd\phi \\ &+\frac{\Sigma}{\Delta}dr^2 + \Sigma d\theta^2 + \left(r^2+a^2+\frac{2Ma^2r\sin^2\theta}{\Sigma}\right)\sin^2\theta d\phi^2 \end{aligned}}, \tag{1.5}$$

where M is the BH mass, a is the BH angular momentum per unit mass per speed of light ($|a| \leq M$), and the metric functions are defined by

$$\Delta = r^2 - 2Mr + a^2\,, \quad \Sigma = r^2 + a^2\cos^2\theta. \tag{1.6}$$

Since the metric coefficients in Boyer-Lindquist coordinates are independent of t and ϕ, both $\xi_t = (\partial_t)_{r,\theta,\phi}$ and $\xi_\phi = (\partial_\phi)_{r,\theta,\phi}$ are the Killing vectors for the metric. In Boyer-Lindquist coordinates, their components are (1, 0, 0, 0) and (0, 0, 0, 1), respectively. The vector ξ_ϕ generates rotations about the axis of symmetry z. On the other hand, the vector ξ_t corresponds asymptotically to time translation; that is, the Killing vector field which is directed along the lines of time t shifts the three-dimensional space to another identical to it. Thus, the coordinate t, the time of the distant observers, can be thought as the universal time enumerating the three-dimensional slices. In other words, the space-time is split into a family of three-dimensional slices of constant t plus the universal time t which enumerates these slices. This is called the 3+1 decomposition of the space-time. In the Schwarzschild reference frame, the condition t = const meant simultaneity in the entire external space. In the Kerr space-time this condition does not hold anymore because the metric has non-vanishing off-diagonal components. The Killing vector ξ_t becomes space-like at points close to the event horizon, and the grid of the three-dimensional space would move at superluminal speed with respect to any observer. The scalar products[5] of the Killing

term. It seems that the first recorded use of the term was through a report by Ewing (1962).

[5]The scalar product of any two (tangent) vectors is $\mathbf{v}\cdot\mathbf{w} = g_{\mu\nu}v^\mu w^\nu$.

vectors with themselves and each other are (Misner et al. 1973)

$$\xi_t \cdot \xi_t = g_{tt}\,,\ \ \xi_\phi \cdot \xi_\phi = g_{\phi\phi}\,,\ \text{ and }\ \xi_t \cdot \xi_\phi = g_{t\phi}. \tag{1.7}$$

The Killing vectors are geometric properties of the space-time, so that they are independent of the coordinate system in which the metric is written. The fact that these scalar products are equal to the metric components is a result of a good choice of Boyer-Lindquist coordinates. Therefore, the metric components g_{tt}, $g_{\phi\phi}$, and $g_{t\phi}$ keep the information about the space-time symmetry, being responsible for different features of Kerr space-time, such as the time dilation, the stationary limit surface, or the dragging of inertial frames.

The standard metric form valid for any stationary, axisymmetric, and asymptotically flat space-time is (Bardeen 1970)

$$\boxed{ds^2 = -e^{2\nu}dt^2 + e^{2\Psi}\left(d\phi - \omega dt\right)^2 + e^{2\mu_1}dr^2 + e^{2\mu_2}d\theta^2}, \tag{1.8}$$

which is reduced to the Kerr metric in Boyer-Lindquist coordinates if

$$e^{2\nu} = \frac{\Sigma\Delta}{A} = \alpha^2\,,\ \ e^{2\Psi} = \frac{A}{\Sigma}\sin^2\theta\,,\ \ e^{2\mu_1} = \frac{\Sigma}{\Delta}\,,\ \ e^{2\mu_2} = \Sigma\,,\ \ \omega = \frac{2Mar}{A}\,,\ \ \tilde{\omega} = \frac{\sqrt{A}}{\Sigma}, \tag{1.9}$$

with the metric function $A = \left(r^2 + a^2\right)^2 - a^2\Delta\sin^2\theta$.

The physical and geometrical interpretation of the terms in the metric equation (Eq. 1.8) is as follows: the lapse function α relates the proper time of zero-angular-momentum observers (see below) τ to the universal time t, time of the distant observers (gravitational redshift factor); ω is the frame-dragging angular velocity; $\tilde{\omega}$ is the cylindrical radius such that $2\pi\tilde{\omega} = 2\pi\sqrt{g_{\phi\phi}}$ is the circumference of a circle around the axis of the symmetry; and Δ and Σ are geometrical functions which introduce the event horizon and the stationary limit surface, respectively.

The Kerr metric has coordinate singularities at $\Delta = 0$ and $\Sigma = 0$ (see later in this section). For $\Delta = 0$, there are three possibilities: $M^2 < a^2$, $M^2 = a^2$, and $M^2 > a^2$. Only for the last one, the space-time allows an event horizon. The equation $\Delta = 0$ has two solutions, the outer or the **event horizon** r_+ and the inner r_- horizon,

$$\boxed{r_\pm = M \pm \sqrt{M^2 - a^2}}, \tag{1.10}$$

see Fig. 1.2. The difference between the Schwarzschild and Kerr geometry is the existence of the **ergosphere (or stationary limit surface)** in the Kerr case, which is caused by the dragging of inertial reference frames due to a non-vanishing angular momentum. The time-like Killing vector becomes null at the stationary limit surface $r_{\rm sl}$, rather than at the event horizon. First, we consider

$$\xi_t \cdot \xi_t = g_{tt} = -\left(1 - \frac{2Mr}{\Sigma}\right) = 0, \tag{1.11}$$

for $(\Sigma - 2Mr) = 0$. This gives two surfaces of infinite red-shift:

$$r = M \pm \left(M^2 - a^2\cos^2\theta\right)^{1/2}. \tag{1.12}$$

The inner surface of infinite red-shift is located inside of the event horizon. The outer surface of infinite red-shift,

$$\boxed{r_{\rm sl} = M + \left(M^2 - a^2\cos^2\theta\right)^{1/2}}, \tag{1.13}$$

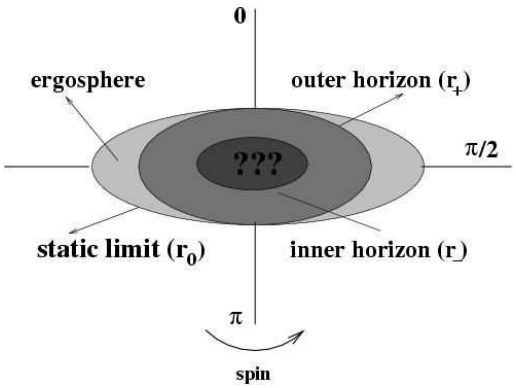

Figure 1.2: Schematic representation of a Kerr BH.

is called the stationary limit surface, and coincides with the event horizon only at the poles ($\theta = 0, \pi$). For $r < r_{\rm sl}$, the Killing vector ξ_t becomes space-like ($\xi_t \cdot \xi_t > 0$). The region between the stationary limit surface and the event horizon defines the ergoregion. Stationary observers moves along world lines (r, θ) = const with constant angular velocity relative to the local geometry. For them, the space-time geometry is unchanged in their neighborhood. If their angular velocity is zero, so that they move only in time along world lines (r, θ, ϕ) = const, they can be though as being static with respect to the asymptotic rest frame (the frame of distant observers at rest in the Boyer-Lindquist coordinates). Static observers, whose world lines would have ξ_t as tangent vectors, cannot exist inside the ergosphere since ξ_t is space-like there. The angular velocity relative to distant observers is $\Omega = d\phi/dt > 0$ for $a > 0$ and $r < r_{\rm sl}$; that is, an observer moving along a non-spacelike world line inside the ergosphere must co-rotate with BH. Nothing inside the ergosphere can remain at rest with respect to distant observers. This process is called **dragging of inertial frames**, or in short frame dragging. Stationary observers cannot have angular velocities of any value. The angular velocity is constrainted by the condition that the four-velocity of stationary observers must lie inside the future cone; that is,

$$g_{tt} + 2\Omega g_{t\phi} + \Omega^2 g_{\phi\phi} > 0. \tag{1.14}$$

This gives the limits of angular velocity,

$$\Omega_- \leqslant \Omega \leqslant \Omega_+, \text{ where } \Omega_\pm = \omega \pm \frac{\alpha}{\tilde{\omega}}. \tag{1.15}$$

Figure 1.3 shows the angular velocity of the frame dragging in comparison with its prograde (Ω_+) and retrograde (Ω_-) limits.[6] At the stationary limit surface $\Omega_- = 0$. Inside this limit, all stationary observers must orbit the BH with positive angular velocity, so that static observers cannot exist there. The frame-dragging "strength" increases as the observers approach the event horizon. At the event horizon, all angular velocities are the same, that is, the BH forces everything to rotate with it.

To study the motion of particles, one must introduce a reference frame which does not rotate. This frame is called the locally non-rotating frame of zero angular momentum observers (ZAMOs). In the picture of 3+1 decomposition of the space-time, the frame is chosen such that its world lines are orthogonal to the slices of constant t; that is, the world

[6] We use the normalization to the gravitational radius $r_{\rm g} = GM/c^2$; thus, the BH spin parameter is $a_* = a/r_{\rm g}$ and the radius is $r_* = r/r_{\rm g}$.

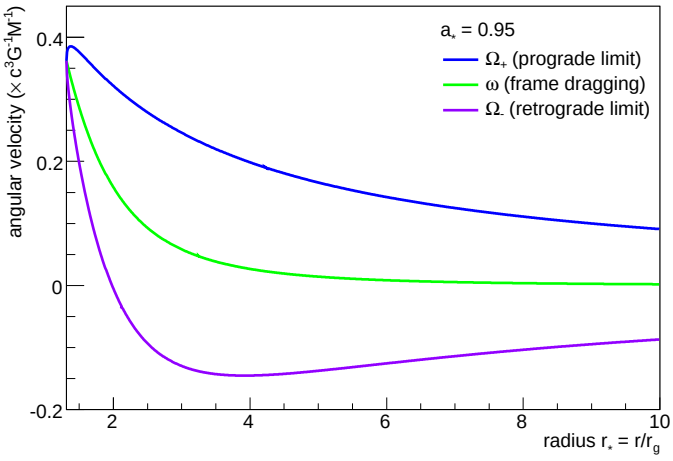

Figure 1.3: Frame-dragging process for a BH with a spin parameter of $a_* = 0.95$. The middle curve is the frame-dragging angular velocity ω, whereas the upper and lower curves are the prograde and retrograde limits, Ω_+ and Ω_-, respectively. Note that Ω_- changes signs at the stationary limit surface, which is $2\,r_{\rm g}$ in the equatorial plane of the BH. At the horizon, which is located at $r_H \simeq 1.3\,r_{\rm g}$, all curves coincide (for an angular velocity of ~ 0.36 c^3 G^{-1} M^{-1}); that is, everything must rotate with the angular velocity of the BH.

lines are time-like lines which are not twisted. The ZAMOs are at rest in this frame, and move with respect with the Boyer-Lindquist coordinate system. So that, they move in the absolute space at constant r and θ, and at constant, in time, angular velocity in ϕ.

Both Killing vectors ξ_t and ξ_ϕ are tangent to the horizon, and are space-like there. The null geodesic generators of the horizon are tangent to the null vectors $\xi = \xi_t + \Omega_H \xi_\phi$, where Ω_H is called the BH angular velocity,

$$\Omega_H \equiv \omega(r_{\rm H}) = \frac{a}{2Mr_{\rm H}} = \frac{a}{r_{\rm H}^2 + a^2}. \tag{1.16}$$

The BH angular velocity is constant over the horizon, so that the event horizon rotates rigidly.

Now, we go back to the coordinate singularity for $\Sigma = 0$. This gives $r^2 + a^2\cos^2\theta = 0$, so that $r^2 = 0$ for $\theta = \pi/2$. The Boyer-Lindquist coordinates were obtained from the Kerr coordinates (x, y, z, t) applying a set of transformations. In this picture, the singularity at $r = 0$ corresponds to a ring of radius a: $x^2 + y^2 = a^2$ for $z = 0$.

1.4 Orbits in the Kerr metric

In the case of a thin accretion disk, the disk particles orbit around the BH and lose energy and angular momentum in some processes (e.g., viscosity). The particle orbits in Kerr space-time can be described by three constants of motion (Carter 1968). They are: the particle specific energy, the particle angular momentum, and the so-called Carter's constant. The motion of particles, if it was initially in the equatorial plane of the BH, remains in the equatorial plane the whole time if Carter's constant vanishes. Using Carter's formalism, Bardeen et al. (1972) derived the equations governing the particle trajectory for orbits in the equatorial plane of the BH. For circular motion, the particle specific energy and angular momentum are

$$E^\dagger = E/m = \frac{r^{3/2} - 2Mr^{1/2} \pm aM^{1/2}}{r^{3/4}(r^{3/2} - 3Mr^{1/2} \pm 2aM^{1/2})^{1/2}}, \tag{1.17}$$

$$L^\dagger = L/m = \frac{\pm M^{1/2}(r^2 \mp 2aM^{1/2}r^{1/2} + a^2)}{r^{3/4}(r^{3/2} - 3Mr^{1/2} \pm 2aM^{1/2})^{1/2}}, \tag{1.18}$$

and the particle angular velocity is

$$\Omega = \frac{d\phi}{dt} = \pm \frac{M^{1/2}}{r^{3/2} \pm M^{1/2} a}, \tag{1.19}$$

where the upper sign refers to direct orbits, whereas the lower sign refers to retrograde orbits. At large radii, both direct and retrograde orbits are bound, with nearly equal binding energies (Bardeen 1973a). A *spin-orbit coupling effect*, which increases the binding energy of the direct orbit and decreases the binding energy of the retrograde orbit relative to the Schwarzschild value, becomes important at small radii. Nonetheless, circular orbits do not exist for all radii. The denominator of equations (1.17) and (1.18) must have a real value,

$$r^{3/2} - 3Mr^{1/2} \pm 2aM^{1/2} \geq 0. \tag{1.20}$$

Next, we mention the particle orbits that are possible around a Kerr BH. They can be found in more detail in (Bardeen et al. 1972; Chandrasekhar 1983).

Photon orbits: The photon orbit is obtained from the limiting condition in Eq. 1.20,

$$\boxed{r_{\rm ph*} = 2\left\{1 + \cos\left[2/3 \cos^{-1}\left(\mp a_*\right)\right]\right\}}, \tag{1.21}$$

where the normalization to the gravitational radius was used (see the footnote on page 8). At $r = r_{\rm ph*}$ the specific particle energy (Eq. 1.17) becomes infinity, therefore it is a photon orbit. This photon orbit represents the innermost boundary of the circular orbits, but it is unstable (it can also be seen in Fig. 1.4, where the photon orbit is inside the innermost stable orbit). The envelope of the photon orbits represents the so-called photon sphere.

Marginally bound orbits: An unbound circular orbit is an orbit with $E^\dagger > 1$. A small outward perturbation to the particles in such an orbit can produce an escape of the particles to infinity. The marginally bound orbits correspond to $E^\dagger = 1$, for particles falling towards the BH from rest, as seen at infinity,

$$\boxed{r_{\rm mb*} = 2 \mp a_* + 2\left(1 \mp a_*\right)^{1/2}}. \tag{1.22}$$

A particle with an orbit $r < r_{\rm mb}$ falls directly into the BH.

Innermost stable (circular) orbits: Bound circular orbits are not all stable. The condition of stability implies a maximum binding energy of the particles in the BH gravitational potential $(1 - E^\dagger)$, which gives a minimum particle angular momentum of

$$\boxed{r_{ms*} = 3 + z_2 \mp \left[\left(3 - z_1\right)\left(3 + z_1 + 2z_2\right)\right]^{1/2}}, \tag{1.23}$$

$$z_1 = 1 + \left(1 - a_*^2\right)^{1/3}\left[\left(1 + a_*\right)^{1/3} + \left(1 - a_*\right)^{1/3}\right], \;\; z_2 = \left(3a_*^2 + z_1^2\right)^{1/2}.$$

In the theory of thin accretion disks (Shakura & Sunyaev 1973), or its general relativistic approach (Novikov & Thorne 1973a; Page & Thorne 1974), the inner edge of the disk is located at the innermost stable radius. When the disk particles reach this radius, they drop out of the disk and go directly into the BH.

Figure 1.4 shows the orbit radii as a function of BH spin parameter for the whole interval $-1 \leqslant a_* \leqslant 1$. The left side corresponds to retrograde orbits, the right side to direct orbits, and the middle to a Schwarzschild BH ($a_* = 0$). The radii from top to bottom are: the marginally stable orbit, the marginally bound orbit, the photon radius, the stationary

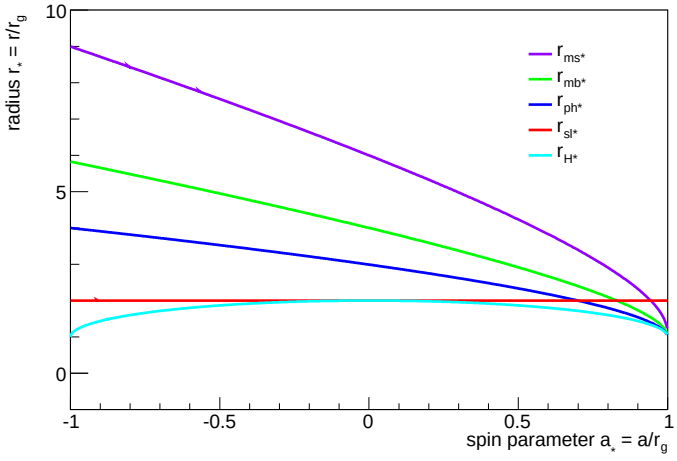

Figure 1.4: Characteristic orbit radii as a function of BH spin parameter for the whole interval $-1 \leqslant a_* \leqslant 1$. The radii from top to bottom are: the marginally stable orbit $r_{\mathrm{ms}*}$, the marginally bound orbit $r_{\mathrm{mb}*}$, the photon orbit $r_{\mathrm{ph}*}$, the stationary limit surface in the equatorial plane $r_{\mathrm{sl}*}$, and the event horizon $r_{\mathrm{H}*}$. Note that the stationary limit surface is $2\,r_{\mathrm{g}}$ for any value of the BH spin parameter.

limit radius in the equatorial plane, and the event horizon. Note that the stationary limit surface is $2\,r_{\mathrm{g}}$ for any value of the spin parameter. For a maximal rotating BH ($a_* = 1$), there is an apparent coincidence of the first three orbits with the BH event horizon. This is induced by general relativistic effects. To calculate the proper distance between any of the three radii and the BH radius, one needs to include the square root of the metric component g_{rr}. This implies a non-zero limit for the proper distance between the orbits.

1.5 Stretched horizon – membrane paradigm

The BH can be surrounded by a boundary surface, so that the interaction of the BH with the outside world can be described in terms of special boundary conditions at this boundary surface. Znajek (1978) and Damour (1978) developed a formalism in which the BH horizon is identified with such a boundary surface. There is a physical distinction between the horizon and the boundary of an ordinary body; the BH horizon is a null surface, while the boundary of an ordinary body is a time-like surface. To overcome this problem, Thorne & Macdonald (1982); Thorne et al. (1986), chose the boundary surface representing the BH slightly outside of the event horizon. The horizon is then stretched to cover up this boundary surface; this is known as **stretched horizon**. In this way, the null horizon is replaced with a physical membrane endowed with electrical, mechanical, and thermodynamical properties. For example, Macdonald & Thorne (1982) presented, in details, the electrodynamics of Kerr BHs from the membrane paradigm point of view by using the 3+1 decomposition of space-time. The motion of coordinates within a surface is described by the shift vector, whose ϕ component is the reverse sign of the frame-dragging angular velocity.

Blandford & Znajek (1977) proposed a mechanism for extracting the rotational energy of the BH, where the angular momentum and rotational energy of the BH are transferred to a large-scale magnetic field and transported out as a Poynting flux. They derived the equations for a stationary and axisymmetric force-free magnetosphere in curved space-time and reduced the set of equations to a constraint equation relating the toroidal magnetic field to the charge density and toroidal current density. The mechanism is explained from the membrane paradigm point of view, where the equations were written using the electric and magnetic three-vectors in absolute space whose time dependence is governed by Maxwell-type equations. We will refer to the membrane paradigm in the following chapter.

Chapter 2

Magnetic Connection Model for Launching Relativistic Jets from Kerr Black Holes

In this chapter, we present a model for launching relativistic jets in active galactic nuclei (AGN) from an accreting Kerr black hole (BH) as an effect of the rotation of the space-time, where the gravitational energy of the accretion disk inside the ergosphere, which can be increased by the BH rotational energy transferred to the disk via closed magnetic field lines that connect the BH to the disk (BH-disk magnetic connection), is converted into jet energy. The main role of the BH-disk magnetic connection is to provide the source of energy for the jets when the mass accretion rate is very low. We assume that the jets are launched from the disk inside the BH ergosphere, where the rotational effects of the space-time become much stronger, being further accelerated by magnetic processes. Inside the ergosphere, we consider a split topology of the magnetic field, where parts of the disk connect to the BH and other parts to the jets via magnetic field lines. The rotation of the space-time channels a fraction of the disk energy (i.e., the gravitational energy of the disk plus the rotational energy of the BH which is deposited into the disk by magnetic connection) into a population of particles that escape from the disk surfaces, carrying away mass, energy and angular momentum in the form of jets, allowing the remaining disk gas to accrete. Since the accretion disk can be cooled very efficiently as its energy is taken away by jets, the accretion disk beneath the jets is left non-radiant. In this picture, the BH can undergo recurring episodes of its activity with: (i) a first phase when the accretion power dominates and (ii) a second phase when the BH spin-down power dominates. In the limit of the spin-down power regime, the model proposed here can be regarded as a variant of the Blandford-Znajek mechanism, where the BH rotational energy is transferred to the disk inside the ergosphere and then used to drive the jets. As a result, the jets driven from a disk inside the BH ergosphere can have a relatively strong power for low mass accretion rates. We use general-relativistic conservation laws to calculate the mass flow rate into the jets, the launching power of the jets and the angular momentum transported by the jets for BHs with a spin parameter $a_* \geqslant 0.95$. As far as the BH is concerned, it can (i) spin up by accreting matter and (ii) spin down due to the magnetic counter-acting torque on the BH. We found that a stationary state of the BH ($a_* = \text{const}$) can be reached if the mass accretion rate is larger than $\dot{m} \sim 0.001$. The maximum value of the BH spin parameter

depends on $\dot{m}$ being less but close to 0.9982 (Thorne's model). For $\dot{m} < 0.001$, the BH spins down continuously, unless a large amount of matter is provided. In addition, the maximum AGN lifetime can be much longer than $\sim 10^7$ yr when using the BH spin-down power. We also study the relation between the BH spin-down power and the particle maximum energy in the jets and the relation between the BH spin-down power and the observed radio flux-density from flat-spectrum core source.

2.1 Introduction

Relativistic jets are highly collimated plasma outflows present in extragalactic radio sources, which are associated with many AGN. The radio emission from the jets is synchrotron radiation produced by relativistic electrons and positrons in the jets. The particles interact with their own synchrotron photons by inverse Compton process, which leads to a boosting of the self-generated synchrotron photons to higher energies like X- and γ-rays. Therefore, the jets can be observed over a wide range of the electromagnetic spectrum. Moreover, the observed radio emission from the jets proves the presence of magnetic fields and particles accelerated to the relativistic regime. The magnetic fields can accelerate plasma by magnetic gradient forces, and then collimated it by hoop stresses.[1]

If the matter accreted by a BH has enough angular momentum compared to that of a particle moving in a circular orbit around and near the BH, an accretion disk can be formed.

The launching power of the jet can generally be provided by the accretion disk, by the BH rotation, or both. Moreover, as the jet is launched, the BH can evolve towards a stationary state with a spin parameter whose maximum value is less but close to one ($a_* \lesssim 1$, where theoretically $-1 \leqslant a_* \leqslant +1$). One can consider the launching power of the jet to be a fraction of the disk power. A number of questions come to mind: Is this fraction generally valid for astrophysical jets from BHs with the same mass and spin? Can the disk manage to launch the jet by itself as the BH accretes at low rates? How does the magnetic field get involved? Can the BH take over and support the disk to launch the jet as the mass accretion rate goes down? How does the BH spin evolve while the jet is launched, and what is the maximum spin parameter in this case? We try to answer these questions using the model proposed in this chapter.

A supermassive BH ($M \sim 10^9 M_\odot$) can be fed and spun up by accreting matter with a consistent sense of the angular momentum [the first calculations for a Kerr BH were performed by Bardeen (1970)] or by merging with another BH (e.g., Berti & Volonteri 2008; Gergely & Biermann 2009).

The disk luminosity is generated by the release of accreting rest mass-energy in the BH gravitational field. The accretion process is usually described by (i) the efficiency of converting the accreting rest mass-energy into radiation energy ε (which also establishes the relation between the AGN bolometric luminosity and the BH growth rate) and (ii) the Eddington ratio $\dot{m}$, which relates the bolometric luminosity to the Eddington luminosity. The Eddington luminosity describes the balance between the gravitational force and the radiation pressure on the accreting matter. If the radiation pressure dominates, that is, the

[1] By 'hoop' stress, a large-scale and predominantly toroidal magnetic field exerts an inward force on the jet particles. The hoop stress is balanced either by the gas pressure of the jet or by centrifugal force if the jet is spinning.

accretion rate is larger than the Eddington limit ($\dot{m} > 1$), the accretion stops. Jet formation is usually associated with a radiatively-inefficient accretion flow ($\dot{m} < 1$). Among the first proposed models of accretion onto supermassive BHs were those of Prendergast & Burbidge (1968) and Lynden-Bell (1969). Lüst (1952) developed the first mathematical description of an optically thin accretion disk.

The general relativistic effects on the structure of the inner regions of an accretion disk surrounding a Kerr BH were first studied by Novikov & Thorne (1973a) and Page & Thorne (1974) using Bardeen et al.'s (1972) orthonormal frames of the locally nonrotating observers. These studies resulted in a geometrically thin, optically thick accretion disk model [see also Shakura & Sunyaev (1973) for a quasi-Newtonian approach to the description of the disk accretion onto a Schwarzschild BH]. This is known as the standard, thin-accretion disk model. The model assumes that the disk is quasi-Keplerian (i.e., the radial pressure is negligible and the radial velocity of the flow is much smaller than its azimuthal component), and extends to the innermost stable (circular) orbit. The disk is driven by internal viscous torque, which transports the angular momentum of the disk outwards, allowing the disk matter to be accreted onto the BH. It is assumed that the torque vanishes at the innermost stable orbit, so that the disk matter plunges into the BH carrying the specific energy and angular momentum that it has had at the innermost stable orbit. In the general relativistic regime, accretion onto the BH implies the conversion of the rest mass-energy of the infalling matter in the BH potential wall into kinetic and thermal energy of the accreting mass flow. If the thermal energy is efficiently radiated away, the orbiting gas becomes much cooler than the local virial temperature, and the disk remains geometrically thin. In the inner regions of the disk, the radiation pressure dominates the gas pressure. The opacity is dominated by electron scattering; i.e., the photons random-walk before leaving the disk as they scatter off of electrons. Since the half-thickness of the disk at a given radius, r, is much smaller than the radius itself, $h(r) \ll r$, the disk structure can be described through one-dimensional (1-D) hydrodynamic equations which are integrated in the vertical direction. Donea & Biermann (1996) developed a model of thin accretion disk driven jets, which can explain the shape of UV spectra from an AGN when the disk is sub-Eddington. Models of jet/wind formation from an accretion disk typically invoke specific magnetic field structures, as the synchrotron radio emission observed in (extra)galactic jets is possible only if magnetic fields are present. The jet can be launched and collimated, for instance, by centrifugal and magnetic forces (e.g., Blandford & Payne 1982). A possible condition for centrifugal launching of jets from a thin accretion disk is that the coronal particles, which are found just above the disk, should go into unstable orbits around the BH (Lyutikov 2009). The jets/winds can also be launched from either (i) a geometrically thick disk with, e.g., an advection-dominated accretion flow (e.g., Narayan & Yi 1994; Armitage & Natarajan 1999), a convection-dominated flow (Meier 2001), or an advection-dominated inflow and outflow (Blandford & Begelman 1999), or (ii) a layer located between the accretion disk and the BH corona which consists of a highly diffusive, super-Keplerian rotating and thermally dominated by virial-hot and magnetized ion-plasma (Hujeirat et al. 2002). [See also the work by Kuncic & Bicknell (2004) for the first fully analytic description of a turbulent magnetohydrodynamics (MHD) accretion disk coupled to a corona.] Falcke & Biermann (1995, 1999) proposed a jet-disk symbiosis model for powering jets; starting from the assumption that radio jets and accretion disks are symbiotic features present in radio quasars, these objects consist of a maximal jet power with a total equipartition (i.e., the magnetic energy flow along the jet is comparable to the kinetic jet power), and the total jet power is a particular fraction of the disk power. This

fraction can be found by fitting the jet parameters to the observational data.

The energy and angular momentum of a BH can be electromagnetically extracted in the presence of a strong magnetic field threading the BH and supported by external currents flowing in the accretion disk, as shown by Blandford & Znajek (1977). In this case, the energy flux of the jets is provided by conversion of the BH rotational energy into Poynting flux, which is then dissipated at large distances from the BH by current instabilities (Lyutikov & Blandford 2002). The Blandford–Znajek mechanism has been widely applied to jet formation in AGN, as well as to microquasar jets and gamma ray bursts, in an attempt to match a number of observational data. Macdonald & Thorne (1982) explained this mechanism in terms of the BH membrane paradigm, in which case an imaginary stretched horizon (a conducting surface located just outside of the BH event horizon) mimics the BH electrodynamics as seen by outside observers. The electric charge that falls into the stretched horizon do not cross it. Instead, it circulates on the stretched horizon, being conserved, until a charge of opposite sign falls into the stretched horizon to annihilate it. The electric current can flow into the stretched horizon, stay there, and then flow out again. The charge and the current on the stretched horizon are fictitious to an observer which falls through the stretched horizon, whereas they look perfectly real to an observer who stays outside of the stretched horizon. From the viewpoint of Thorne et al. (1986), the membrane paradigm implies not only the existence of a stretched horizon, but also a 3+1 split of space-time into (absolute) space and (universal) time. Therefore, the stretched horizon is regarded as a 2-D space-like surface that resides in 3-D space and evolves in response to driving forces from the external universe (Price & Thorne 1986). As a result, outside observers can make measurements at the stretched horizon and describe the physical properties of the horizon using modified pre-relativistic equations, such as Ohm's law. As another possibility, Poynting jets can be driven by an ergospheric disk, as a result of gravitohydromagnetics processes (i.e., interactions between a large-scale magnetic field and the plasma inside the BH ergosphere), which were first described by Punsly & Coroniti (1990).

Different theoretical models of jet formation have been tested already by using numerical simulations. For instance, general relativistic magnetohydrodynamics (GRMHD) simulation results are consistent with models of gas pressure and magnetically driven jets (e.g., Koide et al. 1999; Mizuno et al. 2004a; Nishikawa et al. 2005b; Hawley & Krolik 2006), as well as with the Blandford–Znajek mechanism (e.g., Komissarov 2001; Koide 2003; McKinney & Gammie 2004). On the other hand, Punsly et al. (2009) performed fully relativistic 3-D MHD simulations of jets driven through the interaction of the magnetic field with the accreting gas in the BH ergosphere. Once again, the BH ergosphere is a part of the stationary asymptotically flat space-time (as the Kerr space-time) in which the Killing[2] vector that corresponds asymptotically to time translation becomes space-like (Friedman 1978). The ergosphere lies outside of the BH event horizon, and its boundary intersects the event horizon only at the poles. At the stationary limit surface, an observer must move at the speed of light opposite the rotation of the BH just in order to stay still. Inside the ergosphere, the space-time itself is dragged in the direction of the BH rotation; i.e., nothing can stay there at rest with respect to distant observers, but it must orbit the BH in the same direction in which the BH rotates. This process is called the dragging of inertial frames

[2]Since the Kerr space-time is stationary (i.e., time-independent) and axially symmetric, there are two Killing vectors associated with these two symmetries (e.g., Kerr 2007).

(e.g., Misner et al. 1973).

The BH-disk magnetic connection, first mentioned by Zeldovich & Schwartzman and quoted in Thorne (1974), can occur and change the energy-angular-momentum balance of the accreting gas in the disk (e.g., Macdonald & Thorne 1982; Thorne et al. 1986; Blandford 1999; van Putten 1999). Li (2000a,b, 2002a) derived the equations for the energy and angular momentum transferred from a Kerr BH to a geometrically-thin accretion disk (which consists of a highly-conducting ionized gas) by magnetic connection, and we shall use these equations. [But also see the work by Wang et al. (2003).] As the BH rotates relative to the disk, an electromotive force is generated. This drives a poloidal electric current flowing through the BH and the disk and produces an additional power on the disk. From the conservation laws of energy and angular momentum for a thin Keplerian accretion disk torqued by a BH, Li (2002a) calculated the radiation flux, the internal viscous torque, and the total power of the disk, and found that the disk can radiate even without accretion. Li (2002b) also looked for observational signatures of the BH-disk magnetic connection as more energy is radiated away from the disk and showed that the magnetic connection can produce a steeper emissivity compared to the standard, thin-accretion disk model. Uzdensky (2004, 2005) obtained the numerical solution of the Grad-Shafranov equation for a BH-disk magnetic-connection configuration in the case of both Schwarzschild and Kerr BHs. The Grad-Shafranov equation is a non-linear, partial differential equation that describes the magnetic flux distribution of plasma in an axisymmetric system. Uzdensky found that the BH-disk magnetic connection can only be maintained very close to the BH (see in the next section). In recent years, a number of models that also include the BH-disk magnetic connection have been developed. A BH magnetic field configuration with both open and closed magnetic field lines was considered by Lei et al. (2005), who described the field configuration by the half-opening angle of the magnetic flux on the horizon, which can evolve to zero in some range of the power-law index of the radial distribution of the magnetic field on the disk. Wang et al. (2007) proposed a toy model for the magnetic connection, in which case a poloidal magnetic field is generated by a single electric current flowing in the equatorial plane around a Kerr BH. Ma et al. (2007) derived the energy and angular momentum fluxes for a Kerr BH surrounded by an advection-dominated accretion disk. To solve the equations of the accretion flow, they used a pseudo-Newtonian potential. Gan et al. (2009) solved the dynamic equations for a disk-corona system and simulated its X-ray spectra by using the Monte Carlo method. Zhao et al. (2009) studied the magnetic field configuration generated by a toroidal distributed continuously in a thin accretion disk, as well as the role of magnetic reconnection in the disk to produce quasi-periodic oscillations in BH binaries. In the context of GRMHD, Koide et al. (2006) presented a 2-D GRMHD result of jet formation driven by a magnetic field produced by a current loop near a rapidly-rotating BH, in which case the magnetic flux tubes connect the region between the BH ergosphere and a co-rotating accretion disk. Furthermore, relativistic Poynting jets driven from the inner region of an accretion disk that is initially threaded by a dipole-like magnetic field were studied by Lovelace & Romanova (2003). Their model is derived from the special relativistic equation for a force-free electromagnetic field. [See also Lynden-Bell (1996, 2003).]

In this chapter, we propose a model for launching relativistic jets from a (geometrically-thin) disk inside the ergosphere as an effect of the rotation of the space-time. We consider here the BH-disk magnetic connection, whose main role is to provide the source of energy

for the jets when the mass accretion rate is very low. We use the general relativistic form of the conservation laws for the matter in a thin accretion disk to describe the disk structure when both the BH-disk magnetic connection and the jet formation are considered. The model is based on the calculations of Novikov & Thorne (1973a), Page & Thorne (1974), and Li (2002a), being mainly influenced by the work of Znajek (1978) and Macdonald & Thorne (1982). [Some incipient ideas which are at the base of this model were exposed in Duţan & Biermann (2005).] This is the first work that studies the process of jet launching from a (geometrically-thin) accretion disk inside the BH ergosphere when the energy and angular momentum are transferred from the BH to the disk via closed magnetic field lines, whithin the framework of general relativity. An important result of the model proposed here, with impact on observation of the AGN jets, is that the power of the jets does not depend linearly on the mass accretion rate all the way down to very low accretion rates for BHs of a given mass. This result is different from that of Allen et al. (2006), who found a linear dependence between the power of the jet and the mass accretion rate by considering a spherical Bondi-type accretion onto BHs (in which case the accreting matter has zero or very low angular momentum). In their calculations, the power of the jet is estimated from the energy and time scale required to inflate the cavity observed in the surrounding X-ray emitting gas. The model proposed here combines two regimes associated with the driving of the jets, an accretion power regime and a (BH) spin-down power regime, where the switch from the former to the latter regime corresponds to a mass accretion rate of $\dot{m} \sim 10^{-1.8}$. In the accretion power regime, the power of the jets is linearly dependent on the mass accretion rate, whereas in the spin-down power regime the power of the jets depends very weakly on the mass accretion rate. In the accretion power regime, the energy and angular momentum are extracted and transported away from the disk inside the BH ergosphere by both the kinetic flux of particles and Poynting flux in the form of jets. Instead, in the spin-down power regime the energy and angular momentum are extracted and carried away from the disk inside the ergosphere predominantly in the form of Poynting flux with just little amount of kinetic flux of particles. The work presented in this chapter is different from that of Wang et al. (2008), in which the production of Poynting flux jets is associated with a combination of the Blandford–Znajek mechanism, the BH-disk connection, and the Blandford–Payne mechanism. Furthermore, we argue that the accretion, which is initially at either close to the Eddington rate or at low rates, can be driven in a non-radiant, geometrically thin, and quasi-Keplerian disk inside the BH ergosphere by the external jet torque. This is distinctly different from optically thin, advection-dominated accretion flow models (e.g., Narayan & Yi 1994), in which the accretion at low rates is advection-dominated (i.e., the thermal energy generated via viscous dissipation is mostly retained by the accreting mass flow rather than being radiated, and the energy is advected in towards the BH) and quasi-radial (i.e., the flow is geometrically thick, having roughly a spherical structure), which results from the increase of the gas temperature. Our first goal in the present work is to obtain estimations for jet-related quantities, in particular the mass loading, power and Lorentz factor of the jet, when the BH rotational energy is transferred to the disk inside the ergosphere and then to compare them with those derived from the Blandford-Znajek mechanism. In the limit of the spin-down power regime, the model proposed here can be regarded as a variant of the Blandford-Znajek mechanism, where the BH rotational energy is transferred to the disk inside the ergosphere rather than transported to remote astrophysical loads. Our second goal is to determine the upper limit of the spin attained by a stationary Kerr BH when both jet formation and BH-disk magnetic connection are considered and to investigate how

the value of the mass accretion rate can influence the departure of the BH spin parameter from its theoretical maximum limit of $a_* = 1$.

Chapter outline

In Section 2.2, we describe the assumptions of the model. In Section 2.3, we derive the mass flow rate into the jets. Using the general-relativistic conservation laws for energy and angular momentum of the matter in the accretion disk (Section 2.4), we derive the launching power of the jets (Section 2.5) and the angular momentum removed by the jets (Section 2.6). In Section 2.7, we calculate the efficiency of launching the jets and show that when the BH accretes at low rates, the spin-down of the BH is an efficient mechanism to launch the jets via the accretion disk. In Section 2.8, we study the spin evolution of the BH and discuss conditions of BH stationary states for given mass accretion rates. In Section 2.9, we refer to the long lifetime of an AGN from the BH spin-down power as a particular relevance of the proposed model to the observational data. In Section 2.10, we present a summary of the key points, as well as our conclusions, and suggest further work to be done.

2.2 Basic assumptions

- We consider that matter outside of the BH has negligible gravitational effects compared to the BH gravity and that an

- We consider that matter outside of the BH has negligible gravitational effects compared to the BH gravity and that an accretion disk settles down in the equatorial plane of a Kerr BH. We assume that the accretion disk is geometrically thin and quasi-Keplerian, therefore the physical quantities integrated over the vertical direction can be used in order to describe the radial structure of the disk. The inner part of the accretion disk is located inside the BH ergosphere, extending from the stationary limit surface (or ergosphere) inward to the innermost stable orbit (see Fig. 2.1). In the BH equatorial plane, the stationary limit surface is located at $r_{\rm sl} = 2\,r_{\rm g}$ and does not depend on the BH spin parameter, whereas the radius of the innermost stable orbit depends on a_* [cf. eq. 2.21 of Bardeen (1970)]; so that, $r_{\rm ms}(a_*) = 2\,r_{\rm g}$ for $a_* = 0.95$ and $\sim 1.2\,r_{\rm g}$ for $a_* \sim 1$. Here, $r_{\rm g} = GM/c^2$ is the gravitational radius [$r_{\rm g} = r_{\rm g}^{\dagger}(M/10^9 M_\odot) = 1.48 \times 10^{14}(M/10^9 M_\odot)$ cm], G is the Newtonian gravitational constant, M is the BH mass and c is the speed of light.

- We adopt the viewpoint of the BH membrane paradigm of Thorne et al. (1986) and represent the BH by the stretched horizon.

- We consider the case of rapidly-spinning BHs with a spin parameter $a_* \geqslant 0.95$, based on the argument by Bardeen (1973b) that a strong preference for a particle to orbit in the equatorial plane requires the BH spin parameter to be close to its maximum value.

- We consider that closed magnetic field lines connect the BH to the accretion disk (e.g., Blandford 1999; Li 2000b). The poloidal component of the magnetic field transfers angular momentum and energy (in the form of Poynting flux) from the BH to the disk, thereby increasing the amount of the gravitational energy which is released from

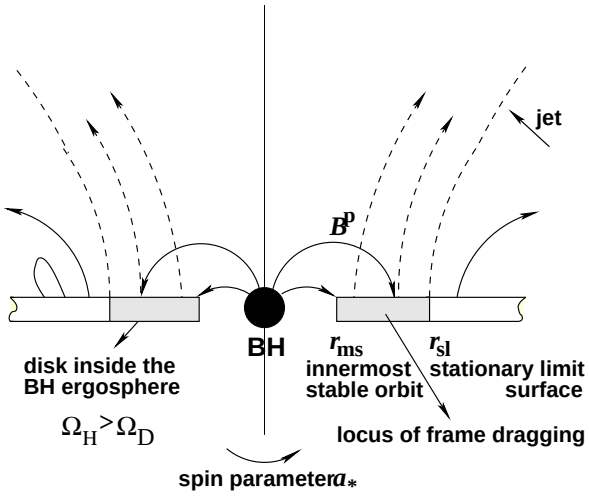

Figure 2.1: Schematic representation of the inner part of the accretion disk-BH-jet system, where the BH is represented by the stretched horizon (Thorne et al. 1986). Above the surface of the disk inside the BH ergosphere, the closed magnetic field lines (solid lines) do not cross the open magnetic field lines (dashed lines); they overlap only in the line-of-sight projection. For some explanation on the structure of the magnetic field in the ergospheric disk, the reader is referred to the text below.

the accretion disk. This energy is liberated very close to the BH, where most of the gravitational energy of the accretion disk is available (in our case, from the disk inside the BH ergosphere). Next, we assume that the disk energy (which, once again, represents the disk gravitational energy plus the BH rotational energy deposited into the disk by magnetic connection) is used to launch the jets. In this way, the disk remains cool and geometrically thin. By comparison, in a standard, thin accretion disk, the thermal energy is efficiently radiated away, so that the orbiting gas becomes much cooler than the local virial temperature, and the disk remains geometrically thin.

- As the numerical results obtained by Uzdensky (2005) indicate, a closed magnetic field configuration can only be maintained in a region close to the BH. This region is limited to the radius of $\sim 12\, r_{\rm ms} = 72\, r_{\rm g}$ for a static BH ($a_* = 0$) and decreases to $\sim 6\, r_{\rm ms} = 20.4\, r_{\rm g}$ as the BH spin parameter increases to $a_* = 0.7$. Therefore, it might be possible that, for a BH with $a_* \geqslant 0.95$, the closed magnetic field configuration to exist only in the region bounded by the BH ergosphere.

- We constrain the jet formation to the disk inside the ergosphere, where the rotational effects of the space-time become much stronger. The slope of the specific energy of disk particles (Eq. 2.13) for $a_* \geqslant 0.95$ steepens in the BH ergosphere, indicating that most of the gravitational energy of the accretion disk is realeased from there. Moreover, inside the ergosphere, the space-time is dragged in the direction of the BH rotation and everything must co-rotate with the BH. (We shall ignore the possibility for the plasma inside the BH ergosphere to have negative mechanical energy at infinity.) Outside the ergosphere, it is plausible that patches of the disk gas may counter-rotate with the BH due to some instability or turbulence in the disk. If some magnetic field lines are frozen in such patches, they likely reconnect with the co-rotating magnetic field lines, and the closed magnetic field configuration can be destroyed. On the other hand, as discussed above, it seems that a closed magnetic field configuration might exist only in the region bounded by the BH ergosphere. And it is this magnetic field that transferres rotational energy from the BH to the accretion disk.

- A more general magnetic field threading the BH would consist of a combination of

closed magnetic field lines, as discussed above, and open magnetic field lines (extending from the BH to infinity), which can enable the extraction of BH rotational energy through the Blandford–Znajek mechanism. Now, one can wonder: (i) How much of the rotational energy of the BH is directly extracted by jets and how much is transferred to the disk, and (ii) under which specific conditions? These questions can be addressed in some future work. We limit the present work to the case of a BH threaded only by closed magnetic field lines and compare the values of some basic physical quantities (such as the power) of a jet driven solely from the disk inside the BH ergosphere with those of a jet powered by the Blandford-Znajek mechanism.

- We assume that the jets remove angular momentum from the disk, enabling the accretion process. The external torques acting on the disk inside the BH ergosphere (i.e., magnetic BH-disk torque and jet torque) can dominate over the internal viscous torque of the disk (Blandford 2001), where the internal torque can be produced by magneto-rotational instability (e.g., Balbus & Hawley 1991), which is driven by the free energy available from the differential rotation of the gas flow. This is based on the fact that the magnetic BH-disk and jet torques have lever arms that are external to the accretion disk, and therefore potentially very large[see, e.g., the discussion on the winds from accretion disks in Pudritz (2000)].

- To form the jet, at some point, the particles must cross the magnetic field lines. One can picture this as being due to drifts and instabilities inside the disk (Balbus & Hawley 1994, 1996, 1998). In addition to the closed magnetic field lines that connect the BH to the disk inside the ergosphere, the magnetic field in the disk can be represented similar to the magnetic field on the Sun surface. In a direct top-down view, it looks mottled, with arcs of magnetic fields connecting different regions and other magnetic flux tubes extending into free space and allowing matter to flow out [see also fig. 36 of Thorne et al. (1986)]. [An accretion disk with a magnetic field configuration similar to that of the Sun was studied by Yuan et al. (2009) for driving episodic magnetohydrodynamic (MHD) jets.] However, the closed (BH-disk) and open (disk-infinity) magnetic field lines are supposed to be dominant in the model proposed here.

- To examine the fate of the magnetic field in the space around the BH, we follow the ideas of Thorne et al. (1986) on the 'cleaning' of the magnetic field by the BH stretched horizon to maintain an ordered magnetic field [see fig. 36 of Thorne et al. (1986)]. Since the magnetic field is frozen into the accretion disk, the field lines are transported in toward the BH by the accretion flow. Once the flow reaches the innermost stable orbit, it drops out of the disk and falls directly into the BH, and becomes causally disconnected from the field lines to which it was attached. However, the flux conservation law assures that the field lines, although disconnected from their source, will be pushed onto the BH by the Maxwell pressure of the adjacent field lines or thread through the near-vacuum region between the accretion disk and the BH or pushed back into the disk via Rayleigh-Taylor instabilities. If this cleaning works efficiently enough, an approximately stationary and axisymmetric magnetic field of the type described in the paragraph above can be formed [see also Li (2000c)], otherwise the process discussed in this chapter is not continuous and a different description than that presented here must be employed. Furthermore, our approach here is simple in

the sense that with the assumption of an approximately stationary and axisymmetric magnetic field, the outflow near the launching region is thereby taken to be quasi-stationary ($\partial/\partial t = 0$). Therefore, we are limited by not being able to specify time-dependent effects in the outflow. We concentrate here on the launching region of the jets, determining the mass flow rate into the jets and other conserved quantities of the outflow, and discuss the importance of the magnetic field in accelerating the jets on sub-parsec scales without solving the entire flow problem (see Section 2.5).

- To allow for jet formation, we assume that the surface density of the disk and the mean radial velocity combine themselves in such a way to keep their product constant over the disk inside the BH ergosphere (see Section 2.3). This can be thought of as being an effect of the BH rotation. By comparison, in the model of Blandford & Payne (1982) the disk particles are driven upwards by the gradient of the pressure in the disk to fill the corona around the disk. The plasma should be sufficient to produce whatever charge and current densities are required for an MHD flow. The magnetic field lines that pass through the corona will be bent from near vertical to make a certain angle with the disk surface. If this angle is greater than 60°, the particles will fling outwards under centrifugal forces. Then, as magnetic stresses become important, the particles will be further accelerated by the gradient of the magnetic pressure. Far from the disk, the particles inertia will cause the magnetic field to become increasingly toroidal. As a result, the flow will be collimated by the magnetic hoop stresses to a cylindrical shape outside the (outer) light cylinder. In the model proposed here, the rotation of the space-time is responsible for ejecting particles in the direction perpendicular to the disk. The escape particles then slide along the open magnetic field lines (dashed lines in Fig. 2.1), being accelerated by magnetic forces (see Section 2.5).

- Due to the motion of the disk plasma in which magnetic field lines are frozen, it is also possible that magnetic reconnection will take place at the interface of closed and open magnetic field lines. (Such a non-ideal MHD effect, which is common to impulsive and gradual flares, can convert magnetic energy into kinetic energy and thermal energy, and topologically change field lines; this can have significant consequences for the global evolution of a system. This effect is also connected with a violation of the magnetic flux conservation.) Such a magnetic reconnection that allows outflows to be driven has been observed in time-dependent resistive MHD simulations of jet/wind formation from neutron stars performed by Romanova et al. (2009). This role of magnetic reconnection in driving outflows can also be extended to accreting BH systems. To estimate the rate of the magnetic energy that can be extracted through reconnection, we follow the work by de Gouveia dal Pino & Lazarian (2005); de Gouveia Dal Pino et al. (2010). If we apply eq. 12 of de Gouveia dal Pino & Lazarian (2005) to a BH of $10^9\,M_\odot$, we obtain a value of $\sim 10^{43}$ erg s^{-1}, which is about two orders of magnitude smaller than the minimum value of the power of the jet that we obtain in the model proposed here.

- We use the Kerr metric (Kerr 1963) in cylindrical coordinates. In and near the BH equatorial plane, the metric is given by

$$ds^2 = -e^{2\nu}dt^2 + e^{2\psi}\left(d\phi - \omega dt\right)^2 + e^{2\mu}dr^2 + dz^2, \tag{2.1}$$

where r, ϕ and z are defined as the cylindrical coordinates in the asymptotic rest frame, and t is the physical time of an observer removed to infinity (Page & Thorne

1974). The components of the metric tensor in (2.1) are specified by

$$e^{2\nu} = \frac{r^2\Delta}{A},\ e^{2\psi} = \frac{A}{r^2},\ e^{2\mu} = \frac{r^2}{\Delta},\ \omega = 2r_{\rm g}aA^{-1}, \tag{2.2}$$

where the metric functions read

$$\Delta = r^2 - 2r_{\rm g}r + a^2,\ A = r^4 + r^2a^2 + 2r_{\rm g}ra^2, \tag{2.3}$$

where $a = J/(Mc)$ is the angular momentum of the BH about the spinning axis (J) per unit mass and per speed of light. The BH spin parameter is defined as $a_* \equiv J/J\mathrm{max}\,(= a/r_{\rm g})$, where $J_{\rm max} = GM^2/c$ is the maximal angular momentum of the BH.

To describe the structure of a thin accretion disk (Novikov & Thorne 1973a), the reference frames used in their calculations are: (i) the frame of Boyer-Lindquist coordinates for the space-time outside of a Kerr BH (in our case, the Boyer-Lindquist coordinates are transformed to cylindrical coordinates); (ii) the orbiting orthonormal frames of zero angular momentum observers (ZAMOs), and (iii) the mean local rest frame of gas particles.

The Boyer-Lindquist coordinates (and the cylindrical coordinates) are, to some degree, unphysical in the BH ergosphere because physical observers cannot stay at rest, due to the frame-dragging effect of the BH rotation. Therefore, the physical processes around a Kerr BH must be studied in a reference frame which does not rotate with respect to the reference frame of the Boyer-Lindquist coordinates (or the cylindrical coordinates). The reference frame in question is the frame of ZAMOs (Bardeen et al. 1972). The observers carry with them an orthonormal tetrad of 4-vectors, their locally Minkowskian coordinate basis vectors, so that the physical quantities are described by their projections on the orthonormal tetrad.

Novikov & Thorne (1973a) proved that the mean local rest frame of the gas particles is nearly identical to the orbiting orthonormal frame of ZAMOs if the motion of gas particles is nearly geodesical. Since the disk is assumed to be in a quasi-steady state, the gas-related quantities are averaged on a scale comparable to the thickness of the disk. All physical quantities (vectors, tensors, etc.) related to the matter in the accretion disk are described in ZAMO's reference frame.

2.3 Mass flow rate into the jets

First, let us explain the terms used for the (rest-)mass flow rates, which are measured by observers at infinity. The term mass accretion rate refers to the mass flow rate through the disk up to the ergosphere ($\dot{M}_{\rm D} = \dot{m}\dot{M}_{\rm Edd}$). In the ergosphere, $\dot{M}_{\rm D}$ is divided into the mass outflow rate into the jets ($\dot{M}_{\rm jets}$) and the mass inflow rate onto the BH ($\dot{M}_{\rm in}$). Now, we can write the mass outflow rate as

$$\dot{M}_{\rm jets} = \dot{M}_{\rm in}(\mathrm{r_{sl}}) - \dot{M}_{\rm in}(\mathrm{r_{ms}}), \tag{2.4}$$

where $\dot{M}_{\rm in}(\mathrm{r_{sl}})$ and $\dot{M}_{\rm in}(\mathrm{r_{ms}})$ denote the mass inflow rate at the stationary limit surface and at the innermost stable orbit, respectively. The mass outflow rate can also be expressed as

$$\dot{M}_{\rm jets} = q_{\rm jets}\dot{M}_{\rm in}, \tag{2.5}$$

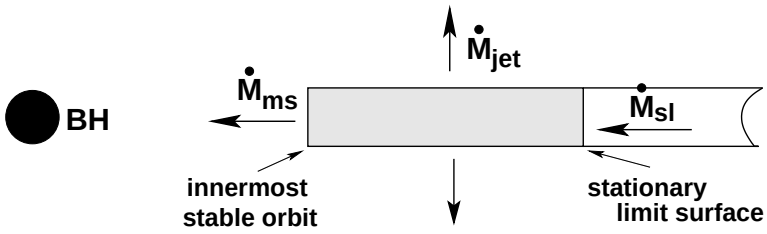

Figure 2.2: Schematic representation of the mass flow through the disk inside the BH ergosphere.

where the parameter $q_{\rm jets}$ indicates the fraction of the mass of the disk inside the BH ergosphere that goes into the jets. Figure 2.2 shows a schematic representation of the mass flow in the disk inside the BH ergosphere.

The amount of mass that flows inward across a cylinder of radius r during a coordinate time interval Δt, when averaged by the method in Novikov & Thorne (1973a), is

$$\dot{M} = -2\pi\sqrt{|g|}\,\Sigma\,\bar{v}^{\hat{r}}\,\mathcal{D}^{1/2}, \tag{2.6}$$

where $\sqrt{|g|} = e^{\nu+\psi+\nu} = r$ is the square root of the metric determinant (Eqs. 2.1 and 2.2), $\Sigma = 2h < \rho_0 >$ is the surface density of the disk (with h being the half-thickness of the disk and $< \rho_0 >$ the density of rest mass), $\bar{v}^{\hat{r}}$ is the mass-averaged radial velocity, and $\mathcal{D} = (1 - 2/r_* + a_*^2/r_*^2)$ is one of the functions used to calculate general relativistic corrections to the Newtonian accretion disk structure. Here, $r_* = r/r_{\rm g}$ is the dimensionless radius. We mention that Eq. 2.6 does not include the jet outflow, yet.

Next, we estimate the mass inflow rate at one specific radius of the disk inside the BH ergosphere using Eq. 2.6, so that the mass outflow rate becomes

$$\dot{M}_{\rm jets} = \left[-2\pi r\,\Sigma\,\bar{v}^{\hat{r}}\,\mathcal{D}^{1/2}\right]_{\rm r_{sl}} - \left[-2\pi r\,\Sigma\,\bar{v}^{\hat{r}}\,\mathcal{D}^{1/2}\right]_{\rm r_{ms}}. \tag{2.7}$$

The mass inflow rate at the stationary limit surface is also given by $\dot{m}\dot{M}_{\rm Edd}$. Then,

$$\dot{M}_{\rm jets} = \dot{m}\dot{M}_{\rm Edd}\left[1 - \frac{\dot{M}(\rm r_{ms})}{\dot{M}(\rm r_{sl})}\right]. \tag{2.8}$$

By analogy with a standard, thin accretion disk [eqs. 5.9.5 and 5.9.10 of Novikov & Thorne (1973a)], the product of the surface density and the mass-averaged radial velocity can depend on the disk radius as $\Sigma\bar{v}^{\hat{r}} \propto r^p$. One can recover a standard, thin accretion disk by setting $p = -1$, in which case the mass accretion rate [Eq. 2.6, also eq. 5.6.2 of Novikov & Thorne (1973a)] is independent of the radius. Now, instead of trying to obtain an exact condition for jet launching, let us simply take $p = 0$, as this gets rid of the requirement to know Σ and $\bar{v}^{\hat{r}}$ precisely. Let us examine the consequences of this choice. Clearly, $p = 0$ corresponds to a product $\Sigma\bar{v}^{\hat{r}}$ constant for any radius of the disk inside the ergosphere, and consequently the mass inflow rate on to the BH decreases with radius as $\dot{M}_{\rm in}(r) \sim r$, and the difference flows into the jets. Then, $\dot{M}_{\rm in}(r)$ at a given radius is specified by the general relativistic factor $\mathcal{D}^{1/2}$, which depends on the BH spin parameter. For an ADAF disk that allows outflows, $\dot{M}_{\rm in}(r) \sim r^q$, where $0 \leqslant q < 1$ [eq. 13 of Blandford & Begelman (1999)]. Therefore, our choice of $q = 1$ (or $p = 0$) represents a limiting case in the model by Blandford & Begelman (1999).

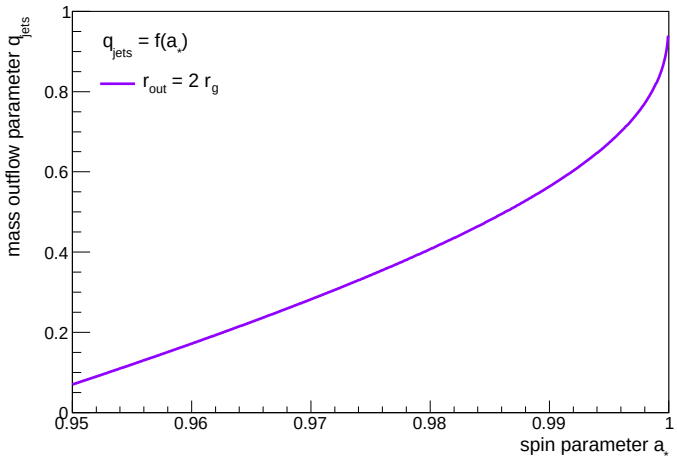

Figure 2.3: Mass outflow parameter ($q_{\rm jets}$) as a function of the BH spin parameter (a_*). For $a_* \sim 1$, almost the whole material of the disk inside the BH ergosphere flows into the jets ($q_{\rm jets} \simeq 0.98$); that is, the BH almost stops being fed by accreting matter.

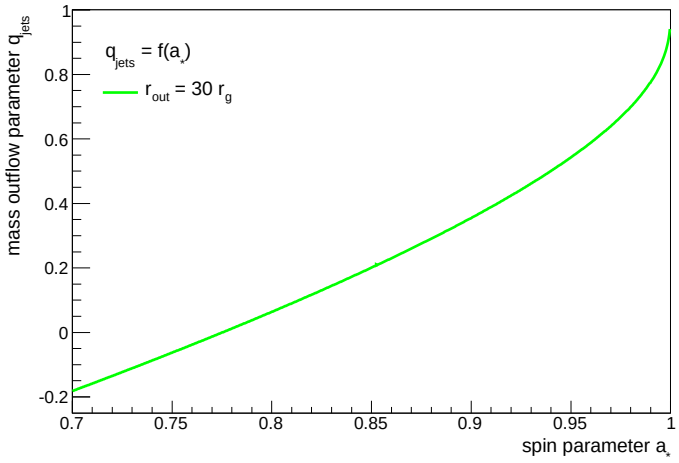

Figure 2.4: Mass outflow parameter as a function of the BH spin parameter if the inner disk would have been extended beyond the stationary limit surface. The jet formation occurs for $a_* > 0.755$, which corresponds to $q_{\rm jets} > 0$.

Using equations (2.5) and (2.8), as well as the expression of $\mathcal{D}$, we obtain the fraction of the mass inflow that goes into the jets (or the mass outflow parameter) as

$$\boxed{q_{\rm jets}(a_*) = 1 - \frac{r_{\rm ms_*}}{r_{\rm sl_*}} \left(\frac{1 - 2/r_{\rm ms_*} + a_*^2/r_{\rm ms_*}^2}{1 - 2/r_{\rm sl_*} + a_*^2/r_{\rm sl_*}^2} \right)^{1/2}}, \tag{2.9}$$

where $r_{\rm ms_*} = r_{\rm ms}/r_{\rm g}$ and $r_{\rm sl_*} = r_{\rm sl}/r_{\rm g}$.

Figure 2.3 shows the mass outflow parameter as a function of the BH spin parameter. For $a_* = 0.95$, the mass outflow into the jets is only about 8 percent of the available mass inflow through the disk inside the BH ergosphere. Instead, for the extreme value of the spin parameter $a_* \sim 1$, the mass outflow is about 98 percent of the available mass inflow. This means that in the case of extreme spin, the BH almost stops being fed by accreting matter.

Suppose the inner disk would have been extended beyond the stationary limit surface. In this case, the disk particles can form the jets ($q_{\rm jets} > 0$) if and only if the BH spin parameter were $a_* > 0.755$ (Fig. 2.4).

We mention that the results presented in this section are valid for our choice of $p = 0$. This, of course, need not be a necessary condition for jet launching, since we have examined the mass outflow parameter for just one value of p, that which makes $\Sigma \overline{v}^{\hat{r}}$ constant

for any radius of the disk inside the BH ergosphere and $q_{\rm jets}$ dependent only on the BH spin parameter, but it is certainly sufficient. The BH rotation causes an outflow of particles from the disk, where the energy (and angular momentum) carried by the escape particles is taken from the accretion disk. The escape particles then slide along the open magnetic field lines, being accelerated by magnetic forces (see Section 2.5).

2.4 Angular momentum and energy conservation laws

To describe the structure of the disk inside the BH ergosphere, we use the angular momentum and energy conservation laws derived by Page & Thorne (1974) and include both the BH-disk magnetic connection and the jet formation. When deriving the conservation laws, Page & Thorne (1974) do not make any assumption about the type of stress-energy present (e.g., magnetic fields, viscous stresses, etc.). The calculations performed by Page & Thorne (1974) are valid even if the disk is highly dynamical, but can also be applied to steady-state and quasi-steady-state disks, in which case the mass accretion rate is constant throughout the disk. Here, we consider that the removal of the angular momentum of the disk inside the BH ergosphere can be produced by the external jet torque and that the external torques acting on the disk inside the BH ergosphere (i.e., BH-disk magnetic torque and jet torque) dominate over the internal viscous torque of the disk. In this case, we can write the angular momentum conservation law[3] as

$$\boxed{\frac{d}{dr}\left[\left(1-q_{\rm jets}\right)\dot{M}_{\rm D}cL^{\dagger}\right]+4\pi rH=4\pi rJL^{\dagger}}, \tag{2.10}$$

where on the left-hand side, the first term describes the angular momentum carried by the accreting mass of the disk inside the BH ergosphere, and the second term describes the angular momentum transferred from the BH to the disk inside the ergosphere. The term on the right describes the **angular momentum carried away by the jets**. $L^{\dagger}$ is the specific angular momentum of a gas particle orbiting in the accretion disk, J is the total flux of energy (of particle and magnetic origin) carried away by jets, and H is the flux of angular momentum transferred from the BH to the disk inside the ergosphere. H is defined through the magnetic torque produced by the BH on both surfaces of the accretion disk $T_{\rm HD}$ (Li 2002a)

$$T_{\rm HD}=2\int_{r_1}^{r_2}2\pi rHdr, \tag{2.11}$$

where the limits of integration are two radii of the accretion disk with $r_1<r_2$.

Similar to the angular momentum conservation law, we can write the energy conservation law as

$$\boxed{\frac{d}{dr}\left[\left(1-q_{\rm jets}\right)\dot{M}_{\rm D}c^2E^{\dagger}\right]+4\pi rH\Omega_{\rm D}=4\pi rJE^{\dagger}}, \tag{2.12}$$

where on the left hand-side, the first term describes the rate of the energy flow through the disk inside the BH ergosphere, and the second term is the magnetic torque per unit area of the disk inside the ergosphere $T_{\rm HD}\Omega_{\rm D}$ (here $\Omega_{\rm D}$ is the Keplerian angular velocity of the gas particles in the disk). The third term describes the **energy flow along the jets**. $E^{\dagger}$

[3]The equation describing the angular momentum conservation is derived in Appendix 1.

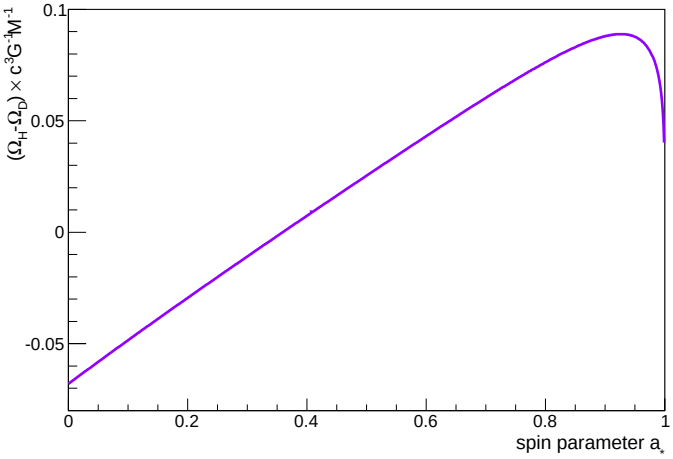

Figure 2.5: Difference between the angular velocities of the BH and the inner edge of the accretion disk. When $\Omega_{\rm H} > \Omega_{\rm D}$, energy and angular momentum are transferred from the BH to the accretion disk. When $\Omega_{\rm H} < \Omega_{\rm D}$, energy and angular momentum are transferred from the accretion disk to the BH. For $a_* = 0.35$, $\Omega_{\rm H} = \Omega_{\rm D}$, and there is no transfer of energy (or angular momentum) in either direction. For $a_* = 0.999999$, $\Omega_{\rm H} - \Omega_{\rm D} = 0.0052\,{\rm c}^3{\rm G}^{-1}{\rm M}^{-1}$. The turning point corresponds to $a_* = 0.9275$.

is the specific energy of a gas particle having mass μ and orbiting in the same direction as the BH rotation (Bardeen et al. 1972):

$$E^\dagger \equiv \frac{E}{\mu} = \frac{r^{3/2} - 2r_{\rm g}r^{1/2} + r_{\rm g}^{1/2}a}{r^{3/4}\left(r^{3/2} - 3r_{\rm g}r^{1/2} + 2r_{\rm g}^{1/2}a\right)^{1/2}}. \tag{2.13}$$

The flux of angular momentum transferred from the BH to the disk inside the ergosphere by magnetic connection has the following expression (Li 2002a):

$$H = \frac{1}{8\pi^3 r}\left(\frac{d\Psi_{\rm D}}{c\,dr}\right)^2 \frac{\Omega_{\rm H} - \Omega_{\rm D}}{(-dR_{\rm H}/dr)}, \tag{2.14}$$

where $\Psi_{\rm D}$ is the flux of the poloidal magnetic field lines which thread the surface of the disk inside the BH ergosphere, and $\Omega_{\rm H}$ is the BH angular velocity. The derivation of Eq. (2.14) is based on the supposition that the accretion disk consists of a highly conducting ionized gas. This implies that (i) the accretion disk resistance is neglected in comparison with the BH surface resistance and (ii) the magnetic field lines are frozen in the accretion disk, being transported by the disk gas and rotating with $\Omega_{\rm D}$. On the other hand, the angular velocity of the magnetic field lines threading the horizon is $\Omega_{\rm H}$, due to the effect of the frame-dragging at the BH horizon. **For $a_* > 0.35$ and $r \geq r_{\rm ms}$, one obtains $\Omega_{\rm H} > \Omega_{\rm D}$, so that the BH transfers energy (and angular momentum) to the disk** (Fig. 2.5). For $a_* < 0.35$, one obtains $\Omega_{\rm H} < \Omega_{\rm D}$, and this time the accretion disk transfers energy (and angular momentum) to the BH. For $a_* = 0.35$, it yields $\Omega_{\rm H} = \Omega_{\rm D}$; this condition implies that there is no energy (nor angular momentum) transfer between the BH and the accretion disk by magnetic connection. The maximum value of the flux of angular momentum transferred from the BH to the accretion disk corresponds to $a_* = 0.9275$.

2.5 Launching power of the jets

We are now in the position to calculate the launching power of the jets with the help of the conservation laws previously derived. First, we define the launching power of both jets as

$$\boxed{P_{\rm jets} = 2\int_{r_{\rm ms}}^{r_{\rm sl}} 2\pi J E^\dagger r dr}. \tag{2.15}$$

Integrating the equation of the energy conservation law (Eq. 2.12) over the disk inside the BH ergosphere, we find the launching power of the jets:

$$\boxed{P_{\rm jets} = (1 - q_{\rm jets})\, \dot{M}_{\rm D} c^2 \left(E^{\dagger}_{\rm sl} - E^{\dagger}_{\rm ms} \right) + 4\pi \int_{r_{\rm ms}}^{r_{\rm sl}} r H \Omega_{\rm D} dr}. \tag{2.16}$$

The first term describes the rest energy of the accreting matter onto the BH, and the second term describes the energy transfer from the rotating BH to the disk inside the ergosphere. $E^{\dagger}_{\rm sl}$ and $E^{\dagger}_{\rm ms}$ are the specific energy of the gas particle (Eq. 2.13) evaluated at the stationary limit surface and at the innermost stable orbit, respectively.

Using Eq. (2.14), we obtain the launching power of the jets as

$$P_{\rm jets} = (1 - q_{\rm jets})\, \dot{M}_{\rm D} c^2 \left(E^{\dagger}_{\rm sl} - E^{\dagger}_{\rm ms} \right) + \frac{1}{2\pi^2} \int_{r_{\rm ms}}^{r_{\rm sl}} \left(\frac{d\Psi_{\rm D}}{c\, dr} \right)^2 \frac{\Omega_{\rm H} - \Omega_{\rm D}}{(-dR_{\rm H}/dr)} \Omega_{\rm D} dr, \tag{2.17}$$

where the angular velocities of the BH and the accretion disk, respectively, are

$$\Omega_{\rm H} \equiv \frac{c}{2r_{\rm g}} \frac{a_*}{1 + (1 - a_*^2)^{1/2}} = \frac{c}{r_{\rm g}}\, \Omega_{\rm H*}, \tag{2.18}$$

$$\Omega_{\rm D} \equiv \frac{c}{r_{\rm g}} \frac{1}{r_*^{3/2} + a_*} = \frac{c}{r_{\rm g}}\, \Omega_{\rm D*}. \tag{2.19}$$

To calculate the launching power of the jets, we need to evaluate both $\Psi_{\rm D}$ and $(-dR_{\rm H}/dr)$. First, we write the magnetic flux that threads the accretion disk surface,

$$\Psi_{\rm D} = \int B_{\rm D} (dS)_{z=0}, \tag{2.20}$$

where $B_{\rm D}$ is the poloidal component of the magnetic field that threads the disk. The surface area between two equatorial surfaces in a Kerr space-time can be calculated from

$$(dS)_{z=0} = \sqrt{\det g_{(r\phi)}}\, dr\, d\phi, \tag{2.21}$$

where the determinant of the surface metric is

$$\det g_{(r\phi)} = \begin{vmatrix} g_{rr} & g_{r\phi} \\ g_{\phi r} & g_{\phi\phi} \end{vmatrix} = \begin{vmatrix} e^{2\mu} & 0 \\ 0 & e^{2\psi} \end{vmatrix} = \frac{A}{\Delta}. \tag{2.22}$$

This result follows from Eqs. (2.1), (2.2), and (2.3). With these, the surface area in Eq. (2.21) reads

$$(dS)_{z=0} = \left(\frac{A}{\Delta} \right)^{1/2} 2\pi\, dr. \tag{2.23}$$

The poloidal component of the magnetic field that threads the BH horizon, $B_{\rm H}$, and the poloidal component of the magnetic field at the inner edge of the accretion disk, $B_{\rm D}(r_{\rm ms})$, can be of the same order (e.g., Livio et al. 1999) and related by

$$B_{\rm H} = \zeta B_{\rm D}(r_{\rm ms})\,, \text{ where } \zeta \geq 1. \tag{2.24}$$

On the other hand, the poloidal component of the magnetic field that threads the accretion disk surface scales as $B_{\rm D} \propto r^{-n}$, where $0 < n < 3$ (Blandford 1976). Consequently,

$$B_{\rm D} = B_{\rm D}(r_{\rm ms}) \left(\frac{r}{r_{\rm ms}} \right)^{-n} = \frac{B_{\rm H}}{\zeta} \left(\frac{r}{r_{\rm ms}} \right)^{-n}. \tag{2.25}$$

Since the BH horizon behaves, in some aspects, like a rotating conducting surface (e.g., Damour 1978; Znajek 1978; Thorne et al. 1986), it can be thought of as being a "battery" driving currents around a circuit. The energy for this comes from the BH rotation (Znajek 1978). The internal resistance of the battery in the horizon, i.e., the resistance between two magnetic surfaces that thread the horizon, is

$$dR_{\rm H} = R_{\rm H}\frac{dl}{2\pi r_{\rm H}}, \tag{2.26}$$

where $R_{\rm H} = 4\pi/c = 377$ ohm, dl is the horizon distance between two magnetic surfaces (see Fig. 2.1), $2\pi r_{\rm H}$ is the cylindrical circumference at $r = r_{\rm H}$, and $r_{\rm H} = r_{\rm g}[1+(1-a_*^2)^{1/2}] = r_{\rm g} r_{\rm H*}$ is the radius of the BH horizon (Thorne et al. 1986).

The voltage difference generated by the BH has a maximum magnitude of $V = \Omega_{\rm H}\Psi_{\rm H}$, where $\Psi_{\rm H} = B_{\rm H}A_{\rm H}$ is the magnetic flux threading the BH, and $A_{\rm H} = 8\pi r_{\rm g} r_{\rm H} = 8\pi r_{\rm g}^2 r_{\rm H*}$ is the surface area of the BH.

Assuming that the magnetic field is carried into the BH by the accreting disk gas, we set the BH potential drop to the energy of the gas particles carried into the BH, the latter being the particle specific energy at the innermost stable orbit. Suppose that during a first epoch, the BH accretes at a rate approximately equal to the Eddington rate.[4] This supposition provides $V^2 = \dot{M}_{\rm acc} E^\dagger_{\rm ms} c^2$. Therefore, the maximum value of the magnetic field that threads the BH horizon is

$$\boxed{(B_{\rm H}^{\rm max})^2 = \frac{\dot{M}_{\rm Edd} c E^\dagger_{\rm ms,lim}}{4\pi r_{\rm g}^2 (a_{*,\rm lim})^2}}, \tag{2.27}$$

where $a_{*,\rm lim} = 0.9982$ is the BH limiting spin in the case of a radiatively-efficient accretion disk (Thorne 1974), and the corresponding particle specific energy at the innermost stable orbit is $E^\dagger_{\rm ms,lim} = 0.6759$. Although this limit of the BH spin may be even closer to its maximum value $a_* \sim 1$, it produces a negligible variation in the maximum value of the BH magnetic field. Using the expression of the gravitational radius (see page 18), the maximum value of the magnetic field that threads the BH horizon (Eq. 2.27) becomes

$$(B_{\rm H}^{\rm max})^2 = \frac{\dot{M}^\dagger_{\rm Edd} c E^\dagger_{\rm ms,lim}}{4\pi\, \varepsilon_{\rm lim} (r_{\rm g}^\dagger)^2 (a_{*,\rm lim})^2} \left(\frac{M}{10^9 M_\odot}\right)^{-1}, \tag{2.28}$$

or

$$B_{\rm H}^{\rm max} = 0.56 \times 10^4 \left(\frac{M}{10^9 M_\odot}\right)^{-1/2} \text{ gauss}. \tag{2.29}$$

This result is similar to the calculation performed by Znajek (1978). [See also Lovelace (1976).] The only difference is that we set the BH potential drop to the specific energy of the particles at the innermost stable orbit, whereas Znajek (1978) makes use of the fact that the Eddington luminosity sets an upper bound on the radiation pressure (as the disk is radiatively efficient), and thus $V^2 \sim L_{\rm Edd}$.

[4]The Eddington accretion rate is defined from the Eddington luminosity as $\dot{M}_{\rm Edd} = L_{\rm Edd}/(\varepsilon c^2) = 4\pi GM/(\varepsilon \kappa_{\rm T} c)$, where ε is the efficiency of converting the accreting rest mass-energy into radiation energy, and $\kappa_{\rm T}$ denotes the Thomson opacity. ε depends on the BH spin parameter as $\varepsilon = 1 - E^\dagger_{\rm ms}$ (Thorne 1974), so that $\varepsilon = 0.06$ for a Schwarzschild BH and $\varepsilon = 0.42$ for an extremely spinning Kerr BH. We scale the BH mass to $10^9 M_\odot$, so that $\dot{M}_{\rm Edd} = \dot{M}^\dagger_{\rm Edd}\varepsilon^{-1}(M/10^9 M_\odot)$, where $\dot{M}^\dagger_{\rm Edd} = 1.38 \times 10^{26}$ g s^{-1}.

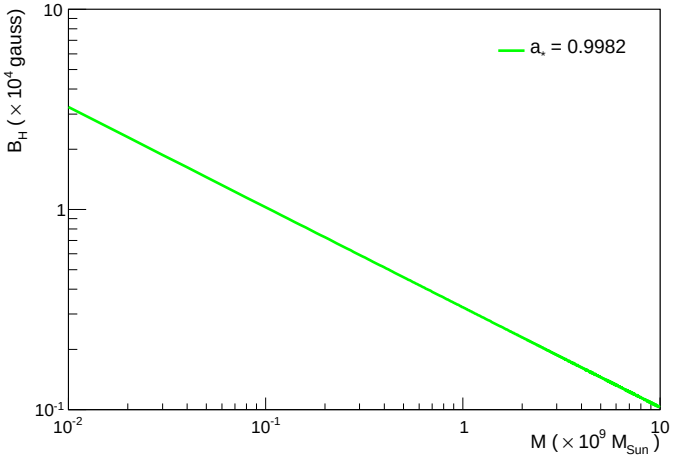

Figure 2.6: BH magnetic field strength established during the early epoch when the BH accretes at the Eddington limit and reaches a stationary state with the spin parameter $a_* = 0.9982$. It is given for a BH mass in the $(10^7 - 10^{10})\, M_\odot$ range.

The dependence of $B_{\rm H}$ on the BH mass is shown in Figure 2.6, given the limiting BH spin parameter $a_* = 0.9982$ for a BH of mass in the range of $(10^7 - 10^{10})\, M_\odot$. For $a_* \geqslant 0.95$, the magnetic field is weakly dependent on the spin parameter for a given mass of the BH.

The continuum of the magnetic field within a narrow strip between two magnetic surfaces, which connect the BH to the disk inside the ergosphere, $d\Psi_{\rm H} = d\Psi_{\rm D}$ (e.g., Wang et al. 2007), gives

$$B_{\rm H} 2\pi r_{\rm H}\, dl = -B_{\rm D} \left(\frac{A}{\Delta}\right)^{1/2} 2\pi\, dr. \tag{2.30}$$

Making use of Eqs. (2.25), (2.26), and (2.30), we obtain

$$(-dR_{\rm H}/dr) = \frac{2}{c\, r_{\rm H}^2}\, \frac{1}{\zeta} \left(\frac{r}{r_{\rm ms}}\right)^{-n} \left(\frac{A}{\Delta}\right)^{1/2}. \tag{2.31}$$

Next, we write the particle specific energy (Eq. 2.13) using the dimensionless radius and the spin parameter. Then, we substitute this equation (evaluated at $r_{{\rm sl}_*}$ and $r_{{\rm ms}_*}$, respectively) together with (2.18) – (2.27), (2.30), and (2.31) for Eq. (2.17). So, the launching power of the jets becomes

$$\boxed{\begin{aligned} P_{\rm jets} = {} & \dot{m} \dot{M}^\dagger_{\rm Edd} c^2 \varepsilon^{-1} (1 - q_{\rm jets}) \left(E^\dagger_{{\rm sl}_*} - E^\dagger_{{\rm ms}_*}\right) \left(\frac{M}{10^9 M_\odot}\right) \\ & + \dot{M}^\dagger_{\rm Edd} c^2\, C_* \left(\frac{B_{\rm H}}{B^{\rm max}_{\rm H}}\right)^2 \left(\frac{M}{10^9 M_\odot}\right) \int_{r_{{\rm ms}_*}}^{r_{{\rm sl}_*}} r_*^{1-n} {\rm R}_*^{1/2} \left(\Omega_{{\rm H}_*} - \Omega_{{\rm D}_*}\right) \Omega_{{\rm D}_*} dr_* \end{aligned}}, \tag{2.32}$$

where

$${\rm C}_* = \frac{r^2_{{\rm H}_*} r^n_{{\rm ms}_*} E^\dagger_{{\rm ms}_*,{\rm lim}}}{4\pi\zeta (a_{*,{\rm lim}})^2 \varepsilon_{\rm lim}},\ {\rm R}_* = \frac{1 + a_*^2 r_*^{-2} + 2 a_*^2 r_*^{-3}}{1 - 2 r_*^{-1} + a_*^2 r_*^{-2}}. \tag{2.33}$$

For the following calculations, we consider the strength of the magnetic field in Eq. (2.32) to be as high as its maximum value $B_H \cong B^{\rm max}_{\rm H}$. On the right-hand side, the first term represents the accretion power of the disk inside the BH ergosphere, and the second term represents the BH spin-down power transferred to the disk inside the ergosphere by magnetic connection. So, Eq. (2.32) can also read:

$$\boxed{P_{\rm jets} = P^{\rm acc}_{\rm jets} + P^{\rm rot}_{\rm jets}}. \tag{2.34}$$

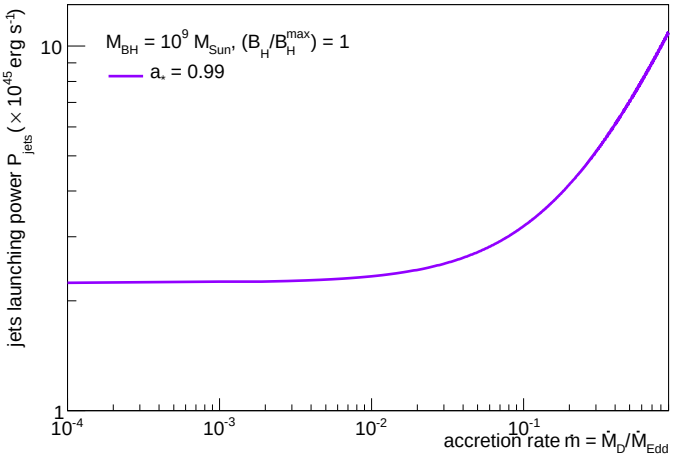

Figure 2.7: Launching power of the jets as a function of the mass accretion rate $\dot{m}$ (Eq. 2.32) for a given BH spin parameter $a_* = 0.99$. The switch from an accretion power regime to a spin-down power regime corresponds to a mass accretion rate $\dot{m} \simeq 10^{-1.8}$.

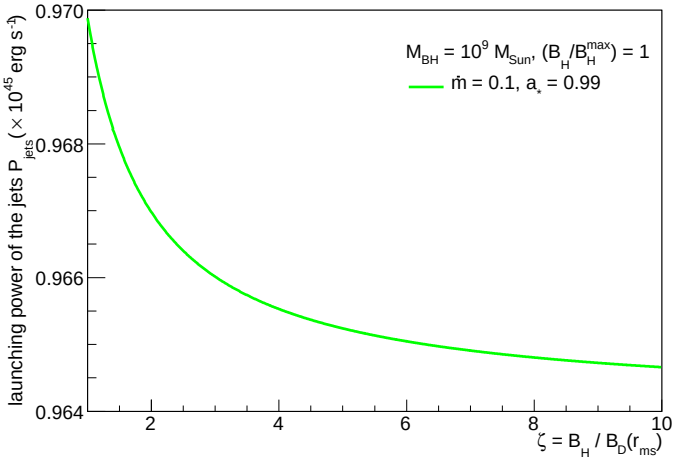

Figure 2.8: Launching power of the jets as a function of ζ given that $a_* = 0.99$ and $\dot{m} = 0.1$; its maximum corresponds to $\zeta = 1$. The same behavior is obtained for any $a_* \in [0.95, 1]$ and $\dot{m}$; thus, we set ζ for our calculations by taking its value corresponding to the maximum of the launching power of the jets; i.e., $\zeta = 1$.

In Fig. 2.7, we plot the launching power of the jets as a function of the mass accretion rate. The plot shows that a transition from an accretion power regime to a spin-down power regime is produced for $\dot{m} \simeq 10^{-1.8}$. So, we have: (1) an **accretion power regime** in which case $\dot{m} > 10^{-1.8}$ and the dominating term in the launching power of the jets is $P_{\rm jets}^{\rm acc}$, and (2) a **spin-down power regime** in which case $\dot{m} < 10^{-1.8}$ and the dominating term in the launching power of the jets is $P_{\rm jets}^{\rm rot}$. This is an important result, which can directly be related to observations. As we mention in the introduction of this chapter, the dependence of the power of the jet on the mass accretion rate differs for the two regimes; that is, in the accretion power regime, the power of the jets is linearly dependent on the mass accretion rate (see Eq. 2.32), whereas in the spin-down power regime the power of the jets depends very weakly on the mass accretion rate.

In Eq. (2.32), the launching power of the jets depends on: (i) the mass accretion rate $\dot{m}$, (ii) the BH mass M, (iii) the BH spin parameter a_*, (iv) the power-law index n, and (v) the ratio of the magnetic field strengths ζ. We chose the last two parameters as follows: the power-law index n is taken to be '2' as for a frozen magnetic field (Alfvén 1963), and ζ is set by taking its value corresponding to the maximum of the launching power of the jet, which is one (see Fig. 2.8). Therefore, for the following calculations, we consider $\boxed{n = 2 \text{ and } \zeta = 1}$.

In Fig. 2.9, we plot the launching power of the jets as a function of the BH

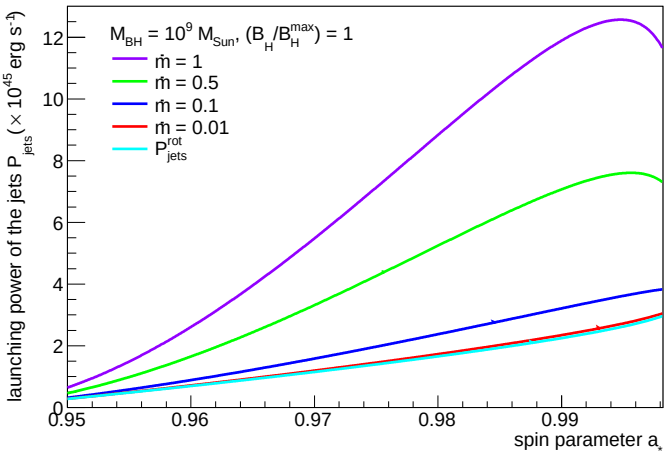

Figure 2.9: Launching power of the jets as a function of a_* (Eq. 2.32) for four values of the mass accretion rate. The mass accretion rates from top to bottom are 1, 0.5, 0.1, and 0.01. The bottom curve represents the power of the jets given by the BH spin-down $P_{\rm jets}^{\rm rot}$. Note that there is a slight difference between the two bottom curves (red and turquoise curves). In the case of very low mass accretion rates, $\dot{m} < 10^{-1.8}$, $P_{\rm jets}$ is approximately equal to the BH spin-down power.

spin parameter, for a BH mass of $10^9 M_\odot$, given four values of the mass accretion rate ($\dot{m} = 1, 0.5, 0.1,$ and 0.01), as well as the BH spin-down power contribution to the jets power (bottom curve). Since the area of the disk inside the BH ergosphere increases with an increase of a_*, there is a dominating trend of the jet power to increase as well, except for a_* close to the extreme value. The turn-over of the curve is produced due to the general relativistic factor that appears in the term $(1 - q_{\rm jets})$ of the accretion power. In the case of the spin-down power regime, the jet power is $\sim 10^{45}$ erg s^{-1}, which is only 10^{-2} of the Eddington luminosity of a 10^9 solar mass BH. This value of $P_{\rm jets}^{\rm rot}$ is comparable to the maximum rate of energy extraction by the Blandford–Znajek mechanism, which is $\sim 10^{45}$ erg s^{-1} for a BH mass of $10^9 M_\odot$ and a_* close to the extreme value [Eq. 4.50 of Thorne et al. (1986)]. For a lower mass of the BH, the jet power decreases, as the launching power of the jets is proportional to the BH mass.

On sub-parsec scales, the jets are likely to be dominated by electromagnetic processes (MHD or pure electrodynamic), where the energy is transported along the jets via Poynting flux, and are potentially unstable if significant thermal mass load is present (Meier 2003). Next, we estimate the magnetization parameter of the jet plasma at the launching points, σ, which reflects the effect of a rotating magnetic field on accelerating the jet plasma by measuring the Poynting flux in terms of particle flux (e.g., Michel 1969; Camenzind 1986; Fendt & Greiner 2001). The initial magnetization parameter of the jets (denoted by an index '0') is given by

$$\sigma_0 = \frac{\Psi^2 \Omega_{\rm D}^2}{4\pi \dot{M}_{\rm jets} c^3}, \tag{2.35}$$

where $\Psi = \int B\, dS$ and $\Omega_{\rm D}$ is here taken as the angular velocity of the magnetic field lines frozen in the disk. For illustration, we evaluate σ_0 for three values of the mass accretion rate ($\dot{m} = 1, 0.1, 0.01$ and 0.001) in the case of a BH with the spin parameter of $a_* = 0.99$ (see Fig. 2.10). The magnetization parameter increases with decreasing mass accretion rate ($\sigma_0 \sim \dot{m}^{-1}$), as well as with decreasing radius. When $\sigma_0 > 1$, the Poynting flux dominates in the jets and the energy can be transferred from the magnetic field to the particles. As a result, the jets can be accelerated on the expense of the stored energy in the magnetic field as the Poynting flux is converted into kinetic energy flux by magnetic forces (e.g., Fendt 2004). The magnetic force can be split in two components: the magnetic pressure force ($\sim \nabla B_\phi^2$), which points in positive outward direction, and the magnetic tension

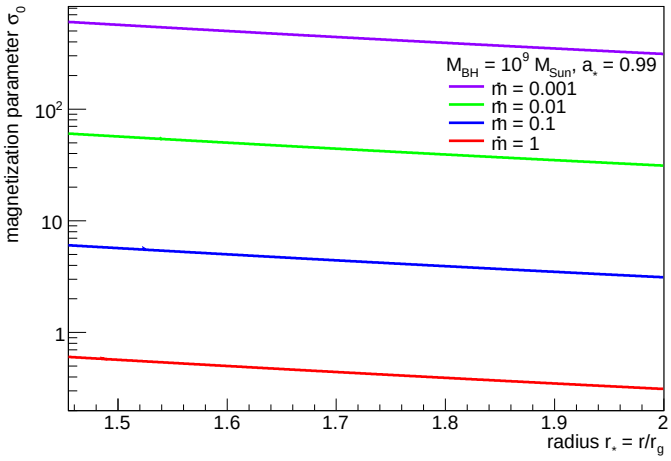

Figure 2.10: Initial magnetization parameter of the jet plasma as a function of the disk radius for three values of the mass accretion rate when the BH spin parameter is $a_* = 0.99$. The mass accretion rates from top to bottom are 0.01, 0.1 and 1. For $\sigma \geqslant 1$, the jets are Poynting flux-dominated outflows; i.e., the energy content of the jets is mainly in the magnetic part. For $\sigma < 1$, the jets are particle-dominated outflows. Note that $\sigma_0 \sim \dot{m}^{-1}$.

force ($\sim B_\phi^2$), which points in negative inward direction. (B_ϕ denotes the strength of the toroidal component of the magnetic field.) In the case of a ballistic jet, which expands with a constant speed, the two forces cancel each other and the toroidal component of the magnetic field decreases as $B_\phi \sim z^{-1}$ due to the magnetic flux conservation. (z denotes the distance along the jet.) To accelerate the flow, the magnetic pressure gradient must prevail over the magnetic tension force. This can be possible, in principle, due to the decrease in the strength of the toroidal magnetic field as the jet propagates away from the source, but one has to solve the full problem to verify whether the magnetic pressure gradient dominates over the magnetic tension force. The magnetic acceleration process is limited by the free energy available in the magnetic field, and saturation must occur at some point. When the kinetic energy flux becomes dominant in the jet, strong shocks can occur. These shocks can further accelerate the jet. However, if the magnetic field becomes highly twisted, the magnetic field itself will not be able to explain the acceleration of the jet, as the magnetic reconnection or other instability in the jet can lead to magnetic energy dissipation and shock formation. (Strong toroidal magnetic fields are subject to the kink instability, which excites large-scale helical motions that can distort or even disrupt the jet [e.g., Mizuno et al. (2009a) and references therein]. However, the growth rate of the kink mode may be reduced, for instance, by increasing the magnetic pinch or by including a gradual shear, an external wind or relativistic bulk motion.) How far the magnetic acceleration of the jets can occur depends from one case to another, and the ambient medium into which jets propagate can play a significant role. On parsec scales, relativistic shocks are expected to be prominent (Lobanov 2007). A first stationary, strong shock can be produced in the approximate range $(3 - 6) \times 10^3\, r_g$ (Markoff et al. 2001; Marscher et al. 2008), whereas moving shocks can occur between 20 and 200 r_g. For very large values of the magnetization parameter, the MHD approximation breaks down (Mizuno et al. 2009a). For $\sigma_0 = 1$ the Poynting flux and the particle kinetic energy flux are in equipartition, whereas for $\sigma_0 < 1$ the jets are kinetic energy flux-dominated outflows. For given mass accretion rate and BH spin parameter, the value of σ_0 is not much less than one, being only within one order or magnitude smaller than one. Therefore, it is possible that the jets will be stable and propagate initially with a constant speed. However, plasma processes can become more important in this case.

For given mass accretion rate and radius, σ_0 increases with the BH spin parameter; i.e., the Poynting flux in the jets increases as the BH rotates faster. For $\dot{m} = 1$ (Fig. 2.10), the maximum value of σ_0 is 0.993, which is obtained at the innermost stable orbit for a

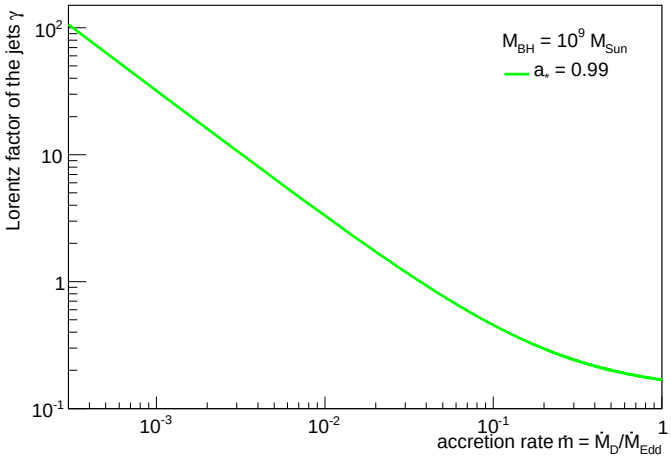

Figure 2.11: Lorentz factor of the jets as a function of $\dot{m}$ (Eq. 2.36). The jets have a bulk Lorentz factor $\gamma > 2$ when the mass accretion rate $\dot{m} < 10^{-1.8}$, which corresponds to the spin-down power regime. In the case of the accretion power regime, $\dot{m} > 10^{-1.8}$, the jets are mildly- and sub-relativistic, $\gamma < 2$.

BH spin parameter of 0.9982. (However, σ_0 increases for higher spins but we limit here the value of the BH spin parameter to that of Thorne's model.) For $\dot{m} = 10^{-1.8}$, which delimits the accretion power regime from the spin-down power regime, the initial magnetization parameter is larger than ~ 5 for any $a_* > 0.95$.

One can consider a relation between the magnetization parameter (Eq. 2.35) and the initial Lorentz factor of the jets of the form $\gamma_0 = \sigma_0^{1/q}$, where the value of the power low index depends on the magnetic field configuration. For a radial outflow with negligible gas pressure, $q = 3$ (Michel 1969). For a collimated MHD jet, the value of q is also 3 if the flux distribution is the same (Fendt & Greiner 2001). With the power low above, the jets can present a radial distribution of the initial Lorentz factor, which increases with decreasing radius. Note that γ_0 differs from the bulk Lorentz factor of the jets (γ) that is defined below (Eq. 2.36), where it is assumed that the Poynting flux in the jets has been fully converted into kinetic energy flux.

The bulk Lorentz factor of the jets γ, defined by

$$P_{\rm jets} = \gamma \dot{M}_{\rm jets} c^2 = \gamma q_{\rm jets} \dot{m} \dot{M}_{\rm Edd} c^2, \tag{2.36}$$

[which follows, e.g., from Falcke & Biermann (1995); see also Vila & Romero (2010)] is drawn in Fig. 2.11 as a function of the mass accretion rate. The jets have a relativistic speed of $0.9 - 0.995\,c$ (or $\gamma = 2 - 10$, which is the typical bulk Lorentz factor for an AGN jet) when the mass accretion rate $\dot{m} \in [10^{-2.5}, 10^{-1.8}]$; i.e., these jets correspond to the spin-down power regime. In the case of the accretion power regime, the jets are mildly- and sub-relativistic ($\gamma < 2$). There is no significant variation of γ with the BH spin parameter ($a_* \geqslant 0.95$) for a given mass accretion rate.

2.6 Rate of the disk angular momentum removed by the jets

Now, we define the rate of the disk angular momentum removed by the jets as

$$\boxed{J_{\rm jets} = 2 \int_{r_{\rm ms}}^{r_{\rm sl}} 2\pi J L^{\dagger} r dr}\,. \tag{2.37}$$

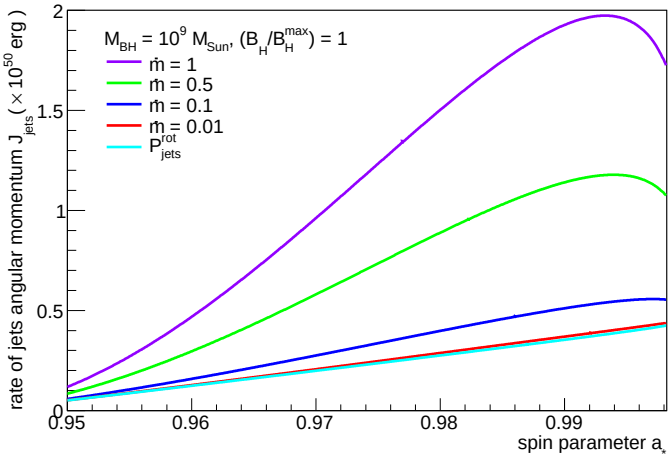

Figure 2.12: Rate of the disk angular momentum removed by the jets (Eq. 2.40) as a function of the BH spin parameter a_* for four values of the mass accretion rate. The mass accretion rates from top to bottom are 1, 0.5, 0.1, and 0.01. The bottom curve represents the BH spin-down transferred to the disk inside the ergosphere by magnetic connection. Note that there is a slight difference between the two bottom curves (red and turquoise curves).

Using the angular momentum conservation law (Eq. 2.10), the rate of the disk angular momentum removed by the jets can be written as

$$\boxed{J_{\rm jets} = (1-q_{\rm jets})\,\dot{M}_{\rm D} c \left(L^{\dagger}_{\rm sl} - L^{\dagger}_{\rm ms}\right) + 4\pi \int_{r_{\rm ms}}^{r_{\rm sl}} r H dr}, \tag{2.38}$$

where the dimensionless specific angular momentum of the gas particle orbiting in the accretion disk is

$$J^{\dagger}(r_*) = r_*^{-1/2} \frac{1 - 2a_* r_*^{-3/2} + a_*^2 r_*^{-2}}{\left(1 - 3r_*^{-1} + 2a_* r_*^{-3/2}\right)^{1/2}}. \tag{2.39}$$

Combining equation (2.38) with equations (2.18) – (2.27) and (2.30) – (2.31), the rate of the disk angular momentum removed by the jets becomes

$$\boxed{\begin{aligned} J_{\rm jets} = {} & \dot{m}\dot{M}^{\dagger}_{\rm Edd} c\, r_{\rm g} \varepsilon^{-1} (1-q_{\rm jets}) \left(L^{\dagger}_{{\rm sl}_*} - L^{\dagger}_{{\rm ms}_*}\right) \left(\frac{M}{10^9 M_\odot}\right) \\ & + \dot{M}^{\dagger}_{\rm Edd} c\, r_{\rm g} {\rm C}_* \left(\frac{B_{\rm H}}{B^{\rm max}_{\rm H}}\right)^2 \left(\frac{M}{10^9 M_\odot}\right) \int_{r_{{\rm ms}_*}}^{r_{{\rm sl}_*}} r_*^{1-n} {\rm R}_*^{1/2} \left(\Omega_{{\rm H}_*} - \Omega_{{\rm D}_*}\right) dr_*, \end{aligned}} \tag{2.40}$$

where C_* and R_* are defined by equation (2.33). We can also write the disk angular momentum removed by the jets as the sum of two components, the accretion and the rotation parts,

$$\boxed{J_{\rm jets} = J^{\rm acc}_{\rm jets} + J^{\rm rot}_{\rm jets}}. \tag{2.41}$$

Figure 2.12 shows the rate of the disk angular momentum removed by the jets as a function of the spin parameter of the BH, given four values of the mass accretion rate ($\dot{m}$ = 1, 0.5, 0.1, and 0.01), as well as the BH spin-down $J^{\rm rot}_{\rm jets}$ (bottom curve). To know how this angular momentum is transported by the jets, further models must be employed.

2.7 Efficiency of jet launching

We define the efficiency of jet launching as the ratio of the launching power of the jets to the total power that comes from the accreting rest mass-energy and from the

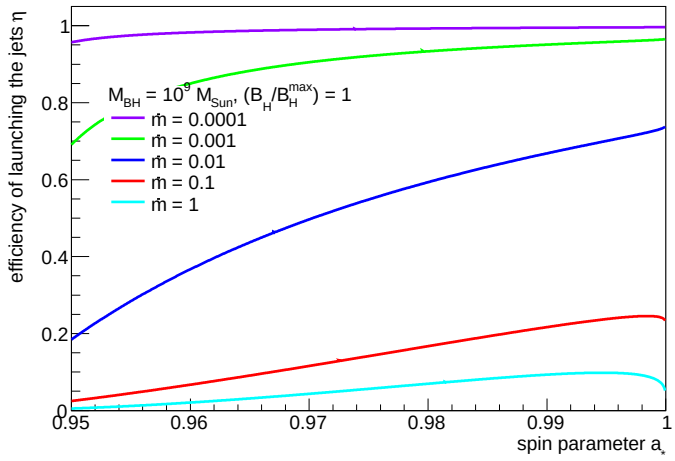

Figure 2.13: Efficiency of jet launching (Eq. 2.42) as a function of the BH spin parameter a_* for different mass accretion rates. The mass accretion rates from the top to bottom are 0.0001, 0.001, 0.01, 0.01, and 1. For very low mass accretion rates, $\dot{m} < 0.001$, the BH spin-down becomes a very efficient mechanism of launching the jets via the accretion disk.

rotational energy of the BH. Thus,

$$\boxed{\eta = \frac{P_{\rm jets}}{\dot{m}\dot{M}_{\rm Edd}c^2 + P_{\rm jets}^{\rm rot}}}. \tag{2.42}$$

In Figure 2.13, we plot the efficiency of jet launching for the range of the mass accretion rate $\dot{m} \in [0.0001, 1]$. For very low mass accretion rates, $\dot{m} < 0.001$, the efficiency of jet launching reaches values close to unity, in which case the spin-down of the BH becomes a very efficient mechanism to launch the jets via the accretion disk. For the spin-down power regime, the efficiency of jet launching is higher than the maximal efficiency of converting the gravitational energy of the accretion disk into radiation ($\varepsilon = 0.42$), as a result of transferring the BH rotational energy to the accretion disk via BH-disk magnetic connection.

2.8 Spin evolution of the black hole

Theoretically, a Kerr BH can be spun up to a state with a spin parameter whose maximum value is $a_* = 1$. As the spin evolves, a Kerr BH can achieve a stationary state. A theorem established by Hawking (1972) states that a BH is in a stationary state if and only if the BH is either static or axisymmetric. Suppose we have a Kerr BH. Perturbating fields can, however, deflect the spin orientation away from the symmetry axis. In this case, the BH must either spin down until a static (Schwarzschild) BH is reached or evolve in such a way that it aligns its spin with the perturbative field orientation. This can be the case of an warped accretion disk, which is, for instance, directly observed in NGC 4258 [see Moran (2008)].

Next, we study the BH spin evolution and seek the maximum spin parameter that corresponds to a stationary state of the BH, when both the BH-disk magnetic connection and the jet formation are considered. Thorne (1974) calculated the influence of photon capture on the spin evolution of the BH and found a limiting state of $a_{*,\rm lim} \simeq 0.9982$. This limit does not apply to our model since the disk inside the BH ergosphere is not radiative, as in the case of Thorne's model. Instead, it drives the jets. We consider this limit only to determine the maximum value of the BH magnetic field, given at the time when the BH accretes at near the Eddington limit.

Bardeen (1970) showed that the mass and angular momentum of the BH can be changed by the specific energy and angular momentum of the particles carried into the BH. The BH mass (and the angular momentum) variation equals the value of the particle specific energy (and angular momentum) at the innermost stable orbit multiplied by the rest mass accreted (dM_0) if no other stress energy is allowed to cross the horizon. That is,

$$dM = E^{\dagger}_{\rm ms}\, dM_0 \ \text{ and } \ dJ = J^{\dagger}_{\rm ms}\, dM_0, \tag{2.43}$$

where $E^{\dagger}_{\rm ms}$ and $J^{\dagger}_{\rm ms}$ are the specific energy and angular momentum of the particles evaluated at the innermost stable orbit. Using Eq. (2.43), one can obtain the differential equation that describes the spin evolution of the BH due to matter accretion:

$$\boxed{\left(\frac{da_*}{d\,\ln M}\right)_{\rm matter} = \frac{c}{GM}\left(\frac{dJ}{dM}\right) - 2a_*}. \tag{2.44}$$

Now, we consider the magnetic extraction of the BH rotational energy through the BH-disk magnetic connection. **The spin evolution law (Eq. 2.44) will be changed due to the counter-acting torque exerted on the BH by the magnetic field that connects the BH to the disk inside the ergosphere**. The energy and angular momentum lost (or gained, depending on the angular velocities of the BH and disk, cf. Eq. 2.14) by the BH through the BH-disk magnetic connection are (see, e.g., Li 2002a):

$$c^2\left(\frac{dM}{dt}\right)_{\rm HD} = 2P_{\rm HD} \ \text{ and } \ \left(\frac{dJ}{dt}\right)_{\rm HD} = 2T_{\rm HD}, \tag{2.45}$$

where $P_{\rm HD} = \Omega_{\rm H} T_{\rm HD}$, and the factor '2' comes from the fact that the accretion disk has two surfaces, as well as two jets. Adding the effects of the BH spin-up by accretion (Eq. 2.43) and the BH spin-down by magnetic connection (Eq. 2.45), the equations for evolution of the BH mass and the BH angular momentum become:

$$c^2\left(\frac{dM}{dt}\right) = (1-q_{\rm jets})\,\dot{M}_{\rm D} c^2 E^{\dagger}_{\rm ms} + c^2\left(\frac{dM}{dt}\right)_{\rm HD}, \tag{2.46}$$

$$\left(\frac{dJ}{dt}\right) = (1-q_{\rm jets})\,\dot{M}_{\rm D} L^{\dagger}_{\rm ms} + \left(\frac{dJ}{dt}\right)_{\rm HD}. \tag{2.47}$$

Using these two equations, we can express the BH spin evolution as

$$\boxed{\left(\frac{da_*}{d\,\ln M}\right)_{\rm total} = \frac{c}{GM}\frac{(1-q_{\rm jets})\dot{M}_{\rm D} L^{\dagger}_{\rm ms} + \left(\frac{dJ}{dt}\right)_{\rm HD}}{(1-q_{\rm jets})\dot{M}_{\rm D} E^{\dagger}_{\rm ms} + \left(\frac{dM}{dt}\right)_{\rm HD}} - 2a_*}, \tag{2.48}$$

when both the BH spin-up by accreting matter and the BH spin-down due to the angular momentum transferred from the BH to the disk inside the ergosphere are considered. From Eqs. (2.44) and (2.48), the spin-down of the BH by means of BH-disk magnetic connection is described by

$$\boxed{\left(\frac{da_*}{d\,\ln M}\right)_{\rm HD} = \left(\frac{da_*}{d\,\ln M}\right)_{\rm total} - \left(\frac{da_*}{d\,\ln M}\right)_{\rm matter}}. \tag{2.49}$$

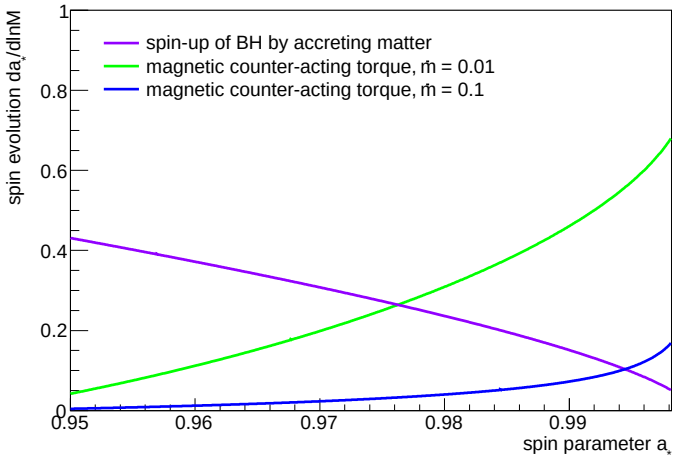

Figure 2.14: Spin evolution of a Kerr BH. The purple line represents the driving torque by which the matter spins up the BH (Eq. 2.44). The blue and green lines represent the counter-acting torque on the BH due to transfer of rotational energy from the BH to the disk (Eq. 2.49) for $\dot{m} = 0.1$ and $\dot{m} = 0.01$, respectively. For these two cases of the mass accretion rate, the stationary state of the BH corresponds to $a_* \simeq 0.9944$ and $a_* \simeq 0.9762$, respectively.

Figure 2.14 shows the spin evolution of a Kerr BH for two values of the mass accretion rate $\dot{m} = 0.1$ and $\dot{m} = 0.01$, respectively. The purple line represents the driving torque by which the matter spins up the BH [Eq. 2.44; see also fig. 6 in Thorne (1974)], and the blue and green lines represent the counter-acting torque on the BH due to transfer of rotational energy from the BH to the disk (Eq. 2.49) for $\dot{m} = 0.1$ and $\dot{m} = 0.01$, respectively. The crossing point of the plots corresponds to the spin parameter for which the BH is in a stationary state. For $\dot{m} = 0.1$, if the BH initially rotates with $a_* = 0.9982$, the BH may spin down to a stationary state with a maximum spin parameter of $a_* = 0.9944$. For $\dot{m} = 0.01$, the maximum spin parameter is $a_* = 0.9762$, whereas for $\dot{m} = 0.001$, the maximum spin parameter is $a_* = 0.9525$. Thus, as the mass accretion rate decreases, the maximum spin parameter corresponding to a stationary BH decreases as well. On the other hand, as the mass accretion rate decreases, the magnetic torque reaches values close to unity, so it is greater than 0.43, which is the maximum value of the matter torque. This implies deviations from pure Keplerian orbits, and so the possibility to drive away the excess angular momentum of the disk in the form of jets when the BH spin-down power is considered. A further analysis of the spin evolution (which is not explicitly shown in Fig. 2.14) suggests that a BH needs a mass accretion rate of at least $\dot{m} \sim 0.001$ for its spin to stay high ($a_* \geqslant 0.95$). For lower mass accretion rates ($\dot{m} < 0.001$), the BH may spin down continuously until the BH reaches a static state. It can spin-up again to $a_* \geqslant 0.95$ if a large amount of matter is provided by accretion (or by merging, which is not discussed here). In this case, the amount of accreting mass should be a factor of about 1.84 from the initial mass of the BH (Thorne 1974).

2.9 Relevance to the observational data

2.9.1 Maximum lifetime of the AGN from the black hole spin-down power

In this section, we calculate the time-scale needed for a Kerr BH to spin down from $a_* \sim 1$ to 0.95, which can then be related to the maximum lifetime of the AGN, provided that the BH was spun up to nearly its maximum spin during a phase when the AGN was active. The AGN can be active as long as the accreting rest mass-energy is converted into observed radiation energy. Such an AGN can have a longer lifetime through the additional use of its BH spin-down power, despite having a very-low mass-accretion rate ($\dot{m} < 0.1$).

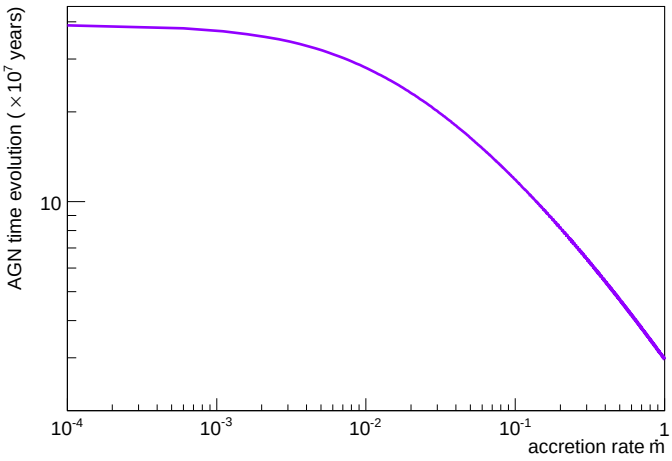

Figure 2.15: Lifetime of the AGN from the BH spin-down power as a function of the mass accretion rate. The lifetime of the AGN is $\sim 3 \times 10^7$ yr when using the accretion power. The BH spin-down power adds to the lifetime of the AGN, for instance, 2.8×10^8 yr, 3.9×10^8 yr, and $\sim 4 \times 10^8$ yr when $\dot{m} = 10^{-2}$, $\dot{m} = 10^{-3}$, and $\dot{m} < 10^{-4}$, respectively (while the BH spin parameter decreases from $a_* \sim 1$ to 0.95).

Following the well-known work by Salpeter (1964), the time needed to fuel the AGN to a bolometric luminosity $L_{\rm bol} \sim 10^{45}$ erg s^{-1} can be $\sim 10^7$ yr for a typical radiative efficiency of $\varepsilon = 0.1$. Moreover, the lifetime of high accreting AGN (and quasars) was constrained by recent observations to the range $\sim 10^7 - 10^8$ yr (e.g., Porciani et al. 2004; Hopkins & Hernquist 2009). These numbers have been essentially the same since the 1960s, just a bit smaller now than originally.

Next, we estimate the maximum lifetime of the AGN. Differentiating the BH angular momentum $J = Mca = (GM^2/c)\, a_*$ with respect to time t, the BH time evolution is specified by

$$\left(\frac{da_*}{dt}\right) = \frac{c}{GM^2}\left(\frac{dJ}{dt}\right) - 2\frac{a_*}{M}\left(\frac{dM}{dt}\right). \tag{2.50}$$

Integrating this equation, the time interval over which the BH spin evolves between two given values of a_* is

$$\boxed{t = \int_{a_{*1}}^{a_{*2}} \left[\frac{c}{GM^2}\left(\frac{dJ}{dt}\right) - 2\frac{a_*}{M}\left(\frac{dM}{dt}\right)\right]^{-1} da_*}, \tag{2.51}$$

where (dJ/dt) can be obtained from Eqs. (2.47) and (2.49), and (dM/dt) from Eqs. (2.46) and (2.49). With the above equation, we can estimate the lifetime of the AGN. We specify that the time interval (Eq. 2.51) is not dependent on the BH mass.

In Fig. 2.15, we plot the time evolution of the AGN as a function of the mass accretion rate (Eq. 2.51), when the BH spin parameter decreases from $a_* \sim 1$ to 0.95. For a mass accretion rate close to the Eddington limit, the lifetime of the AGN is about 3×10^7 yr. The lifetime curve moves toward lower mass accretion rates for another $\sim 10^8$ yr, when the AGN uses its BH spin-down power to launch the jets. Therefore, the total lifetime of the AGN can be much longer than the Hubble time ($t_{\rm H} \sim 10^{10.14}$ yr). The maximum lifetime of the AGN is, however, dependent on the mass accretion rate. The maximum lifetime of the AGN from the BH spin-down power is, for instance, $\sim 2.8 \times 10^8$ yr, $\sim 3.9 \times 10^8$ yr, $\sim 4 \times 10^8$ yr for $\dot{m} = 10^{-2}$, $\dot{m} = 10^{-3}$, and $\dot{m} < 10^{-4}$, respectively. In the latter case, the BH may not attain a stationary state and spins down until a static BH is reached. The lifetime of the AGN scales with the strength of the BH magnetic field relative to its maximum value as $t \sim (B_{\rm H}/B_{\rm H}^{\rm max})^{-2}$. Therefore, if the $B_{\rm H}$ is a factor of k lower than $B_{\rm H}^{\rm max}$, then the maximum lifetime of the AGN will be a factor of k^2 larger. For instance, when $k = 7$ and $\dot{m} = 10^{-2}$, one obtains the exact Hubble time.

Now, we compare our results to the lifetime of an AGN powered by the Blandford–Znajek mechanism. The total energy that can be extracted by the Blandford–Znajek mechanism is (e.g., Li 2000a):

$$E_{\rm BZ} \simeq 0.09 Mc^2 \simeq 1.6 \times 10^{62}\ {\rm erg}\ \left(\frac{M}{10^9 M_\odot}\right). \tag{2.52}$$

The maximum rate of energy extraction by the Blandford–Znajek mechanism is [Eq. 4.50 of Thorne et al. (1986)]:

$$P_{\rm BZ} \simeq 10^{45}\ {\rm ergs}^{-1}\ \left(\frac{B_{\rm H}}{10^4 {\rm G}}\right)^2 \left(\frac{M}{10^9 M_\odot}\right)^2, \tag{2.53}$$

for a BH with $a_* \sim 1$. Therefore, the lifetime of an AGN powered by the Blandford–Znajek mechanism is:

$$t_{\rm BZ} = \frac{E_{\rm BZ}}{P_{\rm BZ}} \simeq 5 \times 10^9\ {\rm yr} \left(\frac{B_{\rm H}}{10^4 {\rm G}}\right)^{-2} \left(\frac{M}{10^9 M_\odot}\right)^{-1}, \tag{2.54}$$

which is not dependent of the BH mass, as $B_{\rm H}$ scales with $(M/10^9 M_\odot)^{-1/2}$. Except for the exact time scale, our result (Eq. 2.51) scales with the magnetic field and with the BH mass exactly the same way as for the Blandford-Znajek mechanism.

Moving back to our results, if the mass accretion rate changes over the whole life of the AGN from $\dot{m} \sim 10^{-1.8}$ to $\dot{m} < 10^{-4}$, the maximum lifetime of the AGN can be even longer than that of an AGN powered by the Blandford–Znajek mechanism. In summary, the maximum lifetime of the AGN can be much longer than $\sim 10^7$ yr when using the BH spin-down power. The lifetime is dependent on the mass accretion rate, as well as on the factor $(B_{\rm H}/B_{\rm H}^{\rm max})$. We mention that the results presented here refer only to rapidly-spinning BHs ($a_* \geqslant 0.95$).

2.9.2 On the relation between the spin-down power of a black hole and the particle maximum energy in the jets

Particles (electrons/positrons and protons) can be accelerated by shocks in the jets to the relativistic regime and then produce the synchrotron spectrum observed from radio jets. Cosmic ray protons can survive the radiative cooling, propagate through the intergalatic medium, and produce secondary particles through interaction with Earth's atmosphere. A model for the ultra-high-energy cosmic ray contribution from the spin-down power of BHs is discussed in Chapter 3.

In this section, we seek the relation between the BH spin-down power and the particle maximum energy in the jets. From Eq. 2.32, the BH spin-down power contribution to the jet power is

$$P_{\rm jets}^{\rm rot} = \dot{M}_{\rm Edd}^{\dagger} c^2 C_* \left(\frac{M}{10^9 M_\odot}\right) \cdot \int_{r_{\rm ms*}}^{r_{\rm sl*}} r_*^{-1} {\rm R}_*^{1/2} \left(\Omega_{\rm H_*} - \Omega_{\rm D_*}\right) \Omega_{\rm D_*} dr_*, \tag{2.55}$$

where C_* and R_* are specified by equation 2.33.

In the case of the spatial (geometrical) limit, which means that the jet particle orbits must fit into the Larmor radius, the particle maximum energy is derived in Section

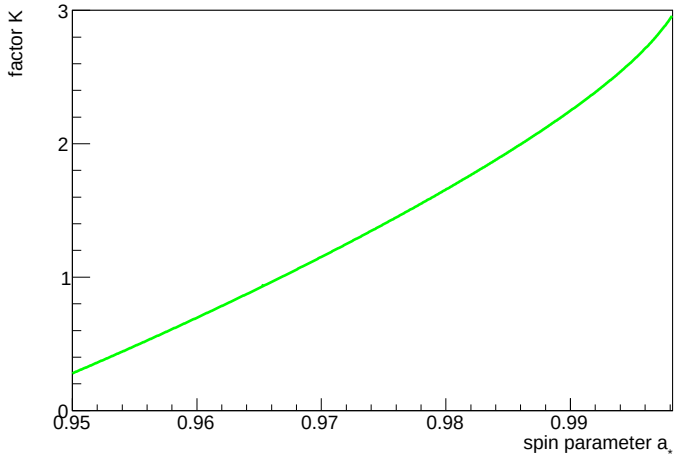

Figure 2.16: Factor $k = (P^{\rm rot}_{\rm jets}/10^{45}\,{\rm erg\ s^{-1}})/(E^{\rm sp}_{\rm max}/10^{20}\,{\rm eV})^2$ as a function of the BH spin parameter. A maximum particle energy of 10^{20} eV corresponds to a jet power of $\sim 3\times10^{45}$ erg s^{-1} for an spin parameter close to the maximum allowed value. Therefore, particles can be accelerated to ultra-high-energy regime in low-luminosity AGN.

3.4. The equation reads

$$E^{\rm sp}_{\rm max} = 5\times10^{20}\left(\frac{M}{10^9 M_\odot}\right)^{1/2}\,({\rm eV})\,, \tag{2.56}$$

for a jet launched from within the ergosphere, $r_0 = 2\,r_{\rm g}$.

The BH spin-down power and the particle maximum energy are related through the equation

$$\boxed{\left(\frac{P^{\rm rot}_{\rm jets}}{10^{45}\,{\rm erg\ s^{-1}}}\right) = K\left(\frac{E^{\rm sp}_{\rm max}}{10^{20}\,{\rm eV}}\right)^2}\,, \tag{2.57}$$

where

$$K = (4\times10^{-47})\dot{M}^{\dagger}_{\rm Edd}c^2 C_* \int_{r_{\rm ms*}}^{r_{\rm sl*}} r_*^{-1}{\rm R}_*^{1/2}\left(\Omega_{\rm H_*}-\Omega_{\rm D_*}\right)\Omega_{\rm D_*}dr_*. \tag{2.58}$$

Figure 2.16 shows that factor K is weakly dependent on the BH spin parameter, when the latter varies in the [0.95, 0.9982] range. Therefore, a maximum particle energy of 10^{20} eV corresponds to a jet power of $\sim 3\times10^{45}$ erg s^{-1} for a spin parameter close to the maximum allowed value. This means that a jet with an energy flow of 10^{45} erg s^{-1}, which is powered by the BH spin-down, can be a site of particle acceleration to ultra-high energies of $\geqslant 100$ EeV. Since the jet luminosity is the lower limit of the energy flow along the jet, $L^{\rm bol}_{\rm jets} \leqslant P_{\rm jets}$, we can conclude that ultra-high-energy cosmic rays can be produced in low-luminosity AGN ($L_{\rm bol} < 10^{45}$ erg s^{-1}).

2.9.3 On the relation between the spin-down power of a black hole and the observed radio flux-density from flat-spectrum core source

Blandford & Königl (1979) showed that the flat-spectrum radio synchrotron emission of a compact jet core can be produced by superposition of self-absorbed synchrotron spectra at different positions of the jet. In their model, the observed radio flux-density depends on the jet power and the distance to the jet source $D_{\rm s}$:

$$F_\nu \sim P^{17/12}_{\rm jet}\,D_{\rm s}^{-2}. \tag{2.59}$$

This 'luminosity' reflects the radiative property of the jet, in which case the radiated energy is replaced by dissipation of the jet kinetic energy. In comparison with the disk emission, the jet luminosity in Eq. 2.59 does not depend on the BH mass.

Falcke & Biermann (1995) found that for radio-loud AGN, the jet luminosity depends non-linearly on the BH mass:

$$F_\nu \sim M^{17/12} \mathcal{D}_{\rm jet}^{2.2}\, \gamma_{\rm jet}^{-1.8}, \tag{2.60}$$

where $\mathcal{D}_{\rm jet}$ is the Doppler factor of the jet, and $\gamma_{\rm jet}$ is the bulk Lorentz factor of the jet. The result is obtained for the case of an accretion-dominated jet, i.e., $P_{\rm jet} \sim L_{\rm disk}$, where $L_{\rm disk}$ is the luminosity of the disk (also see Falcke et al. 1995).

Heinz & Sunyaev (2003) obtained a generalization of Eq. 2.59, for any scale-invariant jet model producing a power-law synchrotron spectrum with an index α in the form of:

$$F_\nu \sim P_{\rm jet}^{(17+8\alpha)/12} M^{-\alpha}, \tag{2.61}$$

where M is the BH mass. Because of the large mass difference between AGN and microquasars, this non-linearity function of the observed radio flux-density with the BH mass indicates that the AGN jets are more radio-loud that the microquasar jets.

In Chapter 3, we derive the expression of the observed radio flux-density (see equation 3.46) for a conical jet, where the magnetic field along the jet scales with the distance, $B \sim z^{-1}$, and the electron number density in the jet scales as $C' \sim z^{-2}$. We showed that the observed radio flux-density is dependent on the energy flow along the jet, the distance to the jet source, and the BH mass as

$$\boxed{F_\nu \sim P_{\rm jet}^{5/6}\, D_{\rm s}^{-2}\, M^{7/12}\, \mathcal{D}_{\rm jet}^{-3}\, \gamma_{\rm jet}^{33/5} (\tan\theta)^{6/5}}, \tag{2.62}$$

where θ is the half-opening angle of the jet. Therefore, **in the BH spin-down power regime, the jet luminosity is dependent on the BH mass, but with a different exponent than in the case of the accretion-dominated regime**. Similar to Eqs. 2.59, 2.60, and 2.61, the expression of observed radio flux-density in equation 2.62 is not dependent on the distance along the jet; thus, it can be applied to microquasars as well.

2.10 Summary and conclusions

Starting from the general-relativistic conservation laws for matter in a thin accretion disk, we included both the BH-disk magnetic connection and the jet formation. The jets are launched from the disk inside the BH ergosphere, where the rotational effects of the space-time become much stronger. In the BH ergosphere, the frame-dragging effect ensures that the magnetic field lines frozen in the disk co-rotate everywhere with the BH, reducing the effect of magnetic reconnection and keeping the magnetic field configuration globally the same. Furthermore, the jets can extract mass, energy, and angular momentum from the disk inside the BH ergosphere. For this situation, we derived the mass flow rate into the jets, the launching power of the jets, the angular momentum removed by the jets, the efficiency of launching the jets, the maximum spin parameter attained by a stationary BH, and the maximum lifetime of an AGN.

- We found that the mass flow rate into the jets is dependent on the BH spin parameter, where the mass outflow into the jets can be associated with the rotation of the space-time itself. For the extreme value of the spin parameter $a_* \sim 1$, the mass outflow into the jets is about 98 percent of the available mass flow through the disk inside the BH ergosphere, whereas for $a_* = 0.95$ this is only about 8 percent. This means that in the case of extreme spin, the BH stops being fed by accreting matter. As a possible alternative, the jets may have no matter right at the beginning (i.e., they are Poynting flux jets) and get it only very quickly from drifts just above the disk or the surrounding wind (i.e., indirectly from the disk). This may only be relevant for extremely low accretion rates.

- In this work, we considered the case of rapidly-spinning BHs with a spin parameter of $a_* \geqslant 0.95$ and a mass of $10^9 M_\odot$, and we assumed that the power of the disk inside the BH ergosphere is used to drive the jets. This fraction is specified by mass outflow into the jets through the parameter $q_{\rm jets}$, which in turn depends on the BH spin parameter, as well as on the mass accretion rate 2.42. The efficiency of jet launching is higher at low mass accretion rates, reaching values close to unity for $\dot{m} \sim 10^{-4}$, in which case, the jet power can be supplied by the BH rotational energy via the disk inside the ergosphere. The switch from an accretion power regime to a spin-down power regime corresponds to a mass accretion rate of $\dot{m} \simeq 10^{-1.8}$. In the case of the spin-down power regime ($\dot{m} < 10^{-1.8}$), the jet power is $\sim 10^{45}$ erg s^{-1}, which is only 10^{-2} of the Eddington luminosity of a 10^9 solar mass BH. This is comparable to the maximum rate of energy extraction by the Blandford–Znajek mechanism, which is $\sim 10^{45}$ erg s^{-1} for a BH mass of $10^9 M_\odot$ and $a_* \sim 1$. This implies that, in principle, both the Blandford–Znajek mechanism and launching the jets from the disk inside the ergosphere via the BH-disk magnetic connection can operate. We intend to study the driving of the jets when the BH is threaded by a combination of open and closed magnetic field lines in future work.

- The jets can have a relativistic speed, $0.9 - 0.995\,c$ (or $\gamma = 2 - 10$, which is the typical bulk Lorentz factor for an AGN jet), when the mass accretion rate $\dot{m} \in [10^{-2.5}, 10^{-1.8}]$. In the case of the accretion power regime, the jets are mildly- and sub-relativistic. However, after launching the jets can be accelerated through magnetic processes. The jets remove the angular momentum of the disk inside the BH ergosphere at a rate which is dependent on the BH spin parameter. To know how this angular momentum is transported by the jets, further models have to be employed. The efficiency of jet launching is higher at low mass accretion rates, reaching values close to unity for $\dot{m} \sim 10^{-4}$. In this case, the BH spin-down power is efficiently used to launch the jets.

- Considering the balance between the BH spin-up by accreting matter and the BH spin-down due to the magnetic counter-acting torque on the BH, we determined the maximum spin parameter which corresponds to a stationary state of the BH. The maximum spin value shifts towards $a_* = 0.95$ as the mass accretion rate decreases. For instance, the maximum spin parameter corresponding to $\dot{m} = 0.1$, $\dot{m} = 0.01$, and $\dot{m} = 0.001$ is $a_* = 0.9944$, $a_* = 0.9762$, and $a_* = 0.9525$, respectively. At lower mass accretion rates ($\dot{m} < 0.001$), the BH may undergo a spin-down process towards a static BH. The BH never reaches a stationary state unless a large amount of matter is provided (perhaps by star capture or by merging) to spin up the BH again to

$a_* \geqslant 0.95$.

- We showed that an AGN can have a much longer lifetime than $\sim 10^7$ yr when using the BH spin-down power, and the maximum lifetime is dependent on the mass accretion rate, as well as on the factor $(B_{\rm H}/B_{\rm H}^{\rm max})$. After an accretion-dominated phase of about 3×10^7 yr, the AGN can live off of the BH spin-down power for another 10^8 yr. The BH spin-down power adds to the lifetime of the AGN, for instance, $\sim 2.8 \times 10^8$ yr, $\sim 3.9 \times 10^8$ yr, $\sim 4 \times 10^8$ yr for $\dot{m} = 10^{-2}$, $\dot{m} = 10^{-3}$, and $\dot{m} < 10^{-4}$, respectively. Moreover, if the $B_{\rm H}$ is a factor of k lower that $B_{\rm H}^{\rm max}$, then the lifetime of the AGN will be a factor of k^2 larger. For $k = 7$ and $\dot{m} = 10^{-2}$, one obtains the exact Hubble time. Another possibility is that the mass accretion rate changes over the whole life of the AGN from $\dot{m} \sim 10^{-1.8}$ to $\dot{m} < 10^{-4}$. In this case, the maximum lifetime of the AGN can be even longer than that of an AGN powered by the Blandford–Znajek mechanism, which is $\sim 5 \times 10^9$ yr for a BH with a_* close to the extreme value. However, it will be difficult to predict a maximum lifetime of the AGN for this case, since there is no mechanism, to date, to control the change of the mass accretion rate over long intervals of time.

- We determined the relation between the BH spin-down power and the particle maximum energy in the jets. Considering the production of ultra-high-energy cosmic rays ($\geqslant 100$ EeV) by shocks in AGN jets, we found that low-luminosity AGN can be sites of particle acceleration to such high energies.

- We obtained the relation between the BH spin-down power and the observed radio flux-density from flat-spectrum core source, and found that the observed radio flux-density depends non-linearly on the BH mass and energy flux along the jet.

In the limit of the BH spin-down regime, the model proposed here can be thought of as being a variant of the Blandford-Znajek mechanism. It is a variant of to the Blandford-Znajek mechanism if an insignificant fraction of the rotational energy is transported away by jets through open magnetic field lines that might thread the BH. If we were to consider the open magnetic field lines in addition to the closed magnetic field lines that thread the BH, our calculations would have been completed such that they would include the Blandford-Znajek mechanism.

The results presented in this chapter are dependent on our assumptions that a BH-disk magnetic connection exists. Closed magnetic field lines in the BH ergosphere may be produced by a current ring in the vicinity of the BH. Models for the magnetic connection where a poloidal magnetic field is generated by a single electric current flowing in the BH equatorial plane or at the inner edge of the accretion disk were proposed, for instance, by Li (2002c) and Wang et al. (2007). The key parameters of our model are, however, the BH mass, the BH spin, and the mass accretion rate.

One indirect way to test whether this mechanism operates in reality is to study the relation between the observed radio flux density from AGN (e.g., from flat-spectrum core sources) and their mass accretion rates in order to fit the model prediction with respect to the relation between the power of the jet and the mass accretion rate (see Fig. 2.7). The latter shows that the power of the jet does not depend linearly on the mass accretion rate all the way down to very low accretion rates, so that there can be sources with relatively strong jet power but low mass accretion rate. In this case the jet power is mainly dependent on the BH parameters, such as the mass and the spin of the BH. The first step is to find

a relation between the power of the jets and the observed radio flux density, $F_{\rm obs}$. For a conical jet (where the magnetic field along the jet scales with the distance, $B \sim z^{-1}$, and the electron number density in the jet scales as $C' \sim z^{-2}$) from a flat-spectrum core source, we found the dependence: $P_{\rm jets} \sim F_{\rm obs}^{6/5} D^{12/5} M^{-7/10}$, where D is the distance to the AGN and M is the BH mass (see Chapter 3). The second step is to produce a complete sample of AGN with known jet parameters, as the Doppler factor, and whose mass accretion rate can be constrained by observational data, and then to fit the model prediction.

Furthermore, if AGN were in the Poynting flux limit disregarding the mass accretion rate, then one might expect that the power in the jet from a large sample runs into a lower limit, which is given by the minimum Poynting flux.

The model presented here can also be extended to microquasars considering that physical quantities (e.g., BH magnetic field, jet power, etc.) scale with the BH mass.

Although numerical simulations of jet formation from the ergosphere of a rapidly-spinning BH with closed magnetic field lines that connect the BH to the disk inside the ergosphere has not been performed yet, this can be one of the challenges to be faced by numerical relativists.

Chapter 3

Ultra-High-Energy Cosmic Ray Contribution from the Spin-Down Power of Black Holes

We propose a model for the ultra-high-energy cosmic ray (UHECR) contribution from the spin-down power of BHs in low-luminosity active galactic nuclei (LLAGN), which present a jet power $P_{\rm j} \leqslant 10^{46}$ erg s^{-1}. This is in contrast to the general opinion that only powerful AGN can accelerate particles to energies $\geqslant 100$ EeV.[1] The jet launched from the ergospheric disk propagates along a cylinder of length z_0 (a few gravitational radii), using the spin-down power of the BH, and then opens in a conical shape. Due to the lateral expansion, the internal pressure drops rapidly below the outside pressure and a recollimation shock is produced. A first strong shock, which accelerates the jet particles with a power-law energy distribution, can be produced at $z \sim 3 \times 10^3$ gravitational radii. Under the conditions of the proposed model, we rewrite the equations which describe the synchrotron self-absorbed emission of such a non-thermal particle distribution to obtain the observed radio flux-density from flat-spectrum core sources. In general, the jet power provides the UHECR luminosity and so, its relation to the observed radio flux-density. As a result, we obtain the expressions for the minimum luminosity and flux of the UHECR as a function of the observed radio flux-density and jet parameters. We apply the model to M87 and Cen A, two possible sources of UHECRs whose jet parameters can be inferred from observational data. In addition, both sources are LLAGN with an accretion rate relative to the Eddington accretion rate $< 10^{-2.5}$, therefore they can be powered by the BH spin down. We use a complete sample of 29 steep-spectrum radio sources (Caramete 2010) with a total flux density greater than 0.5 Jy at 5 GHz to make predictions for the maximum particle energy, luminosity, and flux of the UHECRs. They indicate that, although the jet power is $\leqslant 10^{46}$ erg s^{-1}, the jet particles can be accelerated to energies $\geqslant 100$ EeV.

3.1 Introduction

Cosmic rays (CRs) are relativistic particles of extraterrestrial origin, consisting mainly of protons, alpha particles, and other atomic nuclei but also including some high-

[1] EeV $= 10^{18}$ eV, where 1 eV $= 1.6 \times 10^{-19}$ J.

energy electrons and photons. They enter Earth's atmosphere, collide with atomic nuclei, and produce many secondary particles, principally pions, muons, electrons, neutrinos, as well as gamma rays, which all together form the so-called CR air shower.

CR astrophysics began with a discovery by Victor Hess, who in 1912 made measurements of radiation levels at different altitudes with electroscopes aboard a balloon. He found that the radiation levels increased with altitude and concluded that such radiation must enter the atmosphere from outer space, therefore the name "cosmic radiation."[2] Since then, questions about from where these particles come and how they are accelerated have not yet been answered. The study of CR secondaries, as "little" showers in cloud chambers, has led to great discoveries in physics of new particles such as positrons and muons.

At first, CRs were believed to be photons, and later on, based on the so-called latitude effect (the intensity of radiation at equator is less than the intensity of radiation at higher latitudes), it was established that CRs consist of charged particles as well. This result was an essential ingredient in the theory by Baade & Zwicky (1934), who were the first to propose that CRs are produced in supernova explosions. A stronger indication for the charged CR came from the East-West effect (see, e.g., the review by Gaisser & Stanev 2008). Furthermore, using broadly separated detectors, Auger et al. (1939) observed extended air showers generated by CRs, with energies of the primary particles up to 10^{14} eV, which was quite unexpected. The energy spectrum, which is usually taken to be the number of particles within some energy interval dE and counted per surface area per time per solid angle can be expressed as a power-law $\sim E^{-p}$ with a spectral index $p = 2.7$.[3] Later, the primary particles at GeV energies were identified as mostly protons and, with a lesser abundance, heavier nuclei (e.g., helium).

The present-day understanding of the CR acceleration process has its roots in the seminal papers by Fermi (1949, 1954). In his first paper, Fermi proposed a mechanism by which particles injected into the interstellar medium with energy above a particular threshold are accelerated randomly by collisions with magnetic irregularities in moving clouds. In his second paper, Fermi proposed specific models for the magnetic field which would imply an increase in the energy gain. Fermi's idea led to the development of the **diffusive shock acceleration theory** by various authors in the late 1970s (see, e.g., Axford et al. 1977; Krymsky 1977; Bell 1978a,b; Blandford & Ostriker 1978). The theory of diffusive acceleration at shock fronts describes the interaction of (test) particles with a non-relativistic fluid flow at a given parallel shock front (where the normal to the shock front is parallel to both the direction of fluid flow and magnetic field). In the initial form of the theory, the particles were considered reactionless, i.e., the back-reaction of accelerated particles on the shock structure was neglected. Furthermore, the theory assumed that particles undergo scattering off magnetic irregularities (waves), with a scattering mean path larger than the shock thickness. In this way, the particles can cross the shock many times and gain momentum at each crossing cycle as a result of the velocity difference between the upstream (ahead of the shock) and downstream (behind the shock) scatters, which is caused by the shock compression. For an isotropic particle distribution, in the shock frame, the mean energy[4] gain ($\Delta E/E$) depends linearly on the shock velocity (β_{sh}): $\Delta E/E \sim \beta_{sh}$,

[2]The term "cosmic rays" was introduced by Millikan (1926).

[3]Latest data on the CRs energy spectrum are presented later in this section.

[4]Here, we use energy and later momentum. One should bare in mind that the shock acceleration theory

where $\beta_{sh} \leq 10^{-1}$. The energy gain differs, however, when different background conditions are imposed at the shock front, such as the particle back-reaction on the shock, the shock velocity, perturbations of the magnetic field, or the obliquity of the shock (see, e.g., Drury 1983; Jokipii 1987; Gallant & Achterberg 1999; Kirk et al. 2000; Keshet & Waxman 2005; Meli et al. 2008). After crossing the shock many times, the particles lose the information about the initial momentum, and without a momentum scale, their distribution becomes a power-law in momentum $f \sim P^{-s}$ (here, P is the particle momentum and s is the power-law index of the phase-space density of the injected particles with some Lorentz factor). Due to being scale-free in particle momentum, the acceleration process can produce a power-law spectrum in particle energy, at least for ultrarelativistic particles, whose velocity is nearly independent of the energy (Kirk 2005). The estimated value of the power-law index of the accelerated particle density $[N(E) \sim E^{-p}]$ matches the observed spectral slope of the synchrotron emission from a non-thermal electron distribution ($I_\nu \sim \nu^{-\alpha}$), for example, in AGN (see, e.g., Wiita 1985). The slopes are related through $\alpha = (p-1)/2$ with $s = 2 + p$. Now, if we refer to radio galaxies, a flat-spectrum core source has a spectral index which is typically $\alpha \leqslant 0.5$ at the very center and $\alpha \simeq 0.5 - 0.7$ at a larger radius (the compact radio core can be extremely weak compared with the very bright and luminous radio lobes, suggesting that the radio core might suffer absorption). The latter spectral index corresponds to a power-law index of the accelerated particle of $p \simeq 2.0 - 2.4$. The power-law index of the accelerated particle can be considered, in different models, as that of the injection spectrum of UHECR. To determine the formation of the UHE spectrum after propagation from the acceleration region (which is here considered to be an AGN) to the outer Earth atmosphere, one needs to consider the followings: (i) UHECR source distribution; (ii) cosmic ray source luminosity, (iii) cosmic ray injection (acceleration) spectrum, (iv) maximum acceleration energy, (v) cosmic ray chemical composition, and (vi) cosmic ray source cosmological evolution (Stanev 2008). Berezinsky et al. (2006) have argued that the injection spectrum of (pure proton composition) UHECR is $E^{-2.7}$. Their model fits the observed UHECR HiRes spectrum, but it does not appear to fit the Auger spectrum (some details on the cosmic-ray research projects, such as Hires and Auger, are given later in this section).

Hillas (1984) identified possible sites of accelerating particles to UHEs in either a one-shot process by electric fields, along large-distance, strong magnetic fields of neutron stars or BH accretion disks, or at parallel shock waves. The maximum energy of a particle of charge eZ accelerated within a region of size L was found by balancing the acceleration time with the escape time from the acceleration region, when the diffusion mean free path is comparable to the particle gyro-radius. Hence,

$$E_{\max} = \beta Z B L, \tag{3.1}$$

where B is the magnetic field inside the acceleration region and β is the velocity of the shock wave. For oblique shocks, the β term is replaced with a geometrical factor of order unity $\lesssim 1$ (Jokipii 1987). The magnetic field needs to be strong enough to confine the particles within their acceleration region, and the acceleration region must be large enough so that the particles can gain sufficient energy before they escape. This criterion was used to select possible acceleration sites, which are plotted in a $Log(B)$ vs. $Log(L)$ diagram (known as

uses momentum only. Just for relativistic energies, energy and momentum are equivalent [see later in the same paragraph or in Kirk (2005)].

the Hillas diagram). Using the acceleration versus available times, the hot spots in radio galaxies were considered to be the only possible sites for accelerating UHECR. Biermann (1994) was the first to introduce γ-ray bursts (GRBs) as possible accelerators for UHECR, and later Waxman (1995) and Vietri (1995) developed quantitative theories. Particles with energies below 100 EeV may originate from within our Galaxy [for e.g., supernova remnants (SNRs) or Galactic disk].

After taking into account the transport through the interstellar medium, particle acceleration in diffusive parallel shock waves implies a power-law index which matches the slope of the galactic CR spectrum (~ 2.7). Thus, this mechanism has been largely considered for accelerating cosmic rays in SNRs. Even so, the particles can achieve a maximum energy as high as ~ 1 PeV (see, e.g., Lagage & Cesarsky 1983; van der Swaluw & Achterberg 2004). Therefore, to explain the production of UHECRs (> 100 EeV), one must look for different mechanisms. Relativistic shock acceleration, unipolar induction, and magnetic flares are the most plausible acceleration mechanisms, and oblique shocks can help a great deal (see, e.g., Meli & Biermann 2006). Alternative scenarios are given by "top-down" models; that is, UHECRs are generated through the decay of some supermassive particles released from topological defects (relics of cosmological phase transitions which might have been produced in the early universe). This is only valid if the UHECRs are protons. We note that Auger now publicly claims that the particles are heavy nuclei, while HiRes claims the opposite (see, e.g., Abraham et al. 2010; Abbasi et al. 2010).

The magnetic field plays an important role for the particle acceleration mechanism. The field should be strong enough to confine the particles in the acceleration region, but at the same time, weak enough to avoid too much loss by radiative cooling. In AGN jets of kpc scales, the magnetic field strength is typically $\sim 10^{-2} - 10^{-4}$ G, which provides a maximum energy up to $E_{\max} \sim 1$ ZeV for a particle (Biermann & Strittmatter 1987). The requested value may not be reachable in GRBs if the particles are accelerated at superluminal, ultrarelativistic shocks (see, e.g., Meli et al. 2008). Nonetheless, the detection of high-energy ($\geqslant 1$ TeV) neutrinos can be used as an indicator for acceleration sites of UHECRs, either AGN or GRBs, since neutrino production is expected to occur when UHECRs interact with matter or radiation fields. Since neutrinos are not deflected by magnetic fields in the interstellar and intergalatic space, they can point back directly to their sources. For charged particles, models of particle propagation from the acceleration region to the outer Earth atmosphere must be taken into account.

A first identification of a CR with energy 10^{20} eV was reported by Linsley (1963), as a result of observing the fluorescent light from an air shower with the Volcano Ranch Array. Soon after the discovery of the cosmic microwave background (CMB, Penzias & Wilson 1965), Greisen (1966) and Zatsepin & Kuzmin (1966) realized that the universe is not empty at all; it is filled with photon gas, so that the universe is not transparent to UHECRs. They showed that UHE particles, if they are protons with energy larger or about equal to 50 EeV, cannot propagate freely. (50 EeV is not the threshold but the de facto feature in the resulting spectrum.) The particles are subject to energy loss by pion photo-production by scattering off of the CMB photons: $p\gamma \to p\pi^0(n\pi^-)$, with subsequent decays in neutrinos, electrons, and γ-rays. The mean free path collisions (of protons with respect to CMB photons) is less than 10 Mpc, but since the energy loss in a single collision is about 20 percent only, the mean free path for losing a significant amount of energy is of order 50 Mpc; that is, the effective radius of free penetration of protons from a source to the observer is ~ 50 Mpc. The mean free path is a function of energy beyond the threshold

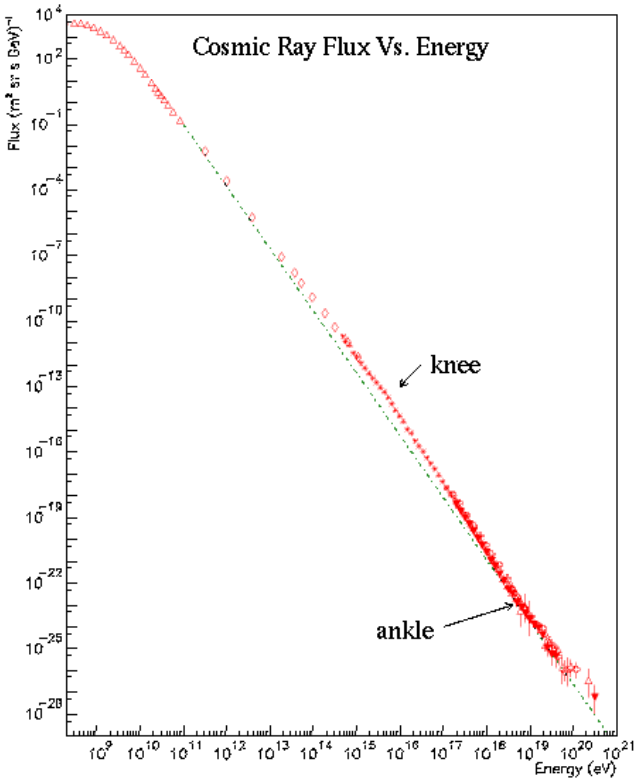

Figure 3.1: CR energy spectrum (from http://www.telescopearray.org). The spectrum is formed from measurements of different instruments to cover the energy range from 10^8 to 10^{21} eV. The spectrum steepens around 1 PeV (the "knee"), as the power-law index α changes from 2.7 to about 3.1, and then flattens around 3 EeV (the "ankle"). The GZK effect implies a suppression of the spectrum beyond 50 EeV.

(see, e.g., Allard et al. 2008). Therefore, the energy of CR protons is highly unlikely to be $\geqslant 10^{20}$ eV, unless their sources are within a few tens of Mpc. This is known as the **GZK cutoff**. The CR energy spectrum is shown in Fig. 3.1. It needs to be stressed that: (i) the GZK is not really a cutoff, only a strong turn-off of the spectrum (it does continue); (ii) it was obvious from the beginning that the nearby few sources (of UHECRs) would dominate (see, e.g., Ginzburg & Syrovatskii 1963; Cunningham et al. 1980); (iii) since the argument on the GZK cutoff uses Δ-resonances in the $p\gamma$ interaction, then arguments change when heavy nuclei are taken into account; and (iv) the GZK cutoff becomes a paradox if one considers that there are no really powerful radio galaxies in our neighborhood as sources of UHECRs.

With the introduction of new techniques for observing the air fluorescence and detecting e^-/e^+, muons, and Cerenkov photons with ground-based detectors, as well as the construction of large arrays,[5] new UHECR were detected in the 1990s. The data released from a number of experiments has been widely discussed, because they show discrepant results with respect to the GZK cutoff. As of the year 2001, the HiRes spectrum showed a GZK cutoff, whereas the AGASA spectrum did not. Moreover, data from AGASA showed an intriguing feature (at that time): a small angle anisotropy in angular distribution of the arrival direction of the primary particles. The arrival direction of the primary particles is not expected to point to their sources. One can obtain a weak correlation with the distribution of the sources only if the particles are protons (see, e.g., Das et al. 2008; Ryu

[5]Since the flux of particles with energy exceeding 10^{20} eV is 1 particle/km^2/per century/steradian, very large ground-based air-shower arrays are needed to study the energy spectrum, chemical composition, or large-scale (an)isotropy of the UHECR.

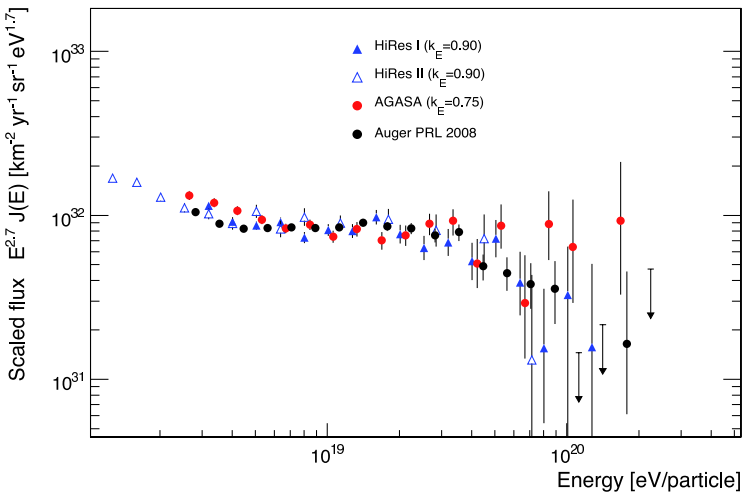

Figure 3.2: Expanded view of the highest energy portion of the CR spectrum [from (Biermann et al. 2008)]. Except for AGASA data, the measurements point to the possibility of the GZK cutoff occurrence.

et al. 2008). The data discrepancy between HiRes and AGASA (Fig. 3.2) might be resolved by the Pierre Auger Observatory, designed to use both techniques, air fluorescence (e.g., HiRes) and ground-based detectors (e.g., AGASA), on a larger scale. Auger Observatory, by far the biggest array, is located in Argentina and has surface detector stations covering ~ 3000 km^2.

The results released by the Auger Collaboration of 27 UHECR events with energies $E > 52$ EeV (Abraham et al. 2007, 2008a,b) show an anisotropy in the distribution of the arrival direction of CRs, 20 of which are **correlated with the distribution of nearby AGN** in the Véron-Cetty & Véron catalog [VCV catalog, Véron-Cetty & Véron (2006)]. The study of the anisotropy indicates that UHECRs are predominantly protons from sources at less than ~ 75 Mpc, so evidence of the GZK cutoff. The VCV catalog is a high-quality compilation of all published optical identifications of extragalactic AGN. Although the catalog is the largest "critical" collection of known AGN, especially for the southern hemisphere where the Auger exposure is large enough, it is heterogeneous and incomplete;[6] therefore it should not be used in correlation studies. Nonetheless, the Auger collaboration used the catalog as a tracer to the true sources; that is, the observed correlation does not necessarily mean that UHECRs are produced by the sources to which they are correlated. In the absence of a complete full-sky catalog, the correlation of UHECRs with nearby AGN is not yet established.

The current UHECR map found by the AUGER collaboration shows a lack of correlation with the Virgo cluster. This is not a surprise, since the Auger array has very little sensitivity at the location of M87. At first sight, two out of 27 events coincide with Cen A, whereas a few other events are clustered around it. When taking into account the entire radio emission from Cen A, Rachen (2008) found that five Auger events are perfectly aligned with the main lobe axis. There is an intense interest to find out which sources the events can be correlated to and what the source morphology looks like (see, e.g., Nagar &

[6]The completeness is specified by $Log(N) - Log(S)$ distribution of the sources (of the same class) with the usual power-law form $N(> S) = KS^{-a}$, where $N(> S)$ is the number of sources with fluxes higher than S, a is the slope, and K is the normalization factor. For a spatially homogeneous distribution of sources in a static Euclidean universe, N is proportional to the volume of space which encloses the sources, and S is inversely proportional to the square of the distance, so $N \sim S^{-1.5}$. The $Log(N) - Log(S)$ argument gives different powers for the large-scale structure within about 300 Mpc (see, e.g., Cavaliere et al. 1991).

Matulich 2008; Moskalenko et al. 2009). Moskalenko et al. (2009) found eight additional AGN within $\theta \leqslant 3°.2$ with $z \leqslant 0.018$ (the same criteria used by Auger). The sources are mainly LLAGN with a bolometric luminosity of $L_{\rm jet} \leqslant 10^{43}$ erg s^{-1} (Zaw et al. 2009), and just a few of them have known jets.

Poynting flux models for the origin of jets from force-free magnetosphere above a thin accretion disk were first proposed by Lovelace (1976) and Blandford (1976). A rotating magnetic field sweeps ambient matter and, consequently, feels a strong induced poloidal electric field. Since the magnetic field (which is predominantly toroidal at large distances in the jet) has a poloidal component, angular momentum and energy are carried away by a Poynting flux. In the model by Lovelace, the accreting protons are accelerated in the potential drop across the disk by an electric force, which exceeds the BH gravitational attraction by a factor of $\sim 10^{12}$. It is assumed that particles can form two high-current, aligned, and opposite proton beams. The output electrical power in the beams is proportional to the protons' maximum energy squared: $L \sim E_{\rm max}^2$. The maximum energy to which the accretion disk can accelerate the proton beams is set by the Eddington luminosity. If one takes the Poynting flux as a lower limit to the energy flux along a relativistic jet, UHECR production in LLAGN cannot be explained. Biermann et al. (2008) rewrote Lovelace's equation as

$$L_{\rm P} = \frac{c}{4\pi} f_{\rm flare} \left(\frac{E_{\rm max}}{eZ\gamma_{\rm sh}} \right)^2 , \tag{3.2}$$

where Z is the mass number of the nuclei, $\gamma_{\rm sh}$ is the Lorentz factor of the shock, and $f_{\rm flare}(< 1)$ is the jet intermittency. As the authors state, probably all three elements are required if one considers UHECR production by sources like M87 and Cen A, whose energy flow along the jet are $< 10^{45}$ erg s^{-1} and $< 10^{43}$ erg s^{-1}, respectively (Whysong & Antonucci 2003). The energy flow along the jet for Cen A is confirmed by Abdo et al. (2010).

Boldt & Ghosh (1999) suggested that particles with energies $\geqslant 10^{20}$ eV may be accelerated near the event horizon of spinning BHs associated with presently inactive quasar remnants. The required electromagnetic force is generated by the BH induced rotation of externally supplied magnetic field lines threading the horizon. The BH behaves as a battery, driving currents around a circuit, with an electromagnetic force of up to 10^{21} eV (for a BH with a mass of $10^9 M_\odot$). In this case, the production of observed flux of the highest energy cosmic rays would constitute a negligible drain on the BH dynamo. That is, replenishing the particle ejected at high energies ($> 10^{20}$ eV) would require a minimal mass input; a luminosity of 10^{42} erg s^{-1} in such particles (if protons) corresponds to a rest mass loss $< 10^{-5} M_\odot$ in a Hubble time.

In this chapter, we propose a model for UHECR contribution from the spin-down power of BHs in LLAGN. The particles in the jet manage to tap the spin-down power of the BH, and then they are accelerated at relativistic shocks and reached energies up to the UHE domain. The electrons lose their energy through synchroton emission (and also through inverse-Compton emission), whereas the protons are capable of surviving the radiative cooling and perhaps of propagating through the intergalatic medium. Since both particles undergo the same acceleration process, there must be a correlation between the electron synchrotron emission and the UHECR proton energy. We seek this correlation to make predictions for UHECRs from nearby LLAGN.

Chapter outline

In Section 3.2, we provide a description of the model. In Section 3.3, we derive the relation between the luminosity (and flux) of the UHECRs and the observed radio flux-density for a flat-spectrum core source. In Section 3.4, we calculate the particle maximum energy taking into account the spatial limit and synchroton emission losses. In Section 3.5, we present the application of the model to M87 and Cen A. In Section 3.6 we provide the predictions for nearby galaxies as UHECR sources, with specific emphasis on the UHECR contribution from the spin-down power of BHs in LLAGN. In Section 3.7, we present a summary of the key points and discuss the implication of this model for further studies of the UHECRs.

3.2 Model description

3.2.1 Model conditions

- We assume that the UHECRs are accelerated by shocks in AGN jets, which are launched from the ergospheric disk (see Chapter 2). The ergospheric disk extends from the stationary limit surface $r_{\rm sl}$ inward to the innermost stable orbit $r_{\rm ms}$. When the accretion rate relative to the Eddington accretion rate is $< 10^{-1.8}$ (which is the case of LLAGN), the jets can be powered by the spin down of the BH via the accretion disk, where the rotational energy of the BH is transferred to the ergospheric disk by closed magnetic field lines that connect the BH to the disk. The jet propagates along a cylinder of length z_0 (see Fig. 3.3) using the BH spin-down power and then extends into a conical shape with a constant opening angle $2\,\theta$, as a consequence of the free adiabatic expansion of the jet plasma. (The tip of the cone is located at some $z < z_0$.) A similar geometry of the jet was considered by Markoff et al. (2001).

- We assume that the UHECRs are proton-dominated. This is based on the measurement of a suppression of the CR flux at energies larger than 50 EeV, which indicates that the UHECRs are of extragalactic origin and have a light mass spectrum that is dominated by protons.

- In the observer frame, the magnetic field along the jet varies as $B \sim \gamma_{\rm j}^{-1} z^{-1}$ and the electron number density in the jet scales as $\sim \gamma_{\rm j} z^{-2}$, where $\gamma_{\rm j}$ is the bulk Lorentz factor of the jet. (See discussions below.)

- We set the slope of the particle density distribution to $p = 2$ (which corresponds to flat-spectrum core sources with a spectral index $\alpha = 0.5$) and the strength of the BH magnetic field to its maximum value ($B_{\rm H}^{\rm max}$). The latter condition provides, in turn, the minimum value for the particle maximum energy, luminosity, and flux of the UHECRs.

3.2.2 Magnetic field scaling along a steady jet

To describe the jet physics, we use the following reference frames: (i) the frame comoving with the matter in the jet and (ii) the (rest) frame of the observer, in which the relativistic jet moves with the bulk Lorentz factor.

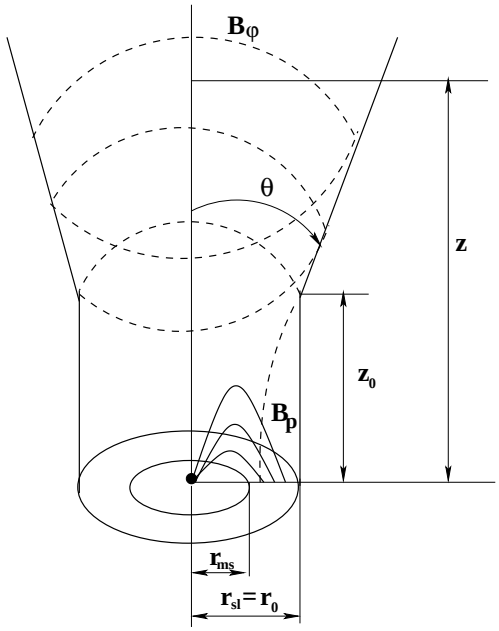

Figure 3.3: Schematic representation of the jet geometry. The jet is launched from the ergospheric disk and propagates along a cylinder up to a distance z_0. Then, it expands freely into a conical shape with a constant opening angle $2\,\theta$. The open magnetic field that threads the ergospheric disk (dashed line) is wound up, far from the BH, into a toroidal magnetic field B^{ϕ} which collimates the jet. In the region of the ergospheric disk, the closed magnetic field connects the BH to the ergospheric disk (solid line). In addition, the magnetic field structure in the ergospheric disk contains magnetic field lines similar to those on the Sun surface; i.e., it contains magnetic loops which connect distant regions of the inner disk and field lines which extend out very far from the disk and allow matter to flow out. The closed magnetic field lines do not cross the open magnetic field lines.

In a frame comoving with the jet, the poloidal component of the magnetic field is considered to vary as $B_{\rm p} \sim z^{-2}$. This variation follows from the conservation of magnetic flux along the axis z. To keep the field divergence-free, the toroidal component must vary as $B_{\phi} \sim z^{-1}$. This topology of $B_{\phi} \sim z^{-1}$ was first derived by Parker (1958) for the magnetohydrodynamics solution of a spherical-symmetric flow (so that, a jet can be considered a conical cut along the flow surfaces). [See also Blandford & Königl (1979).] The observational support to this variation of B_{ϕ} is specified later on in this section. At a distance, say, z_0, the poloidal and toroidal components of the comoving magnetic field become approximately equal $B_{\rm p0} \simeq B_{\phi 0}$. We consider z_0 of a few gravitational radii, based on the fact that the VLBI observation, for instance, of the jet in M87 at 7 mm gives evidence on the jet collimation (by the toroidal magnetic field) on scales of $60 - 200\, r_{\rm g}$ (Biretta et al. 2002) and the global 3.5 mm VLBI observations have resolved sizes for the compact radio sources of $\sim 10\, r_{\rm g}$ (see, e.g., Lee et al. 2008). A large-scale and predominantly toroidal magnetic field can exert an inward force (hoop stress), confining and collimating the jet (see, e.g., Bisnovatyi-Kogan & Ruzmaikin 1976; Blandford & Payne 1982). The magnetic hoop stress is balanced either by the gas pressure of the jet or by centrifugal force if the jet is spinning. From z_0 upward, the poloidal component of the magnetic field becomes weaker, so that the field lines are soon wound up in the azimuthal direction by the jet rotation. Thus, above z_0, the magnetic field along the jet is nearly azimuthal $B \sim B_{\phi}$ (for a steady jet) and varies inversely proportional to the distance along the jet,

$$B = B_0 \left(\frac{z}{z_0} \right)^{-1}, \tag{3.3}$$

where $B_0 \equiv B_{\phi 0} \simeq B_{\rm p0}$ is the strength of the magnetic field at the height $z = z_0$ above the equatorial plane of the BH. This z-dependence of the magnetic field appears to be contradicted by radio-polarization observations (Bridle & Perley 1984). These observations strongly suggest that the magnetic field is predominantly parallel to the jet axis initially and

only later becomes perpendicular to the jet axis, with some parallel magnetic field left over. Becker & Biermann (2009) argued that the basic pattern of the magnetic field is indeed $B_\phi \sim z^{-1}$, and that the observational evidence for a parallel magnetic field is due to highly oblique shocks. Their argument is based on the observations of the jet structure which indicate the occurrence of moving shocks between 20 and 200 $r_{\rm g}$, while the first stationary, strong shock can be produced in the approximate range of $(3-6)\times 10^3\ r_{\rm g}$ (Markoff et al. 2001, 2005; Marscher et al. 2008).

The strength of the magnetic field in the comoving frame B_0 can be related to the poloidal magnetic field in the BH frame $B_{\rm H}$ (see, e.g., Drenkhahn 2002) as

$$B_0 = \frac{1}{\gamma_{\rm j}} B_{\rm H} = \frac{B_{\rm H}^{\rm max}}{\gamma_{\rm j}} \left(\frac{B_{\rm H}}{B_{\rm H}^{\rm max}} \right), \tag{3.4}$$

where the maximum value of the BH magnetic field is given by

$$B_{\rm H}^{\rm max} \simeq 0.56 \times 10^4 \left(\frac{M}{10^9 M_\odot} \right)^{-1/2} \text{ gauss}, \tag{3.5}$$

(Eq. 2.29) which is obtained in a similar manner as the calculation performed by Znajek (1978), with the difference that the BH potential drop (V) is set to the specific energy of the particles at the innermost stable orbit, whereas Znajek (1978) makes use of the fact that the Eddington luminosity sets an upper bound on the radiation pressure (as the disk is radiatively efficient), and thus $V^2 \sim L_{\rm Edd}$. The maximum value of the BH magnetic field corresponds to the time when the accretion rate was as high as the Eddington accretion rate. In this case, the BH spin parameter is limited to $a_* = 0.9982$ (Thorne 1974). Although this limit might be even closer to the maximal value of the spin parameter ~ 1, this will introduce just a small variation of the maximum value of the BH magnetic field.

3.2.3 Electron and proton number densities

The jet is assumed to be composed mainly of electrons, positrons, and protons. We denote by $f_{\rm ep} \equiv n_{\rm e}/n_{\rm p}$ the ratio of the electron to proton number densities, where the number densities are measured in a frame comoving with the jet plasma. Unless otherwise noted, $n_{\rm e}$ should be assumed to include the positron number density as well. It is straightforward to generalize to a mixed chemical composition, including many heavy nuclei. Furthermore, both electrons and protons can have thermal and non-thermal populations before being accelerated at a shock front. There may also be a substantial number of positrons from pion production and decay processes (also called secondaries).

Now, we look for the expression of the proton and electron number densities injected into the accelerating region. First, we consider the mass flow rate into the jets, which in the observer frame is given by

$$\dot{M}_{\rm j} = \frac{d}{dt}\left(\rho_{\rm j} V_{\rm j}\right) = \frac{d}{dt}\left[nmz(S)_{z=0}\right] = \gamma_{\rm j} n m v_{\rm j} (S)_{z=0}, \tag{3.6}$$

where $\rho_{\rm j}$ is the rest-mass density of the jet, $V_{\rm j}$ is the comoving volume of the jet, $(S)_{z=0}$ is the launching area of the jet, z is the length of the cylinder along which the jet propagates before expanding freely in a conical geometry, and $v_{\rm j} = \beta_{\rm j} c$ is the bulk velocity of the jet.

The surface area between two equatorial surfaces of a Kerr BH can be calculated as

$$(dS)_{z=0} = \left(\frac{A}{\Delta}\right)^{1/2} 2\pi dr, \tag{3.7}$$

where the Kerr metric functions are

$$\Delta = r^2 - 2r_{\rm g}r + a^2 \text{ and } A = r^4 + r^2a^2 + 2r_{\rm g}ra^2, \tag{3.8}$$

where r is the coordinate radius. Next, we use normalizations to the gravitational radius, so that $r_* = r/r_{\rm g}$ is the dimensionless radius. The surface area is then

$$(S)_{z=0} = 2\pi r_{\rm g}^2 \int_{r_{\rm ms*}}^{r_{\rm sl*}} r_* \sqrt{\frac{1 + r_*^{-2}a_*^2 + 2r_*^{-3}a_*^2}{1 - r_*^{-1} + r_*^{-2}a_*^2}}\, dr_* \equiv 2\pi r_{\rm g}^2 k_0, \tag{3.9}$$

where the factor k_0 increases from ~ 2 to ~ 80 as the BH spin parameter increases from 0.95 to ~ 1. For the first equality, we use the fact that the ergospheric disk, from where the jet is launched, has its inner and outer radii at the innermost stable orbit $r_{\rm ms}$ and stationary limit surface $r_{\rm sl} = 2r_{\rm g} \equiv r_0$, respectively.

The comoving density of the jet can be expressed in terms of the ratio of the electron to proton number densities as

$$nm = n_{\rm p}m_{\rm p} + n_{\rm e}m_{\rm e} = n_{\rm p}m_{\rm p}\left(1 + f_{\rm ep}\frac{m_{\rm e}}{m_{\rm p}}\right) \equiv n_{\rm p}m_{\rm p}f_0. \tag{3.10}$$

If one assumes, in average, one electron/positron for each proton in the jet, $f_{\rm ep} = 1$ and $f_0 \simeq 1$. For protons dominating over the electrons, $f_{\rm ep} < 2 \times 10^3$, where electrons and positrons can partially occur as secondaries.

Substituting Eqs. (3.9) and (3.10) for (3.6), we obtain the mass flow rate into the jet,

$$\dot{M}_{\rm j} = \gamma_{\rm j}\beta_{\rm j}cn_{\rm p}m_{\rm p}f_0 2\pi r_{\rm g}^2 k_0. \tag{3.11}$$

This expression provides the proton number density, which in turn we use to derive the electron number density,

$$\boxed{n_{\rm e} = f_{\rm ep}\frac{\dot{M}_{\rm j}}{\gamma_{\rm j}\beta_{\rm j}cm_{\rm p}f_0 2\pi r_{\rm g}^2 k_0}}. \tag{3.12}$$

We shall use this result later for evaluating the self-absorbed synchrotron emission of the jets (Section 3.2.5).

3.2.4 Particle energy distribution

We suppose that a recollimation shock (Sanders 1983) is produced at the jet height $\sim z_0$. As a result, a power-law energy distribution of the particles is established. For a given frequency, the emission from the synchrotron process for electrons and protons gives a factor $(m_{\rm p}/m_{\rm e})^3 \simeq 10^{10}$ in favor of electrons (see, e.g., Novikov & Thorne 1973b). In addition, Biermann & Strittmatter (1987) showed that the proton synchrotron emission can be competitive if one considers that the proton emission ranges to much higher photon energy. Moreover, it is also not at all obvious that they have the same normalization at the

same Lorentz factor of the particle and that the particles have a continuous power-law from rest mass to UHE. The number density of the electrons in the energy interval E, $E + dE$ [or $m_e c^2\gamma$, $m_e c^2(\gamma + d\gamma)$] has the power-law form

$$N(E)dE = CE^{-p}dE, \tag{3.13}$$

or, in terms of the Lorentz factor,

$$N(\gamma)d\gamma = C'\gamma^{-p}d\gamma, \tag{3.14}$$

where $\gamma \in [\gamma_{\min}, \gamma_{\max}]$ is the Lorentz factor of the electrons and p is the power-law index (see, e.g., Rybicki & Lightman 1979). The normalization coefficients of the electron number density in Eqs. 3.13 and 3.14 are related by

$$C = C'(m_e c^2)^{p-1}. \tag{3.15}$$

The normalization of the electron number density C' follows the pressure in a reheating flow ($\sim z^{-2}$), whereas an adiabatic flow would give a steeper dependence, which leads to shocks (see, e.g., Sanders 1983). Adiabatic behavior implies $P \sim \rho^{\gamma_{\rm ad}}$, where $\gamma_{\rm ad}$ is the adiabatic index. Since a relativistic fluid usually has $\gamma_{\rm ad} = 4/3$, in an adiabatic flow the temperature runs as $z^{-2/3}$. Furthermore, one can have a conical flow only if the temperature of the flow is approximately constant. The energy for reheating can be taken from the flow through highly oblique shocks. The normalization of the electron number density, in the case of a conical jet, is therefore

$$C' = C'_0 \left(\frac{z}{z_0}\right)^{-2} (\mathrm{cm}^{-3}). \tag{3.16}$$

Possible values of the power-law distribution indices p of the electrons accelerated by the relativistic shock are discussed later in Section 3.5.

3.2.5 Self-absorbed synchrotron emission of the jets

The spectra from compact radio sources can be explained by self-absorbed synchrotron emission of the jets produced by electrons with a power-law energy distribution. In this section, we rewrite the quantities which describe the self-absorbed synchrotron emission, derived in Rybicki & Lightman (1979), and express them under our model considerations. We first introduce the absorption coefficient, optical depth, synchrotron emissivity, and source function in order to calculate the flux density of the synchrotron emission from radio sources with a flat-spectrum core. (The quantities which describe the self-absorbed synchrotron emission are in cgs units.)

The specific intensity of radiation I_ν is defined as the radiative energy flux per unit frequency, per unit solid angle (i.e., the energy per time, per unit area, per unit frequency, per unit solid angle). The radiative transfer equation for the specific intensity of the radiation I_ν along a distance ds through a medium combines both the absorption and emission effects as

$$\frac{dI_\nu}{ds} = -\alpha_\nu I_\nu + j_\nu, \tag{3.17}$$

where α_ν is the absorption coefficient and j_ν is the emission coefficient. Instead of using the radiative transfer equation of the form in Eq. 3.17, it becomes more convenient to introduce

another variable, the optical depth τ_ν, which is measured along the direction of propagating radiation, as

$$d\tau_\nu = \alpha_\nu ds. \tag{3.18}$$

Therefore, τ_ν can be obtained by integrating Eq. 3.18 along a path through the medium. For $\tau_\nu > 1$ the medium is called optically thick (or opaque), whereas for $\tau_\nu < 1$ the medium is called optically thin (or transparent), in which case a photon of a given frequency ν can travel without being absorbed by the medium itself. If one divides the radiative transfer equation by α_ν and uses the definition of the optical depth, then

$$\frac{dI_\nu}{d\tau_\nu} = -I_\nu + S_\nu, \tag{3.19}$$

where $S_\nu \equiv j_\nu/\alpha_\nu$ is called the source function.

To find how the specific intensity varies as radiation travels through a medium, one needs to specify the coefficients α_ν and j_ν, or alternatively S_ν and τ_ν, for every point along the path length. The solution of the transfer equation (Eq. 3.19), for a constant source function, is written as

$$I_\nu = I_{\nu,0}e^{-\tau_\nu} + S_\nu(1 - e^{-\tau_\nu}), \tag{3.20}$$

where the first term on the right-hand side describes the amount of radiation left over from the intensity after it has passed through an optical depth τ_ν, and the second term represents the contribution of the intensity from the radiation emitted along the path. When there is only emission from a specific region, then

$$I_\nu = S_\nu(1 - e^{-\tau_\nu}). \tag{3.21}$$

Lind & Blandford (1985) showed that the phase space distribution of the emitting particles is not isotropic in any frame of reference, given a relativistic shock. It helps, however, to assume that there is such a frame (to assume that this is approximately true leads to a small errors only in the derived quantities). On the other hand, in the case of weak sources, the beaming could go backwards under special circumstances, whereas for strong superluminal source, the beaming propagates towards us. Next, we also neglect the flux from components moving away from the observer.

For an optically thick case, $e^{-\tau_\nu} \simeq 0$ and $I_\nu = S_\nu$. Thus, when looking at an opaque medium, it does not matter what radiation sources are behind this, the specific intensity is given by the source function of the medium which faces the observer.

The power radiated per unit volume per unit frequency $dP/(dV d\nu) \sim \nu^{-\frac{p+1}{2}}$ has a high-frequency cutoff at the highest frequency produced by the highest energy electrons in the emitting region. There is also a low-frequency cutoff due to the self-absorption of the synchrotron radiation. Computing the absorption and emission of radiation is rather complicated, because the synchrotron emission is not necessarily isotropic since the magnetic field imposes a preferred direction. A way out of this situation is to look at the region in which the magnetic field is chaotic, so it has no net direction. (This looks like a contradiction with the other assumption of $B \sim z^{-1}$, since in a chaotic regime we have $B \sim z^{-4/3}$ for density $\sim z^{-2}$. Of course, the observations show that there is some fraction of regularity, and so the earlier assumption is justified. One could also argue, that in each shock the magnetic field is re-regularized.) Therefore, the emission coefficient can be set as the angle-averaged synchrotron power per unit volume per unit frequency.

The absorption coefficient is dependent on the emitting frequency as $\alpha_\nu \sim \nu^{-\frac{p+4}{2}}$. If $p = 2$, the absorption coefficient will be $\alpha_\nu \sim \nu^{-3}$. This steep dependence on frequency implies that the emission region will be optically thick to synchrotron radiation at sufficiently low frequencies. Instead, at high frequency, the region will be transparent to the synchrotron radiation.

Absorption coefficient

In a frame comoving with the jet plasma, the absorption coefficient of the synchrotron radiation can be calculated as

$$\alpha_\nu = \frac{\sqrt{3}e^3 B \sin\alpha_0}{8\pi m_\mathrm{e}} \left(\frac{3eB\sin\alpha_0}{2\pi m_\mathrm{e}^3 c^5}\right)^{\frac{p}{2}} C\,\Gamma\left(\frac{3p+2}{12}\right)\Gamma\left(\frac{3p+22}{12}\right)\nu^{-\frac{p+4}{2}}\ (\mathrm{cm}^{-1}), \qquad (3.22)$$

where e is the electric charge of the electron, m_e is the electron mass, p is the power-law index of the particles distribution, C is the normalization factor for the power-law electron energy distribution (Eq. 3.13), B is the magnetic field in the frame comoving with the jet, $\Gamma(x)$ is the Gamma function of argument x, and ν is the frequency of the synchrotron radiation [eq. 6.26 in Rybicki & Lightman (1979)]. To average over the pitch angle α, for a local randomly oriented magnetic field with a probability distribution $\frac{1}{2}\sin\alpha d\alpha$, one needs to evaluate the following integral (Longair 1994)

$$\int_0^\pi \frac{1}{2}\sin\alpha(\sin\alpha)^{\frac{p+2}{2}}d\alpha = \frac{\sqrt{\pi}\Gamma\left(\frac{p+6}{4}\right)}{2\Gamma\left(\frac{p+8}{4}\right)}. \qquad (3.23)$$

Including the values of the physical constants and using the expressions for the normalization of the electron distribution function, C and C' (Eqs. 3.15 and 3.16), as well as for comoving magnetic field along the jet (Eq. 3.3), the absorption coefficient becomes

$$\alpha_\nu = K_1 C_0' \left(\frac{z}{z_0}\right)^{-\frac{p+6}{2}} B_0^{\frac{p+2}{2}} \nu^{-\frac{p+4}{2}}, \qquad (3.24)$$

where

$$\begin{aligned} K_1 = {} & 8.4\times10^{-3}(1.25\times10^{19})^{\frac{p}{2}}\left(8.2\times10^{-7}\right)^{p-1} \\ & \frac{\sqrt{\pi}}{2}\Gamma\left(\frac{3p+2}{12}\right)\Gamma\left(\frac{3p+22}{12}\right)\Gamma\left(\frac{p+6}{4}\right)\Gamma^{-1}\left(\frac{p+8}{4}\right). \end{aligned} \qquad (3.25)$$

Optical depth of the self-absorbed region

To calculate the observed distance along the jet where the jet becomes self-absorbed, we first determine the optical depth τ_ν of the jet material. The averaged path of a photon through the jet has the length $r(z)$, which is a reasonable approximation for a jet observed at large inclination angle (see, e.g., Kaiser 2006). This is not in contradiction to the idea that some jets point towards us (see the footnote on page 63). We introduce a factor l_0 in the expression of the path length to account for a small inclination angle. Thus, we can write the optical depth as

$$\tau_\nu = \alpha_\nu r(z) l_0. \qquad (3.26)$$

For conical jets, the intrinsic half-opening angle is given by $\tan\theta = r/z \cong r_0/z_0$. With the absorption coefficient specified through Eq. (3.24), the optical depth can be written as

$$\tau_\nu = K_1 C_0' r_0 l_0 \left(\frac{z}{z_0}\right)^{-\frac{p+4}{2}} B_0^{\frac{p+2}{2}} \nu^{-\frac{p+4}{2}}. \tag{3.27}$$

The distance along the jet where the jet becomes self-absorbed (z_{ssa}) is defined as the distance z for which $\tau_\nu = 1$. Using Eq. (3.27), we obtain

$$z_{ssa} = \left(K_1 C_0' l_0\right)^{\frac{2}{p+4}} (\tan\theta)^{-1} r_0^{\frac{p+6}{p+4}} B_0^{\frac{p+2}{p+4}\nu^{-1}}. \tag{3.28}$$

Synchrotron emissivity

The total power radiated per unit volume per unit frequency by a non-thermal particle distribution equals

$$P_\omega = \frac{\sqrt{3}e^3}{2\pi m_e c^2} \frac{C' B \sin\alpha_0}{p+1} \left(\frac{m_e c\omega}{3eB\sin\alpha_0}\right)^{-\frac{p-1}{2}} \Gamma\left(\frac{p}{4}+\frac{19}{12}\right)\Gamma\left(\frac{p}{4}-\frac{1}{12}\right), \tag{3.29}$$

where $\omega = 2\pi\nu$ [Eq. 6.36 in Rybicki & Lightman (1979)]. Using Eqs. (3.3) and (3.16), as well as the method to calculate the averaged pitch angle employed in Longair (1994), the expression of the total power becomes

$$P_\nu = 2\pi P_\omega = K_2 C_0' \left(\frac{z}{z_0}\right)^{-\frac{p+5}{2}} B_0^{\frac{p+1}{2}} \nu^{-\frac{p-1}{2}}, \tag{3.30}$$

where

$$\begin{aligned} K_2 = {} & 3.7\times10^{-23}\left(1.2\times10^{-7}\right)^{-\frac{p-1}{2}}(p+1)^{-1} \\ & \frac{\sqrt{\pi}}{2}\Gamma\left(\frac{p}{4}+\frac{19}{12}\right)\Gamma\left(\frac{p}{4}-\frac{1}{12}\right)\Gamma\left(\frac{p+5}{4}\right)\Gamma^{-1}\left(\frac{p+7}{4}\right). \end{aligned} \tag{3.31}$$

Next, we derive (z/z_0) from Eq. 3.27 when $\tau_\nu = 1$. With this, the expression for the total power takes the form

$$P_\nu' = K_2 \left(K_1 r_0 l_0\right)^{-\frac{p+5}{p+4}} \left(C_0'\right)^{-\frac{1}{p+4}} B_0^{-\frac{p+3}{p+4}} \nu^3, \tag{3.32}$$

and the emission coefficient is simply: $j_\nu = P_\nu/4\pi$.

Source function

The emission coefficient is defined as the product between the absorption coefficient α_ν and the source function S_ν. At low frequencies, the emitting region is opaque to synchrotron radiation and the observed intensity of radiation I_ν is proportional to the source function, while at high frequencies, the region is transparent and the observed intensity is proportional to the emission coefficient. The two dependences should be matched at the transition from opaque to transparent regime. This transition corresponds to an optical depth $\tau_\nu = 1$. The source function in the self-absorbed limit is then

$$S_\nu = \frac{1}{4\pi}\frac{P_\nu}{\alpha_\nu} = \frac{1}{4\pi}\frac{K_2}{K_1}\left(\frac{z}{z_0}\right)^{\frac{1}{2}} B_0^{-\frac{1}{2}} \nu^{\frac{5}{2}} \ (\text{erg s}^{-1}\text{cm}^{-2}\text{Hz}^{-1}), \tag{3.33}$$

where the last equality was obtained using Eqs. (3.24) and (3.30). Note that in the source function, the emitting frequency does not depend on the power-law index of the electron energy distribution. For $\tau_\nu = 1$, the source function becomes

$$S'_\nu = K_3 \left(C'_0 r_0 l_0\right)^{\frac{-1}{p+4}} B_0^{-\frac{1}{p+4}} \nu^2 \ (\mathrm{erg\ s^{-1} cm^{-2} Hz^{-1}}), \tag{3.34}$$

where $K_3 = K_1^{-\frac{p+3}{p+4}} K_2$.

Flux density of the synchrotron emission

To obtain the emission spectrum, one needs to solve the equation for the radiative transfer through a homogeneous medium. Because the angular sizes of the jets are small, instead of the specific intensity of the radiation, one usually measures the flux density F_ν (energy per unit time, per unit frequency interval, that passes through a surface of unit area). Thus,

$$dF_\nu = I_\nu d\Omega = S_\nu \left[1 - \exp(-\tau_\nu)\right] d\Omega. \tag{3.35}$$

Since the frequency shift of the approaching photons, specified by the Doppler factor,[7] is $\nu_{\rm obs} = \mathcal{D}_{\rm j}\nu$, the transformation of the specific intensity to the observer frame is

$$I_{\nu,{\rm obs}} = \mathcal{D}_{\rm j}^3 I_\nu, \tag{3.36}$$

where the relativistic invariant quantity I_ν/ν^3 was used. The solid angle corresponding to the source is

$$d\Omega = \frac{2\pi r dz}{D_{\rm s}^2}, \tag{3.37}$$

where $D_{\rm s}$ is the distance from the observer to the jet source, and $r = z\tan\theta$. If we insert Eq. (3.37) into Eq. (3.35) and integrate it from z_0 to z, we obtain the flux density of the synchrotron emission in the case of $\tau_\nu = 1$ as

$$F'_\nu = S'_\nu [1 - \exp(-1)] \pi (\tan\theta) D_{\rm s}^{-2} z^2 \left[1 - \left(\frac{z_0}{z}\right)^2\right], \tag{3.38}$$

where the second term in the last squared bracket can be neglected with respect to the first term for $z \gg z_0$ (where the jet emission becomes self-absorbed). Using Eqs. (3.28) and (3.34), the flux density is then

$$\boxed{F' = K_4 (C'_0 l_0)^{\frac{5}{p+4}} r_0^{\frac{2p+13}{p+4}} B_0^{\frac{2p+3}{p+4}} D_{\rm s}^{-2} (\tan\theta)^{-1}}, \tag{3.39}$$

where $K_4 = 0.16 K_1^{-\frac{p-1}{p+4}} K_2$. The radio flux density in Eq. (3.39) does not depend on the emitted frequency of the radiation since we already adopted the case of flat-spectrum core sources when $\tau_\nu = 1$.

[7] The Doppler factor of the jet is $\mathcal{D}_{\rm j} = \gamma_{\rm j}^{-1}(1 - \beta_{\rm j}\cos\varphi)^{-1}$, where φ is the inclination angle of the jet axis with respect to the line of sight (which is Lorentz transformed through $\sin\varphi_{\rm obs} = \mathcal{D}_{\rm j}\sin\varphi$). The angles are rotated by the Lorentz transformation, so that a jet seen at angle $\gamma_{\rm j}^{-1}$ is rotated basically to a transverse view for large $\gamma_{\rm j}$.

For a power-law synchrotron spectrum of the form $F_{\rm obs} \sim \nu_{\rm obs}^{-\alpha}$, the observed flux density is related to the intrinsic flux density as

$$F_{\rm obs} = \mathcal{D}_{\rm j}^{3+\alpha} F', \tag{3.40}$$

where Eq. (3.36) was used. Equation (3.40) is valid for a single blob emission (see, e.g., Blandford & Königl 1979). For a continuous jet consisting of uniformly-spaced blobs, one needs to consider the emission per unit length in the observer frame. Therefore,

$$F_{\rm obs} = \mathcal{D}_{\rm j}^{2+\alpha} F', \tag{3.41}$$

due to the fact that the number of the blobs observed per unit length is $\sim 1/\mathcal{D}_{\rm j}$.

3.3 Luminosity and flux of the ultra-high-energy cosmic rays

In this section, we look to find the UHECR luminosity flux $F_{\rm CR}$ specified as a function of the observed radio flux-density $F_{\rm obs}$. First, we consider the kinetic luminosity defined as

$$\boxed{L_{\rm CR} = \epsilon_{\rm CR} \gamma_{\rm j}^2 \dot{M}_{\rm j} c^2}, \tag{3.42}$$

where we assume that the spin-down power of the BH drives the jet, and the UHECR luminosity is a fraction of the jet power, therefore $L_{\rm CR} \sim \epsilon_{\rm CR} L_{\rm j} = \epsilon_{\rm CR}(L_{\rm kin} + L_{\rm magn} + L_{\rm CR})$. If we were to adopt the point of view that the jet power is shared equally in a comoving frame between the baryonic matter, magnetic field and cosmic rays extending to the highest energy, then $\varepsilon_{\rm CR} \simeq 1/3$. In the jet-disk model of Falcke & Biermann (1995), the energy equipartition in the comoving frame appears to be a good approximation. If it were also true here, it would determine the Lorentz factor and would suggest that AGN driven by the BH spin-down power, and suffering from a low accretion rate, may attain a higher Lorentz factor, consistent with some observations.

An upper limit for the electron density is given by $n_{\rm e} \leqslant C_0'$. Next, we use this result (Eq. 3.12) in the expression for the observed radio flux-density (Eq. 3.40 and Eq. 3.41) and find the mass flow rate into the jet $\dot{M}_{\rm j}$. On the other hand, the magnetic field B_0 follows from equations 3.4 and 3.5. After performing these calculations, we obtain the UHECR luminosity

$$\begin{aligned} L_{\rm CR} \;=\; & K_5 f \beta_{\rm j} \mathcal{D}_{\rm j}^{-h} \left(\frac{\gamma_{\rm j}}{5}\right)^{\frac{2p+13}{5}} \left(\frac{\tan\theta}{0.05}\right)^{\frac{p+4}{5}} \left(\frac{r_0}{2r_{\rm g}}\right)^{-\frac{2p+13}{5}} \left(\frac{B_{\rm H}}{B_{\rm H}^{\rm max}}\right)^{-\frac{2p+3}{5}} \\ & F_{\rm obs}^{\frac{p+4}{5}} D_{\rm s}^{\frac{2(p+4)}{5}} \left(\frac{M}{10^9 M_\odot}\right)^{-\frac{2p+3}{10}} \ {\rm ergs}^{-1}, \end{aligned} \tag{3.43}$$

where

$$K_5 = \frac{\pi}{6} m_{\rm p} c^3 K_4^{-\frac{p+4}{5}} (5)^{\frac{2p+13}{5}+h} (2.96\times10^{14})^{-\frac{2p+3}{5}} (0.56\times10^4)^{-\frac{2p+3}{5}} (0.05)^{\frac{p+4}{5}}, \tag{3.44}$$

where $h = [(p+5)(p+4)]/10$ for single blob emission (Eq. 3.40) or $[(p+3)(p+4)]/10$ for continuous blob emission (Eq. 3.41), and $f = f_0 k_0 (l_0 f_{\rm ep})^{-1}$. We use a normalization value for the jet Lorentz factor, say 5, although the jet Lorentz factor can range from ~ 2 to ~ 100, as observational data suggest. We adopt $f_{\rm ep} \sim 1 - 10$ (and $f_0 \simeq 1$), which means

that there is one electron for at least one proton in a jet powered by a rapidly-spinning BH ($a_* \geqslant 0.95$) and observed at a large angle ($\geqslant 10^\circ$). Sadly, there is a very poor constraint on the BH spin parameter from the UHECR luminosity.

Given the UHECR luminosity, one can easily obtain the UHECR flux,

$$F_{\rm CR} = \frac{L_{\rm CR}}{4\pi D_{\rm s}^2}. \tag{3.45}$$

Mildly-relativistic shocks ($1 \lesssim \gamma_{\rm s} \lesssim 10$) are believed to occur in the AGN jets. Gallant & Achterberg (1999) have shown that at relativistic shocks, the particles typically perform a fraction $\sim \gamma_{\rm s}^{-1}$ of the Larmor orbit upstream before recrossing the shock, and the particle energy gain increases by a factor of $\gamma_{\rm sh}^2$ in the first shock-crossing cycle. In the subsequent shock-crossing cycles, the energy gain is of the order of 2. The predicted spectral index is $\simeq 2$. A series of Monte Carlo simulations,[8] performed under a wide range of background conditions at the shock front, indicate a value $p \simeq 2.2 - 2.3$ for the slope (see, e.g., Bednarz & Ostrowski 1998; Achterberg et al. 2001; Kirk et al. 2000; Keshet & Waxman 2005). It follows that in the regime of arbitrarily high Lorentz factor shocks, the acceleration process generates particle spectra which are quasi-independent of the considered background conditions, leading to a quasi-universal slope of ~ 2.2. The picture can be changed when one considers more realistic conditions in the vicinity of the shock. For example, Niemiec & Ostrowski (2006) studied possible models for perturbed magnetic field upstream of the shock and found that for superluminal mildly-relativistic shocks ($\gamma_{\rm sh} \sim 5 - 30$), a flattening of the spectrum occurs, $p \simeq 1.5$, with a cutoff at lower energies than as expected for UHECRs. A flattening of the spectrum, $p \sim 2.1 - 1.5$, is also observed in simulation results obtained by Meli et al. (2008) for the case of superluminal ultra-relativistic shocks ($100 < \gamma_{\rm sh} < 1000$), with a turbulent magnetic field and various shock obliquity; however, for subluminal mildly-relativistic shocks, the spectral slope has values between $2.0 < p < 2.3$.

We adopt $\boxed{p = 2}$, which is the upper value of the spectral index for flat-spectrum core sources. The cosmic ray luminosity (Eq. 3.43) becomes

$$\boxed{\begin{aligned} L_{\rm CR} =& 3.6 \times 10^{38} \beta_{\rm j} \mathcal{D}_{\rm j}^{-3} \left(\frac{\gamma_{\rm j}}{5}\right)^{17/5} \left(\frac{\tan\theta}{0.05}\right)^{6/5} \left(\frac{r_0}{2r_{\rm g}}\right)^{-17/5} \left(\frac{B_{\rm H}}{B_{\rm H}^{\rm max}}\right)^{-7/5} \\ & \left(\frac{F_{\rm obs}}{\rm mJy}\right)^{6/5} \left(\frac{D_{\rm s}}{\rm Mpc}\right)^{12/5} \left(\frac{M}{10^9 M_\odot}\right)^{-7/10} \end{aligned}}, \tag{3.46}$$

where a continuous jet was considered ($h = 3$). For $p \lesssim 2$, the results for the CR luminosity are slightly reduced.

3.4 Maximum particle energy of ultra-high-energy cosmic rays

3.4.1 Spatial limit

Now, we look for the maximum energy of the UHECR in the case of the spatial (geometrical) limit (Falcke & Biermann 1995); i.e., the jet particle orbits must fit into the

[8] Monte Carlo simulations are meant to find a way of constructing the trajectories of particles whose distribution obey the desired transport equation.

Larmor radius. Following Gallant & Achterberg (1999), the maximum particle energy in the downstream rest frame can be written as

$$E_{\rm max}^{\rm sp} = \gamma_{\rm s} eZBr, \tag{3.47}$$

where $\gamma_{\rm s}$ is the shock Lorentz factor, Z the particle mass number, and B is the magnetic field in the comoving frame. Using the expression for the magnetic field along the jet (Eqs. 3.3 and 3.4) and the fact that $\tan\theta = r_0/z_0$, the CRs maximum energy (in the observer frame) becomes

$$E_{\rm max}^{\rm sp} = eZB_{\rm H}^{\rm max} r_0 \left(\frac{\gamma_{\rm s}}{\gamma_{\rm j}}\right)\left(\frac{B_{\rm H}}{B_{\rm H}^{\rm max}}\right), \tag{3.48}$$

where $B_{\rm H}$ is the magnetic field in the BH frame. For protons,

$$\boxed{E_{\rm max}^{\rm sp} = 5\times 10^{20}\left(\frac{B_{\rm H}}{B_{\rm H}^{\rm max}}\right)\left(\frac{r_0}{2r_{\rm g}}\right)\left(\frac{M}{10^9 M_\odot}\right)^{1/2}\ ({\rm eV})}, \tag{3.49}$$

where $\gamma_{\rm s} \simeq \gamma_{\rm j}$ was used.

3.4.2 Synchrotron loss limit

Setting synchrotron losses equal to diffusive shock acceleration gains, Biermann & Strittmatter (1987) showed that a ubiquitous cutoff in the non-thermal emission spectra of AGN, knots and hot spots in the jets can be explained. This requires that protons to be accelerated near 10^{21} eV. The cutoff frequency, ν_*, might be produced at about $3000 - 6000\, r_{\rm g}$. Rewriting their expression for the maximal proton energy,

$$E_{\rm max}^{\rm loss} \simeq 1.4\times 10^{20}\left(\frac{\nu_*}{3\times 10^{14}{\rm Hz}}\right)^{1/2} B^{-1/2}\ ({\rm eV}), \tag{3.50}$$

and using the expression for the magnetic field, we obtain the maximal proton energy in the loss limit:

$$\boxed{E_{\rm max}^{\rm loss} \simeq 4.2\times 10^{18}\left(\frac{\nu_*}{3\times 10^{14}{\rm Hz}}\right)^{1/2}\left(\frac{\gamma_{\rm j}}{5}\right)^{1/2}\left(\frac{B_{\rm H}}{B_{\rm H}^{\rm max}}\right)^{-1/2}\left(\frac{M}{10^9 M_\odot}\right)^{1/2}\left(\frac{z}{z_0}\right)^{1/2}\ ({\rm eV})} \tag{3.51}$$

3.5 Application to M87 and Cen A

In this section, we investigate the UHECR luminosity flux for two possible sources of UHECR, M87 and Cen A, whose jet parameters can be inferred from observational data.

M87 (NGC 4486) is a giant elliptical galaxy located at ~ 16 Mpc, perhaps the dominant galaxy in the closest big galaxy cluster to us, the Virgo Cluster. Although the galaxy hosts a supermassive BH with mass of $(3.2 \pm 0.9)\times 10^9 M_\odot$ (Macchetto et al. 1997), its radio morphology places it near the FR-I/FR-II division.[9] Its giant optical jet was

[9]The Fanaroff-Riley classification (Fanaroff & Riley 1974) of a galaxy depends on its radio luminosity. The definition of FR-I and FR-II follows from the radio morphology, FR-I have the lobe emission center-brightened, whereas FR-II have the lobe emission edge-brightened. The radio morphology strongly correlates with the radio luminosity at low radio frequency (see, e.g., the review by Miley 1980). Most galaxies that are brighter than $2\times 10^{25} h_{100}^{-2}{\rm WHz}^{-1}{\rm str}^{-1}$ at 178 MHz are of the FR-II type, while less luminous galaxies belong mainly to the FR-I class. The division between the two classes becomes sharper if the distribution as a function of the radio luminosity, as well as of the absolute optical magnitude, is taken into account (see, e.g., Barthel 1989).

discovered by Curtis (1918) and was the first extragalactic large-scale jet ever observed. Since then, the jet has been observed over a wide range of the electromagnetic spectrum. The radio map at 7 mm with VLBI (Biretta et al. 2002) reveals the structure of the jet on the sub-parsec scale and indicates a jet (apparent) opening angle of approximately 60° on scales of about 0.04 pc. On large scales, the jet shows apparent superluminal motion of $\sim 6c$, which implies a small angle to the line of sight, of just a few degrees. Whysong & Antonucci (2003) have estimated an energy flow along the jet of $L_{\rm jet} \sim 10^{45}$ erg s^{-1}.

Cen A (NGC 5128) is the nearest active galactic nucleus at a distance of ~ 3.5 Mpc. There are quite a few distance measurements with values in the $3.4 - 4.4$ Mpc range (see, e.g., Tonry et al. 2001; Rejkuba 2004; Ferrarese et al. 2007). The giant elliptical galaxy features a dark lane and a twisted edge-on disk of gas and dust which contain H II regions obscuring the nucleus at optical wavelengths. They are believed to be remnants of a merger of a giant elliptical galaxy with a smaller spiral galaxy, which has occurred about $10^7 - 10^8$ years ago (Malin et al. 1983). Due to its radio morphology, Cen A has been classified as a FR-I radiogalaxy. The radio maps show jet structures extending from the core on pc and kpc scales to giant outer lobes which extend to an apparent diameter of 10° on the sky. The jets point in a very different direction from the overall lobes (Junkes et al. 1993a,b), and this may have two reasons: (i) there may have been a spin-flip, so that the big radio lobes refer to the old spin direction and the jets to the new spin direction; or (ii) a cosmologically large scale structure (LSS) shear flow (Ryu et al. 1998, 2008) pulls the relativistic gas ejected by the active BH along the local LSS shear. A general relativistic approach for the spin-flip of the BH was described by Gergely & Biermann (2009). A recent determination of its BH mass of $M = (5.5 \pm 3.0) \times 10^7 M_\odot$ (Cappellari et al. 2009) was obtained by using high-resolution integral-field observations of the stellar kinematics.

Taking $r = 2\,r_{\rm g}$ and $B_{\rm H} \simeq B_{\rm H}^{\rm max}$, the equations for the maximum particle energy in the spatial (Eq. 3.49) and loss (Eq. 3.51) limits, as well as for the UHECR luminosity (Eq. 3.46), become

$$
\begin{aligned}
E_{\rm max}^{\rm sp} &= 5 \times 10^{20} \left(\frac{M}{10^9 M_\odot} \right)^{1/2} \ ({\rm eV}), \\
E_{\rm max}^{\rm loss} &\simeq 4.2 \times 10^{18} \left(\frac{\nu_*}{3 \times 10^{14} {\rm Hz}} \right)^{1/2} \left(\frac{\gamma_{\rm j}}{5} \right)^{1/2} \left(\frac{M}{10^9 M_\odot} \right)^{1/2} \left(\frac{z}{z_0} \right)^{1/2} \ ({\rm eV}), \\
L_{\rm CR} &= 3.65 \times 10^{38} \beta_{\rm j} \, (1 - \beta_{\rm j} \cos\varphi)^3 \left(\frac{\gamma_{\rm j}}{5} \right)^{32/5} \left(\frac{\tan\theta}{0.05} \right)^{6/5} \\
&\quad \left(\frac{F_{\rm obs}}{\rm mJy} \right)^{6/5} \left(\frac{D_{\rm s}}{\rm Mpc} \right)^{12/5} \left(\frac{M}{10^9 M_\odot} \right)^{-7/10} \ ({\rm erg\,s^{-1}}).
\end{aligned}
\tag{3.52}
$$

This set of equations is used for the following estimations on UHECR contribution from the BH spin-down power. For the expression of $E_{\rm max}^{\rm loss}$ in Eq. (3.52), we use $(z/z_0) \sim 10^3$. Our choice is based on the results obtained by Becker & Biermann (2009), which show that a first large steady shock can be produced at about $z \sim 3 \times 10^3\, r_{\rm g}$ [following the work by Markoff et al. (2001)]. This is confirmed by observations of a blazar inner jet as revealed by a radio-to-γ-ray outburst (Marscher et al. 2008). The same conclusion was reached earlier by Biermann & Strittmatter (1987) using the observed cutoff in the radio emission of AGN.

Table 3.1 contains our estimations for the UHECR maximum particle energy, luminosity, and flux in the case of M87 and Cen A, whose jet parameters can be obtained from observational data. The observed radio-core flux-density corresponds to the frequency

Table 3.1: The jet parameters for M87 and Cen A, and the corresponding maximum particle energy (spatial and loss limits), UHECR luminosity and flux. Here, the quantities assume that the particles are protons.

Source	$\gamma_{\rm j}$	φ	θ	$D_{\rm s}$	M	$F_{\rm core}^{\rm 5GHz}$	$E_{\rm max}^{\rm sp}$	$E_{\rm max}^{\rm loss}$	$L_{\rm CR}$	$F_{\rm CR}$
		($\circ$)	($\circ$)	(Mpc)	($\times 10^9 M_\odot$)	(mJy)	(ZeV)	(ZeV)	(erg s^{-1})	(erg s^{-1}cm^{-2})
(1)	(2)	(3)	(4)	(5)	(6)	(7)	(8)	(9)	(10)	(11)
M87	6	10	19	16	3	2875.1	0.86	0.25	2.03×10^{43}	7.03×10^{-10}
Cen A	2	65	5	3.5	0.055	6984	0.11	0.21	3.16×10^{42}	2.28×10^{-9}

NOTE: Col. (1) Source name; Col. (2) Jet Lorentz factor; Col. (3) Angle to the line of sight; Col. (4) Jet semi-opening angle; Col. (5) Distance to the source; Col. (6) BH mass; Col. (7) Core flux density at 5 GHz; Col. (8) maximum particle energy (spatial limit); Col (9) maximum particle energy (loss limit); Col. (10) UHECR luminosity for a power-law index of particle distribution $p = 2$; Col. (11) UHECR flux. REFERENCES: Jet Lorentz factor: Biretta et al. (1999) and Meisenheimer et al. (2007); Angle to the line of sight: Biretta et al. (1999) and Tingay et al. (1998); Distance to the source for M87 Macri et al. (1999) and for Cen A we assume a distance $D_{\rm s} = 3.5$ Mpc to be consistent with the BH mass determination; BH mass: Macchetto et al. (1997) and Cappellari et al. (2009); Core flux density at 5 GHz: Nagar et al. (2001) and Slee et al. (1994). The value of the quantities inferred from observational data are the median ones, which we use in our estimations.

of GHz. For comparison, the energy along the jet estimated by Whysong & Antonucci (2003), is $\sim 10^{45}$ erg s^{-1} and $\sim 10^{43}$ erg s^{-1} for M87 and Cen A, respectively. [The energy flow along the jet for Cen A is confirmed by Abdo et al. (2010).] The estimations of the luminosity and flux of the UHECR correspond, however, to the slope of the particle density distribution of $p = 2$. For a steeper slope of the particle density distribution, both the luminosity and flux of the UHECR increase. Although the sources have a low power jet, they are powerful enough to provide the environment for particles to be accelerated to ultra-high energies of ~ 1 ZeV. In this case, the jet power is supplied by the BH spin-down power.

Eliminating the BH mass using the expressions of $E_{\rm max}^{\rm sp}$ and $L_{\rm CR}$ (Eq. 3.52), the UHECR luminosity and the maximum particle energy are related through the following equation

$$\left(\frac{L_{\rm CR}}{10^{45}{\rm erg/s}}\right)^{-10/7} = K \left(\frac{E_{\rm max}^{\rm sp}}{10^{20}{\rm eV}}\right)^{2}, \tag{3.53}$$

where

$$K = 6.27{\times}10^{7} \beta_{\rm j}^{-10/7} \left(1 - \beta_{\rm j} \cos\varphi\right)^{-30/7} \left(\frac{\tan\theta}{0.05}\right)^{-12/7} \left(\frac{\gamma_{\rm j}}{5}\right)^{-64/7} \left(\frac{F_{\rm obs}}{\rm mJy}\right)^{-12/7} \left(\frac{D_{\rm s}}{\rm Mpc}\right)^{-24/7}. \tag{3.54}$$

Equation (3.53) is, therefore, not dependent on the BH mass, instead it is dependent on the jet-related quantities.

3.6 Predictions for nearby galaxies as ultra-high-energy cosmic ray sources

We apply the model to a complete sample of steep-spectrum radio sources (Biermann et al. 2008; Caramete 2010), at redshift $z < 0.025$ (about 100 Mpc), with a total radio flux density larger than 0.5 Jy. The numbers for the estimated flux and maximal energy exclude the GZK effect, but they include the dilution with distance. The selection criteria used by the authors are presented in more detail in their papers. Table 3.2 lists the predictions for the UHECR particle maximum energy, luminosity, and flux. We emphasize

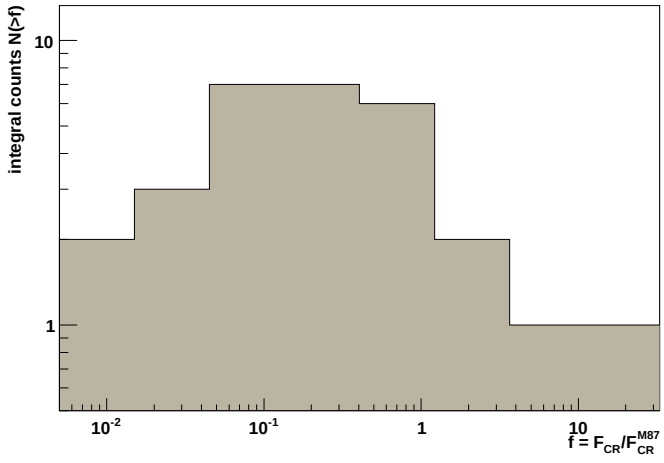

Figure 3.4: Integral source counts of the complete sample of steep-spectrum radio sources (see Table 3.2.), where their UHECR flux is estimated relative to that of M87.

that there could be a common scaling limit, such as a condition that the Larmor radius has to fit three times or five times into the jet. The scaling limit is not critical to our predictions as long as we refer the quantities to, say, M87; therefore, the jet parameters are assumed to be the same as for M87, all scaled by mass, radio power, and distance. That can be seen when comparing the estimated values of the UHECR maximum particle energy and flux for Cen A in Tables 3.1 and 3.2; the differences are within one order of magnitude. Using a scaling relative to M87, one implicitly allows for the possibility that all sources produce heavier nuclei ($Z > 1$). Of course this again assumes that all sources are the same in this respect. We argue that although the sources are LLAGN, they can be sites of accelerating particles to ultra-high energies ~ 1 ZeV with an UHECR luminosity $< 10^{43}$ erg s^{-1}.

In Fig. 3.4, we show the plot of integral source counts (N) versus relative UHECR flux (last column in Table 3.2.), where the data points are split in 8 bins of variable width with the bin upper edge three times larger than the bin lower edge. Although the data points are too sparse to discriminate models of the flux distribution, we estimate the most likely model parameters that could generate those data points. We fit a power-law model ($N = C\, f^{\kappa}$) to the mean values of the data in each bin for $N(> 0.405)$ (see Fig. 3.5) using the log-likelihood method.[10] The errors for the data points are estimated by $\sqrt{N}$. For the best fit that we obtained, the model parameters are: $C = 4.88 \pm 1.74$ and $\kappa = 0.86 \pm 0.45$. (Since the source counts for each bin is too low, especially in the tail of the assumed power-low distribution, we cannot perform a χ^2-test.) Within the errors, we can consider a power-law model with $\kappa > 1$, which implies that weak sources can dominate over the strong sources. In this view, LLAGN (powered by the BH spin down) can make a large contribution to the integrated UHECR flux in the local universe, as the density of LLAGN is significantly higher than the density of powerful AGN.

3.7 Summary and conclusions

In this work we developed a new model for UHECR contribution from BH spin-down power. We relate the observed radio flux-density to the cosmic ray luminosity and flux, and calculate the maximum particle energy in both spatial and loss limits. This model

[10]For plotting numerical results and for data analyzing, we use ROOT, which is an open source, data analysis program developed at CERN.

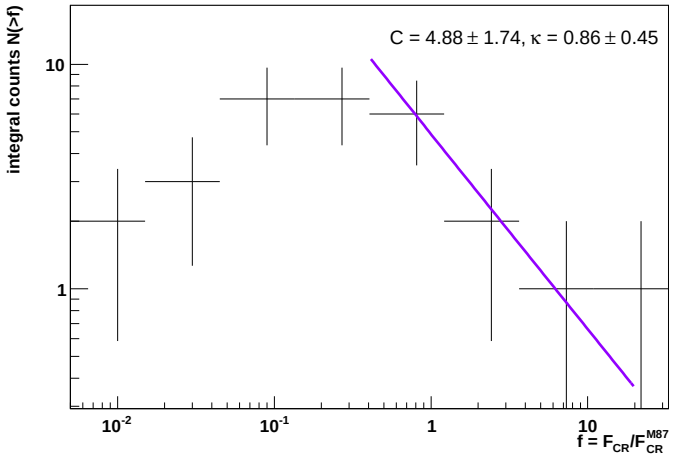

Figure 3.5: Integral source counts of the same sample as in Fig. 3.4. The model parameters for the best fit of a power-law model ($N = C\, f^{\kappa}$) with $N(> 0.405)$ are: $C = 4.88 \pm 1.74$ and $\kappa = 0.86 \pm 0.45$.

is relevant for many radio galaxies, where the accretion rate is very low, and therefore the BH spin-down power is a better option for powering their jets. Our predictions can be used in various propagation codes for UHECR, which typically use the maximal energy and flux of the cosmic rays scaled relative to a canonical radio galaxy, as well as the slope of the CR spectrum. The only difficulty is that the predicted quantities scale a bit differently if some of the UHECRs are heavy nuclei at the origin. That is because for heavy nuclei, the energy scales up with Z. For a middling FIR/Radio ratio,[11] as Cen A has, a starburst may have provided all the necessary pre-accelerated nuclei. Nonetheless, this is not the case for M87. We would like to point out that our model is just an extension of associating sites of the origin of UHECRs to AGN with low accretion rates, beside those of high accretion rates.

Table 3.2. NOTE: Col. (1) Source name; Col. (2) Distance to the source; Col. (3) BH mass; Col. (4) Core flux density at 5 GHz; Col (5) Maximum particle energy (spatial limit); Col. (6) Maximum particle energy relative to the corresponding value for M87; Col. (7) UHECR luminosity; (8) UHECR flux; (8) UHECR flux relative to the corresponding value for M87.

[11] "FIR" is the flux density at 60 μ and "Radio" is the flux density at 5 GHz.

Table 3.2: UHECR predictions for a complete sample of 29 steep-spectrum radio sources (Biermann et al. 2008; Caramete 2010). The numbers for the estimated flux and maximal energy exclude the GZK effect, but include the dilution with distance.

Source	D	M	$F_{\rm core}^{\rm 5GHz}$	$E_{\rm max}^{\rm sp}$	$E_{\rm max}^{\rm sp}/E_{\rm max}^{\rm sp,M87}$	$E_{\rm max}^{\rm loss}$	$E_{\rm max}^{\rm loss}/E_{\rm max}^{\rm loss,M87}$	$L_{\rm CR}$	$F_{\rm CR}$	$F_{\rm CR}/F_{\rm CR}^{\rm M87}$
	(Mpc)	($\times 10^9 M_\odot$)	(mJy)	(10^{20} eV)		(10^{20} eV)		(erg s^{-1})	(erg s^{-1} cm^{-2})	
(1)	(2)	(3)	(4)	(5)	(6)	(7)	(8)	(9)	(10)	(11)
ARP 308	69.7	0.1	67.8	1.57	0.18	0.45	0.18	8.39×10^{43}	1.52×10^{-10}	0.21
CGCG 114-025	67.4	0.19	443.39	2.16	0.25	0.63	0.25	4.70×10^{44}	9.15×10^{-10}	1.30
ESO 137-G006	76.2	0.92	631.32	4.76	0.55	1.38	0.55	3.19×10^{44}	4.87×10^{-10}	0.69
IC 4296	54.9	1	214	4.97	0.57	1.44	0.57	3.75×10^{43}	1.10×10^{-10}	0.15
IC 5063	44.9	0.2	29	2.22	0.25	0.64	0.25	6.49×10^{42}	2.84×10^{-11}	0.04
NGC 0193	55.5	0.2	40	2.22	0.25	0.64	0.25	1.58×10^{43}	4.55×10^{-11}	0.06
NGC 0383	65.8	0.55	92	3.68	0.42	1.07	0.42	3.19×10^{43}	6.52×10^{-11}	0.09
NGC 1128	92.2	0.2	39	2.22	0.25	0.64	0.25	5.20×10^{43}	5.41×10^{-11}	0.07
NGC 1167	65.2	0.46	243	3.37	0.39	0.98	0.39	1.13×10^{44}	2.36×10^{-10}	0.33
NGC 1316	22.6	0.92	26	4.76	0.55	1.38	0.55	3.76×10^{41}	6.51×10^{-12}	0.01
NGC 1399	15.9	0.3	10	2.72	0.31	0.79	0.31	1.12×10^{41}	3.94×10^{-12}	0.005
NGC 2663	32.5	0.61	160	3.88	0.45	1.13	0.45	1.06×10^{43}	8.89×10^{-11}	0.12
NGC 3801	50	0.22	635	2.33	0.27	0.67	0.27	3.19×10^{44}	1.12×10^{-9}	1.60
NGC 3862	93.7	0.44	1674	3.29	0.38	0.96	0.38	2.83×10^{45}	2.85×10^{-9}	4.06
NGC 4261	16.5	0.52	390	3.58	0.41	1.04	0.41	6.80×10^{42}	2.20×10^{-10}	0.31
NGC 4374	16	1	168.7	4.97	0.57	1.44	0.57	1.46×10^{42}	5.05×10^{-11}	0.07
NGC 4486	16	3	2875.1	8.61	1	2.50	1	2.03×10^{43}	7.03×10^{-10}	1
NGC 4651	18.3	0.04	15	0.99	0.11	0.28	0.11	1.05×10^{42}	2.78×10^{-11}	0.03
NGC 4696	44.4	0.3	55	2.72	0.31	0.79	0.31	1.02×10^{43}	4.59×10^{-11}	0.06
NGC 5090	50.4	0.74	268	4.27	0.49	1.24	0.49	4.94×10^{43}	1.72×10^{-10}	0.24
NGC 5128	3.5	0.055	6984	1.16	0.13	0.33	0.13	2.53×10^{43}	1.82×10^{-8}	25.95
NGC 5532	104.8	1.08	77	5.16	0.6	1.50	0.6	4.92×10^{43}	3.96×10^{-11}	0.05
NGC 5793	50.8	0.14	95.38	1.86	0.21	0.54	0.21	4.67×10^{43}	1.60×10^{-10}	0.22
NGC 7075	72.7	0.25	20	2.48	0.28	0.72	0.28	1.13×10^{43}	1.89×10^{-11}	0.02
UGC 01841	84.4	0.1	182	1.57	0.18	0.45	0.18	4.34×10^{44}	5.39×10^{-10}	0.76
UGC 02783	82.6	0.42	541	3.22	0.37	0.93	0.37	5.58×10^{44}	7.23×10^{-10}	1.02
UGC 11294	63.6	0.29	314	2.67	0.31	0.78	0.31	2.01×10^{44}	4.39×10^{-10}	0.62
VV 201	66.2	0.1	88	1.57	0.18	0.45	0.18	1.01×10^{44}	2.04×10^{-10}	0.29
WEIN 45	84.6	0.27	321.6	2.58	0.3	0.75	0.3	4.31×10^{44}	5.33×10^{-10}	0.75

Chapter 4

General Relativistic Magnetohydrodynamics Simulation of Jet Formation from Kerr Black Holes

The first GRMHD code for simulating jet formation from accreting BHs was developed by Koide et al. (1999) using the conservation form of the ideal GRMHD equations on fixed geometry (either Schwarzschild or Kerr). Using the simulation code by Koide et al., we present numerical results of jet formation from a rapidly-spinning BH ($a_* = 0.95$), when the accretion disk co-rotates with the BH rotation and the coronal plasma falls freely towards the BH.[1] The main result of the numerical simulation presented here consists of an electromagnetically-driven component of the jet which, near the BH, is developed inside the gas pressure-driven component of the jet. This is different from the previous results obtained by Koide et al., where the jet has two separately components (the pressure-driven and magnetically-driven components). The jet consists of plasma coming from the disk, as well as from the BH corona. Far from the BH, the jet is basically driven by electromagnetic forces, whereas the gas-pressure forces of the coronal plasma, which decelerate the jet, are somewhat weaker than the driving electromagnetic forces. The maximum velocity of the plasma in the jet is $\sim 0.4\,c$ (i.e., the jet is sub-relativistic). This is considerable lower than the velocity of the inner parts of some AGN jet for which the observations indicate relativistic speeds. However, the outer parts of the jet can have mildly- and sub-relativistic speeds. Despite this low velocity in the inner part of the jet, the electromagnetically-driven component of the jet is important by itself as it shows that the extraction of the rotational energy from the BH via a Penrose-like process in the BH ergosphere is possible, although for transient jets. Further development of the code may accomplish the attempt to fully match the AGN observational data.

[1]The simulations using the code by Koide et al., as well as the tests with the RAISHIN code by Mizuno et al., were performed on a machine at the National Center for Supercomputing Applications at the University of Illinois at Urbana-Champaign, USA, through the collaboration with Ken-Ichi Nishikawa and Yosuke Mizuno.

4.1 Introduction

General relativistic magnetohydrodynamics (GRMHD) describes the dynamics of relativistic, electrically conducting fluids, when magnetic fields are present, in the gravitational field of compact objects. Connecting magnetohydrodynamics (MHD) to general relativity, the GRMHD provides a suitable framework to study time-dependent accretion flow and jet formation from the region near BHs or neutron stars (NSs). Here, we make use of the GRMHD laws written in 3+1 language for a general space-time. The laws are expressed in terms of quantities (magnetic field, flow velocity, etc.) which are measured by the fiducial observers[2] whose world lines are orthogonal to the hypersurfaces of constant time (see Section 4.2.1 for details).

The formation of relativistic jets in AGN and microquasars, explained (i) by magnetohydrodynamical effects as in the jet model of Blandford & Rees (1974), (ii) by MHD centrifugal acceleration as in the Blandford-Payne mechanism (Blandford & Payne 1982), or (iii) by electromagnetic extraction of energy as in the Blandford-Znajek mechanism (Blandford & Znajek 1977), involves an accretion disk around rotating BHs. The discovery of quasi-periodic oscillations in X-ray binaries extended the frequency range over which these oscillations occur into timescales associated with the relativistic, innermost regions of accretion disks (e.g., Mirabel & Rodriguez 1999). A relativistic description is also necessary in scenarios involving the explosive collapse of massive stars to a BH (collapsar model, see, e.g., Woosley 1993) or during the last phases of the coalescence of neutron star binaries. These catastrophic events are believed to exist at the central engine of highly energetic gamma-ray bursts (GRBs, see, e.g., Piran 2000). In addition, non-spherical gravitational collapse leading to BH formation or to a supernova explosion, and neutron star binary coalescence are among the most promising sources of short GRBs.

Powerful tools to improve our understanding of these astrophysical phenomena are accurate, large-scale, 3-D numerical simulations. Nowadays, computational general-relativistic astrophysics is an increasingly important field of research. In addition to the large amount of observational data by X- and gamma-ray satellites such as BATSE, BeppoSAX, Chandra, XMM-Newton, INTEGRAL, SWIFT, FERMI, formerly GLAST (e.g., Abdo et al. (2009) and also http://fermi.gsfc.nasa.gov/], or in the future IXO (http://ixo.gsfc.nasa.gov/), and EXIST (http://exist.gsfc. nasa.gov/)], and the new generation of gravitational wave detectors [LIGO and LISA (http://www.ligo.org/ and http://www.lisa.org/)], the rapid increase in computing power through parallel supercomputers and the associated advance in software technologies is making large-scale numerical simulations in the framework of general relativity possible.

Recent observations and theoretical research suggest that magnetic fields play a crucial role in determining the evolution of many astrophysical objects. In any highly conducting astrophysical plasma, a frozen-in magnetic field can be amplified appreciably by gas compression or shear. Even when an initial seed field is weak, the field can grow in the course of time to significantly influence the gas dynamical behavior of the system. This process is called the magnetorotational instability [MRI, e.g., Balbus & Hawley (1998) and references therein], and it is an efficient mechanism to magnetically induce the transport of angular momentum in a thick torus-like accretion disk (with $H/r > 0.1$, where H is the

[2]Also known as the Eulerean observers, which are the zero angular momentum observers in the case of Kerr space-time.

half-thickness of the disk at the disk radius r) around a BH. Perturbations in a differentially rotating disk grow when the magnetic pressure is smaller than the gas pressure. As a result, weak magnetic fields are amplified on dynamic time scales. In fact, the angular momentum in a GRMHD disk can generally be transported by either the MRI or the magnetic braking. The latter is observed in the GRMHD jet formation obtained by Koide et al. (1998) when a thin accretion disk is considered. In this case, the differential rotation of the accretion disk winds up a toroidal magnetic field, which then begins to transport angular momentum from the inner to the outer part of the accretion disk. The MRI does not grow in a thin accretion disk since the wavelength at the maximum grow rate is larger than the height of the disk (Mizuno et al. 2006a). If, in addition, the gravitational field is strong and dynamical, magnetic fields can even affect the entire geometry of space-time, according to general relativity. In this situation, terms involving magnetic and electric fields are important not only as electromagnetic forces acting on the matter in the equations of relativistic hydrodynamics but also as stress-energy sources governing the metric in Einstein's gravitational field equations.

In the most general case, the equations governing the dynamics of relativistic astrophysical systems form a coupled system of time-dependent partial differential equations comprised of the MHD equations and the Einstein gravitational-field equations. To investigate the dynamics of accretion disks and the associated jet formation in AGN or in microquasars, GRMHD simulation codes have been developed (e.g., the review by Font 2008). The first distinction between the GRMHD codes is the way the equations are written: in a **conservation** or **non-conservation** form.

In short, a conservation GRMHD code[3] is based on: (i) the choice of coordinates (e.g., Boyer-Lindquist coordinates or Kerr-Schild coordinates); (ii) the discretization of the system (the finite difference methods, the finite element methods, or the finite volume methods); (iii) the scheme to integrate the non-linear hyperbolic system of GRMHD equations and handle the discontinuities [e.g., a (Godunov-type[4]) high-resolution shock-capturing schemes]; (iv) the scheme to keep the magnetic field divergence-free (e.g., constrained transport); (v) the recovery scheme to derive primitive variables from the conserved ones (see later in this chapter); and (vi) the validation tests (e.g., 1-D tests in Minkowski space-time that include Alfvén wave propagation, fast and slow magnetosonic shocks, or non- and relativistic shock tubes).

As long as the electric resistivity is negligible, the electric and displacement currents do not need to be explicity calculated when the conservation form of the GRMHD equations is applied. Therefore, the numerical errors that can occur when calculate the electric current density are eliminated. This is one advantage of using the GRMHD equations in conservation form in comparison with using forms of the GRMHD equations that include explicity the electric current density (Koide 2003).

For non-conservation forms, a ZEUS-like (Stone & Norman 1992) approach is employed. De Villiers & Hawley (2003) numerically simulated an accretion disk by considering

[3]Some details on the GRMHD code used in this chapter are given in Section 4.3.

[4]Godunov-type scheme, encouraged by successful applications to the Euler equations, are considered to be highly effective in resolving discontinuities, such as shock waves, for high-speed flow problems (Myong & Roe 1998). Godunov (1959) used the local characteristic structure obtained from solving a Riemann problem to define an upwind method. The Riemann problem concerns the evolution of an arbitrary initial discontinuity, which can be described by various self-similar waves and contact discontinuity, as well as shock waves.

a magnetized gas disk and the ideal MHD equations. They developed a scheme to permit the integration of an internal energy equation rather than a total energy equation (as for the conservation schemes), which is, however, suitable in regions of a flow where the internal energy is small compared to the total energy (highly supersonic flows). As a result, the kinetic energy, as well as the magnetic energy, can be lost at the grid scale. Therefore, an artificial viscosity term which is added in the internal energy equation enables some of the kinetic energy to be captured as heat. As the authors state, the shortcoming of their simulation code revealed by the validation tests is due to the artificial viscosity algorithm of the underlying hydrodynamic solver. Nevertheless, their numerical code can be applied to the study of the MRI thick tori evolution for both the Schwarzschild and Kerr BHs. Their numerical simulation also shows significant outflow driven by the accretion disk (see also De Villiers et al. 2005; Hawley & Krolik 2006).

Unless otherwise noted, the next numerical GRMHD codes which are next mentioned are based on conservation schemes.

The first GRMHD simulations of jet formation were performed by Koide et al. (1998, 1999, 2000a) using the 3+1 formalism of general relativistic conservation laws of mass, momentum, and energy, and Maxwell equations with infinite electric conductivity (ideal MHD approximation) with the static metrics. These conditions are the base of most studies of jet formation. The GRMHD equations are solved in the test-fluid approximation,[5] using the simplified total variation diminishing (TVD) method.[6] The background geometry is either Schwarzschild or Kerr space-time with Boyer-Lindquist coordinates. In particular, Koide et al. (1999) investigated (in 2-D) the dynamics of an accretion disk initially threaded by a uniform magnetic field [described by the vacuum solution of Wald (1974)] in a non-rotating corona (either in a state of steady fall or in hydrostatic equilibrium) around a Schwarzschild BH. The GRMHD numerical results show that matter in the disk loses angular momentum by magnetic braking, and then it falls into the BH. The disk falls faster in this simulation than in the non-relativistic case because of the general-relativistic effects that are important below $3\,r_{\rm S}$, where $r_{\rm S} \equiv 2GM/c^2$ is the Schwarzschild radius. A centrifugal barrier at $r = 2\,r_{\rm S}$ strongly decelerates the infalling material. Plasma near the shock at the centrifugal barrier is accelerated by the $\mathbf{J} \times \mathbf{B}$ force (where $\mathbf{J}$ and $\mathbf{B}$ denote the current density vector and the magnetic field vector, respectively) and forms bipolar jets. Inside this magnetically driven jet, the gradient of gas pressure also generates a jet above the shock region (gas-pressure driven jet). This two-layered jet structure is formed both in a hydrostatic corona and in a steady-state falling corona. Koide et al. (2000a) also developed a GRMHD code using the Kerr geometry and found that with a rapidly-rotating BH magnetosphere of a spin parameter $a_* = 0.95$, the maximum velocity of the jet is $(0.3 - 0.4)\,c$. The simulations show how the BH drags the inertial frames around in the ergosphere. Simulations with free-falling corona and initial uniform magnetic field as initial conditions were performed also by Koide (2003, 2004) and Nishikawa et al. (2005b).

3-D GRMHD simulation results of jet formation from a Schwarzschild BH obtained

[5]In this case, the self-gravity of the fluid is neglected in comparison with the background gravitational field, so that the energy-momentum of the fluid does not couple to the metric and does not deform the Kerr geometry.

[6]The code represents an extension of the jet formation in the case of non-steady Newtonian MHD (Shibata & Uchida 1986; Uchida & Shibata 1985). MHD formation of the jet (in 2-D and 3-D) has been obtained for relativistic regime, for instance, by Koide et al. (1996), Nishikawa et al. (1997), and Nishikawa et al. (1998).

by Nishikawa et al. (2003, 2005b) show a bipolar jet with velocity $\sim 3\,c$. In the later stage, a wind with a much wider angle than the early-stage jet's angle and a thick disk are formed. The jet is formed from the initially accreting matter and, since at the outer boundary of the disk no matter is further injected, the power to generate the jet is dissipated and the jet is transformed into a wind. Compared to the previous 2-D numerical results, due to a longer simulation time, a thickening of the disk is also observed by the end of simulation run.

Mizuno et al. (2004a) presented results of jet propagation through progenitor stellar models of collapsar. In this case, 2.5-D GRMHD simulations of the gravitational collapse of a rotating magnetized massive star with a Kerr BH at the center are performed [for a Schwarzschild BH see Mizuno et al. (2004b)]. These simulations show the formation of a disk-like structure and the generation of a mildly relativistic jet ($\sim 0.3\,c$). The jet-like outflow is accelerated mainly by the magnetic field; when the rotation of the BH is faster, the magnetic field is twisted strongly owing to the frame-dragging effect. The magnetic energy stored by the twisting magnetic field is directly converted into kinetic energy of the jet rather than propagating as an Alfvén wave. Thus, as the rotation of the BH becomes faster, the poloidal velocity of the jet becomes faster. The obtained kinetic energy of the jet is about 10^{54} erg, which is large enough to explain the standard energy in GRBs ($\sim 10^{51}$ erg). The jet velocity is, however, too low to account for the jet velocity in GRBs, therefore new mechanisms need to be considered, perhaps neutrino-annihilation or shock acceleration of particles. Nonetheless, these results can be applied to baryon-rich outflows associated with failed GRBs, which may be observed as hypernovae (e.g., SN 2002ap).

More GRMHD simulations were developed (e.g., Gammie et al. 2003; Komissarov 2004; Anninos et al. 2005; McKinney 2006; Mizuno et al. 2006a; Del Zanna et al. 2007; Giacomazzo & Rezzolla 2007; McKinney & Blandford 2009). In the paper series by Gammie et al. (2003), McKinney & Gammie (2004), or McKinney (2006), the numerical scheme HARM (High Accuracy Relativistic Magnetohydrodynamics) was employed, in which case a conservation, shock-capturing scheme is applied. The Kerr metric is written in Kerr-Schild coordinates, such that the inner radial computational boundary can be placed inside the horizon and so out of causal contact with the flow. The jets have two components: (i) a matter-dominated outflow moving at about 0.3 c along the centrifugal barrier surrounding an evacuated axial funnel and (ii) a highly-relativistic Poynting-flux-dominated jet, within the funnel, which is accelerated and collimated by magnetic and gas pressure forces in the inner torus and the surrounding corona. The latter paper is an extention of the previous ones to study the Poynting-flux-dominated jets, which are accelerated by continuous mass-loading from the disk. In this case, large Lorentz factors are obtained, $\Gamma \sim 10$, with a maximum terminal Lorentz factor of $\Gamma_\infty \lesssim 10^3$ (McKinney 2006). Komissarov (2004) obtained the first numerical results of a magnetically-dominated monopole BH magnetosphere. He found that the numerical solution evolves towards a stable steady-state solution, which corresponds to the Blandford-Znajek force-free solution. Furthermore, Anninos et al. (2005) developed a code (Cosmos++) to solve the GRMHD equations in fixed background space-times using time-explicit, finite-volume discretization. The code has options for solving the GRMHD equations using traditional artificial viscosity or non-oscillatory, central difference methods, or a new extended artificial viscosity scheme using artificial viscosity together with a dual energy/flux-conserving formulation. This code is applied, for instance,

by Fragile & Meier (2009) to investigate how the hard-state objects[7] behave if they would radiate efficiently. Giacomazzo & Rezzolla (2007) presented a new code (WhiskyMHD) developed to solve the full set of GRMHD equations in a dynamical and arbitrary space-time with high-resolution shock-capturing techniques on domains with adaptive grid refinements.

Mizuno et al. (2006a) developed a new code, RAISHIN,[8] which is based on a 3+1 formalism of the general-relativistic conservation laws of particle number and energy momentum, Maxwell equations, and Ohm's law with no electrical resistance (ideal MHD condition). In the RAISHIN code, a conservation, high-resolution shock-capturing scheme is employed. The numerical fluxes are calculated using the Harten et al. (1983) approximate Riemann solver scheme. The flux-interpolated, constrained transport scheme is used to maintain a divergence-free magnetic field. The RAISHIN code has proven to be accurate to the second order and has passed a number of numerical tests, including highly relativistic cases and highly magnetized cases in both special and general relativity. The RAISHIN code has been used in its relativistic MHD configuration (Mizuno et al. 2007) to study the effects of strong magnetic fields and weakly relativistic sheath motion, $c/2$, on the Kelvin-Helmholtz instability associated with a relativistic, $\gamma = 2.5$, jet spine-sheath interaction, as well as the development of current-driven kink instability through 3-D relativistic MHD simulations (Mizuno et al. 2009b).

In many cases, equations which describe non-adiabatic processes (such as viscosity, resistivity, or radiative transfer) or sophisticated microphysics (e.g., realistic equations of state for nuclear matter), which can be important contributors to the dynamics of the accretion flows, must be added to the GRMHD equations. Radiative transfer calculations in general relativity were considered, for instance, by Fuerst & Wu (2004), Nishikawa et al. (2005a), De Villiers (2008), and Wu et al. (2008).

In this chapter, we present the numerical results of jet formation from rapidly-spinning BHs ($a_* = 0.95$), surrounded by a thin accretion disk with a free-falling corona, using the GRMHD code developed by Koide et al. (1998, 1999, 2000a) and Mizuno et al. (2004a). The results are compared to the numerical simulations performed with the RAISHIN code (Mizuno et al. 2006a), as well as with other work. Geometrized units (G = c = 1) are used throughout this chapter, except where explicitly indicated. The signature of 4-metric is +2 and Greek (Latin) indices run from 0 to 3 (1 to 3); the Einstein summation convention is used. Four-vectors are denoted through index notation or boldface letters, e.g., v^μ or $\mathbf{v}$.

For the theoretical part exposed on this chapter, we generally follow Baumgarte & Shapiro (2003) and Wilson & Mathews (2003) for 3+1 decomposition of the space-time, as well as Koide (2003), Nishikawa et al. (2005b), Mizuno et al. (2006b), Camenzind (2007), Font (2008), and Nishikawa[9] for specific aspects of GRMHD.

---

[7] In X-ray binaries (BH-BH or BH-NS), the hard X-ray state (10-20 keV) is usually observed when the source is faint, having a photon spectrum index of about 1.7; thus, the name low/hard state (e.g., Remillard & McClintock 2006). This state is associated with emission from all three components: the accretion disk, the hot corona, and the jet. Objects in hard-state usually produce jets with speeds of $\sim 0.3\,c$.

[8] RAISHIN stands for RelAtIviStic magnetoHydrodynamics sImulatioN; it is also the ancient Japanese god of lightning.

[9] Nishikawa, K.-I.: book on "Black Hole Simulations," which is work in progress.

Chapter outline

In Section 4.2 we assemble the complete set of GRMHD equations in conservation form using the 3+1 decomposition of space-time. They determine the self-consistent evolution of a relativistic MHD fluid in Kerr space-time. In Section 4.3, we describe the GRMHD simulation code (Koide et al. 1998, 1999, 2000a; Mizuno et al. 2004a) employed further in this chapter. In Section 4.4 we present the numerical results of jet formation from rapidly-spinning BHs ($a_* = 0.95$). The simulation results show that a jet with velocity of about $0.4\,c$ is formed. By the end of simulations and far from the BH, the jet is accelerated mainly by electromagnetic forces, where the simulations ran over one hundred light-crossing time units ($\tau_{\rm S} = r_{\rm S}/c$). A comparison with the code developed by Mizuno et al. (2006a), RAISHIN, as well as other work, is also presented. A summary and conclusions are presented in Section 4.5.

4.2 General relativistic magnetohydrodynamics equations in conservation form

The set of GRMHD equations are obtained from the local conservation laws of the energy-momentum tensor,[10] the continuity equation (conservation of the matter density), and the Maxwell equations. In addition, an equation of state for the fluid must be specified. Here, we consider only ideal MHD; that is, the fluid is a perfect conductor with no resistivity and no viscous loss. Effects due to viscosity, as well as radiation transport, are neglected.

In the case of numerical relativity, an appropriate formalism to study the time evolution of a system is, among others [e.g., characteristic methods (Gómez et al. 1998)], the Cauchy approach in 3+1 decomposition of the space-time. This formalism, which is applied to a large extent in GRMHD numerical simulations, is described in the following section.

4.2.1 3+1 decomposition of the space-time (in the Eulerean formulation)

In the standard covariant form, Einstein equations (e.g., Misner et al. 1973),

$$G_{\mu\nu} = 8\pi T_{\mu\nu}, \tag{4.1}$$

do not explicitly describe the time evolution of a system. To produce numerical solutions of the Einstein equations, the equations are recast into a so-called 3+1 formulation (in which the coordinate time is split from the three spatial coordinates) and reformulated as an initial value (or Cauchy) problem; that is, the gravitational field is considered to be the time history of the geometry of a space-like 3-D hypersurface on which the initial value problem is solved, and the evolution equations are integrated along the trajectories of a chosen reference frame.

The usual 3+1 decomposition of the Einstein equations is the Arnowitt-Deser-Misner (ADM, Arnowitt et al. 1962) formalism, by which the space-time is foliated into a family of space-like 3-D hypersurfaces $\Sigma(t)$, labeled by the time coordinate t. This time

[10] In general relativity, the distribution of the mass, momentum, and stress due to matter, and to any non-gravitational fields, is described by the energy-momentum tensor $T^{\mu\nu}$.

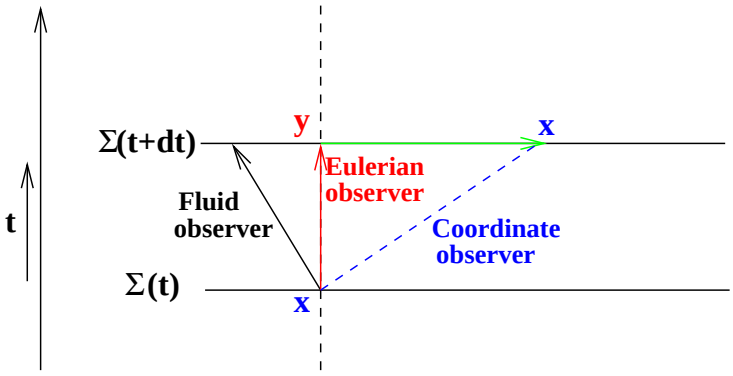

Figure 4.1: Schematic representation of observer frames in the ADM metric [adapted from Wilson & Mathews (2003)].

coordinate is chosen along a normal unit vector to the 3-D hypersurfaces. These hypersurfaces are separated by differential displacements in coordinate time, dt (see Fig. 4.1). The data on each space-like hypersurface is specified by both $\gamma_{\mu\nu}$ and $K_{\mu\nu}$, where

$$\gamma_{\mu\nu} = g_{\mu\nu} + n_\mu n_\nu, \tag{4.2}$$

is the spatial metric induced by the space-time metric $g_{\mu\nu}$ onto each slice $\Sigma(t)$, and $\mathbf{n}$ is the future directed unit vector normal to $\Sigma(t)$. This unit vector satisfies the normalization relation $n_\mu n^\mu = -1$. The extrinsic curvature, $K_{\mu\nu}$, can be written in terms of the Lie derivatives[11] of the spatial metric along the unit normal vector, $K_{\mu\nu} = -(1/2)\mathcal{L}_{\mathbf{n}}\gamma_{\mu\nu}$.

Since $\mathbf{n}$ is a unit time-like vector, the vector $c\,\mathbf{n}$ (c is the speed of light[12]) can be interpreted as the 4-velocity field of the observers that are instantaneously at rest in the spatial slices Σ. These observers are usually referred to as the **Eulerean observers**. In the case of Kerr space-time, the Eulerean observers are called zero angular momentum observers (ZAMOs). They move through space-time in a direction orthogonal to the spatial slices with clocks showing the proper time τ. This implies that from the point of view of the Eulerean observer, the hypersurface $\Sigma(t)$ can be locally regarded as a set of simultaneous events. The frame of a Eulerean observer is an appropriate frame in which to measure physical quantities such us the fluid velocity, etc., since this frame is defined independently of the choice of coordinates.

The general covariance of general relativity provides four degrees of freedom, which are used to adjust the coordinate system as desired. This freedom is embodied in four functions: the lapse function α and the spatial shift vector β^μ (which has, at most, three non-zero components).

The orthogonal proper time interval between two slices is $\alpha\, d\tau$, so that one can choose $N^\mu = \alpha\, n^\mu$ as the (orthogonal) vector field connecting the slices and then $\alpha = (-g_{\mu\nu}N^\mu N^\nu)^{1/2}$. So that, any 4-vector field $\mathbf{t}$ can be decomposed into a part proportional to $\mathbf{n}$ (the time-like part) and the other part tangent to the hypersurface Σ (the spatial part) as

$$t^\mu = \alpha\, n^\mu + \beta^\mu, \tag{4.3}$$

where $\beta^\mu n_\mu = 0$ (since the shift vector is tangent to the hypersurface Σ, whereas the vector $\mathbf{n}$ is normal to Σ). The lapse function and the shift vector determine how the coordinates

[11] An introduction to Lie derivatives can be found, for example, in Schutz (1980).

[12] Here, we include c in the 4-velocity definition, but later we shall drop it.

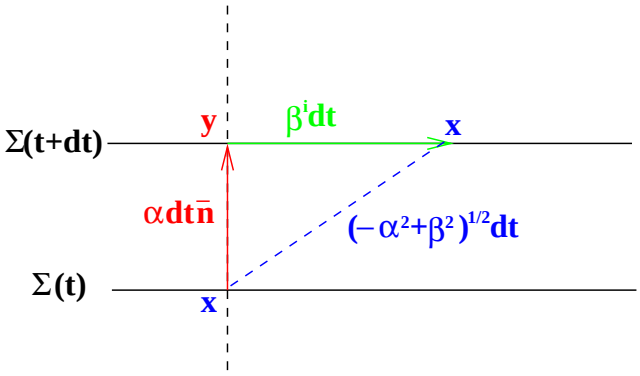

Figure 4.2: Schematic representation of the ADM metric [adapted from Wilson & Mathews (2003)].

evolve from one slice to the next, in the sense that the lapse function determines how much proper time elapses between slices along the unit normal vector, while the shift vector determines by how much the spatial coordinates are shifted with respect to the normal vector (see Figs. 4.2 and 4.3).

Similarly, any 4-D tensor can be decomposed into a spatial part and a time-like part. The spatial part is obtained by contracting the tensor with the projection operator,

$$\gamma^{\mu}_{\ \nu} = g^{\mu\sigma}\gamma_{\sigma\nu} = g^{\mu}_{\ \nu} + n^{\mu}n_{\nu} = \delta^{\mu}_{\ \nu} + n^{\mu}n_{\nu}, \tag{4.4}$$

and the time-like part by contracting it with $-n^{\mu}n_{\nu}$. For example, the 3+1 decomposition of a 4-D tensor can be applied to the energy-momentum tensor of a magnetized fluid, which gives, in fact, the GRMHD equations (see later in this chapter).

To describe a system in the 3+1 approach, the following reference frames are used: (i) the coordinate frame, (ii) the Eulerean frame, and (iii) the fluid frame (see Fig. 4.1).

The **coordinate frame** is defined by the coordinate basis $\{\mathbf{e}_{\mu}\}$, whose time leg is the vector $\mathbf{t}$, so that the scalar products of the tangent vectors constitute the metric $\mathbf{e}_{\mu} \cdot \mathbf{e}_{\nu} = g_{\mu\nu}$. The components of the coordinate basis vectors are $(\mathbf{e}_{\mu})^{\nu} = \delta_{\mu}^{\ \nu}$ and $(\mathbf{e}_{\mu})_{\nu} = g_{\mu\nu}$.

For any vector $\mathbf{V}$, the following holds: $n_{\mu}V^{\mu} = n_t V^t = -\alpha V^t$. By definition, the contraction of any spatial vector with the unit normal vector is zero, so if $\mathbf{V}$ is spatial, we then have $n_{\mu}V^{\mu} = 0$. Using Eq. 4.6, the time component of the contravariant spatial vector is then zero, $V^t = 0$. Since the shift vector is spatial, we have $\beta^t = 0$, and thus $\beta^{\mu} = (0, \beta^i)$. From Eq. 4.6 and taking into account that $n_{\mu}n^{\mu} = -1$, we have $n^t = \alpha^{-1}$. The contravariant component of the unit normal vector is then obtained from the definition in Eq. 4.3, together with $\beta^{\mu} = (0, \beta^i)$, as

$$n^{\mu} = \frac{1}{\alpha}(1, -\beta^i). \tag{4.5}$$

Since $n_{\mu}n^{\mu} = -1$, the components of the unit normal vector $\mathbf{n}$ in the coordinate frame are

$$n_{\mu} = (-\alpha, 0, 0, 0), \tag{4.6}$$

which, when inserted into the definition of the spatial metric (Eq. 4.2), gives $\gamma_{ij} = g_{ij}$. In addition, $\gamma^{\mu t} = 0$, which follows from the fact that the time components of contravariant, spatial tensors are zero. With these ingredients, the inverse of the 4-metric can be written as

$$\begin{pmatrix} g^{tt} & g^{tj} \\ g^{it} & g^{ij} \end{pmatrix} = \begin{pmatrix} -\frac{1}{\alpha^2} & \frac{\beta^j}{\alpha^2} \\ \frac{\beta^i}{\alpha^2} & \gamma^{ij} - \frac{\beta^i\beta^j}{\alpha^2} \end{pmatrix}. \tag{4.7}$$

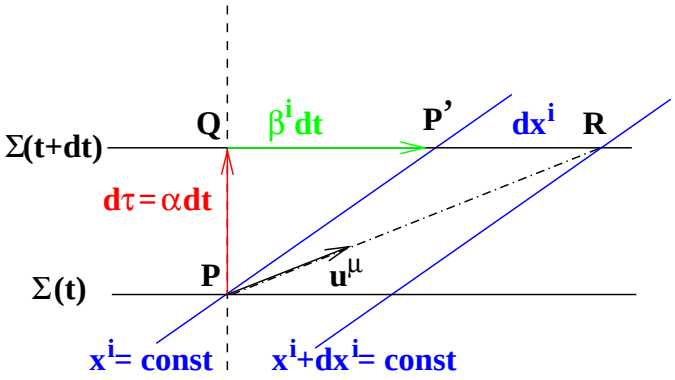

Figure 4.3: Geometrical interpretation of the lapse function α and the shift vector β^i.

Using $n_i = 0$, $\gamma_{ij} = g_{ij}$, $\gamma^{\mu t} = 0$, and $\gamma^{ik}\gamma_{kj} = \delta^i_{\ j}$, the components of the 4-metric with respect to a coordinate system, x^μ, can be written in terms of the lapse function α, the shift vector β^i, and the 3-metric γ_{ij} as

$$\begin{pmatrix} g_{tt} & g_{tj} \\ g_{it} & g_{ij} \end{pmatrix} = \begin{pmatrix} \beta_k\beta^k - \alpha^2 & \beta_j \\ \beta_i & \gamma_{ij} \end{pmatrix}. \tag{4.8}$$

So, the line element between any two points in a 3+1-dimensional space-time (also called the ADM metric) is

$$\begin{aligned} ds^2 &= g_{\mu\nu}dx^\mu dx^\mu = -(\alpha^2 - \beta_i\beta^i)dt^2 + 2\beta^i dx^i dt + \gamma_{ij}dx^i dx^j \\ &= -\alpha^2 dt^2 + \gamma_{ij}(dx^i + \beta^i dt)(dx^j + \beta^j dt). \end{aligned} \tag{4.9}$$

Figure 4.2 shows a schematic representation of the ADM metric.

A coordinate observer moves through space-time in a direction such that the spatial coordinates x^i on slice $\Sigma(t)$ are equal to the space coordinates of his location at time $t + dt$ (the blue curves in Fig. 4.3). Besides this, one has complete freedom to choose where those coordinates connect to the next spatial slice, i.e., where the point P' should be located. Though, this freedom is restricted by causality if causality is automatically obeyed. The shift of the space coordinates from one 3-D hypersurface to the next one is then specified by β^i (the green line in Fig. 4.3). If point Q, where the normal to the slice $\Sigma(t)$ connects with the slice $\Sigma(t + dt)$, has the coordinate y^i, one can write

$$x^i(t) = x^i(t + dt) = y^i + \beta^i dt. \tag{4.10}$$

Thus, the length of the space-time vector stretching from the coordinate observer's position at point P to point P' is the one specified by the observer's watch,

$$(ds^2)_{c.o.} = (-\alpha^2 + \beta_i\beta^i)dt^2, \tag{4.11}$$

so that the lapse of proper time shown by a clock moving in the coordinate observer's frame is given by

$$d\tau = \sqrt{\alpha^2 - \beta^2}\, dt. \tag{4.12}$$

Let us consider the points $P(t,\, x^i)$, $Q(t + dt,\, x^i - \beta^i dt)$, and $R(t + dt,\, x^i + dx^i)$ in the coordinate frame. In this frame, the 4-velocity of a particle $\mathbf{u}$, normalized so that $u_\mu u^\mu = -1$, has the components

$$u^\mu = \frac{(dt, dx^i)}{d\tau} = (u^t, u^i) = \left(\frac{dt}{d\tau}, \frac{dx^i}{d\tau}\right), \tag{4.13}$$

which, in the Eulerean reference frame,[13] reads

$$u'^{\mu} = \frac{(\alpha dt, dx^i + \beta^i dt)}{d\tau} = (\alpha u^t, u^i + \beta^i u^t) = \alpha u^t \left(1, \frac{u^i}{\alpha u^t} + \frac{\beta^i}{\alpha}\right). \tag{4.14}$$

The Lorentz factor between the Eulerean frame and the coordinate frame is given by $W = -n_\mu u^\mu = \alpha u^t = (1 - v^2)^{-1/2}$, where $v^2 = \gamma_{ij} v^i v^j$ is the squared modulus of the 3-velocity of the particle with respect to the Eulerean observer. From the last term in Eq. 4.14, one can define the particle's 3-velocity in the Eulerean frame as

$$v^i = \frac{u^i}{\alpha u^t} + \frac{\beta^i}{\alpha}, \tag{4.15}$$

with the covariant component $v_i = \gamma_{ij} v^j = u_i/(\alpha u^t) = u_i/W$.

When the 3+1 metric in Eq. 4.9 is applied to the Einstein equations, these equations are decomposed into evolution and constraint equations [for a full description of these equations, see, for example, Wilson & Mathews (2003)]. The constraint equations come from projecting the Einstein equations along the unit normal vector. There is a similar decomposition in the case of electromagnetism; Maxwell equations are split into time-independent (divergence) equations that constrain the electric and magnetic fields at an instant time and time-dependent (curl) equations that determine their evolution from one instant time to the next. For both gravitation and electromagnetism, if the constraint equations are satisfied at some initial time, the evolution equations guarantee that they will be satisfied at subsequent times. However, the decomposition of Einstein equations is not unique, thus various 3+1 methods have been developed (e.g., Font 2008). Nevertheless, all those methods should produce the same result. In many cases, the evolution equations are replaced with an evolution system which is specialized to the matter being described. This is also the case of GRMHD, where the evolution equations of GRMHD are based on the 3+1 decomposition of the energy-momentum tensor (fluid plus electromagnetic field tensor).

4.2.2 3+1 decomposition of the energy-momentum tensor

The energy-momentum tensor can be decomposed into quantities which refer to the slice alone. These quantities, which are measured by an Eulerean observer, are:

- the total energy density,
$$E = T^{\mu\nu} n_\mu n_\nu, \tag{4.16}$$
which follows from the fact that the 4-velocity of the Eulerean observer is the unit normal vector $\mathbf{n}$;

- the momentum density in the λ direction, tangent to $\Sigma(t)$,
$$S_\lambda = -T^\mu_\nu n_\mu \gamma^\nu_\lambda \text{ ; and} \tag{4.17}$$

- the spatial stress tensor,
$$S_{\lambda\sigma} = T_{\mu\nu} \gamma^\mu_\lambda \gamma^\nu_\sigma. \tag{4.18}$$

[13] In the Eulerean reference frame, the coordinates of the points P, Q, and R read: $P(t', x'^i)$, $Q(t' + \alpha dt, x'^i)$, and $R(t' + \alpha dt, x'^i + \beta^i dt + dx^i)$.

4.2.3 Perfect fluid approximation

A perfect fluid is defined as having no forces between the particles and no heat conduction or viscosity in the fluid rest frame. In this approximation, the matter is characterized by various thermodynamic quantities, such as the rest-mass density ρ ($\rho = n\, m_{\rm B}$, where n is the baryon number density and $m_{\rm B}$ is the average rest mass of the baryons), the specific internal energy ε, the average pressure p, and the average 4-velocity of the fluid $\mathbf{u}$. These quantities are defined in the rest frame of a fluid element at a point x^μ. It is convenient to use the relativistic specific enthalpy defined as

$$h = 1 + \varepsilon + \frac{p}{\rho}. \tag{4.19}$$

With these ingredients, the energy-momentum tensor for a perfect fluid can be written as

$$T^{\mu\nu}_{\rm fluid} = \rho h u^\mu u^\nu + p g^{\mu\nu}. \tag{4.20}$$

The energy-momentum tensor must be boosted from the fluid frame into the Eulerean frame when the Einstein equations are written in the Eulerean frame.

If the fluid is assumed to be in local thermodynamic equilibrium, one can write an equation of state of the form $p = p(\rho, \varepsilon)$, which relates the pressure with ρ and ε.

In the case of a magnetized fluid, the energy-momentum tensor is obtained by adding the electromagnetic tensor to the fluid tensor (elaborated on later in this chapter).

4.2.4 Evolution of the electromagnetic fields

In this section, the evolution equation of the magnetic field is derived. This equation enters into the GRMHD conservation system of equations. In general relativity, the electromagnetic field is described by the Faraday electromagnetic tensor $F^{\mu\nu}$. This tensor is expressed by the electric field E^μ and the magnetic field B^μ, which are measured by an Eulerean observer (having the 4-velocity n^μ), as

$$F^{\mu\nu} = n^\mu E^\nu - n^\nu E^\mu + n_\lambda \epsilon^{\lambda\mu\nu\sigma} B_\sigma, \tag{4.21}$$

where $\epsilon^{\lambda\mu\nu\sigma}$ is the antisymmetric Levi-Civita tensor density.[14] Both electric and magnetic fields are orthogonal to n^μ ($E^\mu n_\mu = B^\mu n_\mu = 0$), and they are given by

$$E^\mu = F^{\mu\nu} n_\nu \text{ and } B^\mu = \frac{1}{2}\epsilon^{\mu\nu\kappa\lambda} n_\nu F_{\kappa\lambda} = n_\nu\, {}^*F^{\nu\mu}, \tag{4.22}$$

where the quantity

$${}^*F^{\mu\nu} = \frac{1}{2}\epsilon^{\mu\nu\kappa\lambda} F_{\kappa\lambda} \tag{4.23}$$

denotes the dual of electromagnetic field tensor.

[14] The components of the Levi-Civita tensor density are the same in any coordinate system. Antisymmetry means that the tensor changes sign if any two indices are exchanged; e.g., $\epsilon^{\lambda\mu\nu\sigma} = -\epsilon^{\mu\lambda\nu\sigma}$. This tensor density has the values $+1$ for an even permutation of the reference sequence, -1 for an odd permutation of the reference sequence, and 0 if any two indices are the same. One can form an ordinary contravariant tensor by multiplying $\epsilon^{\lambda\mu\nu\sigma}$ by $|g|^{1/2}$, where $g = \det g_{\mu\nu}$ is the determinant of 4-metric (Weinberg 1972).

In ideal MHD, the fluid is considered to be a perfect conductor; that is, the fluid has infinite conductivity, and in order to keep the current finite, the conduction current must vanish,

$$F^{\mu\nu}u_\nu = 0, \tag{4.24}$$

which means that the electric field in the rest frame of the fluid is zero. The electric and magnetic fields measured by a comoving observer are

$$\hat{E}^\mu = F^{\mu\nu}u_\nu \text{ and } \hat{B}^\mu = u_\nu {}^*F^{\nu\mu}. \tag{4.25}$$

The ideal MHD condition (Eq. 4.24) implies that the electric field measured by a comoving observer becomes zero ($\hat{E}^\mu = 0$). Moreover, $\hat{B}^\mu$ is orthogonal to u_μ, i.e. $u_\mu \hat{B}^\mu = 0$. Both the electromagnetic tensor and its dual can be expressed in terms of $\hat{B}^\mu$ as

$$F^{\mu\nu} = u_\lambda \epsilon^{\lambda\mu\nu\sigma}\hat{B}_\sigma \text{ and } {}^*F^{\mu\nu} = \hat{B}^\mu u^\nu - \hat{B}^\nu u^\mu. \tag{4.26}$$

Using the spatial metric in Eq. 4.2 and the fact that $\hat{B}^\mu$ is orthogonal to u_μ, we have $\gamma^\mu_\nu \hat{B}^\nu = \hat{B}^\mu$. From Eqs. 4.22 and 4.26, one can obtain

$$\gamma^\mu_\nu B^\nu = -n_\lambda u^\lambda \hat{B}^\mu. \tag{4.27}$$

Therefore, the magnetic field measured by a comoving observer becomes

$$\hat{B}^\mu = -\frac{\gamma^\mu_\nu B^\nu}{n_\nu u^\nu}, \tag{4.28}$$

whose time and space components are given by

$$\hat{B}^t = \frac{W v_i B^i}{\alpha} \text{ and } \hat{B}^i = \frac{B^i + \alpha \hat{B}^t u^i}{\alpha u^t}. \tag{4.29}$$

The evolution equation for the magnetic field can be obtained in conservation form from the dual of Maxwell's equation,

$$F_{\mu\nu,\lambda} + F_{\lambda\mu,\nu} + F_{\nu\lambda,\mu} = 0, \tag{4.30}$$

which in a coordinate basis reads

$${}^*F^{\mu\nu}_{;\nu} = \frac{1}{\sqrt{|g|}}\frac{\partial}{\partial x^\nu}(\sqrt{|g|}\ {}^*F^{\mu\nu}) = 0. \tag{4.31}$$

Since $\sqrt{|g|} = \alpha\sqrt{\gamma}$ and ${}^*F^{it} = B^i/\alpha$, the time component of Eq. 4.31 gives the divergence-free magnetic field constraint,

$$\frac{1}{\sqrt{|g|}}\frac{\partial}{\partial x^i}(\sqrt{\gamma}\, B^i) = 0, \tag{4.32}$$

whereas the spatial components give the induction equation,

$$\frac{1}{\sqrt{|g|}}\frac{\partial}{\partial t}(\sqrt{\gamma}\, B^i) + \frac{1}{\sqrt{|g|}}\frac{\partial}{\partial x^i}[\sqrt{|g|}\,(u^j \hat{B}^i - u^i \hat{B}^j)] = 0. \tag{4.33}$$

From the spatial part of the comoving magnetic field in Eq. 4.29, one can obtain

$$u^j \hat{B}^i - u^i \hat{B}^j = (\tilde{v}^j B^i - \tilde{v}^i B^j), \tag{4.34}$$

where $\tilde{v}^i = v^i - \beta^i/\alpha$. Therefore, the induction equation can be written as

$$\boxed{\frac{1}{\sqrt{|g|}}\frac{\partial}{\partial t}(\sqrt{\gamma}\,B^i) + \frac{1}{\sqrt{|g|}}\frac{\partial}{\partial x^i}[\sqrt{|g|}\,(\tilde{v}^j B^i - \tilde{v}^i B^j)] = 0}. \tag{4.35}$$

Generally, the electromagnetic tensor reads

$$T^{\mu\nu}_{\rm EM} = \frac{1}{4\pi}\left(F^{\mu\lambda}F^{\nu}_{\lambda} - \frac{1}{4}g^{\mu\nu}F_{\alpha\beta}F^{\alpha\beta}\right), \tag{4.36}$$

which in the ideal MHD condition, can be simply expressed in terms of the magnetic 4-vector $b^\mu = \hat{B}^\mu/\sqrt{4\pi}$ as

$$T^{\mu\nu}_{\rm EM} = b^2 u^\mu u^\nu + \frac{b^2}{2}g^{\mu\nu} - b^\mu b^\nu, \tag{4.37}$$

where $b^2 = b^\mu b_\mu$.

4.2.5 Conservation Equations

The evolution equations for matter can be expressed as the local conservation laws for particle number and energy-momentum. The particle number conservation equation is written as

$$(\rho u^\mu)_{;\mu} = 0, \tag{4.38}$$

where ρ is the rest-mass density of the fluid and u^μ is its 4-velocity. Equation 4.38 can be written in a coordinate basis as

$$\frac{1}{\sqrt{|g|}}\frac{\partial}{\partial x^\mu}(\sqrt{|g|}\,\rho u^\mu) = 0. \tag{4.39}$$

On the other hand, the energy-momentum conservation equation is given by $T^{\mu\nu}_{;\nu} = 0$, which in a coordinate basis can be written as

$$\frac{1}{\sqrt{|g|}}\frac{\partial}{\partial x^\mu}(\sqrt{|g|}T^{\mu\nu}) = 0, \tag{4.40}$$

and

$$\frac{1}{\sqrt{|g|}}\frac{\partial}{\partial t}(\sqrt{|g|}T^{t\nu}) + \frac{1}{\sqrt{|g|}}\frac{\partial}{\partial x^i}(\sqrt{|g|}T^{i\nu}) - \Gamma^{\nu}_{\mu\sigma}T^{\mu\sigma} = 0, \tag{4.41}$$

where $\Gamma^{\nu}_{\mu\sigma}$ is the Christoffel symbol.

For a magnetized fluid, the energy-momentum tensor is obtained by adding the energy-momentum tensor of the fluid to that of the electromagnetic field,

$$T^{\mu\nu} = T^{\mu\nu}_{\rm fluid} + T^{\mu\nu}_{\rm EM}. \tag{4.42}$$

Now, if we consider Eqs. 4.20 and 4.37, the total energy-momentum tensor becomes

$$T^{\mu\nu} = (\rho h + b^2)u^\mu u^\nu + \left(p + \frac{b^2}{2}\right)g^{\mu\nu} - b^\mu b^\nu. \tag{4.43}$$

In the case of 3+1 formalism, one can define the following **conserved variables**:[15]

$$\boxed{\begin{aligned} &D = -J^{\mu} n_{\mu} = -\rho u^{\mu} n_{\mu} = \rho W \,, \\ &S_j = \alpha T^{t}_{j} = (\rho h + b^2) W^2 v_j \,, \\ &E = T^{\mu\nu} n_{\mu} n_{\nu} = \alpha^2 T^{tt} = (\rho h + b^2) W^2 - \left(p + \frac{b^2}{2} \right) \end{aligned}}, \tag{4.44}$$

where $J^{\mu} = \rho u^{\mu}$ denotes the rest-mass flux. For numerical calculations, it is useful to include a derived conserved variable,

$$\tau = E - D \,, \tag{4.45}$$

instead of the total energy density E.

Using the conserved variables, one can obtain the conservation laws of

- the baryon number conservation,

$$\boxed{\frac{1}{\sqrt{|g|}} \frac{\partial}{\partial t} (\sqrt{\gamma}\, D) + \frac{1}{\sqrt{|g|}} \frac{\partial}{\partial x^i} (\sqrt{|g|}\, D \tilde{v}^i) = 0}; \tag{4.46}$$

- the momentum equation, from the spatial components of the energy-momentum conservation equation,

$$\boxed{\frac{1}{\sqrt{|g|}} \frac{\partial}{\partial t} (\sqrt{\gamma}\, S_j) + \frac{1}{\sqrt{|g|}} \frac{\partial}{\partial x^i} (\sqrt{|g|}\, T^{i}_{j}) = T^{\mu\nu} \left(\frac{\partial g_{\nu j}}{\partial x^{\mu}} - \Gamma^{\sigma}_{\nu\mu} g_{\sigma j} \right)}; \tag{4.47}$$

- the energy equation, from the time component of the energy-momentum conservation equation,

$$\boxed{\frac{1}{\sqrt{|g|}} \frac{\partial}{\partial t} (\sqrt{\gamma}\, \tau) + \frac{1}{\sqrt{|g|}} \frac{\partial}{\partial x^i} [\sqrt{|g|}\, (\alpha T^{ti} - D \tilde{v}^i)] = \alpha \left(T^{\mu t} \frac{\partial \ln \alpha}{\partial x^{\mu}} - T^{\mu\nu} \Gamma^{t}_{\nu\mu} \right)}. \tag{4.48}$$

To form the GRMHD system of equations, the equations 4.46, 4.47, and 4.48 are augmented by the induction equation (Eq. 4.35). To complete the system of equations, one needs to specify the fluid equation of state (EOS); a Γ-law EOS is assumed next, thus

$$p = (\Gamma - 1) \rho u, \tag{4.49}$$

where Γ is the adiabatic index.

In a compact form, the evolution equations of GRMHD can be written as

$$\boxed{\frac{1}{\sqrt{|g|}} \frac{\partial (\sqrt{\gamma}\, \mathbf{U})}{\partial t} + \frac{1}{\sqrt{|g|}} \frac{\partial (\sqrt{|g|}\, \mathbf{F})}{\partial x^i} = \mathbf{S}}, \tag{4.50}$$

[15] The derivation of the conserved variables as well as the conservation equations are provided in Appendix 2.

where the quantities **U** (conserved variables), **F** (fluxes), and **S** (source terms) are

$$\mathbf{U} = \begin{bmatrix} D \\ S_j \\ \tau \\ B^i \end{bmatrix}, \tag{4.51}$$

$$\mathbf{F} = \begin{bmatrix} D\tilde{v}^i \\ T^i_j \\ \alpha T^{ti} - D\tilde{v}^i \\ \tilde{v}^i B^j - \tilde{v}^j B^i \end{bmatrix}, \tag{4.52}$$

and

$$\mathbf{S} = \begin{bmatrix} 0 \\ T^{\mu\nu}\left(\frac{\partial g_{\nu j}}{\partial x^\mu} - \Gamma^\sigma_{\nu\mu} g_{\sigma j}\right) \\ \alpha\left(T^{\mu t}\frac{\partial \ln\alpha}{\partial x^\mu} - T^{\mu\nu}\Gamma^t_{\nu\mu}\right) \\ 0^i \end{bmatrix}, \tag{4.53}$$

where $0^i \equiv (0,0,0)^{\mathrm{T}}$.

The GRMHD system of equations (Eq. 4.50) is a set of eight non-linear hyperbolic partial differential equations (PDEs) written in conserved form.[16] In general, the hyperbolic equations represent wave propagation. The main difficulty to be encountering when solving non-linear hyperbolic PDEs is the spontaneous development of discontinuous solutions even for smooth initial data (e.g, when a supersonic flow has shock waves). Numerical methods in conservation form are likely to be employed in GRMHD for the following reason: the conservation form is preserved during the integration of the equations and assures the correct jump conditions across discontinuities (but only if there are no phase transitions, like in an ionization front). The behavior of the conservation form is based on the theorem by Lax & Wendroff (1960), which states that if the numerical solution converges, it converges to a weak solution (solution with shocks and contact discontinuities) of the original system of equations. However, weak solutions are not uniquely determined by their initial values, so in order to find a physically admissible solution an additional condition must be satisfied such as the entropy condition.[17] A wide variety of different methods have been employed to obtain numerical solutions to the systems of non-linear hyperbolic PDEs. Among them, we mention two classes of shock-capturing methods: (i) high-resolution shock-capturing schemes which are based on Riemann solvers[18] and make use of the characteristic information of the system, so that the schemes take into account the direction of signal propagation (or wave propagation), e.g., McKinney & Gammie (2004), Mizuno et al. (2006a); and (ii) high-order methods which do not explicitly use the information on wave propagation. The

[16]Strict conservation law is possible only in flat space-time. For Minkowski metric, the source term **S** vanishes itself.

[17]The entropy of any fluid element should increase when running through a discontinuity.

[18]An exact (and an approximate) solution to the Riemann problem on the cell interfaces describes the evolution of an initial discontinuity at these interfaces which is then used to evaluate the numerical fluxes. To compute the fluxes, one must differ between the left-going and right-going waves with respect to the cell interface, which can be regarded as an upwind procedure. For details on Riemann solvers see, e.g., Toro (2009).

methods of the first class are said to be upwind-based methods.[19] The schemes of the second class are based on either high-order central TVD[20] schemes as the Lax-Wendroff scheme with an additional diffusion term (e.g., Koide et al. 1999), or on non-oscillatory high-order extensions of first-order central schemes as the Lax-Friedrichs scheme (see Font 2008, and reference therein).

Any conserved GRMHD scheme updates the vector of conserved variables (**U**, Eq. 4.51), which contains eight variables (D, S_j, τ, and B^i). However, to model the flow the "primitive" (or physical) variables (density, pressure, and velocity components of the flow) must be known. There is no analytic solution to the problem of deriving primitive variables from the conserved variables, therefore root-finding algorithms must be employed.

The wave property of the GRMHD equations is intimately related to the construction, analysis, and implementation of the corresponding discrete approximations, although the eigenstructure of the problem, i.e., the characteristic decomposition of the flux **F**, may not be explicitly known. This approach is also specific to Davis' simplified total-variation-diminishing (STVD) method, which is employed by Koide et al. for their GRMHD simulation code (Section 4.3.3).

4.3 General relativistic magnetohydrodynamics simulation code (Koide et al.)

As we already mentioned, the first GRMHD code for simulating jet formation from accreting BHs was developed by Koide et al. (1999) using the conservation form of the ideal GRMHD equations on fixed geometry (either Schwarzschild or Kerr). The code can be applied to the study of jets propagation through a magnetized corona, as well as the early stages of jet formation from (non-)rotating BHs. The code is very stable when jets with a Lorentz factor less than 10 are simulated.

Using Koide et al. simulation code, we present numerical results of jet formation from rapidly-spinning BHs, $a_* = 0.95$, focusing on the effect of the BH rotation when simplified microphysics is used; i.e., processes such as neutrino cooling and photodisintegration are ignored.

4.3.1 Metric and coordinates

As the accreting mass is sufficiently small on the simulation timescale, the space-time metric does not evolve with time. The space-time is described by the metric tensor $g_{\mu\nu}$, which is expressed in Boyer-Lindquist coordinates $(x^0, x^1, x^2, x^3) = (ct, r, \theta, \phi)$, with a modified tortoise coordinate in the radial direction, $x = \ln(r/r_{\rm S})$. This coordinate transformation compensates to some degree the Boyer-Lindquist coordinate singularity at the BH horizon by increasing the numerical spatial resolution as one approaches the BH horizon. The line element can be written as

$$ds^2 = g_{\mu\nu}dx^\mu dx^\nu = -h_0^2(cdt)^2 + \sum_{i=1}^{3}[h_i^2(dx^i)^2 - 2h_i^2\omega_i dt dx^i], \tag{4.54}$$

[19] The term upwind schemes, as well as central (or symmetric) schemes, refers to spatial discretization.

[20] The order of accuracy for time-accurate calculations refers to both the time and spatial discretization. Once again, TVD stands for total variation diminishing, and it will be discussed later.

where

$$g_{00} = -h_0^2\,, \quad g_{ii} = h_i^2\,, \quad g_{i0} = g_{0i} = -h_i^2\omega_i/c. \tag{4.55}$$

Using the definition of the lapse function α and the shift velocity β^i as

$$\alpha = \sqrt{h_0^2 + \sum_{i=1}^{3}\left(\frac{h_i\omega_i}{c}\right)^2}, \tag{4.56}$$

$$\beta^i = \frac{h_i\omega_i}{c\,\alpha}, \tag{4.57}$$

the line element becomes

$$ds^2 = -\alpha^2(cdt)^2 + \sum_{i=1}^{3}(h_i dx^i - c\beta\alpha dt)^2. \tag{4.58}$$

The contravariant metric components are then

$$g^{00} = -\frac{1}{\alpha^2}\,, \quad g^{i0} = g^{0i} = -\frac{1}{\alpha^2}\frac{\omega_i}{c}\,, \quad g^{ij} = \frac{1}{h_i h_j}(\delta^{ij} - \beta^i\beta^j), \tag{4.59}$$

where δ^{ij} is the Kronecker's δ symbol.

In the Boyer-Lindquist coordinates, the metric of Kerr space-time is written as

$$h_0 = \sqrt{1 - \frac{2r_{\rm g}r}{\Sigma}}, \quad h_1 = \sqrt{\frac{\Sigma}{\Delta}}, \quad h_2 = \sqrt{\Sigma}, \quad h_3 = \sqrt{\frac{A}{\Sigma}}\sin\theta, \tag{4.60}$$

$$\omega_1 = \omega_2 = 0, \quad \omega_3 = \frac{2cr_{\rm g}^2 a_* r}{A}, \tag{4.61}$$

where $\Delta = r^2 - 2r_{\rm g}r + (a_* r_{\rm g})^2\cos^2\theta$, $\Sigma = r^2 + (a_* r_{\rm g})^2\cos^2\theta$, and $A = \{r^2 + (a_* r_{\rm g})^2\}^2 - \Delta(a_* r_{\rm g})^2\sin^2\theta$ are the metric functions (Section 1.3). The lapse function is $\alpha = \sqrt{\Delta\Sigma/A}$ and the radius of the event horizon is $r_{\rm H} = r_{\rm g}(1 + \sqrt{1 - a_*^2})$.

4.3.2 General relativistic magnetohydrodynamics equations in zero angular momentum observer's frame

Now, using the notations that were introduced in the previous section, the GRMHD equations (Eq. 4.50) in the fiducial observer (FIDO) frame, which once again is a locally inertial frame, are rewritten following Koide (2003) and Koide et al. (2006). Once again, FIDOs are the ZAMOs in the case of the Kerr metric. Therefore, the GRMHD equations are expressed in a form based on fluid and field quantities which are measured by ZAMOs directly, the ZAMO-measured magnetic field and fluid velocity, and the mass density and pressure as seen in the comoving frame.[21]

[21] An observer in the comoving frame rides on the fluid and sees events locally. Since any quantity observed in this frame is by nature a fluid characteristic, it is usually called proper value.

The conserved variables[22] (Eq. 4.44) are defined as a function of the variables measured in the ZAMO's frame (denoted with hat):

$$\begin{aligned} D &= \gamma\rho\,, \\ \hat{P}^i &= \frac{1}{c^2}\mathfrak{h}\gamma^2\hat{v}^i + \frac{1}{c^2}\left(\hat{\mathbf{E}}\times\hat{\mathbf{B}}\right)_i\,, \\ \epsilon &= \mathfrak{h}\gamma^2 - p - Dc^2 + \frac{\hat{B}^2}{2} + \frac{\hat{E}^2}{2c^2}\,, \end{aligned} \tag{4.62}$$

where $\hat{P}^i$ is the momentum density and ϵ is the total energy density. The boosting Lorentz factor from the coordinate frame to the ZAMO's frame is $\hat{\gamma} \equiv \gamma = [1 - \sum_{i=1}^{3}(\hat{v}^i/c)^2]^{-1/2}$, where $\hat{v}^i$ is the three-velocity and the relativistic enthalpy density is $h = \rho c^2 + \Gamma p/(\Gamma - 1) = e_{\rm int} + p$. The electric charge density is $\hat{\rho}_{\rm e} \equiv \rho_{\rm e} = c^{-1}\alpha J^0$, where J^0 is the time component of the electric four-current density, $J^\mu = (J^0, J^1, J^2, J^3)$. The total energy-momentum tensor (fluid + electromagnetic field) is

$$\hat{T}^{ij} = p\delta^{ij} + \frac{h}{c^2}\gamma^2\hat{v}^i\hat{v}^j + \left(\frac{\hat{B}^2}{2} + \frac{\hat{E}^2}{2c}\right)\delta^{ij} - \hat{B}_i\hat{B}_j - \frac{\hat{E}_i\hat{E}_j}{c^2}, \tag{4.63}$$

where δ^{ij} is the Kronecker symbol.

With these ingredients, the GRMHD equations in ZAMO's frame become

$$\frac{\partial D}{\partial t} = -\frac{1}{h_1h_2h_3}\sum_i \frac{\partial}{\partial x^i}\left[\frac{\alpha h_1h_2h_3}{h_i} D\left(\hat{v}^i + c\beta^i\right)\right], \tag{4.64}$$

$$\begin{aligned} \frac{\partial \hat{P}^i}{\partial t} = &- \frac{1}{h_1h_2h_3}\sum_j \frac{\partial}{\partial x^j}\left[\frac{\alpha h_1h_2h_3}{h_j}\left(\hat{T}^{ij} + c\beta^j\hat{P}^i\right)\right] - \left(\epsilon + Dc^2\right)\frac{1}{h_i}\frac{\partial \alpha}{\partial x^i} \\ &+ \alpha f^i_{\rm curv} - \sum_j \hat{P}^j\sigma_{ji} + \sum c\alpha\beta^j\left(G_{ij}\hat{P}^i - G_{ji}\hat{P}^j\right)\,, \end{aligned} \tag{4.65}$$

$$\begin{aligned} \frac{\partial \epsilon}{\partial t} = &- \frac{1}{h_1h_2h_3}\sum_i \frac{\partial}{\partial x^i}\left[\frac{\alpha h_1h_2h_3}{h_i}c^2\left(\hat{P}^i - D\hat{v}^i + \frac{\beta^i}{c}\epsilon\right)\right] \\ &- \sum_i c^2\hat{P}^i\frac{1}{h_i}\frac{\partial \alpha}{\partial x^i} - \sum_{i,j}\hat{T}^{ij}\sigma_{ij} - \sum_i c\alpha\beta^i f^i_{\rm curv}\,, \end{aligned} \tag{4.66}$$

$$\frac{\partial \hat{B}_i}{\partial t} = -\frac{h_i}{h_1h_2h_3}\sum_{j,k}\epsilon^{ijk}\frac{\partial}{\partial x^j}\left[\alpha h_k\left(\hat{E}_k - \sum_{l,m}\epsilon^{klm}c\beta^l\hat{B}_m\right)\right]. \tag{4.67}$$

The system of equations consists of eight conservation laws. To them, the constraint equation for the magnetic field must be added,

$$\sum_i \frac{1}{h_1h_2h_3}\frac{\partial}{\partial x^i}\left(\frac{h_1h_2h_3}{h_i}\hat{B}_i\right) = 0. \tag{4.68}$$

[22] Here, we use the notations by Koide (2003) for the conserved variables.

The electric field, the electric charge density, and the electric current density are calculated using the following expressions:

$$\hat{E}_i = -\sum_{j,k} \epsilon_{ijk} \hat{v}^j \hat{B}_k, \tag{4.69}$$

$$\rho_{\rm e} = \sum_i \frac{1}{c^2} \frac{1}{h_1 h_2 h_3} \frac{\partial}{\partial x^i} \left(\frac{h_1 h_2 h_3}{h_i} \hat{E}_i \right), \tag{4.70}$$

$$\alpha \left(\hat{J}^i + \rho_{\rm e} c \beta^i \right) + \frac{1}{c^2} \frac{\partial \hat{E}_i}{\partial t} = \sum_{j,k} \frac{h_i}{h_1 h_2 h_3} \epsilon^{ijk} \frac{\partial}{\partial x^j} \left[\alpha h_k \left(\hat{B}_k + \sum_{l,m} \epsilon_{klm} \beta^l \frac{\hat{E}_k}{c} \right) \right], \tag{4.71}$$

where $f^i_{\rm curv} \equiv \sum_i (G_{ij} \hat{T}^{ij} - G_{ji} \hat{T}^{ji})$, $G_{ij} \equiv -\frac{1}{h_i h_j} \frac{\partial h_i}{\partial x^j}$, and $\sigma_{ij} \equiv \frac{1}{h_i} \frac{\partial}{\partial x^j} (c \alpha \beta^i)$.

4.3.3 Description of the code

The scheme employed by Koide et al. to solve the system of GRMHD equations belongs to the class of high-order central schemes. It is a two-step Lax-Wendroff scheme with a TVD diffusion term. The algorithm, which is known as the simplified total-variation-diminishing (STVD) method, was developed by Davis (1984) as a shock capturing scheme for hydrodynamics, and adapted to jet formation from accreting BHs by Koide et al. For the STVD method to work, only the maximum speed of the waves is required, no Jacobian and characteristic decompositions are needed. For this reason, the STVD method is simple and less expensive, especially when it is applied to multi-dimensional problems. More on the advantages as well as the disadvantages of applying the STVD method see towards the end of the chapter.

Coordinate system

The code can be used in a wide variety of coordinate systems: (i) Cartesian coordinates; (ii) cylindrical coordinates (also in the general relativistic case); (iii) spherical coordinates; (iv) Boyer-Lindquist coordinates for Schwarzschild BH; and (v) Boyer-Lindquist coordinates for Kerr BH. Evidently, the last two coordinate systems are specific to jet formation from accreting BHs. The code written in Kerr-Schild coordinates is work in progress.

Discretization of the GRMHD equations and the STVD method

The GRMHD system of equations (Eq. 4.50) is a set of non-linear hyperbolic PDEs written in conserved form. Let us consider the conservation equation in one dimension,

$$\frac{\partial u(x,t)}{\partial t} + \frac{\partial f(u,t)}{\partial x} = 0, \tag{4.72}$$

where $\mathbf{u}$ and $\mathbf{f}$ are the state and flux vectors, and let u^n_j be the numerical approximation of $u(x,t)$ at $x = j\Delta x$ and $t = n\Delta t$. The subscript index j runs in the spatial direction, the superscript index n runs for time, Δx is the grid size, and Δt is the time step (see Fig. 4.4).

Any numerical solution to systems of PDEs is based on discretization of the system. For a finite-difference discretization, one must replace the derivatives with approximate, algebraic difference quotients, which are expressed in terms of the state variables at two or more grid points, u_j^n. To build a numerical scheme, it is necessarily to construct the numerical fluxes (starting from the grid point values u_j^n), which must be consistent approximations to the physical fluxes $\mathbf{f}$ across the cell interfaces. Since the problem is time dependent, a time-marching procedure must be used to advance the solution from one time level to the next, such that the solution at a new time can be obtained from the approximations in the previous time steps. To march the solution in time, Koide et al. used a variation of the **two-step Lax-Wendroff scheme**, which is second-order accurate (in space and time).

Numerical methods are devised with specific properties of accuracy, efficiency, stability (in particular, lack of spurious oscillations), etc. Non-linear hyperbolic equations admit discontinuous solutions (called weak solutions), which can arise spontaneously after a finite time even for smooth initial data. Finite differencing across shock and contact discontinuities will inevitably cause oscillations, which can lead to inaccuracies, spurious physical effects, and numerical instabilities. Therefore, numerical schemes must be able to capture any discontinuity that might arise in the solution. By means of difference equations, finite-difference solutions represent, in fact, inexact solutions to the governing PDEs, but exact solutions to the slightly modified PDEs. Such equations are called modified equations, and they contain second, third, or higher-order derivatives of the state variables. For first-order solutions (or monotone schemes), the truncation error contains second-order derivatives in the state variables which act as dissipative terms. These dissipative terms are responsable for producing smooth numerical solutions free of the spurious oscillations. Therefore, the dissipation is needed for the stability of the scheme, but at the same time one may wish to get rid of this dissipation for obtaining good quality solutions. Unfortunately, the first-order schemes usually create too much dissipation which smooth the solution excessively, and cannot produce accurate solutions for complex flow problems. In contrast, higher-order accurate schemes have too little numerical dissipation, and many of them have third derivatives in the modified equation which cause numerical dispersion. The numerical dispersion produces a distortion of the propagation of different phases of a wave, which shows up as wiggles in front of and behind the wave (e.g., Anderson 1995). The error can propagate to smooth regions of the flow and corrupt the accuracy of the solution on a global level. The combined effect of dissipation and dispersion is often referred to as diffusion. Whereas the first-order methods produce physically plausible solutions with poor accuracy, the higher-order methods, on the other hand, may produce solutions in the smooth regions with non-physical fluctuations caused by discontinuities (e.g., reflection at boundaries). A way out of this situation was to design higher-order shock-capturing methods, which are higher-order in the smooth part of the flow with numerical dissipation only in the neighborhood of a discontinuity. Higher-order TVD methods are based on non-linear dissipation terms, which means that the diffusion coefficient depends on the local behavior of the solution, so that the amount of dissipation varies from one grid point to another and usually consists of automatic feedback mechanism without adjustable parameters.[23] These

[23]For classical schemes, the dissipation term (also called artificial viscosity) is either linear, such that the same amount is applied at all grid points, or contain of adjustable parameters (see Yee 1989, and reference therein). In this case, it is difficult to find an appropriate form that introduces just enough dissipation to preserve monotonicity without causing unnecessary smearing of the solutions. For this reason, it is usually not applied to problems with very strong shocks. Another difficulty is the reflection of weak waves from the

methods often use limiters which impose constraints on the gradient of the state variables (slope limiters) or on the flux function (flux limiters).

The class of TVD methods originated in a series of papers by Harten (1983, 1984), Davis (1984), Roe (1984), Sweby (1984), Osher & Chakravarthy (1984), Yee (1985), which are based on the modified flux approach. Although Harten (1983) has introduced the concept of TVD to characterize oscillation-free systems, Harten's method has little in common with other TVD methods (Laney 1998). The stability condition for the flux-limited method design by Harten is, in fact, a stronger stability condition than the TVD condition. The TVD condition is a non-linear stability condition, so that the total variation of a discrete solution is controlled in a non-linear way in order to prevent the appearance of any new extremum. The total variation of the solution, defined as the summed differences $TV(u^n) = \sum_j |u^n_{j+1} - u^n_j|$, is a measure of the overall amount of oscillations in solution. This can be seen in the equivalent definition $TV(u^n) = 2(\sum_j u_{\max} - \sum_j u_{\min})$, where each maximum is counted positively twice and each minimum is counted negatively twice. The formation of spurious oscillations can contribute with new maxima and minima, so that the total variation will increase. So, the TVD condition specifies that, in order to have oscillation-free solutions, the total variation should not grow for any initial condition. It reads

$$\sum_j |u^{n+1}_{j+1} - u^{n+1}_j| \leqslant \sum_j |u^n_{j+1} - u^n_j|. \tag{4.73}$$

The smaller the decrease is in the total variation, the smaller the error is. Nevertheless, the term "TVD" refers to a wide range of modern methods, such as the already mentioned flux-limited methods, and do not necessarily focus on the TVD stability condition, but usually on stronger non-linear stability conditions. These methods were developed after the invention of the term TVD in 1983 (Laney 1998). For more hints on the TVD methods see, for instance, van Leer (2006).

Taking the two-step Lax-Wendroff scheme as an example, the flow tends to be discontinuous at the time-centered cell interfaces, posing particular problems to the computation of the numerical fluxes. These can be avoided using a variant of the two-step Lax-Wendroff scheme such as the MacCormack (1971) method, which is a two-step predictor-corrector algorithm. The MacCormack method reduces to the original Lax-Wendroff scheme in the linear case $\mathbf{f}(\mathbf{u}) = a\mathbf{u}$, with a a constant matrix. Although the MacCormack method suffers as well from oscillatory behavior of the solution near discontinuities and points of extrema, the oscillations can be suppressed when using a TVD method. The MacCormack method can be easily implemented for non-linear problems since it does not require the calculation of the Jacobian matrix of $\mathbf{f}$, $\partial\mathbf{f}/\partial\mathbf{u}$.

The STVD method developed by Davis (1984) for strong shocks is a **variation of the two-step Lax-Wendroff scheme with an additional non-linear term**, using a flux-limited approach (Eq. 4.78). Therefore, the solution is free of spurious oscillations without losing the scheme accuracy in other regions of the flow. The time step is constrained by the Courant-Friedrichs-Lewy [CFL, Courant et al. (1928)] stability condition $c\Delta t/\Delta x < 1$. [See also Courant & Friedrichs (1977) and Richtmyer & Morton (1994)]. A description of the STVD scheme can be also find in Koide et al. 1999 (Appendix D). The following is a presentation of the STVD scheme.

---

boundary of the simulation box, which then get strengthened on axis.

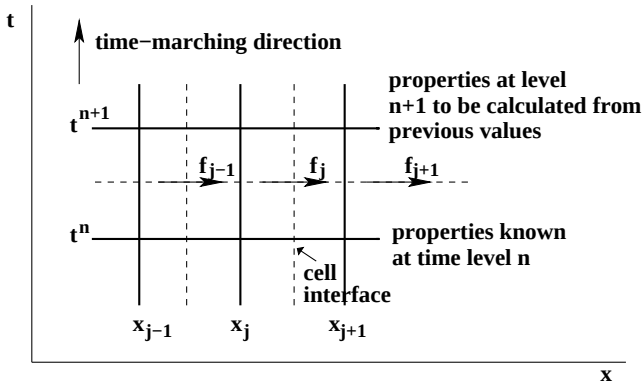

Figure 4.4: Representation of the numerical grid.

Let us consider the conservation equation in one dimension (Eq. 4.72), and let $\kappa = \Delta t/\Delta x$ be the grid ratio (Fig. 4.4). The procedure of updating one time step is based on a sequence of two sub-steps in which the spatial derivatives are taken in alternate directions (backwards and forward, respectively),

$$\begin{aligned} u_j^{(1)} &= u_j^n - \kappa\left(f_j^n - f_{j-1}^n\right), \\ u_j^{(2)} &= \frac{1}{2}\left[u_j^n + u_j^{(1)} - \kappa\left(f_{j+1}^{(1)} - f_j^{(1)}\right)\right], \end{aligned} \tag{4.74}$$

so that the updated solution is given by

$$u_j^{n+1} = u_j^{(2)} + D_{j+1/2}^n - D_{j-1/2}^n, \tag{4.75}$$

where the TVD correction term is added to the last step to eliminate oscillations. The TVD correction term is given by

$$D_{j+1/2}^n = \left[\bar{K}(\nu, r_j^+) + \bar{K}(\nu, r_{j+1}^+)\right]\left(u_{j+1}^n - u_j^n\right), \tag{4.76}$$

with $\nu = \max_m(|c_m|)\kappa$, where c_m is the speed of each wave. So, the scheme is TVD under the CFL stability condition. The coefficients in equation 4.76 are given by

$$\bar{K}^{\pm}(\nu, r_j^{\pm}) = 0.5\, C(\nu)\left[1 - \phi(r^{\pm})\right], \tag{4.77}$$

where ϕ is the flux limiter function, which is defined as

$$\phi(r) = \begin{cases} \min(2r, 1) & \text{for } r > 0, \\ 0 & \text{for } r \leqslant 0, \end{cases} \tag{4.78}$$

and

$$C(\nu) = \begin{cases} \nu(1-\nu) & \text{for } \nu \leqslant 0.5, \\ 0.25 & \text{for } \nu > 0.5, \end{cases} \tag{4.79}$$

$$r_j^+ = \frac{(\Delta u_{j-1/2}^n, \Delta u_{j+1/2}^n)}{(\Delta u_{j+1/2}^n, \Delta u_{j+1/2}^n)}, \tag{4.80}$$

$$r_j^- = \frac{(\Delta u_{j-1/2}^n, \Delta u_{j+1/2}^n)}{(\Delta u_{j-1/2}^n, \Delta u_{j-1/2}^n)}, \tag{4.81}$$

where (.,.) denotes the inner product in $\mathbf{R}^m$, and $\Delta u^n_{j+1/2} = u^n_{j+1} - u^n_j$.

Koide et al. extended the STVD method to a 2-D scheme through the use of the splitting method. This procedure introduces a weak checkerboard numerical instability, which is avoid when the two coefficients $\bar{K}^+$ and $\bar{K}^-$ are combined into a single coefficient $\bar{K}$ defined as

$$\bar{K}(\nu, r^+, r^-) = 0.5\, C(\nu)\, \left[1 - \phi(r^+, r^-)\right], \tag{4.82}$$

with

$$\phi(r^+, r^-) = \max[0, \min(2r^+, r^-, 1), \min(2r^-, r^+, 1)]. \tag{4.83}$$

Method to keep the magnetic field divergence-free

Regarding the evolution of the magnetic field, the induction equation is already part of the GRMHD equation system (Eq. 4.51). The number of the GRMHD equations is reduced from eight to five when the components of the magnetic field are obtained analytically. Here, the magnetic field is initially uniform, as seen by observers at infinity, being represented by Wald's solution (1974). However, the divergence free condition must be maintained throughout the whole computation. Koide et al. uses the so-called magnetic-field cleaning method, a procedure through which the components of the magnetic field are re-defined at each time step.

Method to recover the primitive variables from the conserved variables

The quantities that are updated during the integration of GRMHD equations are the conserved variables. However, one must know the primitive variables in order to describe the flow, and so the primitive variables must be computed as a function of conserved variables at each time step. All conservation GRMHD schemes require methods to transform from primitive variables to conserved variables and vice-versa. The direct transformation (primitive variables $\rightarrow$ conserved variables) is easily obtained using the set of equations 4.62. Instead, the inverse transformation (conserved variables $\rightarrow$ primitive variables) usually involve the numerical solutions of non-linear algebraic equations. There is more than one way to do this. The method which is used by Koide et al. to recover the primitive variables from the conserved variables solves numerically two non-linear, simultaneous algebraic equations with unknown variables $x \equiv \gamma - 1$ and $y \equiv \gamma(\mathbf{v}\cdot\mathbf{B})/c^2$,

$$\begin{aligned} & x\,(x+2)\left[\Gamma R x^2 + (2\Gamma R - d)x + \Gamma R - d + u + \tfrac{\Gamma}{2}y^2\right]^2 \\ &= \left(\Gamma x^2 + 2\Gamma x + 1\right)^2 \left[f^2(x+1)^2 + 2\sigma y + 2\sigma x y + b^2 y^2\right] \text{ and} \end{aligned} \tag{4.84}$$

$$\begin{aligned} & \left[\Gamma\left(R - b^2\right)x^2 + \left(2\Gamma R - 2\Gamma b^2 - d\right)x + \Gamma R - d + u - b^2 + \tfrac{\Gamma}{2}y^2\right] y \\ & \qquad = \sigma\,(x+1)\left(\Gamma x^2 + 2\Gamma x + 1\right), \end{aligned} \tag{4.85}$$

where $R = D + \epsilon/c^2$, $d = (\Gamma - 1)D$, $u = (1 - \Gamma/2)\hat{B}^2/c^2$, $f = \hat{\mathbf{P}}/c$, $b = \hat{\mathbf{B}}/c$, and $\sigma = \hat{\mathbf{B}}\cdot\hat{\mathbf{P}}/c^2$. Equations 4.84 and 4.85 are solved at each cell using a two-variable Newton-Raphson iteration method.

Validation tests

The code is checked by undergoing various test calculations: (i) the steady state infall of a finite pressure gas into the BH (Bondi flow), which is approximately in free fall and presents a transonic solution; (ii) the transonic solution with a shock; (iii) the Keplerian motion in a free-fall corona; (iv) the sub-Keplerian motion in a free-fall corona; and (v) the Keplerian motion in a hydrostatic corona (Koide et al. 1999).

Transonic solution for a free-fall flow

Following Koide et al. (1999), a steady state infall of a finite pressure gas onto the BH (which, in approximation, is a free-fall flow) can be described by the solution of Bondi & Hoyle (1944). The gas inflow is supposed to be spherical symmetric with a polytropic equation of state, $p \propto \rho^{\Gamma}$. The gas equation of motion can be written as a function of two constant of motion, F (a sort of adiabatic invariant) and respectively H ($\sim$ specific enthalpy):

$$F = \left(\frac{H}{\alpha\gamma} - 1\right)\left(\alpha r^2 \gamma \frac{v}{c}\right)^{\Gamma-1}, \tag{4.86}$$

where, once again, α is the lapse function and γ is the Lorentz factor, and

$$H = \alpha_0\gamma_0\left(1 + \frac{\Gamma}{\Gamma-1}\frac{p_0}{\rho_0 c^2}\right), \quad F = \frac{\Gamma}{\Gamma-1}\frac{p_0}{\rho_0 c^2}\left(\alpha_0 r_0^2 \gamma_0 \frac{v_0}{c}\right)^{\Gamma-1}, \tag{4.87}$$

where α_0, γ_0, p_0, ρ_0, and v_0 are evaluated at an arbitrary point $r = r_0$.

For a given H and Γ, the equation of motion $F(v, r)$ admits a transonic solution, which in a radial distribution of the flow velocity passes through the sonic point from the subsonic to supersonic regions. The sonic point is obtained by solving

$$\frac{\partial F}{\partial \gamma} = 0, \quad \frac{\partial F}{\partial \alpha} = 0. \tag{4.88}$$

From the first equation, one obtains the sonic flow condition: $v = v_{\rm s} = (\Gamma p/h)^{1/2} c$, where h, once again, denotes the relativistic enthalpy, $h \equiv \rho c^2 + \Gamma p/(\Gamma - 1)$. When solving for both equation, one can obtain the following reduced equation

$$\left(H^2 - 1\right)x^3 + \left(\frac{9}{4} - 2gH^2\right)x^2 + \left(H^2 g^2 - \frac{3^3}{4^2}\right)x + \left(\frac{3}{4}\right)^3 = 0, \tag{4.89}$$

where $x \equiv r/r_{\rm S}$ and $g \equiv (3\Gamma - 2)/4(\Gamma - 1)$. Therefore, the velocity of the flow at a specific $r = x\, r_{\rm S}$ is determined by $v = v_{\rm s}$ with $\alpha = H(\gamma^{-2} + \Gamma - 2)/[(\Gamma - 1)\gamma]$.

Normalizations

For the thermal, magnetic, and rotational energy, the following non-dimensional parameters are used:

$$E_{\rm th} = \frac{v_{\rm s0}^2}{v_{\rm K0}^2}, \quad E_{\rm mag} = \frac{v_{\rm A0}^2}{v_{\rm K0}^2}, \quad E_{\rm rot} = \frac{v_\phi^2}{v_{\rm K0}^2}, \tag{4.90}$$

where v_{s0} is the relativistic sound speed,

$$v_{s0} = c\sqrt{\frac{\Gamma p_0}{\rho_0 c^2 + \Gamma p_0/(\Gamma - 1)}}, \tag{4.91}$$

v_{A0} is the Alfvén velocity,

$$v_{A0} = c\frac{B_0}{\sqrt{\rho_0 c^2 + \Gamma p_0/(\Gamma - 1) + B_0^2}}, \tag{4.92}$$

and v_{K0} is the relativistic Keplerian velocity,

$$v_{K0} = \frac{c}{\sqrt{2(r_0/r_S - 1)}}, \tag{4.93}$$

which is reduced to the Newtonian Keplerian velocity, $v_K = (GM/r)^{1/2}$, when the non-relativistic limit is considered, $r_S/r \ll 1$. Here, all velocities are evaluated at the innermost stable orbit by ZAMOs, being denoted with the subscript "0."

4.4 Simulation of jet formation from a Kerr black hole

We perform 2.5-D simulations of jet formation from a Kerr BH surrounded by a thin Keplerian accretion disk in the numerical domain $1.5\,r_S \leqslant R \leqslant 15 r_S$, $0 \leqslant \theta \leqslant \pi/2$ with 128×128 grid points.

4.4.1 Initial conditions

- The simulations are performed for a BH spin parameter of $a_* = 0.95$.
- The coordinates are set to: ($x_{1\min} = 1.5$, $x_{1\max} = 30$) in the radial direction, ($x_{2\min} = 0$ rad, $x_{2\max} = 6.28$ rad) for the azimuthal angle, and ($x_{3\min} = 0.03$ rad, $x_{3\max} = 1.57$ rad) for the polar angle.
- A free boundary condition at the inner and outer boundaries is used, so that waves, fluids, and magnetic fields can pass through freely.
- The numerical computation is scale free (i.e., they do not depend on the BH mass), where the physical quantities are normalized as follows:

physical quantity	normalization unit
time (τ_S)	r_S/c
length (r)	r_S
density (ρ)	ρ_0
pressure (P)	$\rho_0 c^2$
velocity (v)	c
magnetic field	$\sqrt{\rho_0 c^2}$

For a BH with mass of $3\,M_\odot$, the Schwarzschild radius is $\sim 8 \times 10^5$ cm and the time unit $\tau_S = 3 \times 10^{-5}$ s. The normalization unit of density ρ_0 is the initial proper mass density of the corona density at $(r, z) = (3\,r_S, 0)$. For a density unit of $\rho_0 = 10^{10}$ g cm^{-3}, the magnetic field strength unit is 3×10^{14} G and the pressure unit is $P = 10^{29}$ dyn cm^{-2}.

- The coronal plasma is considered to be a transonic free-fall flow with the specific enthalpy $h/\rho c^2 = 1 + \Gamma p/[(\Gamma - 1)\rho c^2] = 1.3$, where the specific heat ratio is set to $\Gamma = 5/3$.

- The magnetic field is initially uniform, as seen by observers at infinity, being represented by Wald's solution (Wald 1974). The vector potential[24] of the Wald solution is

$$A_\mu = \frac{B_0}{2}(g_{\mu 3} + 2a_* r_{\rm g} g_{\mu 0}), \tag{4.94}$$

  where B_0 denotes the magnetic field strength. When the metric is written in Boyer-Lindquist coordinates, the components of the magnetic field measured by a comoving observer are (Koide 2003)

$$\hat{B}_r = B_0 \frac{\cos\theta}{\sqrt{A}} \left\{ \Delta + \frac{2r_{\rm g} r \left[r^4 - (a_* r_{\rm g})^4 \right]}{\Sigma^2} \right\}, \tag{4.95}$$

$$\hat{B}_\theta = -B_0 \sqrt{\frac{\Delta}{A}} \sin\theta \left\{ r - r_{\rm g} + \frac{r_{\rm g}}{\Sigma^2} \left\{ \left[r^2 + (a_* r_{\rm g})^2 \right] \Sigma + 2(a_* r_{\rm g})^2 \left[r^2 - (a_* r_{\rm g})^2 \right] \cos^2\theta \right\} \right\}. \tag{4.96}$$

  In the simulations, the magnetic field strength B_0 is set by comparing the magnetic energy density, $u_{\rm B} \sim B_0^2$, to the rest-mass energy density of the plasma, $u_{\rm m} \sim \rho_0 c^2$. For a magnetic-field-dominating case ($u_{\rm B} > u_{\rm m}$), the Alfvén velocity is close to the speed of light (Koide 2003). The magnetic field strength can be written as $B_0 = b_0\sqrt{\rho_0 c^2}$, where b_0 is a simulation parameter.

- The inner edge of the disk is at $r = 3\,r_{\rm S}$.

- The disk inclination angle with respect to the BH equatorial plane is 15°.

- In the disk, the azimuthal component of the velocity is assumed to be the relativistic Keplerian velocity (Eq. 4.93), and the poloidal component vanishes.

- The ratio of the disk mass density to the coronal mass density is 100.

4.4.2 Numerical results

The simulation of jet formation is initiated with a large-scale uniform magnetic field passing through a thin (Keplerian) accretion disk, with the magnetic field being set as for $b_0 = 0.1$ and the pressure of plasma around the BH being set to $p_0 = 1.0\rho_0 c^2$. A magnetic field with $b_0 = 0.1$ is considered to be weak. (Strong fields are those for which $b_0 > 1$.)

Times for various snapshots were chosen to cover the entire computed evolution of the plasma density (Fig. 4.5), the plasma being divided in two parts: (i) the corona around the BH and (ii) the thin accretion disk that co-rotates with the BH (Fig. 4.5a). The rest-mass density is represented in a logarithmic scale. The solid line shows the poloidal

[24]The covariant component of the electromagnetic field tensor can be witten in terms of the four-vector potential as $F_{\mu\nu} = \partial_\mu A_\nu - \partial_\nu A_\mu$, where $A^\mu = (\Phi_{\rm e}, A^1, A^2, A^3)$ is the four-vector potential ($\Phi_{\rm e}$ is the electrostatic potential).

component of the magnetic field ($B_{\rm p}$), and the arrow represents the plasma poloidal velocity as seen in the ZAMO frame normalized to the speed of light ($v_{\rm p}/c$). As the simulation evolves, the disk plasma losses angular momentum by the magnetic field torque and falls toward the BH. Figure 4.5b shows the state at $t = 64\,t_{\rm S}$, when the inner edge of the disk has rotated 1.6 cycles. The centrifugal force decelerates the disk plasma at $r \sim 3\,r_{\rm S}$, and the rapid infall of the plasma in front of this produces a shock inside the disk. The high presure behind the shock begins to produce the jet (we will refer to this as the formation of the pressure-driven component of the jet).

The gas pressure and electromagnetic forces that are used to accelerate (or decelerate) the plasma are, in the ZAMO frame,

$$W_{\rm gp} = -\mathbf{v}\cdot\nabla(\alpha p), \tag{4.97}$$

$$W_{\rm EM} = \alpha\mathbf{v}\cdot(\mathbf{E}+\mathbf{J}\times\mathbf{B})\,, \tag{4.98}$$

where α is, once again, the lapse function.

The disk plasma carries the frozen magnetic field with it, causing a considerable deformation of the field lines. As there is no stable orbit at $r \leqslant 3\,r_{\rm S}$, the accretion disk continues to fall rapidly toward the BH, enters the ergosphere, and then crosses the horizon. This is shown by the crowded magnetic field lines near the BH. Figure 4.5c shows the state at $t = 120\,t_{\rm S}$, by which time the inner edge of the disk has rotated 3 cycles. In the shock region, the matter is accelerated by the electromagnetic force and the increased gas pressure. Figure 4.5d shows the final state at $t = 186\,t_{\rm S}$ when the inner edge of the disk has rotated 4.7 cycles. The jet is formed almost along the poloidal magnetic field lines. The maximum total velocity of the jet is $\sim 0.4\,c$. The time evolution of rest-mass density indicates that the jet consists of:

1. a **gas pressure-driven component** and

2. a **magnetically-driven component** which is developed inside the gas pressure-driven jet.

The former comes from the region of the disk near the shock $r \leqslant 3\,r_{\rm S}$. The latter comes on one hand from the extraction of the BH rotational energy in the ergosphere, and on the other hand from the twisting of the magnetic field far from the BH.

For a better illustration of the distribution of the regions of acceleration (or deceleration) of the plasma by gas-pressure and electromagnetic forces, in Figs. 4.6 and 4.7 we plot these forces in the z direction, (- $W^z_{\rm gp}$) and $W^z_{\rm EM}$ (color), overlapped with the poloidal component of the magnetic field (solid line), and in Figs. 4.8 and 4.9 overlapped with the (negative) toroidal component of the magnetic field, B_ϕ (solid line). The magnetic field lines are twisted counter to the accretion disk rotation, therefore we plot $-B_\phi$. In Figs. 4.6 and 4.8, the light green-orange color shows the region were the plasma is accelerated by the gas-pressure force, whereas the blue color shows the region where the plasma is decelerated. The gas-presure force accelerates the plasma (orange) in the region of the disk where the shock is produced, as well as in the region very close to the BH where the coronal plasma is present. This high gas-pressure force acting on the plasma near the BH reflects the general relativistic effects which are introduced in the system by the lapse function. The gradient (in the z direction) of the lapse function increases about one order of magnitude in the region close to the BH (Fig. 4.10), and then it decreases as one approaches the event horizon.

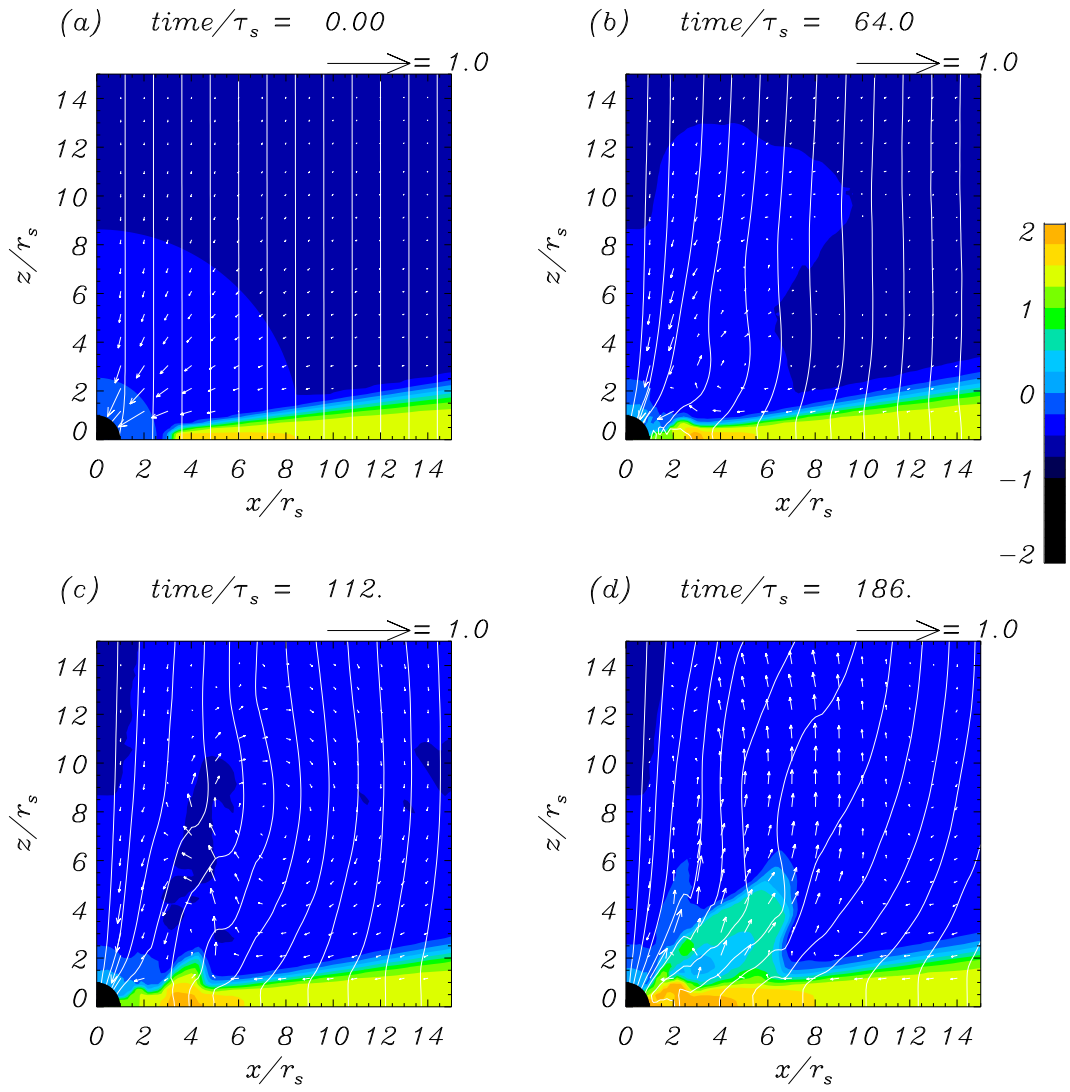

Figure 4.5: Time evolution of the jet formation in the magnetosphere of a BH with a spin parameter $a_* = 0.95$. The black circle indicates the BH. Solid line represents the poloidal component of the magnetic field, B_p. Color shows the logarithm of the proper mass density, ρ. Arrows represent the plasma poloidal velocity as seen in ZAMO frame normalized to the speed of light, v_p/c. The distance and the time are in units of r_S and $\tau_\mathrm{S} \equiv r_\mathrm{S}/c$, respectively. (a) For the initial conditions, a coronal plasma distribution, which is given by a transonic solution with $\Gamma = 5/3$ and $H = 1.3$, and a Keplerian accretion disk around the BH are set up. The density of the disk is 100 greater than that of the corona. (b) $t = 64\,t_\mathrm{S}$. The disk plasma falls towards the BH. The magnetic field lines are twisted through the plasma motion and through the frame dragging effect that occurs in the BH ergosphere. A shock is produced in the accretion disk at $\sim 3\,r_\mathrm{S}$. (c) $t = 112\,t_\mathrm{S}$. In the shock region, the matter is accelerated by the Lorentz force and the increased gas pressure, leading to jet formation. (d) $t = 186\,t_\mathrm{S}$. The jet is formed almost along the magnetic field lines. The maximum poloidal velocity of the jet is $\sim 0.4\,c$.

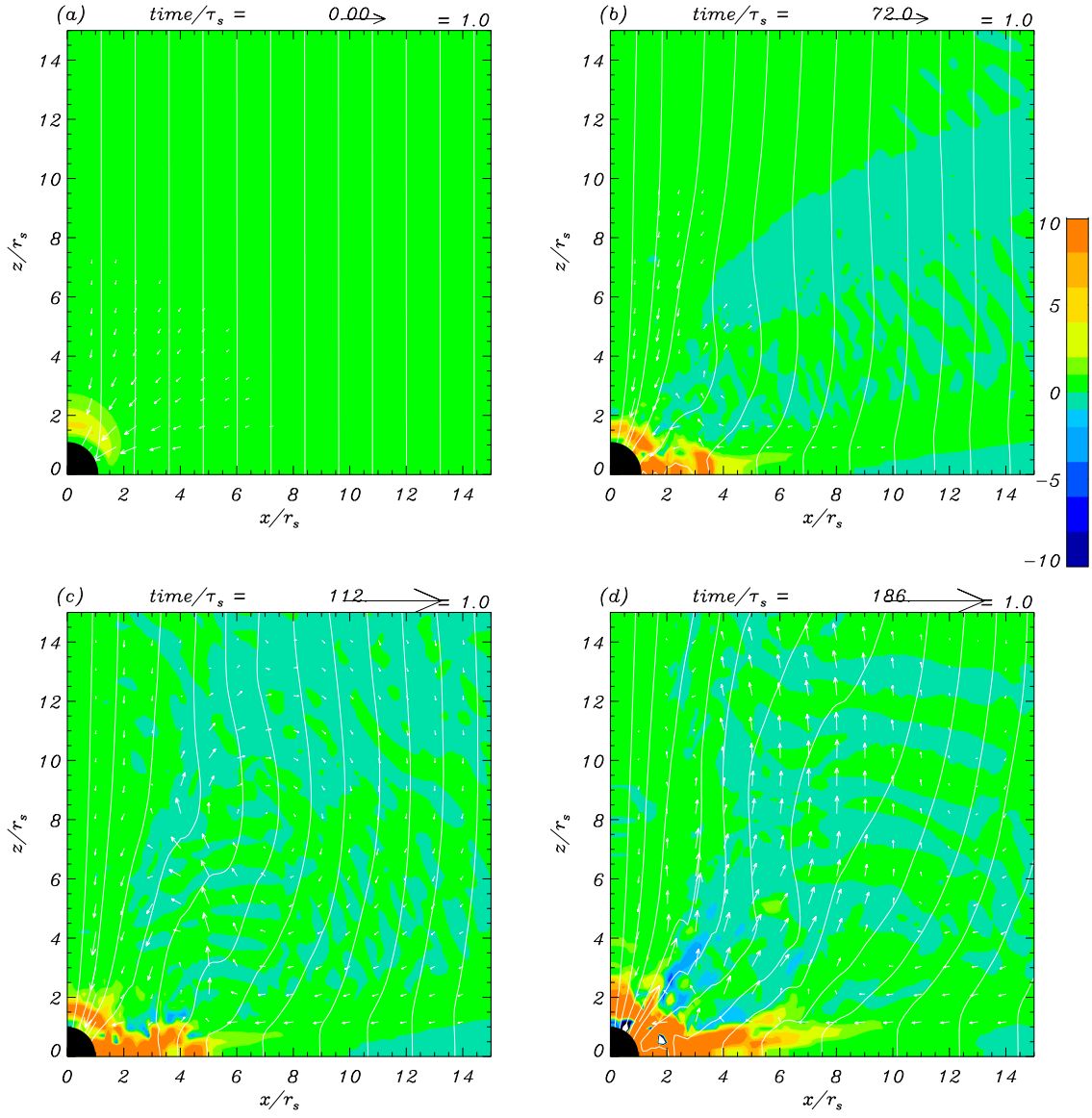

Figure 4.6: Magnitude of the gas-pressure force in the z direction, $W^z_{\rm gp}$ (color), that accelerates (or decelerates) the plasma. Solid line shows the poloidal component of the magnetic field and arrow represents the plasma poloidal velocity. Light green-orange color shows the region were the plasma is accelerated, whereas blue color shows the region where the plasma is decelerated.

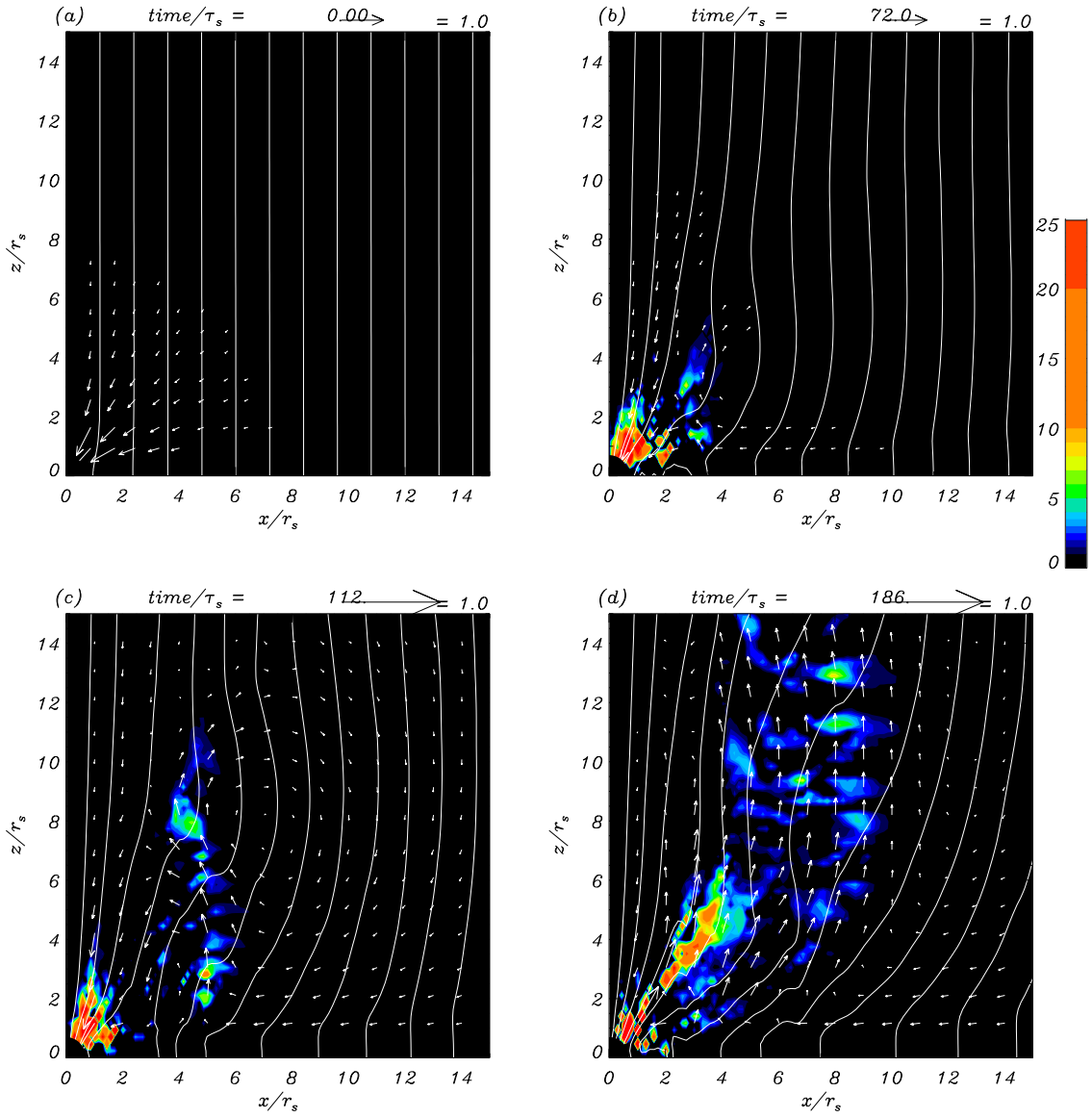

Figure 4.7: Magnitude of the electromagnetic force in the z direction that accelerates the plasma, $W^z_{\rm EM}$ (color). Solid line shows the poloidal component of the magnetic field and arrow represents the plasma poloidal velocity. The plot shows the magnetically-driven jet component which is associated with the twisting of the magnetic field (blue region), as well as with the electromagnetic extraction of the BH rotation energy (red-yellow region close to the BH).

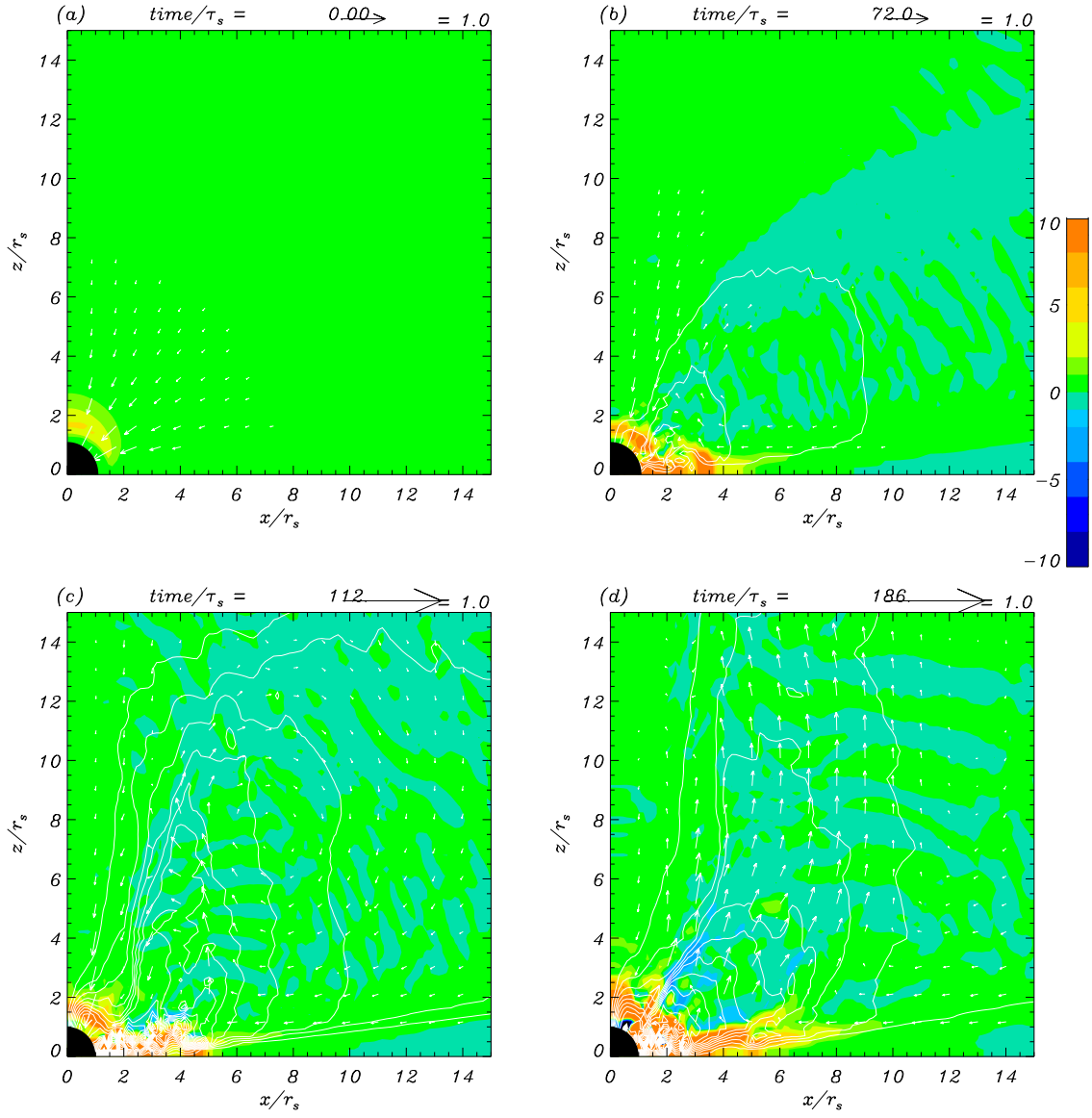

Figure 4.8: Magnitude of the gas-pressure force in the z direction (color) that accelerates (or decelerates) the plasma. Solid line shows the toroidal component of the magnetic field and arrow represents the plasma poloidal velocity. Light green-orange color shows the region were the plasma is accelerated, whereas blue color shows the region where the plasma is decelerated.

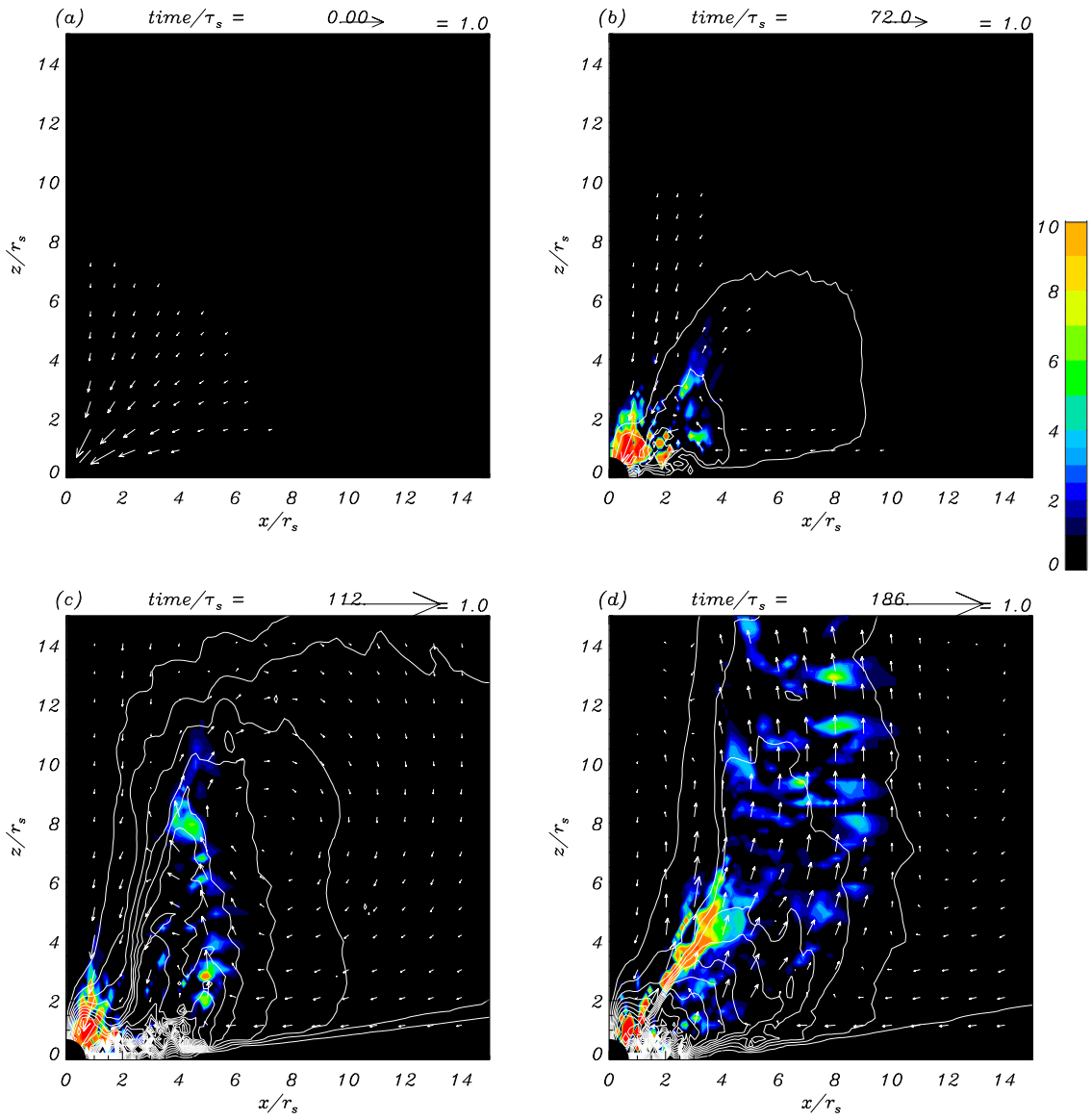

Figure 4.9: Magnitude of the electromagnetic force in the z direction that accelerates the plasma, $W^z_{\rm EM}$ (color). Solid line shows the toroidal component of the magnetic field and arrow represents the plasma poloidal velocity. The plot shows the magnetically-driven jet component which is associated with the twisting of the magnetic field (blue region), as well as with the electromagnetic extraction of the BH rotation energy (red-yellow region close to the BH).

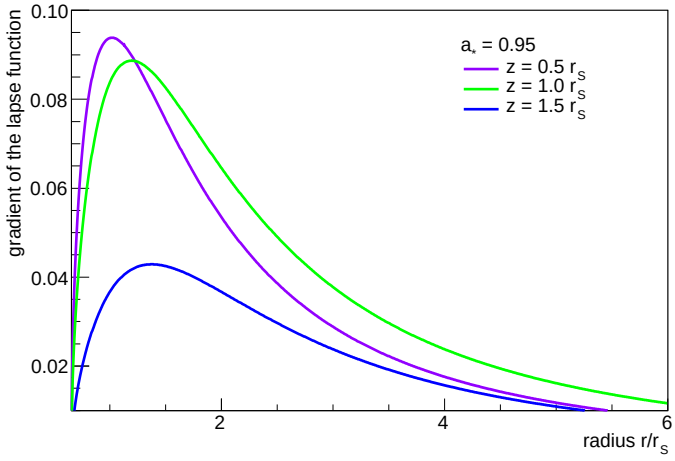

Figure 4.10: Radial distribution of the gradient (in the z direction) of the lapse function in the Boyer-Lindquist reference frame on the three different surface: $z = 0.5\,r_{\rm S}$, $z = 1.0\,r_{\rm S}$, and $z = 1.5\,r_{\rm S}$.

This decrease of the gradient towards a null value close to the BH is explained through the fact that the lapse function in Boyer-Lindquist coordinates becomes null at the event horizon. The horizon is located behind our boundary at $r = 1.5\,r_{\rm S}$, therefore we cannot follow the profile of the gradient of the lapse function very close to the event horizon. (The horizon is located at $r_{\rm H} \sim 0.65\,r_{\rm S}$ for a BH spin parameter of $a_* = 0.95$.) If we compare Fig. 4.8 with Fig. 4.9, we can observe that the region of electromagnetic acceleration of the plasma is clearly associated with the twisting of the magnetic field lines far from the BH, where there is a lack of plasma accelerated by gas pressure.

In Fig. 4.7, the electromagnetic power (color) increases over one order of magnitude from the blue to the light red-yellow. The plot shows the electromagnetically-driven jet component which is associated with the twisting of the magnetic field (blue region in Figs. 4.7c and d), as well as with the electromagnetic extraction of the BH rotation energy (red-yellow region close to the BH). In the BH ergosphere, the electromagnetically-driven jet is accelerated by the magnetic field which is frozen into the accretion disk. Due to the frame dragging effect, the disk is forced to rotate in the same direction as the BH rotation. As a result, both the azimuthal component of the magnetic field and the magnetic tension increase, therefore the plasma is accelerated by the magnetic pressure. Such mechanism of jet production can be thought of as being a MHD Penrose process that uses the magnetic fields to extract rotational energy of the BH and eject a collimated outflow from very near the horizon (Koide et al. 2000a). In contrast, running long-term simulations, Komissarov (2005) concluded that his results can be explained if the rotational energy is extracted from the BH through the purely electromagnetic mechanism of Blandford and Znajek (1977). In the numerical simulations of Komissarov (2005), no regions of negative hydrodynamic "energy at infinity" are seen inside the ergosphere, and therefore the MHD Penrose process does not operate. This might suggest that an MHD Penrose process can be observed only for transient jets. This conclusion might be revised when long-term simulations using the code of Koide et al. (1998, 2000a) and Koide (2003) will be performed.

We refer to the region of stronger acceleration of the plasma by the gas-pressure and electromagnetic forces as the jet-forming region. For a better understanding of the physics of the jet formation mechanism, in Fig. 4.11 we plot the plasma beta, $\beta = p_{\rm gas}/p_{\rm mag}$ (color), and the toroidal component of the magnetic field (contour). The blue color shows the region where the magnetic pressure dominates the gas pressure and light red-yellow-green shows where the gas pressure is dominant. Initially, the dominant component of the

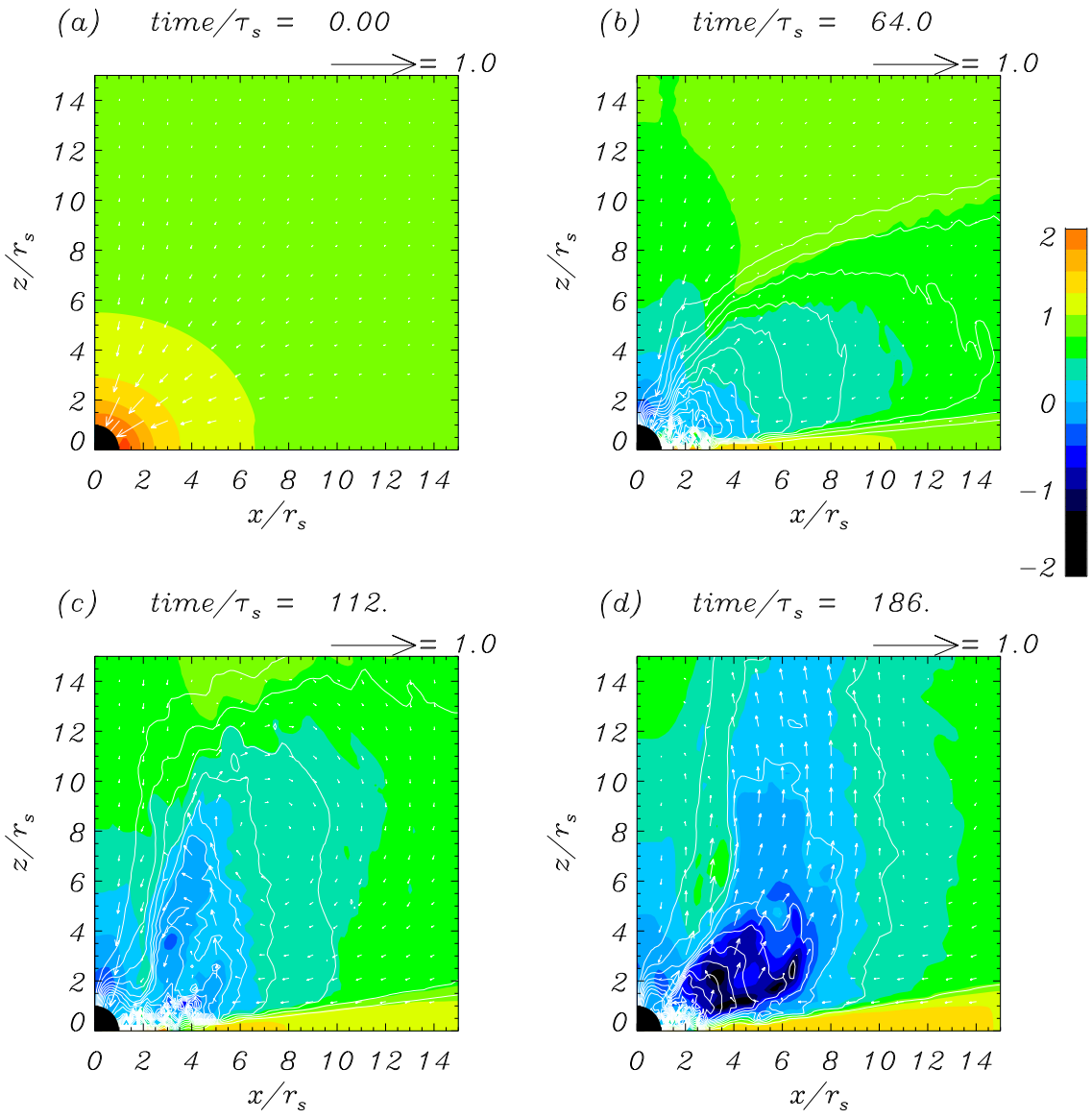

Figure 4.11: Time evolution of the plasma beta $\beta = p_{\rm gas}/p_{\rm mag}$ (color). Solid line shows the toroidal component of the magnetic field and arrow represents the plasma poloidal velocity. In the region where the magnetic field is twisted stronger, the magnetic pressure is higher.

jet is the gas pressure-driven component (blue-green regions in Fig. 4.11b). By the end of the simulation, $t = 186\,t_{\rm S}$, a magnetically-driven jet component had begun to be developed inside the pressure-driven component of the jet (dark blue regions in Fig. 4.11d), as the toroidal component of the magnetic field has increased about five times the initial value (Fig. 4.12d). This amplification is caused by the shear of the plasma flow in the Boyer-Lindquist frame due to the frame dragging effect of the rotating BH, and the magnetic field amplification energy comes from the rotation of the BH itself (Koide et al. 2000a). The magnetic tension accelerates the plasma by the magnetic pressure. The region of the jet where the magnetic pressure dominates (Fig. 4.11d) is clearly associated with the region of electromagnetic extraction of the BH rotation energy (Fig. 4.7d).

To illustrate the physical processes that occur during the simulation, we plot the x-profiles of various physical quantities first on the surface of $z = 0.7\,r_{\rm S}$, which is close to the BH equatorial plane, at $t = 64\,t_{\rm S}$ (Fig. 4.12). (Here, the coordinate x denotes the coordinate r.) In Fig. 4.12a, the density profile shows the presence of a shock at $r \sim 3\,r_{\rm S}$. Behind the shock, the increased gas pressure dominates the magnetic pressure. This dominance is also shown in Fig. 4.12f, where the plasma beta in the region $r \in [1.5, 3.8]\,r_{\rm S}$ is over unity. In this region, the acceleration of the plasma is, therefore, produced by the gas-pressure force (the dotted line in Fig. 4.12e). The azimuthal components of the velocity and of the magnetic field are dominant (Figs. 4.12b and d), suggesting that the disk plasma is also accelerated by centrifugal forces. However, at the shock front, the azimuthal velocity of the plasma decreases (Fig. 4.12b). The total velocity of the plasma is less that the Keplerian velocity, being supersonic and super-Alfvénic. Behind the shock the plasma becomes, however, subsonic and sub-Alfvénic (Fig. 4.12c). Both the sonic and Alfvénic velocities drop from $\sim 0.3\,c$ to zero at the shock front and then increase to $\sim 0.6\,c$ behind the shock. The Keplerian velocity in the shock region is $\sim 0.6\,c$. The jet from the disk has not been formed yet by the time of $t = 64\,t_{\rm S}$. The plasma accelerated in the z-direction corresponding to the region $r < 3\,r_{\rm S}$, where the poloidal component of the plasma velocity increases (Fig. 4.12b), comes from the BH corona. By the end of the simulation, $t = 186\,t_{\rm S}$ (Fig. 4.13), all components of the magnetic field have been increased to values greater than ten times the initial value of the magnetic field and the total velocity of the plasma has reached a value close to the Keplerian velocity. Note that the plasma motion is here studied on a surface close to the BH equatorial plane. The fact that the radial magnetic field is strongly amplified near the BH reflects the dragging of the magnetic field lines by the disk plasma.

In Fig. 4.14, we plot the x-profiles of various physical quantities on the surface of $z = 5.15\,r_{\rm S}$ by the end of the simulation ($t = 186\,t_{\rm S}$). By this time, the total velocity of the plasma flowing in the region $r \in [4, 9]\,r_{\rm S}$ has reached a value greater than the Keplerian velocity of the disk (Fig. 4.14c). On the other hand, the plasma in the very same region has a positive component of the velocity in the z direction (Fig. 4.14b), therefore the disk and coronal plasma is likely to flow out in the z direction and form a jet. The plasma is, on one hand, decelerated by the gas-pressure force (see the corresponding blue-green region in Fig. 4.6) and, on the other hand, accelerated by the electromagnetic force (see the corresponding orange-blue region in Fig. 4.7), the latter being stronger though (see also Fig. 4.14e).

To show the structure of the jet, we plot the z-profiles of various physical quantities on the surface of $x = 4.73\,r_{\rm S}$ at $t = 186\,t_{\rm S}$ which corresponds to the maximum value of the plasma velocity (Fig. 4.15). On this surface, the magnetic pressure dominates the gas pressure up to about $z = 10\,r_{\rm S}$ (Figs. 4.15a and f). The dominant component of the

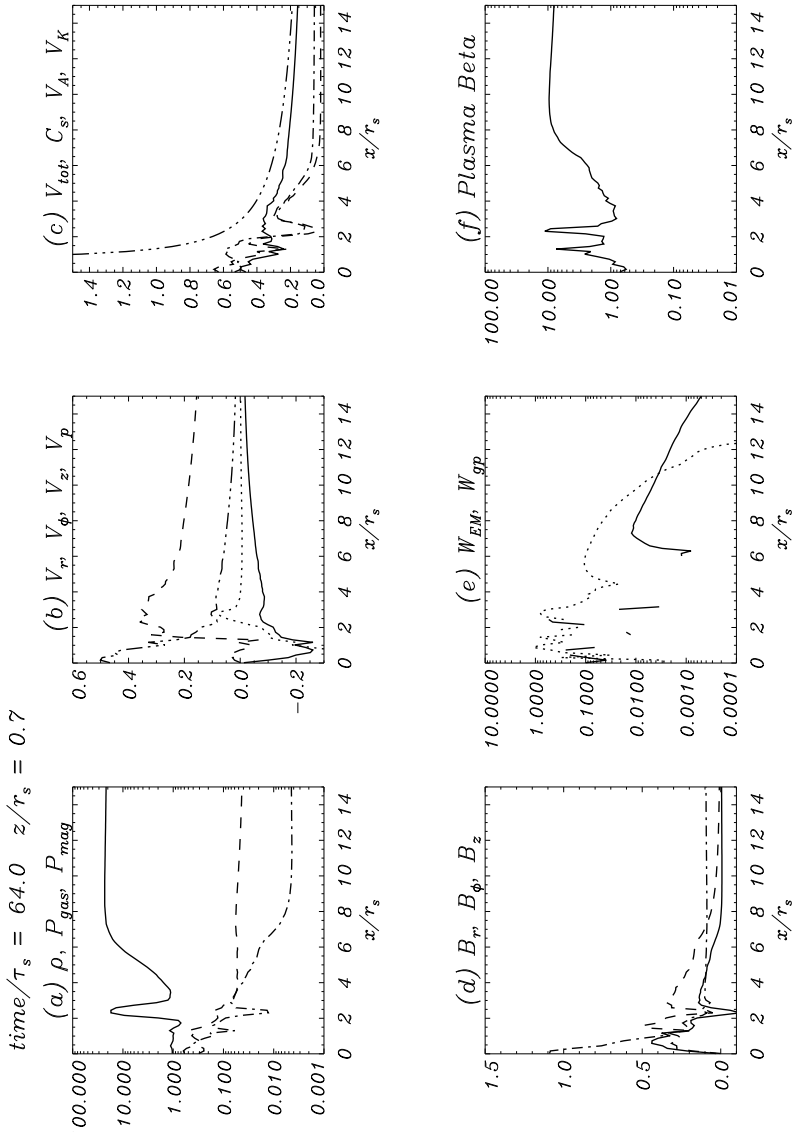

Figure 4.12: The x-profiles of various physical quantities on the surface of $z = 0.7\,r_{\rm S}$ at $t = 64\,t_{\rm S}$, the time at which the shock in the disk starts to be developed. (a) Density ρ (solid line), gas pressure $p_{\rm gas}$ (dashed line), and magnetic pressure $p_{\rm mag}$ (dot-dashed line). (b) Components of the plasma velocity, v_r (solid line), v_z (doted line), v_ϕ (dashed line), and $v_{\rm p}$ (3-dot-dashed line). (c) Total velocity $v_{\rm tot} = (v_r^2 + v_z^2 + v_\phi^2)^{1/2}$ (solid line), Alfvén velocity $v_{\rm A}$ (dashed line), sound velocity $c_{\rm s}$ (dot-dashed line), and Keplerian velocity $v_{\rm K}$ (3-dot-dashed line). (d) Components of the magnetic field, B_r (solid line), B_z (dot-dashed line), and B_ϕ (dashed line). (e) Vertical component of the electromagnetic force $W^z_{\rm EM}$ (solid line) and the gas-pressure force $W^z_{\rm gp}$ (doted line). (f) Plasma beta $\beta = p_{\rm gas}/p_{\rm mag}$.

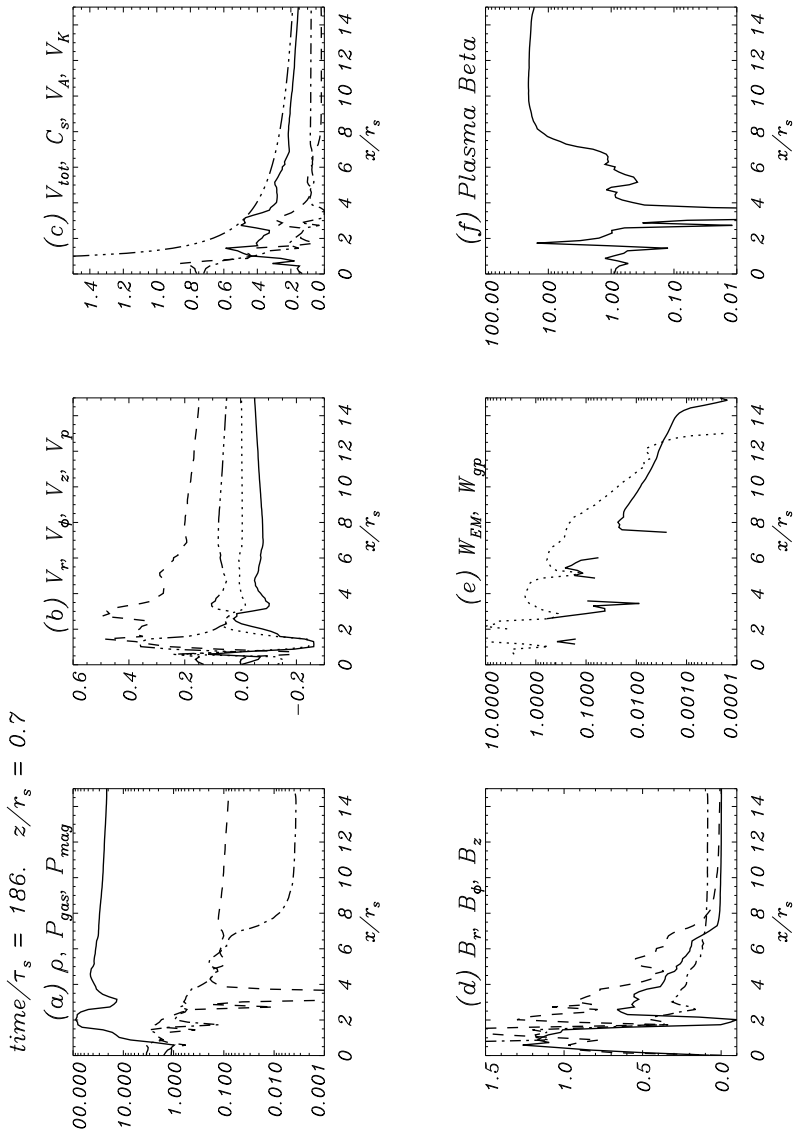

Figure 4.13: The x-profiles of various physical quantities on the surface of $z = 0.7\,r_{\rm S}$ at the end of the simulation $t = 186\,t_{\rm S}$. (a) Density ρ (solid line), gas pressure $p_{\rm gas}$ (dashed line), and magnetic pressure $p_{\rm mag}$ (dot-dashed line). (b) Components of the plasma velocity, v_r (solid line), v_z (doted line), v_ϕ (dashed line), and $v_{\rm p}$ (3-dot-dashed line). (c) Total velocity $v_{\rm tot} = (v_r^2 + v_z^2 + v_\phi^2)^{1/2}$ (solid line), Alfvén velocity $v_{\rm A}$ (dashed line), sound velocity $c_{\rm s}$ (dot-dashed line), and Keplerian velocity $v_{\rm K}$ (3-dot-dashed line). (d) Components of the magnetic field, B_r (solid line), B_z (dot-dashed line), and B_ϕ (dashed line). (e) Vertical component of the electromagnetic force $W^z_{\rm EM}$ (solid line) and the gas-pressure force $W^z_{\rm gp}$ (doted line). (f) Plasma beta $\beta = p_{\rm gas}/p_{\rm mag}$.

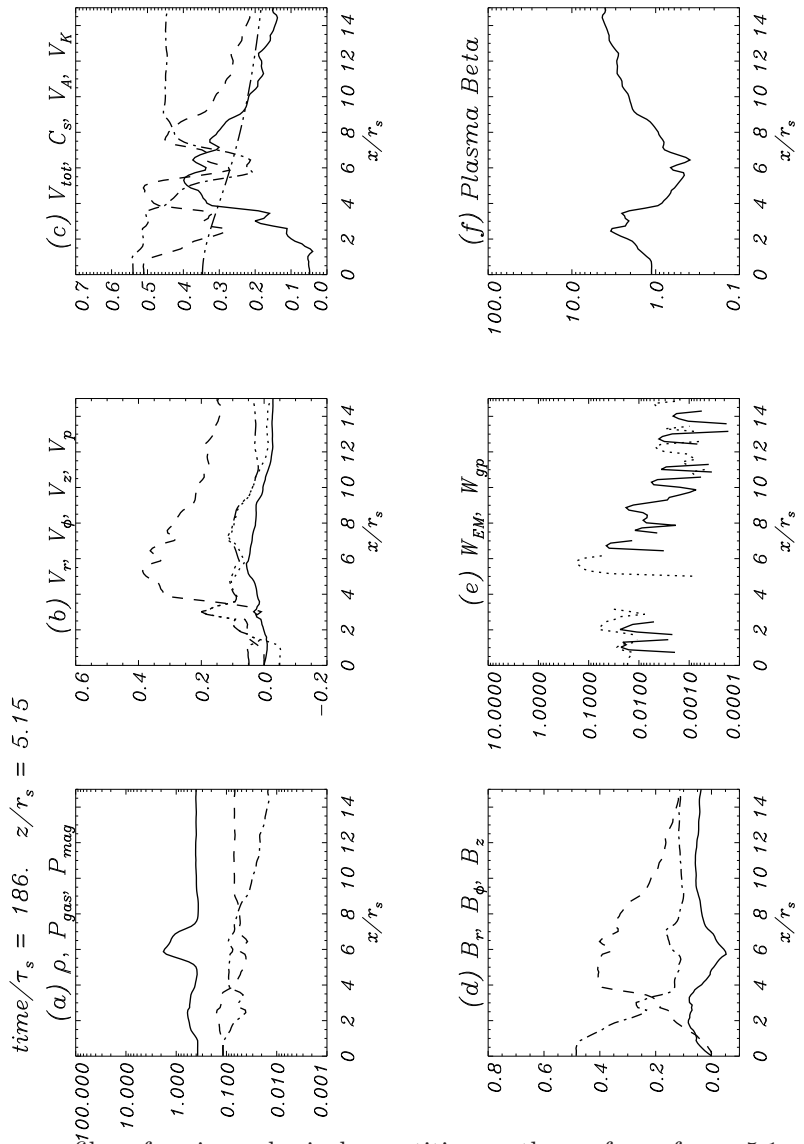

Figure 4.14: The x-profiles of various physical quantities on the surface of $z = 5.1\,r_{\rm S}$ (which corresponds to the base of the jet) at the end of the simulation $t = 186\,t_{\rm S}$. (a) Density ρ (solid line), gas pressure $p_{\rm gas}$ (dashed line), and magnetic pressure $p_{\rm mag}$ (dot-dashed line). (b) Components of the plasma velocity, v_r (solid line), v_z (doted line), v_ϕ (dashed line), and $v_{\rm p}$ (3-dot-dashed line). (c) Total velocity $v_{\rm tot} = (v_r^2 + v_z^2 + v_\phi^2)^{1/2}$ (solid line), Alfvén velocity $v_{\rm A}$ (dashed line), sound velocity $c_{\rm s}$ (dot-dashed line), and Keplerian velocity $v_{\rm K}$ (3-dot-dashed line). (d) Components of the magnetic field, B_r (solid line), B_z (dot-dashed line), and B_ϕ (dashed line). (e) Vertical component of the electromagnetic force $W^z_{\rm EM}$ (solid line) and the gas-pressure force $W^z_{\rm gp}$ (doted line). (f) Plasma beta $\beta = p_{\rm gas}/p_{\rm mag}$.

velocity still remains the azimuthal component (Fig. 4.15b). However, as Fig. 4.15c shows, the jet is likely to be produced from about $z = 3\,r_{\rm S}$ all the way up, becoming subsonic and sub-Alfvénic from about $z = 4\,r_{\rm S}$ though. The total velocity of the particles has the maximum value of about $\sim 0.4\,c$. The dominant component of the magnetic field is the toroidal component (Fig. 4.15d), which increases in the jet-forming region. The ratio of the toroidal to the poloidal component of the magnetic field, $B_\phi/B_{\rm p}$, represents the twist of the magnetic field. This twist increases strongly in the jet-forming region (Fig. 4.15e), where the magnetic energy stored by the twisting magnetic field is converted into kinetic energy of the jet. Such a large twist of the magnetic field implies a large magnetic pressure as well, which is also reflected by a low plasma beta in this region (Fig. 4.15f).

We would like to point out that the main result of the simulation presented in this chapter is the presence of an electromagnetically-driven component of the jet which, close to the BH, is developed inside the gas pressure-driven jet component. In the regions far from the BH, the jet is accelerated by electromagnetic forces. Similar to the previous simulations performed by Koide et al., where the accretion disk co-rotates with the BH rotation in a free-falling corona, the maximum value of the jet velocity is $\sim 0.4\,c$, i.e., the jet is sub-relativistic.

4.4.3 Comparison with the RAISHIN simulation code (Mizuno et al.)

The critical problem of Koide et al. GRMHD code is that the schemes can not maintain a divergence-free magnetic field automatically. Therefore, Mizuno et al. (2006b, 2007, 2009b) have developed a new 3-D GRMHD code, RAISHIN, which is a conservative, high-resolution shock-capturing scheme. A Harten-Lax-van Leer approximate Riemann solver is employed to compute the numerical fluxes. In order to maintain the divergence-free condition, a flux-interpolated, constrained transport scheme is applied. As far as the numerical accuracy and the numerical costs are concerned, one can select a method, which is more computationally efficient, from the following four reconstruction algorithms: the piecewise linear methods with either Minmod or MC slope-limiter function, the convex essentially non-oscillatory method, and the piecewise parabolic method, where a multistep TVD Runge-Kutta method either with second or third-order time accuracy can be applied to advance the solution in time.

Simulations of jet formation from non-rotating ($a_* = 0$) and rapidly-rotating ($a_* = 0.95$) BHs were performed, when a thin accretion disk and a uniform magnetic field are considered initially. The simulation results indicate that mildly relativistic jets ($v \gtrsim 0.4\,c$) are driven by the Lorentz force and the gas pressure gradients. In the case of the rotating BH, an additional, faster, and more collimated matter-dominated inner jet ($v \gtrsim 0.5\,c$) is produced and accelerated through the twisting of the magnetic field that occurs in the BH ergosphere. The jet kinematic structure depends mainly on the BH spin and on the magnetic field configuration and strength. The simulations were carried out for Boyer-Lindquist coordinates. Nevertheless, the RAISHIN code with the Kerr-Schild coordinates is subject to further work by Mizuno et al. This approach may provide a way to overcome the numerical problems that occur when approaching the BH event horizon, as for the boundary conditions. The expected results would be longer term simulations ($\sim 10^3 - 10^4\,t_{\rm S}$) when strong magnetic fields are considered ($b_0 > 1$).

To show the behavior of the Kerr-Schild coordinates at the BH event horizon, which is a physical singularity in the Boyer-Lindquist reference frame, in Fig. 4.16 we plot

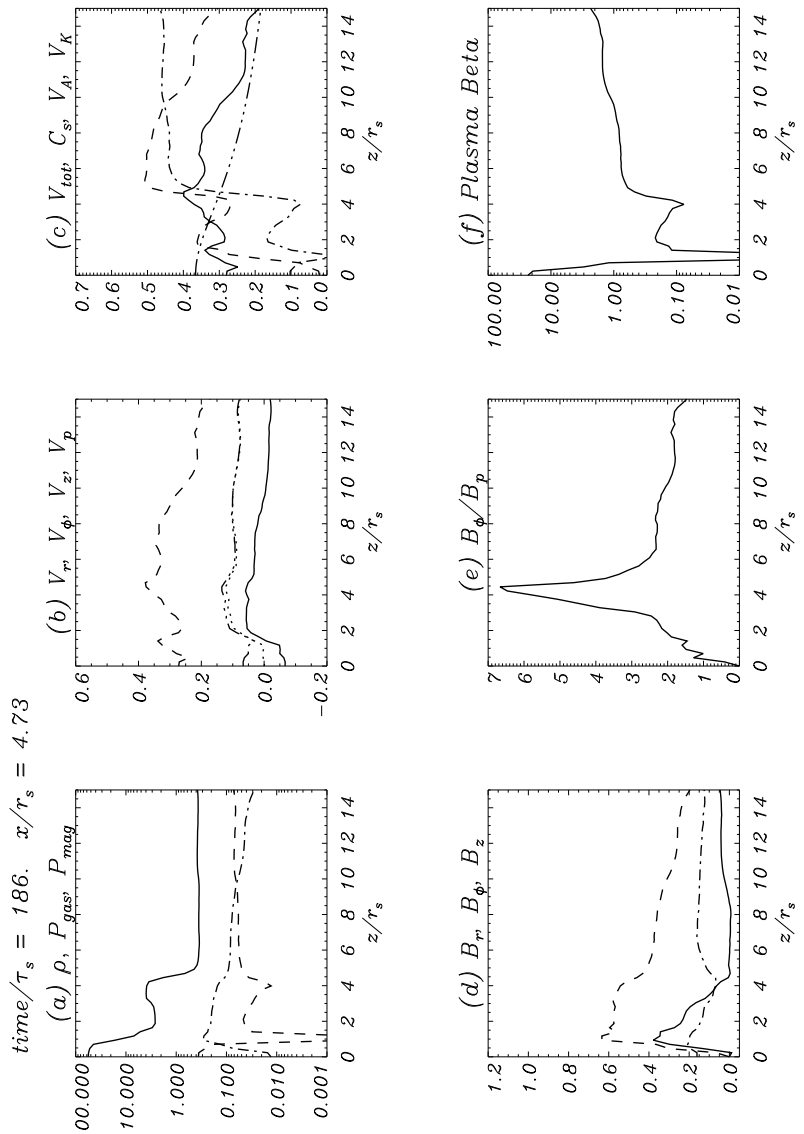

Figure 4.15: The z-profiles of various physical quantities on the surface of $x = 4.73\, r_{\rm S}$ at the end of the simulation $t = 186\, t_{\rm S}$. (a) Density ρ (solid line), gas pressure $p_{\rm gas}$ (dashed line), and magnetic pressure $p_{\rm mag}$ (dot-dashed line). (b) Components of the plasma velocity, v_r (solid line), v_z (dot-dashed line), and v_ϕ (dashed line). (c) Total velocity $v_{\rm tot} = (v_r^2 + v_z^2 + v_\phi^2)^{1/2}$ (solid line), Alfvén velocity $v_{\rm A}$ (dashed line), sound velocity $c_{\rm s}$ (dot-dashed line), and Keplerian velocity $v_{\rm K}$ (double-dot-dashed line). (d) Components of the magnetic field, B_r (solid line), B_z (dot-dashed line), and B_ϕ (dashed line). (e) Ratio of toroidal to poloidal magnetic components $B_\phi/B_{\rm p}$. (f) Plasma beta $\beta = p_{\rm gas}/p_{\rm mag}$.

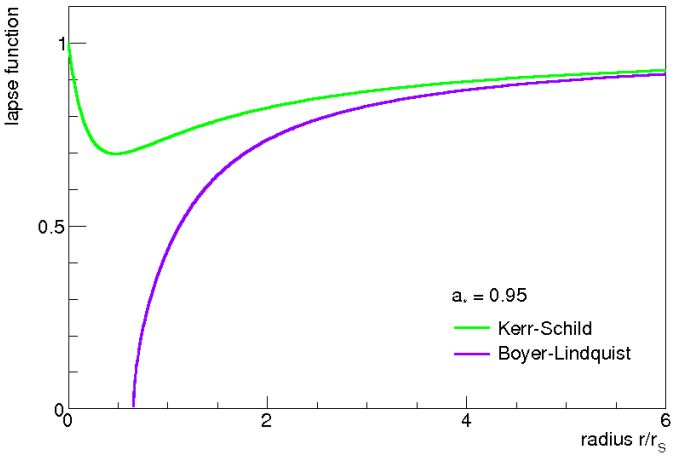

Figure 4.16: Radial distribution of the lapse function in the Boyer-Lindquist reference frame (purple line) and in the Kerr-Schild reference frame (green line). The lapse function in the Boyer-Lindquist frame becomes singular at the event horizon ($r_{\rm H} \sim 0.65\, r_{\rm S}$ for $a_* = 0.95$), whereas the lapse function in the Kerr-Schild frame is a well-behaved function all the way down to the true singularity of the space-time at $r = 0$. We use the normalized radius $r/r_{\rm S}$.

the radial distribution of the lapse function (which in turn gives the acceleration of free-falling particles, the external magnetic field strength, etc.) in the two reference frames: Kerr-Schild (green line) and Boyer-Lindquist (purple line), respectively. We consider here the case when the BH spins at $a_* = 0.95$, so that the horizon radius is $\simeq 0.65\, r_{\rm S}$. The lapse function in the Boyer-Lindquist reference frame, $\alpha_{BL} = \sqrt{\Sigma\Delta/A}$ (Eq. 1.9), becomes singular as one approaches the BH horizon. Instead, the lapse function in the Kerr-Schild reference frame [$\alpha_{KS} = 1/\sqrt{1+Z}$ with $Z = 2r_{\rm g}^2 r_*/\Sigma = r_{\rm S}^2 r_*/(2\,\Sigma)$, e.g., Font et al. (1999)] stays finite. Moreover, the lapse function in the Kerr-Schild frame is a well-behaved function all the way down to the true singularity of the space-time at $r = 0$.

4.4.4 Comparison with other work

The results presented in this chapter are obtained for a geometrically thin accretion disk. Nevertheless, numerical simulations of jet formation for a thick accretion disk were performed, for instance, by McKinney & Gammie (2004); McKinney (2006); Hawley & Krolik (2006). As we already mentioned in the introduction, McKinney & Gammie (2004); McKinney (2006) have developed a conservative shock-capturing scheme (called HARM) for axisymmetric simulations of jet formation. The code uses modified Kerr-Schild coordinates. In one of their models, large-scale magnetic fields are created self-consistently by a thick accretion disk with hight to radius ratio $H/R \gtrsim 0.1$. The jets formed in their simulations also present two components: (i) a highly-relativistic, Poynting flux-dominated "funnel," originating from around the BH poles, and (ii) a "wind," which consists of a cone of material near the edge of the funnel and moves at sub-relativistic speeds ($v \sim 0.3\, c$). The funnel region is nearly force-free and consistent with the Blandford-Znajek mechanism, for which the authors presented a self-contained derivation in Kerr-Schild coordinates. Their results indicate that the rotational energy of the BH is extracted via the Blandford-Znajek mechanism, but not through an MHD Penrose process. Instead, their second component of the jet is similar to the gas pressure-driven component of the jet in our simulations. Hawley & Krolik (2006) also obtained two components of the jet [similarly to McKinney & Gammie (2004) and McKinney (2006)] using a GRMHD code that resembles the algorithms employed in the ZEUS code used for non-relativistic astrophysical MHD simulations, with Boyer-Lindquist coordinates. In the numerical simulations performed by McKinney (2006) and Hawley & Krolik (2006), poloidal-loop magnetic fields inside the torus are considered

initially. This magnetic field is then twisted and expands from the torus (i.e., the thick disk) as a magnetic tower, which fills the funnel region. In our case, the magnetic field is initially vertical, threading the disk and the BH ergosphere, which is then twisted by the frame dragging effect and form a magnetically-driven component of the jet. Although the same basic mechanism of jet formation is used in the work by McKinney & Gammie (2004); McKinney (2006); Hawley & Krolik (2006) as in our work, the jets show different features. These differences can be attributed to a different type of the magnetic field and accretion disk used initially for simulations.

4.5 Summary and conclusions

After an introduction to the GRMHD equations in 3+1 formalism, we presented the results of GRMHD simulation of jet formation from a thin accretion disk that co-rotates with a rapidly-spinning BH ($a_* = 0.95$) in a free-falling corona, using the code developed by Koide et al. (1998, 2000a); Koide (2003).

- For the numerical results presented in this chapter, we set the simulation parameters in such a way to perform a longer term simulation. We used a weak magnetic field of $0.1(\rho_0 c^2)^{1/2}$ and an inner boundary at $1.5\,r_{\rm S}$, so that the final stage of the jet formation corresponds to $t = 186\,t_{\rm S}$. Koide et al. have performed simulations of jet formation from a Kerr BH using a variety of parameter set, including the strength of the magnetic field as strong as $5.57(\rho_0 c^2)^{1/2}$.

- The numerical results show that, as the time evolves, the disk plasma loses angular momentum by the magnetic field torque and falls toward the BH. When the rapid infall of plasma encounters the disk plasma that is decelerated by centrifugal forces near the BH, a shock is produced inside the disk at $\sim 3\,r_{\rm S}$. The high pressure behind the shock pushes the plasma outward by gas-pressure forces and pinches it into a collimated jet. As a result, a gas pressure-driven component of the jet is produced. On the other hand, the magnetic field is frozen in the accretion disk. Therefore, the infalling plasma bends the magnetic field inward, creating a significant radial component of the field which is then twisted by the differential disk rotation into an azimuthal component. As the azimuthal component of the magnetic field increases, and so the magnetic tension, the plasma is accelerated by the magnetic pressure. This electromagnetically-driven component of the jet has two origins: one associated with the extraction of the BH rotational energy in the ergosphere and the other one with the twisting of the magnetic field far from the BH.

- Similar to Koide et al., the maximum jet velocity obtained in this numerical simulation is $\sim 0.4\,c$. This is considerable lower than the velocity of the inner parts of some AGN jet for which the observations indicate relativistic speeds (e.g., Ghisellini et al. 2005). However, the outer parts of the jet can have mildly- and sub-relativistic speeds. Nevertheless, the jet can be accelerated further out at shock fronts. This acceleration might eventually be seen in longer term simulations. A relativistic jet of $\sim 0.9\,c$ has been obtained in the numerical simulations performed by Koide et al. (2000b), in the case of a non-rotating disk around a rapidly-rotating BH though.

- The previous simulations performed by Koide et al. show a two-component jet: (i) an inner, low density, fast, electromagnetically-driven jet and (ii) an outer, high den-

sity, slow, gas pressure-driven jet. In the case of the simulation results presented in this chapter, the dominant component of the jet in the region close to the BH is initially the gas pressure-driven component, which becomes weaker compared to the electromagnetically-driven component as the time goes on. So that, by the end of the simulation, the electromagnetically-driven component of the jet has already been developed inside the gas pressure-driven jet. On the other hand, in the region far from the BH, the jet is mainly driven by electromagnetic forces. There, the gas-pressure forces of the coronal plasma which decelerate the jet are somewhat weaker than the driving electromagnetic forces.

- To illustrate the dependence of jet formation on the BH spin (for a rapidly-rotating BH, $a_* \geqslant 0.95$), we also performed simulations in the case of a higher spin of $a_* = 0.9982$ (not shown in this chapter). The physical quantities obtained as a result of the simulation do not differ between the two cases of the BH spin, therefore we conclude that the eventual differences between them might be revealed when longer term simulations are performed.

The results presented here are strongly dependent on the strength of the magnetic field, as well as on the location of the inner boundary. For stronger magnetic fields, the jet should be totally electromagnetically driven, and we can study the Penrose-like process in the BH ergosphere for the extraction of the BH rotational energy for this case as well. On the other hand, choosing an inner boundary closer to the BH can reveal some physical processes which might not be shown by the numerical results presented here. As stated before, the development of the code for Kerr-Schild coordinates is expected to produce longer term simulations when strong magnetic fields are considered.

Despite intense efforts to understand the processes responsible for formation, acceleration, and collimation of the jets from BHs, we still face the problem of exactly how to explain these processes. The numerical results of jet formation presented in this chapter indicate how outflows from a thin accretion disk co-rotating with a rapidly-spinning BH might be produced within the framework of the GRMHD. The main purpose of these time-dependent simulations was to study the initial transient effects associated with acceleration of the jets. The results presented here, using the code by Koide et al. (1998, 2000a); Koide (2003), are able to shed light on how the jets can be accelerated thanks to the gas-pressure and electromagnetic forcess and to show that the extraction of the rotational energy from the BH via a Penrose-like process in the BH ergosphere is possible, as found by Koide et al. (2000a), but see Komissarov (2005).

Outlook

In this thesis, we have studied some aspects of the physics of jets from spinning BHs that regard their formation, as well as the acceleration of UHECRs. Our main findings were summarized at the beginning of this thesis. Here, we give an outlook and describe future plans.

In Chapter 2, we proposed a model through which AGN jets can be launched from the ergospheric disk surrounded a Kerr BH, when closed magnetic field lines connect the BH to the ergospheric disk. Through such a BH-disk magnetic connection, the BH transfers energy and angular momentum to the disk, and the available accreting rest mass-energy increases. Furthermore, the jets can extract and transport away mass, energy, and angular momentum from the ergospheric disk. A more general magnetic field threading the BH would consist of a combination of closed magnetic field lines and open magnetic field lines, extending from BH to infinity, which can enable the extraction of BH rotational energy through the Blandford–Znajek mechanism. As part of our future work, we plan to extend the work presented in this thesis by including the open magnetic field configuration and develop a self-consistent physical model that may fully describe the energy extraction from the BH.

Turning to the Chapter 3, the possibility to trace sources of UHECRs is of crucial importance to particle astronomy, as it can improve constraints on Galactic and extragalactic magnetic fields, set upper limits on Lorentz invariance through GZK considerations, and probe the AGN engine as an acceleration mechanism. A considerable improvement was achieved by trying to identify the nature of UHECRs using ground-detector arrays' data as, for instance, Auger data. Although the present Auger data indicate that Cen A is a noteworthy source of UHECRs, the UHECR-AGN correlation should be substantiated with further statistics, either from Auger or other observatories. In this context, the contribution of the spin-down power of BHs in LLAGN to the UHECRs may help to understand better this UHECR-AGN correlation by applying the model developed in Chapter 3 to a larger complete sample of AGN.

In Chapter 4, we presented numerical results of jet formation from a thin accretion disk co-rotating with a rapidly-spinning BH within the framework of the GRMHD. A difficulty encountered by us was the short term of the present calculations ($\sim 200\, t_{\rm S}$) due to numerical problems that occur when approaching the BH event horizon. We plan to improve the results by using the code with the Kerr-Schild coordinates, which may allow for longer term simulations ($\sim 10^3 - 10^4\, t_{\rm S}$), to further test and clarify the mechanism of energy extraction from the BH via a Penrose-like process in the BH ergosphere, as well as to perhaps reveal new relevant features of jet formation. Moreover, the Lorentz factor of the jet obtained by our calculations has a lower value than that of the inner jet, as indicated by some observations. An obvious solution is further acceleration along the jet (e.g., Blandford & Königl 1979; Falcke & Biermann 1995).

References

Abbasi, R. U., Abdou, Y., Abu-Zayyad, T., et al. 2010, Phys. Rev. Lett., 104, id. 161101

Abdo, A. A., Ackermann, M., Arimoto, M., et al. 2009, Science, 323, 1688

Abdo, A. A., Ackermann, M., Arimoto, M., et al. 2010, Published online 1 April 2010; 10.1126/Science.1184656

Abraham, J., Abreu, P., Aglietta, M., et al. 2007, Science, 318, 939

Abraham, J., Abreu, P., Aglietta, M., et al. 2008a, Astropart. Phys., 29, 188

Abraham, J., Abreu, P., Aglietta, M., et al. 2008b, Phys. Rev. Lett., 101, id. 061101

Abraham, J., Abreu, P., Aglietta, M., et al. 2010, Phys. Rev. Lett., 104, id. 091101

Achterberg, A., Gallant, Y. A., Kirk, J. G., & Guthmann, A. W. 2001, MNRAS, 328, 393

Alfvén, H. 1963, Cosmical Electrodynamics (Clarendon, Oxford)

Allard, D., Busca, N. G., Decerprit, G., Olinto, A. V., & Parizot, E. 2008, JCAP, 10, 33

Allen, S. W., Dunn, R. J. H., Fabian, A. C., Taylor, G. B., & Reynolds, C. S. 2006, MNRAS, 372, 21

Anderson, J. D. J. 1995, Computational Fluid Dynamics: The Basics with Applications (McGraw-Hill, Inc.)

Anninos, P., Fragile, C. P., & Salmonson, J. D. 2005, ApJ, 635, 723

Antonucci, R. 1993, ARA&A, 31, 473

Armitage, P. J. & Natarajan, P. 1999, ApJ, 523, L7

Arnowitt, R., Deser, S., & Misner, C. W. 1962, Gravitation: An Introduction to Current Research (Wiley, New York, USA), 227

Auger, P. V., Ehrenfest, P., Maze, R., Daudin, J., & Fréon, R. A. 1939, Rev. Mod. Phys., 11, 288

Axford, W. I., Leer, E., & McKenzie, J. F. 1977, in Proceedings of the 15th International Cosmic Ray Conference, Plovdiv, Vol. 11, 132

Baade, W. & Zwicky, F. 1934, in Proceedings of the National Academy of Sciences of the United States of America, Vol. 20, 259

Balbus, S. A. & Hawley, J. F. 1991, ApJ, 376, 214

Balbus, S. A. & Hawley, J. F. 1994, MNRAS, 271, 197

Balbus, S. A. & Hawley, J. F. 1996, ApJ, 467, 76

Balbus, S. A. & Hawley, J. F. 1998, Rev. Mod. Phys., 70, 1

Bardeen, J. M. 1970, Nature, 226, 64

Bardeen, J. M. 1973a, in Black Holes Les Astres Occlus, ed. C. DeWitt & B. S. DeWitt (New-York: Gordon & Breach), 215

Bardeen, J. M. 1973b, in Black Holes Les Astres Occlus, ed. C. DeWitt & B. S. DeWitt (New-York: Gordon & Breach), 221

Bardeen, J. M., Press, W. H., & Teukolsky, S. A. 1972, ApJ, 178, 347

Barthel, P. D. 1989, ApJ, 336, 606

Barvainis, R., Lehár, J., Birkinshaw, M., Falcke, H., & Blundell, K. 2005, ApJ, 618, 108

Baumgarte, T. W. & Shapiro, S. L. 2003, Phys. Rep., 376, 41

Becker, J. K. & Biermann, P. L. 2009, Astropart. Phys., 31, 138

Bednarz, J. & Ostrowski, M. 1998, Phys. Rev. Lett., 80, 3911

Bell, A. R. 1978a, MNRAS, 182, 147

Bell, A. R. 1978b, MNRAS, 182, 443

Berezinsky, V., Gazizov, A., & Grigorieva, S. 2006, Phys. Rev. D, 74, id. 043005

Berti, E. & Volonteri, M. 2008, ApJ, 684, 822

Biermann, P. B., Becker, J. K., Caramete, L., et al. 2008, in Nuclear Physics B Proceedings Supplements: Proceedings of the Origin, Mass, Composition and Acceleration Mechanisms of UHECRs (CRIS 2008), held in Malfa, Italy, Vol. 190, 61, also astro-ph/0811.1848

Biermann, P. L. 1994, in Proceedings of the High Energy Astrophysics. Models and Observations from MeV to EeV, ed. J. M. Matthews (Singapore: World Scientific), 217

Biermann, P. L. & Strittmatter, P. A. 1987, ApJ, 322, 643

Biretta, J. A., Junor, W., & Livio, M. 2002, New Astron. Rev., 46, 239

Biretta, J. A., Sparks, W. B., & Macchetto, F. 1999, ApJ, 123, 351

Bisnovatyi-Kogan, G. S. & Ruzmaikin, A. A. 1976, Ap&SS, 42, 401

Blandford, R. D. 1976, MNRAS, 176, 465

Blandford, R. D. 1990, in 20 Saas-Fee Advanced Course of the Swiss Society for Astrophysics and Astronomy: Active galactic nuclei, ed. T. J.-L. Courvoisier & M. Mayor (Berlin: Springer), 161

Blandford, R. D. 1999, in Proceedings of the Astrophysical Discs - An EC Summer School, Astronomical Society of the Pacific Conference series, ed. J. A. Sellwood & J. Goodman, Vol. 160, 265

Blandford, R. D. 2001, Prog. Theor. Phys. Suppl., 143, 182

Blandford, R. D. & Begelman, M. C. 1999, MNRAS, 303, L1

Blandford, R. D. & Königl, A. 1979, ApJ, 232, 34

Blandford, R. D. & Ostriker, J. P. 1978, ApJ, 221, L29

Blandford, R. D. & Payne, D. G. 1982, MNRAS, 199, 883

Blandford, R. D. & Rees, M. J. 1974, MNRAS, 169, 395

Blandford, R. D. & Znajek, R. L. 1977, MNRAS, 179, 433

Boldt, E. & Ghosh, P. 1999, MNRAS, 307, 491

Bondi, H. & Hoyle, F. 1944, MNRAS, 104, 273

Boyer, R. H. & Lindquist, R. W. 1967, J. Math. Phys., 8, 265

Bridle, A. & Perley, A. 1984, ARA&A, 22, 319

Camenzind, M. 1986, A&A, 162, 32

Camenzind, M. 2007, Compact Objects in Astrophysics: White Dwarfs, Neutron Stars, and Black Holes (Springer-Verlag Berlin Heidelberg New York)

Cappellari, M., Neumayer, N., Reunanen, J., et al. 2009, MNRAS, 394, 660

Caramete, L. 2010, PhD thesis, in preparation

Carter, B. 1968, Phys. Rev, 174, 1559

Cavaliere, A., Colafrancesco, S., & Scaramela, R. 1991, ApJ, 380, 15

Chandrasekhar, S. 1983, The Mathematical Theory of Black Holes (Oxford University Press), 316

Courant, R. & Friedrichs, K. O. 1977, Supersonic Flow and Shock Waves, Applied Mathematical Sciences, v. 21 (Springer), first published in 1948

Courant, R., Friedrichs, K. O., & Lewy, H. 1928, Mathematische Annalen, 100, 32 (English translation in IBM J. 1967, 11, 215)

Cunningham, G., Lloyd-Evans, J., Pollock, A. M. T., Reid, R. J. O., & Watson, A. A. 1980, ApJ, 236, L71

Curtis, H. D. 1918, Publications of Lick Observatory, 13, 31

Damour, T. 1978, Phys. Rev. D, 18, 3598

Das, S., Kang, H., Ryu, D., & Cho, J. 2008, ApJ, 682, 29

Davis, S. F. 1984, ICASE Rep. 84-20, NASA CR-172373, NASA Langley Research Center

de Gouveia dal Pino, E. M. & Lazarian, A. 2005, A&A, 441, 845

de Gouveia Dal Pino, E. M., Piovezan, P. P., & Kadowaki, L. H. S. 2010, A&A, 518, 5

De Villiers, J.-P. 2008, astro-ph/0802.0848

De Villiers, J.-P. & Hawley, J. F. 2003, ApJ, 589, 458

De Villiers, J.-P., Hawley, J. F., Krolik, J. H., & Hirose, S. 2005, ApJ, 620, 878

Del Zanna, L., Zanotti, O., Bucciantini, N., & Londrillo, P. 2007, A&A, 473, 11

Donea, A. C. & Biermann, P. L. 1996, A&A, 315, 43

Drenkhahn, G. 2002, A&A, 387, 714

Drury, L. O. 1983, Rep. Prog. Phys., 46, 973

Duţan, I. & Biermann, P. L. 2005, in Proceedings of the 40th Rencontres de Moriond: Very High Energy Phenomena in the Universe, held in La Thuile, Italy, 12-19 March 2005, also astro-ph/0505403

Elitzur, M. 2006, New Astron. Rev., 50, 728

Elitzur, M. & Ho, L. C. 2009, ApJ, 701, L91

Elitzur, M. & Shlosman, I. 2006, ApJ, 648, L101

Ewing, A. 1962, Science News Letter, 82, 32

Falcke, H. & Biermann, P. L. 1995, A&A, 293, 665

Falcke, H. & Biermann, P. L. 1999, A&A, 342, 49

Falcke, H., Malkan, M. A., & Biermann, P. L. 1995, A&A, 298, 375

Fanaroff, B. L. & Riley, J. M. 1974, MNRAS, 167, 31

Fendt, C. 2004, ApJ, 608, 378

Fendt, C. & Greiner, J. 2001, A&A, 369, 308

Fermi, E. 1949, Phys. Rev., 75, 1169

Fermi, E. 1954, ApJ, 119, 1

Ferrarese, L., Mould, J. R., Stetson, P. B., et al. 2007, ApJ, 654, 186

Font, J. A. 2008, Living Rev. Relativity (http://www.livingreviews.org/lrr-2008-7), 11, 7

Font, J. A., Ibáñez, J. M., & Papadopoulos, P. 1999, MNRAS, 305, 920

Fragile, C. P. & Meier, D. L. 2009, ApJ, 693, 771

Friedman, J. L. 1978, Commun. Math. Phys., 63, 243

Frolov, V. P. & Novikov, I. D. 1998, Black Hole Physics (Kluwer Academic Publishers)

Fuerst, S. V. & Wu, K. 2004, A&A, 424, 733

Gaisser, T. K. & Stanev, T. 2008, http://pdg.lbl.gov/2008/reviews/rpp2008-rev-cosmic-rays.pdf

Gallant, Y. A. & Achterberg, A. 1999, MNRAS, 305, L6

Gammie, C. F., McKinney, J. C., & Tóth, G. 2003, ApJ, 589, 444

Gan, Z.-M., Wang, D.-X., & Lei, W.-H. 2009, MNRAS, 394, 2310

Gergely, L. A. & Biermann, P. L. 2009, ApJ, 697, 1621

Ghisellini, G., Tavecchio, F., & Chiaberge, M. 2005, A&A, 432, 401

Giacomazzo, B. & Rezzolla, L. 2007, Classical and Quantum Gravity, 24, 235

Ginzburg, V. L. & Syrovatskii, S. I. 1963, Astron. Zh., 40, 466, transl. in Sov. Astron. A.J., 7, 357

Godunov, S. K. 1959, Mat. Sb., 47, 271

Gómez, R., Lehner, L., Marsa, R. L., et al. 1998, Phys. Rev. Lett., 80, 3915

Greenstein, J. L. & Matthews, T. 1963, Nature, 197, 1041

Greisen, K. 1966, Phys. Rev. Lett., 16, 748

Harten, A. 1983, J. Comput. Phys., 9, 357

Harten, A., Lax, P. D., & van Leer, B. 1983, SIAM Rev., 25, 35

Hawking, S. & Ellis, G. 1973, The Large Scale Structure of Spacetime (Cambridge Univ. Press)

Hawking, S. W. 1972, Comm. Math. Phys., 25, 152

Hawley, J. F. & Krolik, J. H. 2006, ApJ, 641, 103

Hazard, C., Mackey, M. B., & Schimmins, A. J. 1963, Nature, 197, 1037

Heinz, S. & Sunyaev, R. A. 2003, MNRAS, 343, L59

Hillas, A. M. 1984, ARA&A, 22, 425

Ho, L. C. 2008, ARA&A, 46, 475

Ho, L. C. 2009, ApJ, 699, 626

Ho, L. C. & Peng, C. Y. 2001, ApJ, 555, 650

Hopkins, P. F. & Hernquist, L. 2009, ApJ, 698, 1550

Hujeirat, A., Camenzind, M., & Livio, M. 2002, A&A, 394, L9

Jokipii, J. R. 1987, ApJ, 313, 842

Junkes, N., Haynes, R. F., Harnett, J. I., & Jauncey, D. L. 1993a, A&A, 269, 29

Junkes, N., Haynes, R. F., Harnett, J. I., & Jauncey, D. L. 1993b, A&A, 274, 1009

Kaiser, C. R. 2006, MNRAS, 367, 1083

Kellermann, K. I., Sramek, R., Schmidt, M., Shapper, D. B., & Green, R. 1989, AJ, 98, 1195

Kerr, R. P. 1963, Phys. Rev. Lett., 11, 237

Kerr, R. P. 2007, To appear in "The Kerr Spacetime", Eds D.L. Wiltshire, M. Visser, and S.M. Scott, Cambridge Univ. Press, also arXiv: gr-qc/0706.1109

Kerr, R. P. & Schild, A. 1965a, in Atti del Congregno Sulla Relativita Generale: Galileo Centenario

Kerr, R. P. & Schild, A. 1965b, in Proc. Sym. in Applied Math. XVII, Ed. R. Finn (American Math. Soc, Providence, Rhode Island), 199

Keshet, U. & Waxman, E. 2005, Phys. Rev. Lett., 94, id. 111102

King, A. R. 2010, MNRAS, 402, 1516

Kirk, J. G. 2005, Invited talk at 22nd Texas Symposium on Relativistic Astrophysics, Stanford, 2004 (with video presentation), also astro-ph/050331

Kirk, J. G., Guthmann, A. W., Gallant, Y. A., & Achterberg, A. 2000, ApJ, 542, 235

Koide, S. 2003, Phys. Rev. D, 67, id. 104010

Koide, S. 2004, ApJ, 606, L45

Koide, S., Kudoh, T., & Shibata, K. 2006, Phys. Rev. D, 74, id. 044005

Koide, S., Meier, D. L., Shibata, K., & Kudoh, T. 2000a, ApJ, 536, 668

Koide, S., Meier, D. L., Shibata, K., & Kudoh, T. 2000b, in Nuclear Physics B Proceedings Supplements, Vol. 80, Proceedings of the Texas Symposium on Relativistic Astrophysics and Cosmology, held in Paris, France, 14-18 December 1998, ed. E. Aubourg, T. Montmerle, & J. Paul (World Scientific Press, Paris), 1

Koide, S., Nishikawa, K.-I., & Mutel, R. L. 1996, ApJ, 463, L71

Koide, S., Shibata, K., & Kudoh, T. 1998, ApJ, 495, L63

Koide, S., Shibata, K., & Kudoh, T. 1999, ApJ, 522, 727

Komissarov, S. S. 2001, MNRAS, 326, L41

Komissarov, S. S. 2004, MNRAS, 350, 1431

Komissarov, S. S. 2005, MNRAS, 359, 801

Krymsky, G. F. 1977, Dokl. Akad. Nauk. SSSR Ser. Fiz., 45, 461

Kuncic, Z. & Bicknell, G. V. 2004, ApJ, 616, 669

Lagage, P. O. & Cesarsky, C. J. 1983, A&A, 125, 249

Laney, C. B. 1998, Computational Gasdynamics (Cambridge University Press), 506, 463, 491

Laor, A. 2003, ApJ, 590, 86

Lawrence, A. & Elvis, M. 1982, ApJ, 256, 410

Lax, P. D. & Wendroff, B. 1960, Commun. Pure Appl. Math., 13, 217

Lee, S.-S., Lobanov, A. P., Krichbaum, T. P., et al. 2008, ApJ, 136, 159

Lei, W.-H., Wang, D.-X., & Ma, R.-Y. 2005, ApJ, 619, 420

Li, L.-X. 2000a, ApJ, 533, L115

Li, L.-X. 2000b, Phys. Rev. D, 61, id. 084016

Li, L.-X. 2000c, ApJ, 531, L111

Li, L.-X. 2002a, ApJ, 567, 463

Li, L.-X. 2002b, A&A, 392, L469

Li, L.-X. 2002c, Phys. Rev. D, 65, id. 084047

Lind, K. R. & Blandford, R. D. 1985, ApJ, 295, 358

Linsley, J. 1963, Phys. Rev. Lett., 10, 146

Livio, M., Ogilvie, G. I., & Pringle, J. E. 1999, ApJ, 512, 100

Lobanov, A. 2007, Invited review at the 8th European VLBI Network Symposium. Published electronically by Proeedings of Science (http://pos.sissa.it), arXiv: astro-ph/0708.4280

Longair, M. 1994, High Energy Astrophysics, Vol. 2 (Cambridge Uni. Press), 259

Lovelace, R. V. E. 1976, Nature, 262, 649

Lovelace, R. V. E. & Romanova, M. M. 2003, ApJ, 596, L159

Lüst, R. 1952, Z. Naturforschg., 7a, 87

Lynden-Bell, D. 1969, Nature, 223, 690

Lynden-Bell, D. 1996, MNRAS, 279, 389

Lynden-Bell, D. 2003, MNRAS, 341, 1360

Lyutikov, M. 2009, MNRAS, 396, 1545

Lyutikov, M. & Blandford, R. D. 2002, in Proceedings of the 1st Niels Bohr Summer Institute on Beaming and Jets in Gamma Ray Bursts, held in Copenhagen, Denmark, 12-30 Aug 2002, ed. R. Ouyed, 146, also astro-ph/0210671

Ma, R.-Y., Yuan, F., & Wang, D.-X. 2007, ApJ, 671, 1981

Macchetto, F., Marconi, A., Axon, D. J., et al. 1997, ApJ, 489, 579

MacCormack, R. W. 1971, in Proceedings of the 2nd Inter. Conf. on Numerical Methods in Fluid Dynamics (Springer: Berlin, Germany), 151

Macdonald, D. A. & Thorne, K. S. 1982, MNRAS, 198, 345

Macri, L. M., Huchra, J. P., Stetson, P. B., et al. 1999, ApJ, 521, 155

Malin, D. F., Quinn, P. J., & Graham, J. A. 1983, ApJ, 272, L5

Markoff, S., Falcke, H., & Fender, R. 2001, A&A, 372, L25

Markoff, S., Nowak, M. A., & Wilms, J. 2005, ApJ, 635, 1203

Marscher, A. P., Jorstad, S. G., D'Arcangelo, F. D., et al. 2008, Nature, 452, 966

McKinney, J. C. 2006, MNRAS, 368, 1561

McKinney, J. C. & Blandford, R. D. 2009, MNRAS, 394, L126

McKinney, J. C. & Gammie, C. F. 2004, ApJ, 611, 977

Meier, D. L. 2001, ApJ, 548, L9

Meier, D. L. 2003, NewAR, 47, 667

Meisenheimer, K., Tristram, K. R. W., Jaffe, W., et al. 2007, A&A, 471, 453

Meli, A., Becker, J. K., & Quenby, J. J. 2008, A&A, 492, 323

Meli, A. & Biermann, P. L. 2006, A&A, 454, 687

Michel, F. C. 1969, ApJ, 158, 727

Miley, G. K. 1980, ARA&A, 18, 165

Miller, L., Peacock, J. A., & Mead, A. R. G. 1990, MNRAS, 244, 207

Millikan, R. A. 1926, Popular Astronomy, 34, 232

Miniutti, G., Ponti, G., Greene, J. E., et al. 2008, MNRAS, 394, 443

Minkowski, R. 1960, ApJ, 132, 908

Mirabel, I. F. & Rodriguez, L. F. 1999, ARA&A, 37, 409

Misner, C. W., Thorne, K. S., & Wheeler, J. A. 1973, Gravitation (Freeman and Co.), 879

Mizuno, Y., Hardee, P., & Nishikawa, K.-I. 2007, ApJ, 662, 835

Mizuno, Y., Lyubarsky, Y., Nishikawa, K.-I., & Hardee, P. E. 2009a, ApJ, 700, 684

Mizuno, Y., Lyubarsky, Y., Nishikawa, K.-I., & Hardee, P. E. 2009b, ApJ, 700, 684

Mizuno, Y., Nishikawa, K.-I., Koide, S., Hardee, P., & Fishman, G. J. 2006a, in Proceedings of the VI Microquasar Workshop: Microquasars and Beyond, ed. T. Belloni (Trieste: SISSA), 45

Mizuno, Y., Nishikawa, K. I., Koide, S., Hardee, P. E., & Fishman, G. J. 2006b, astro-ph/0609004

Mizuno, Y., Yamada, S., Koide, S., & Shibata, K. 2004a, ApJ, 615, 389

Mizuno, Y., Yamada, S., Koide, S., & Shibata, K. 2004b, ApJ, 606, 395

Moran, J. M. 2008, in Frontiers of Astrophysics: A Celebration of NRAO's 50th Anniversary ASP Conference Series, Vol. 395, Proceedings of the conference held 18-21 June, 2007, at the National Radio Astronomy Observatory, Charlottesville, Virginia, USA, ed. A. H. Bridle, J. J. Condon, & G. C. Hunt, 87

Moskalenko, I. V., Stawarz, L., Porter, T. A., & Cheung, C. C. 2009, ApJ, 693, 1261

Mushotzky, R. F. 1982, ApJ, 256, 92

Myong, R. S. & Roe, P. L. 1998, J. Comput. Phys., 147, 545

Nagar, N. & Matulich, J. 2008, A&A, 488, 879

Nagar, N. M., Wilson, A. S., & Falcke, H. 2001, ApJ, 559, L87

Narayan, R. & Yi, I. 1994, ApJ, 428, L13

Niemiec, J. & Ostrowski, M. 2006, ApJ, 641, 984

Nishikawa, K.-I., Koide, S., Sakai, J.-I., et al. 1997, ApJ, 483, L45

Nishikawa, K.-I., Koide, S., Sakai, J.-I., et al. 1998, ApJ, 498, 166

Nishikawa, K.-I., Koide, S., Shibata, K., Kudoh, T., & Sol, H. 2003, in Proceedings of the New Views on MICROQUASARS, ed. P. Durouchoux, Y. Fuchs, & J. Rodriguez (Center for Space Physics, Kolkata), 109

Nishikawa, K.-I., Mizuno, Y., Fuerst, S., et al. 2005a, in Proceedings of the Astrophysical Sources of High Energy Particles and Radiation, ed. T. Bulik, B. Rudak, & G. Madejski (AIP Conf. Proc.), 184

Nishikawa, K.-I., Richardson, G., Koide, S., et al. 2005b, ApJ, 625, 60

Novikov, I. D. & Thorne, K. S. 1973a, in Black Holes Les Astres Occlus, ed. C. DeWitt & B. S. DeWitt (New-York: Gordon & Breach), 343

Novikov, I. D. & Thorne, K. S. 1973b, in Black Holes Les Astres Occlus, ed. C. DeWitt & B. S. DeWitt (New-York: Gordon & Breach), 359

Oke, J. B. 1963, Nature, 197, 1040

Osher, S. & Chakravarthy, S. R. 1984, SIAM J. Num. Anal., 21, 955

Page, D. N. & Thorne, K. S. 1974, ApJ, 191, 499

Parker, R. D. 1958, ApJ, 128, 664

Penzias, A. A. & Wilson, R. W. 1965, ApJ, 142, 419

Piran, T. 2000, Phys. Rep., 333, 529

Pooley, G. G. & Fender, R. P. 1997, MNRAS, 292, 925

Porciani, C., Magliocchetti, M., & Norberg, P. 2004, MNRAS, 355, 1010

Prendergast, K. H. & Burbidge, G. R. 1968, ApJ, 151, L83

Price, R. H. & Thorne, K. S. 1986, Phys. Rev. D, 33, 915

Pudritz, R. E. 2000, Royal Society of London Transactions Series A, 358, 741

Punsly, B. & Coroniti, F. V. 1990, ApJ, 354, 585

Punsly, B., Igumenshchev, I. V., & Hirose, S. 2009, ApJ, 704, 851

Rachen, J. P. 2008, astro-ph/0808.0349

Rejkuba, M. 2004, A&A, 413, 903

Remillard, R. A. & McClintock, J. E. 2006, ARA&A, 44, 49

Richtmyer, R. D. & Morton, K. W. 1994, Difference Methods for Initial-Value Problems (Krieger Pub Co; 2 edition)

Rodríguez, L. F. & Mirabel, I. F. 1997, ApJ, 474, L123

Roe, P. L. 1984, ICASE Rep. 84-53, NASA CR-172478, NASA Langley Research Center

Romanova, M. M., Ustyugova, G. V., Koldoba, A. V., & Lovelace, R. V. E. 2009, MNRAS, 399, 1802

Rybicki, G. B. & Lightman, A. P. 1979, Radiative Processes in Astrophysics (John Wiley & Sons)

Ryu, D., Kang, H., & Biermann, P. L. 1998, A&A, 335, 19

Ryu, D., Kang, H., Cho, J., & Das, S. 2008, Science, 320, 909

Salpeter, E. E. 1964, ApJ, 140, 796

Sanders, R. H. 1983, ApJ, 266, 73

Schawinski, K., Urry, C. M., Virani, S., et al. 2010, ApJ, 711, 284

Schmidt, M. 1963, Nature, 197, 1040

Schutz, B. F. 1980, Geometrical Methods of Mathematical Physics (Cambridge Uni. Press, Cambridge)

Seyfert, C. K. 1943, ApJ, 97, 28

Shakura, N. I. & Sunyaev, R. A. 1973, A&A, 24, 337

Shibata, K. & Uchida, Y. 1986, PASJ, 38, 631

Sikora, M., Stawarz, L., & Lasota, J.-P. 2007, ApJ, 658, 815

Slee, O. B., Sadler, E. M., Reynolds, J. E., & Ekers, R. D. 1994, MNRAS, 269, 928

Stanev, T. 2008, To appear in the Focus Issue 'High Energy Cosmic Rays' of New Journal of Physics, ed. M. Teshima and A.A. Watson

Stone, J. M. & Norman, M. L. 1992, ApJS, 80, 753

Sweby, P. K. 1984, SIAM J. Num. Anal., 21, 995

Thorne, K. S. 1974, ApJ, 191, 507

Thorne, K. S. & Macdonald, D. A. 1982, MNRAS, 198, 339

Thorne, K. S., Price, A. A., & Macdonald, D. A. 1986, Black Holes: The Membrane Paradigm (Yale Univ. Press, New Haven)

Tingay, S. J., Jauncey, D. L., Reynolds, J. E., & et.al. 1998, AJ, 115, 960

Tonry, J. L., Dressler, A., Blakeslee, J. P., & et.al. 2001, ApJ, 546, 681

Toro, E. F. 2009, Riemann Solvers and Numerical Methods for Fluid Dynamics: A Practical Introduction (Springer)

Uchida, Y. & Shibata, K. 1985, PASJ, 37, 515

Ulvestad, J. S. & Ho, L. C. 2001, ApJ, 558, 561

Urry, C. M. & Padovani, P. 1995, PASP, 107, 803

Uzdensky, D. A. 2004, ApJ, 603, 652

Uzdensky, D. A. 2005, ApJ, 620, 889

van der Swaluw, E. & Achterberg, A. 2004, A&A, 421, 1021

van Leer, B. 2006, Commun. Comput. Phys., 1, 192

van Putten, M. H. P. M. 1999, Science, 284, 115

Véron-Cetty, M. P. & Véron, P. 2006, A&A, 455, 773

Vietri, M. 1995, ApJ, 453, 883

Vila, G. S. & Romero, G. E. 2010, MNRAS, 403, 1457

Vir Lal, D. & Ho, L. C. 2010, AJ, 139, 1089

Volonteri, M., Sikora, M., & Lasota, J.-P. 2007, ApJ, 667, 704

Wald, R. M. 1974, Phys. Rev. D, 10, 1680

Wang, D.-X., Lei, W.-H., & Ma, R.-Y. 2003, MNRAS, 342, 851

Wang, D.-X., Ye, Y.-C., Li, Y., & Ge, Z.-J. 2008, MNRAS, 385, 841

Wang, D. X., Ye, Y. C., Li, Y., & Liu, D. M. 2007, MNRAS, 374, 647

Waxman, E. 1995, Phys. Rev. Lett., 75, 386

Weinberg, S. 1972, Gravitation and Cosmology (John Wiley & Sons, Inc.), 360

Wheeler, J. A. 1968, Am. Sci., 59, 1

Whysong, D. & Antonucci, R. 2003, New Astron. Rev., 47, 219

Wiita, P. J. 1985, Phys. Rep., 123, 117

Wilson, J. R. & Mathews, G. J. 2003, Relativistic Numerical Hydrodynamics (Cambridge Uni. Press)

Woosley, S. E. 1993, ApJ, 405, 273

Wu, K., Fuerst, S. V., Mizuno, Y., et al. 2008, ChJAS, 8, 226

Yee, H. C. 1985, in Proceedings of the 6th GAMM Conference on Numerical Methods in Fluid Mechanics (Braunschweig: Vieweg), 399

Yuan, F., Lin, J., Wu, K., & Ho, L. C. 2009, MNRAS, 395, 2183

Zatsepin, G. T. & Kuzmin, V. A. 1966, Pis'ma Zh. Eksp. Teor. Fiz., 4, 114, [English translation in JETP Lett., 4, 78 (1966)]

Zaw, I., Farrar, G. R., & Greene, J. E. 2009, ApJ, 696, 1218

Zhao, C.-X., Wang, D.-X., & Gan, Z.-M. 2009, MNRAS, 398, 1886

Znajek, R. L. 1978, MNRAS, 185, 833

Appendix 1

Derivation of the angular momentum conservation law (Eq. 2.10)

Here, we present the derivation of the angular momentum conservation law for the matter that flows in the ergospheric region of the accretion disk (Eq. 2.10). This derivation is based on the general-relativistic angular-momentum conservation law that describes the structure of a geometrically-thin accretion disk (Page & Thorne 1974). Based on this conservation law, Li (2002) derived the conservation law that includes the BH-disk magnetic connection, and Donea & Biermann (1996) derived the conservation law that includes the jet. In a slightly different manner, our result is obtained when both the BH-disk magnetic connection and the jet formation are considered.

The angular-momentum conservation law can be obtained by contracting the energy-momentum tensor of the matter in the disk with the axial Killing vector of Kerr space-time ($\partial/\partial\phi$). The energy-momentum tensor $\mathbf{T}$ can be decomposed with respect to the 4-velocity field $\mathbf{u}$ as (Page & Thorne 1974)

$$\mathbf{T} = \rho_0(1+\Pi)\mathbf{u}\otimes\mathbf{u} + \mathbf{t} + \mathbf{u}\otimes\mathbf{q} + \mathbf{q}\otimes\mathbf{u}, \tag{4.99}$$

where ρ_0 is, again, the density of rest mass, Π is the specific internal energy, $\mathbf{t}$ is the stress tensor in the averaged rest frame (which is a second-rank, symmetric tensor orthogonal to $\mathbf{u}$, $\mathbf{t}\cdot\mathbf{u} = \mathbf{u}\cdot\mathbf{t} = 0$), and $\mathbf{q}$ is the energy-flow vector, which is a 4-vector orthogonal to $\mathbf{u}$, $\mathbf{q}\cdot\mathbf{u} = 0$. Here, geometrical units are used: $c = G = k\,(\text{Boltzmann constant}) = 1$.

For a geometrically thin accretion disk, the internal energy is negligible compared to the gravitational potential energy, $\Pi \ll 1 - E^{\dagger}$.

Page & Thorne (1974) assumed that the only energy flow is in the vertical direction, and the angular momentum is transported mechanically by torques in the disk (by magnetic stress, viscous stress, etc.). This means that: $< t^z_\phi >=< t^z_t >=< t^z_r >=< q_\phi >=< q_t >=< q_r >= 0, \quad \text{at} \quad z = \pm h.$

The quantity $F(r) =< q^z(r, z = h) >=< -q^z(r, z = -h) >$ represents the energy per unit proper time (τ) per unit proper area (A) flowing out of upper face of disk, as measured by an observer on the upper face who orbits with the time-averaged motion of the disk matter (or the time-averaged flux flowing out of lower face), and $W^r_\phi \equiv \int_{-h}^{+h} < t^r_\phi > dz = (g^{rr})^{1/2}\times$ (time-averaged torque per unit circumference acting across a cylinder at radius r, due to the stresses in the disk).

In differential form, the angular-momentum conservation law reads

$$\nabla\cdot\mathbf{J} = 0, \quad \mathbf{J} \equiv \mathbf{T}\cdot\partial/\partial\phi = (\text{density-flux 4-vector for angular momentum}). \tag{4.100}$$

This conservation law can be simplified to a useful form as in equation (23) of Page & Thorne (1974), where the differential form of the conservation law is converted to an integral form by integrating over the 3-volume of the disk between radius r and $r + \Delta r$. Gauss theorem

is then applied to convert the volume integral to a surface integral. Thus,

$$
\begin{aligned}
0 &= \int_{\mathcal{V}} \nabla \cdot \mathbf{J} \sqrt{|g|} dt dr dz d\phi = \int_{\partial\mathcal{V}} \mathbf{J} \cdot d^3\mathbf{\Sigma} = \int_{\partial\mathcal{V}} T^{\alpha}_{\phi} d^3\Sigma_{\alpha} \\
&= \left\{ \int_{-h}^{h} \int_{t}^{t+\Delta t} \int_{0}^{2\pi} \left[\rho_0 (1+\Pi) u_\phi u^r + t^r_\phi + u_\phi q^r + q_\phi u^r \right] (-g)^{1/2} \, d\phi \, dt \, dz \right\}_{r}^{r+\Delta r} \\
&+ \left\{ \int_{r}^{r+\Delta r} \int_{t}^{t+\Delta t} \int_{0}^{2\pi} \left[\rho_0 (1+\Pi) u_\phi u^z + t^z_\phi + u_\phi q^z + q_\phi u^z \right] (-g)^{1/2} \, d\phi \, dt \, dr \right\}_{-h}^{h} \\
&+ \{\text{total angular momentum in the 3-volume}\}_{t}^{t+\Delta t} ,
\end{aligned}
\tag{4.101}
$$

which is equation (23) of Page & Thorne (1974). In the first brace, one can neglect Π (negligible specific heat), as well as the terms $u_\phi q^r$ and $q_\phi u^r$ by comparison with the term $u_\phi q^z$ of the second brace (negligible heat transport along the plane of the disk). Therefore, the first brace reduces to

$$
\left\{ \int_{-H}^{H} (2\pi \Delta t) \left(< \rho_0 > u_\phi u^r + < t^r_\phi > \right) \sqrt{|g|} dz \right\}_{r}^{r+\Delta r} . \tag{4.102}
$$

Now, we calculate this brace taking into account the jet formation as

$$
\left\{ (2\pi \, \Delta t)(\Sigma L^\dagger u^r + W^r_\phi) \sqrt{|g|} \right\}_{r}^{r+\Delta r} = \Delta t \, \Delta r \left[-(\dot{M}_{\rm D} - \dot{M}_{\rm jets}) L^\dagger + 2\pi r W^r_\phi \right]_{,r} , \tag{4.103}
$$

where we made use of the rest-mass conservation law that includes the mass flow into the jets , $\dot{M}_{\rm D} - \dot{M}_{\rm jets} = -2\pi r \Sigma u^r$.

In the second brace of equation 4.101, we keep the term u^z that accounts for the particle motion in the vertical direction and obtain

$$
2 \, (2\pi \, \Delta t)(\Sigma u^z + F) L^\dagger \sqrt{|g|} \Delta r = 2 \, (2\pi r \, \Delta t \, \Delta r) J L^\dagger , \tag{4.104}
$$

where $J = \Sigma u^z + F$ denotes the total flux of energy (of particle and magnetic origin) transported by jets.

The third brace of equation 4.101 is negligible compared with the first brace since, by assumption (Page & Thorne 1974), the time interval Δt is small enough that during this interval the external geometry of the BH changes negligibly.

Combining equations 4.103 and 4.104, equation (23) of Page & Thorne becomes

$$
\left[(\dot{M}_{\rm D} - \dot{M}_{\rm jets}) L^\dagger - 2\pi r W^r_\phi \right]_{,r} = 4\pi J L^\dagger . \tag{4.105}
$$

Using the definition of the magnetic torque produced by the BH on both surfaces of the accretion disk given by Li (see Eqs. 2.11 and 2.14), the angular momentum conservation law (Eq. 4.105), including c, becomes

$$
\frac{d}{dr} \left[(1 - q_{\rm jets}) \, \dot{M}_{\rm D} c L^\dagger \right] + 4\pi r H = 4\pi r J L^\dagger , \tag{4.106}
$$

when both the BH-disk magnetic connection and the jet formation are considered.

Appendix 2

Derivation of the GRMHD equations (Eq. 4.51)

The GRMHD system of equations is a set of eight non-linear hyperbolic partial differential equations (PDEs) which we write in conserved form. The GRMHD equations can be derived from the fundamental conservation laws: the rest-mass, angular momentum, and energy conservation laws. For the following calculations, we use the quantities listed below (see Eq. 4.15 and comments there):

$$\begin{aligned} u^t &= \frac{W}{\alpha}, \\ \frac{u^i}{W} &= v^i - \frac{\beta^i}{\alpha}, \\ \frac{u_i}{W} &= v_i. \end{aligned} \tag{4.107}$$

The conservative variables are defined as

$$\begin{aligned} D &= -J^\mu n_\mu = -\rho u^\mu n_\mu = \rho W, \\ S_j &= -T^\mu_\nu n_\mu (\partial_j)^\nu = \alpha T^t_j = \alpha \left[(\rho h + b^2) u^t u_j + \left(p + \frac{b^2}{2} \right) g^t_j - b^t b_j \right] = (\rho h + b^2) W^2 v_j - \alpha b^t b_j, \\ &\quad \text{where } (\partial_j)^\nu = \delta^\nu_j, \\ E &= T^{\mu\nu} n_\mu n_\nu = \alpha^2 T^{tt} = \alpha^2 \left[(\rho h + b^2) u^t u^t + \left(p + \frac{b^2}{2} \right) g^{tt} - (b^t)^2 \right] \\ &= (\rho h + b^2) W^2 - \left(p + \frac{b^2}{2} \right) - \alpha^2 (b^t)^2. \end{aligned} \tag{4.108}$$

In practical numerical calculations, it is useful to use the quantity $\tau = E - D$.

Next, we calculate the components of the energy-momentum tensor for GRMHD:

$$\begin{aligned} T^{tt} &= \frac{1}{\alpha^2} E, \\ T^{ti} &= (\rho h + b^2) u^t u^i + \left(p + \frac{b^2}{2} \right) g^{ti} - b^t b^i = (\rho h + b^2) \frac{W^2}{\alpha} \left(v^i - \frac{\beta^i}{\alpha} \right) + \left(p + \frac{b^2}{2} \right) \frac{\beta^i}{\alpha} - b^t b^i, \\ T^t_i &= \frac{1}{\alpha} S_i, \\ T^i_j &= (\rho h + b^2) u^i u_j + \left(p + \frac{b^2}{2} \right) g^i_j - b^i b_j = S_j \frac{u^i u_j}{W u_j} \left(v^i - \frac{\beta^i}{\alpha} \right) + \left(p + \frac{b^2}{2} \right) \delta^i_j - b^i b_j \\ &= S_j \left(v^i - \frac{\beta^i}{\alpha} \right) + \left(p + \frac{b^2}{2} \right) \delta^i_j - b^i b_j. \end{aligned} \tag{4.109}$$

In the following, we derive the conservation laws for GRMHD. We start with the rest-mass conservation law, which in the differential form reads

$$J^\mu_{;\mu} = 0, \tag{4.110}$$

where $J^\mu = \rho u^\mu$ denotes the rest-mass flux. The above can be evaluated as

$$\boxed{\begin{aligned} J^\mu{}_{;\mu} &= \frac{1}{\sqrt{-g}}(\sqrt{-g}J^\mu)_{,\mu} = \frac{1}{\sqrt{-g}}(\sqrt{-g}\rho u^\mu)_{,\mu} = \\ &= \frac{1}{\sqrt{-g}}\left(\alpha\sqrt{\gamma}\rho\frac{W}{\alpha}\right)_{,t} + \frac{1}{\sqrt{-g}}\left(\sqrt{-g}\rho W(v^i - \frac{\beta^i}{\alpha})\right)_{,i} = \\ &= \frac{1}{\sqrt{-g}}(\sqrt{\gamma}D)_{,t} + \frac{1}{\sqrt{-g}}D\left(v^i - \frac{\beta^i}{\alpha}\right)_{,i} = 0 \end{aligned}}, \tag{4.111}$$

which represents the first GRMHD equation. Let us obtain the remaining seven. To recap, the Eulerean basis consists of four vectors $\mathbf{e}_\mu = \{\mathbf{n}, \partial_i\}$. Consider now the expression

$$(T^\mu{}_\nu(\mathbf{e}_\gamma)^\nu)_{;\mu} = T^\mu{}_{\nu;\mu}(\mathbf{e}_\gamma)^\nu + T^{\mu\nu}(\mathbf{e}_\gamma)_{\nu;\mu} = T^{\mu\nu}\left((\mathbf{e}_\gamma)_{\nu,\mu} - \Gamma^\lambda_{\nu\mu}(\mathbf{e}_\gamma)_\lambda\right), \tag{4.112}$$

where $T^\mu{}_{\nu;\mu} = 0$ from the conservation law of the energy-momentum tensor.

Next, we obtain the angular-momentum and energy conservation laws by evaluating the above expression. First, we consider the left-hand side of equation(4.112) for the index $\gamma = t$,

$$\begin{aligned} &(T^\mu{}_\nu(\mathbf{e}_t)^\nu)_{;\mu} = (T^{\mu\nu}n_\nu)_{;\mu} = (-\alpha T^{\mu t})_{;\mu} = -\frac{1}{\sqrt{-g}}\left\{(\sqrt{-g}\alpha T^{tt})_{,t} + (\sqrt{-g}\alpha T^{it})_{,i}\right\} \\ &= -\frac{1}{\sqrt{-g}}\left\{(\sqrt{\gamma}\alpha^2 T^{tt})_{,t} + \left(\sqrt{-g}\alpha\left[(\rho h + b^2)\frac{W^2}{\alpha}\left(v^i - \frac{\beta^i}{\alpha}\right) + \left(p + \frac{b^2}{2}\right)\frac{\beta^i}{\alpha^2} - b^i b^t\right]\right)_{,i}\right\} \\ &= -\frac{1}{\sqrt{-g}}\left\{(\sqrt{\gamma}E)_{,t} + \left(\sqrt{-g}\left[\left(E + \left(p + \frac{b^2}{2}\right)\right)\left(v^i - \frac{\beta^i}{\alpha}\right) + \left(p + \frac{b^2}{2}\right)\frac{\beta^i}{\alpha} - \alpha b^i b^t\right]\right)_{,i}\right\} \\ &= -\frac{1}{\sqrt{-g}}\left\{(\sqrt{\gamma}E)_{,t} + \left(\sqrt{-g}\left[E\left(v^i - \frac{\beta^i}{\alpha}\right) + \left(p + \frac{b^2}{2}\right)v^i - \alpha b^i b^t\right]\right)_{,i}\right\}, \end{aligned} \tag{4.113}$$

where we used the fact that $(\rho h + b^2)W^2 = E + \left(p + \frac{b^2}{2}\right)$.

The right-hand side of equation (4.112) reads

$$T^{\mu\nu}\left((\mathbf{e}_t)_{\nu,\mu} - \Gamma^\lambda_{\nu\mu}(\mathbf{e}_t)_\lambda\right) = -T^{\mu t}\alpha_{,\mu} + \alpha\Gamma^t_{\nu\mu}T^{\mu\nu} = \alpha\left(-T^{\mu t}(\ln\alpha)_{,\mu} + \Gamma^t_{\nu\mu}T^{\mu\nu}\right). \tag{4.114}$$

Substituting equations (4.113) and (4.114) for equation (4.112), we obtain the second GRMHD equation (energy conservation law)

$$\boxed{\begin{aligned} &\frac{1}{\sqrt{-g}}\left\{(\sqrt{\gamma}E)_{,t} + \left(\sqrt{-g}\left[E\left(v^i - \frac{\beta^i}{\alpha}\right) + \left(p + \frac{b^2}{2}\right)v^i - \alpha b^i b^t\right]\right)_{,i}\right\} \\ &= \alpha\left(-T^{\mu t}(\ln\alpha)_{,\mu} + \Gamma^t_{\nu\mu}T^{\mu\nu}\right) \end{aligned}}. \tag{4.115}$$

Next, we consider the left-hand side of Eq. (4.112) for the index $\gamma = j$,

$$\begin{aligned}(T^{\mu}{}_{\nu}(\mathbf{e}_j)^{\nu})_{;\mu} = (T^{\mu}{}_{j})_{;\mu} &= \frac{1}{\sqrt{-g}}\left\{\left(\sqrt{-g}T^{\mu}{}_{j}\right)_{,\mu}\right\} \\ &= \frac{1}{\sqrt{-g}}\left\{(\sqrt{-g}T^{t}{}_{j})_{,t} + (\sqrt{-g}T^{i}{}_{j})_{,i}\right\} \\ &= \frac{1}{\sqrt{-g}}\left\{(\sqrt{-\gamma}S_j)_{,t} + \left(\sqrt{-g}\left[S_j\left(v^i - \frac{\beta^i}{\alpha}\right) + \left(p + \frac{b^2}{2}\right)\delta^i_j - b^i b_j\right]\right)_{,i}\right\}.\end{aligned} \tag{4.116}$$

The right-hand side of equation reads

$$T^{\mu\nu}\left((\mathbf{e}_j)_{\nu,\mu} - \Gamma^{\lambda}_{\nu\mu}(\mathbf{e}_j)_{\lambda}\right) = T^{\mu\nu}\left(\left[g_{\nu\lambda}(\mathbf{e}_j)^{\lambda}\right]_{,\mu} - \Gamma^{\lambda}_{\nu\mu}g_{\lambda\sigma}(\mathbf{e}_j)^{\sigma}\right) = T^{\mu\nu}\left(g_{\nu j,\mu} - \Gamma^{\lambda}_{\nu\mu}g_{\lambda j}\right). \tag{4.117}$$

Substituting equations (4.116) and (4.117) for equation (4.112), we obtain the other three GRMHD equations (angular-momentum conservation law),

$$\boxed{\begin{aligned}&\frac{1}{\sqrt{-g}}\left\{(\sqrt{-\gamma}S_j)_{,t} + \left(\sqrt{-g}\left[S_j\left(v^i - \frac{\beta^i}{\alpha}\right) + \left(p + \frac{b^2}{2}\right)\delta^i_j - b^i b_j\right]\right)_{,i}\right\}. \\ &= T^{\mu\nu}\left(g_{\nu j,\mu} - \Gamma^{\lambda}_{\nu\mu}g_{\lambda j}\right)\end{aligned}} \tag{4.118}$$

The remaining three GRMHD equations are the three components of the induction equation, which was derived in Section 4.35. The GRMHD equations can be written in a compact form

$$\boxed{\frac{1}{\sqrt{|g|}}\frac{\partial(\sqrt{\gamma}\,\mathbf{U})}{\partial t} + \frac{1}{\sqrt{|g|}}\frac{\partial(\sqrt{|g|}\,\mathbf{F})}{\partial x^i} = \mathbf{S}}, \tag{4.119}$$

where the quantities $\mathbf{U}$ (conserved variables), $\mathbf{F}$ (fluxes), and $\mathbf{S}$ (source terms) are

$$\mathbf{U} = \begin{bmatrix} D \\ S_j \\ \tau \\ B^i \end{bmatrix}, \tag{4.120}$$

$$\mathbf{F} = \begin{bmatrix} D\tilde{v}^i \\ S_j\tilde{v}^i + \left(p + \frac{b^2}{2}\right)\delta^i_j - b^i b_j \\ \tau\tilde{v}^i + \left(p + \frac{b^2}{2}\right)v^i - \alpha^2(b^t)^2 + D\tilde{v}^i \\ \tilde{v}^i B^j - \tilde{v}^j B^i \end{bmatrix}, \tag{4.121}$$

$$\mathbf{S} = \begin{bmatrix} 0 \\ T^{\mu\nu}\left(\frac{\partial g_{\nu j}}{\partial x^{\mu}} - \Gamma^{\sigma}_{\nu\mu}g_{\sigma j}\right) \\ \alpha\left(T^{\mu t}\frac{\partial \ln\alpha}{\partial x^{\mu}} - T^{\mu\nu}\Gamma^{t}_{\nu\mu}\right) \\ 0^i \end{bmatrix}, \tag{4.122}$$

where $\tilde{v}^i = \left(v^i - \frac{\beta^i}{\alpha}\right)$ and $0^i \equiv (0,0,0)^{\mathrm{T}}$.

List of Publications

1. *Ultra-High-Energy Cosmic Ray Contribution from the Spin-Down Power of Black Holes*, Duţan, I., 2010, to be submitted to MNRAS

2. *Magnetic Connection Model for Launching Relativistic Jets from a Kerr Black Hole*, Duţan, I., 2010, submitted to MNRAS (astro-ph/1001.5434)

3. *Relativistic Jets in Active Galactic Nuclei: Importance of Magnetic Fields*, Duţan, I. and Biermann, P. L., 2008, in Proceedings of the Relativistic Astrophysics and Cosmology - Einstein's Legacy, held in Munich, Germany, 07-11 November 2005. ESO Astrophysics Symposia, p. 431-432

4. *High Energy Phenomena in Active Galactic Nuclei: Relativistic Jets*, Duţan, I. and Biermann, P. L., 2005, in Proceedings of the Astrophysical Sources of High Energy Particles and Radiation, held in Torun, Poland, 20-24 June 2005. Eds. T. Bulik, B. Rudak, and G. Madejski. AIP Conference Proceedings, vol. 801, p. 212-213

5. *Jets Driven by Accretion onto Rotating Black Holes*, Duţan, I. and Biermann, P.L., 2005, in Proceedings of the 40th Rencontres de Moriond: Very High Energy Phenomena in the Universe, held in La Thuile, Italy, 12-19 March 2005 (also astro-ph/0505403)

6. *The Efficiency of Using Accretion Power of Kerr Black Holes*, Duţan, I. and Biermann, P.L., 2005, in Proceedings of the 14th Course of the International School of Cosmic Rays Astrophysics, a NATO Advanced Study Institute, held in Erice, Italy, 2-13 July 2004. Eds. M. M. Shapiro, T. Stanev, and J. P. Wefel. NATO science series II: Mathematics, physics and chemistry, vol. 209, p. 175-181 (also astro-ph/0410194)